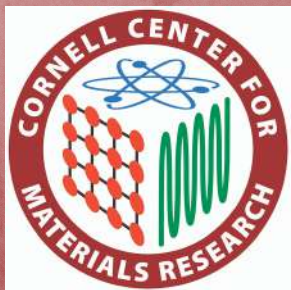
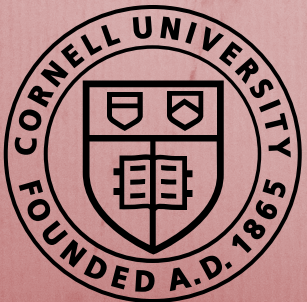




# CORNELL CENTER FOR MATERIALS RESEARCH

REU 2018

RESEARCH PAPERS





## TABLE OF CONTENTS

### Student

- 03 Shaden Albahrani
- 07 Rajeh Alsaadi
- 15 Aaron Coe
- 20 Natalie Cummings
- 26 Rebecca Davis
- 33 Jamie Holber
- 39 Saman Khorasi
- 45 Richard Liebert
- 51 Erin Meyers
- 55 Matthew Molinaro
- 66 Joshua Morales
- 71 Malia Okamura
- 76 Marcos Rodriguez-Munoz
- 78 Mathias Rodriguez
- 98 Margaret "Meg" Tetzloff
- 103 Peter Tomlinson
- 111 Whitney Tso
- 118 Maritha Wang
- 118 Deidra Ward
- 128 John Wilson
- 137 Jiatian "Crystal" Wu

### Faculty Advisor

- Prof. Larry Bonassar
- Prof. Greg Fuchs
- Prof. Dan Ralph
- Prof. Gennady Shvets
- Prof. Kaja Nowack
- Prof. Greg Fuchs
- Prof. Tobias Hanrath
- Prof. Itai Cohen
- Prof. Brett Fors
- Prof. Margaret Frey
- Prof. Héctor Abruna
- Prof. Andrej Singer
- Prof. Larry Bonassar
- Prof. Chris Alabi
- Prof. Chris Ober
- Prof. Nandini Ananth
- Prof. Richard Robinson
- Prof. Paul McEuen
- Prof. Julie Goddard
- Prof. Jeevak Parpia
- Prof. Brad Ramshaw

# **Stribeck Curve Analysis of the Temporomandibular Joint Disc**

Shaden A. Albahrani<sup>1</sup>, Jill M. Middendorf<sup>2</sup>, and Lawrence J. Bonassar<sup>2</sup>

<sup>1</sup>Virginia Tech, Blacksburg, VA, <sup>2</sup>Cornell University, Ithaca, NY

## **Abstract**

Disorders in the temporomandibular joint (TMJ) are common, and current treatments are often temporary. Previous studies showed that the friction may be linked to TMJ disorders. Friction also depends on anatomic regions and sliding direction<sup>2,3</sup>. In this study, we aim to identify the Stribeck curve for the TMJ disc. A glass tribometer was used to obtain the frictional coefficients of the TMJ disc in 6-month-old pigs. The coefficients were fit on a Stribeck curve, and the boundary friction, minimum friction, and transition number were obtained. We found that the minimum friction for samples slid in the medial lateral direction were higher than those for samples slid in the anterior-posterior direction. We also found that the posterior region has the highest transition number, which could indicate that this region decays or dislocates sooner. The Stribeck curve for the healthy TMJ disc can be used as a framework for future studies on TMJ disorders.

## **Introduction**

Temporomandibular joint (TMJ) disorders are very common, affecting 20-25% of the population<sup>1</sup>. Current treatments are usually temporary and require more surgery. Since TMJ disorders are typically associated with abnormal mechanical loading, it is important to understand the mechanics of a healthy TMJ before exploring different treatment options. The healthy TMJ disc acts as a shock absorber during normal function. The disc consists mainly of highly stiff collagen fibers running along the anterior-posterior direction, and joint motion occurs in both the medial lateral and anterior posterior directions.

Previous studies show that TMJ disc frictional coefficients depend on variations in composition and organization associated with anatomic locations and sliding direction<sup>2,3</sup>. Despite such data, there remains a lack of an overarching framework to understand the frictional behavior of the TMJ disc. Stribeck curves have been used for more than century to describe the frictional behavior of traditional engineering materials, and recently, modifications to this framework have been shown to describe soft materials and tissues such as cartilage. Stribeck curves plot the friction coefficient as a function of normal load, fluid viscosity and sliding speed. This curve explains why abnormal mechanical loading on the TMJ, such as high load or speed, would affect the friction in the joint and cause potential dislocation or other disorders. This study

aims to assess whether the Stribeck framework can describe frictional behavior of the TMJ disc and whether it reveals differences in tissue behavior based on anatomic location and sliding direction.

## Method

TMJ discs from 6-month-old pigs ( $n = 6-7$ ) were extracted, then 5mm diameter plugs were taken from four anatomic locations on the disc: medial, lateral, anterior, and posterior (Fig 1A). Friction coefficients were obtained by sliding plugs in both the medial-lateral (ML) and anterior-posterior (AP) direction on a custom cartilage on glass tribometer (Fig 1B). To obtain 5 orders of magnitude in the Sommerfeld number, we slid each plug at 9 speeds (0.1, 0.3, 0.5, 0.7, 1, 3, 5, 7, 10 mm/s) in 3 concentrations of dextran (0%, 9%, and 23%) with viscosities of 1 mPa-s, 31.5mPa-s, and 218 mPa-s. Frictional coefficients obtained were fit on a Stribeck curve to obtain the boundary friction, minimum friction, and transition number.

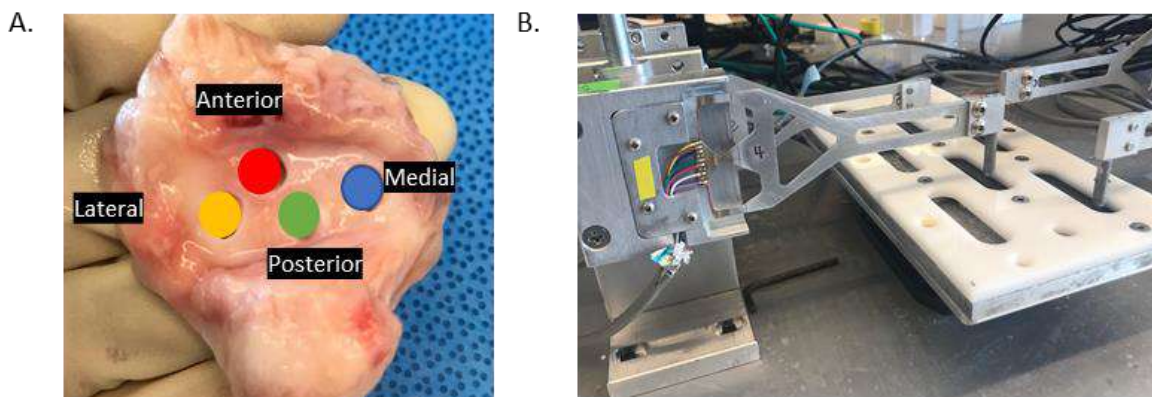
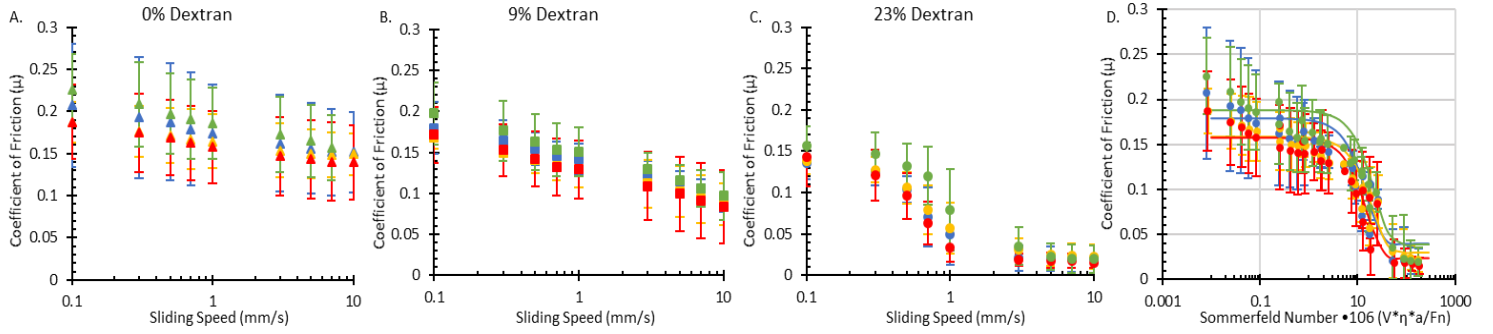


Figure 1: A) Plugs taken from anatomic locations and slid in B) a custom cartilage on glass tribometer.

## Results and Discussion

Samples slid in the AP direction in 0% dextran showed relatively constant coefficients as speed increased (Fig 2A). Increasing the speed in 9% dextran showed larger decrease in coefficients (Fig 2B). Sliding in 23% dextran, which had the highest viscosity, showed a drastic drop in coefficients as speed increased (Fig 2C). As the concentrations of dextran increased, the decrease in friction coefficients was more drastic as speed increased. The frictional behavior of TMJ disc tissue was well described by Stribeck curves (Fig 2D,  $R^2 > 0.8$ ). This is a good indicator that the Stribeck curve can be used to understand the frictional behavior of the TMJ.



**Figure 3:** Samples slid in A-P direction show A) stable frictional coefficients in 0% dextran, B) some decrease in 9% dextran, and C) drastic drop in 23% dextran. D) Stribeck curve for A-P direction.

Samples slid in the ML direction showed similar results. Sliding in 0% dextran showed coefficients of friction remaining in the range of 0.2 (Fig 3A). In 9% dextran, which has a higher viscosity, a more noticeable decrease in coefficients is observed as speed increases (Fig 3B). In 23% dextran with the highest viscosity, coefficients of friction drop the most drastically (Fig 3C). Similar to sliding in the AP direction, the frictional coefficients for the ML direction map well onto a Stribeck curve (Fig 3D,  $R^2 > 0.8$ ).

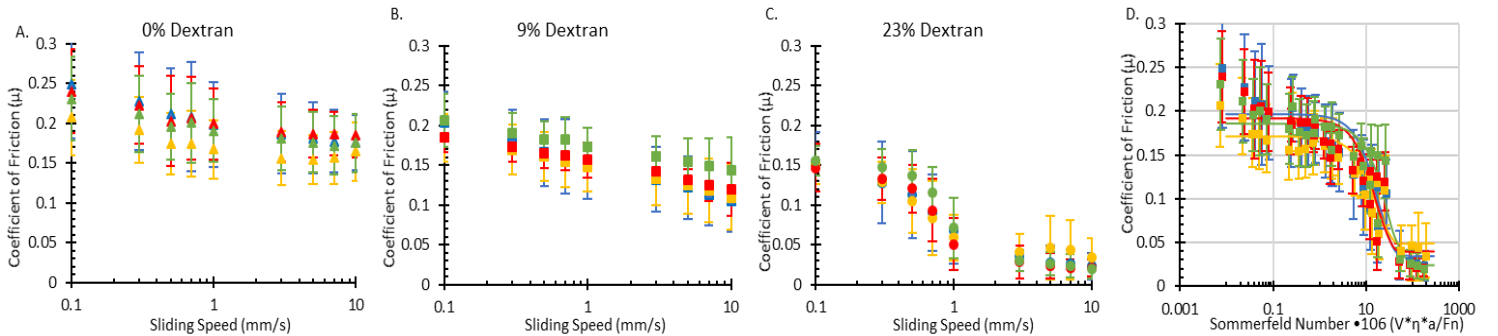


**Figure 2:** Samples slid in M-L direction show A) stable frictional coefficients in 0% dextran, B) some decrease in 9% dextran, and C) drastic drop in 23% dextran. D) Stribeck curve for A-P direction.

The ML direction friction coefficient for high and low friction was always higher than the AP direction at a given anatomic location, except for low friction in the posterior and medial region (Fig 4A, B). This can be a result of the stiffness of the fibers that makes sliding along the fibers easier than sliding against them. There does not seem to be a significant different in the transition number between the anatomic locations. However, the posterior region's transition number (Fig 4C) was almost twice that of other regions. Such differences may suggest that this region may be more susceptible to damage during abnormal loading.

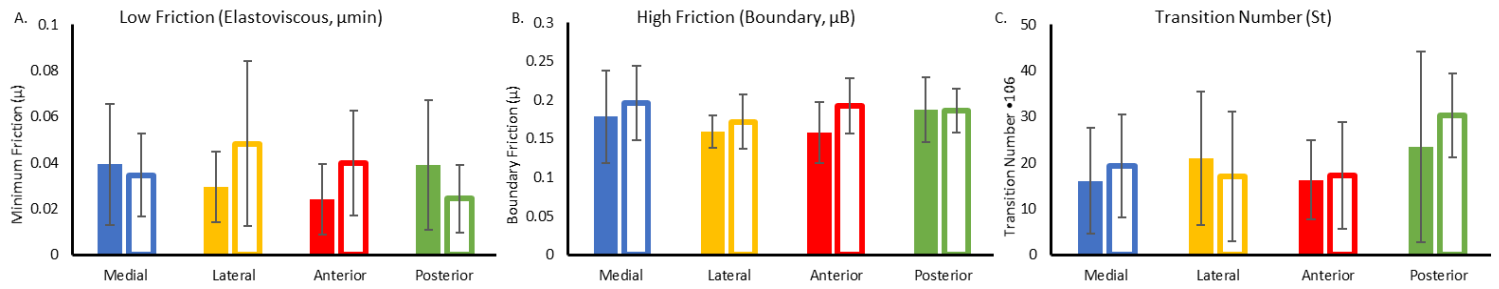


**Figure 4: Summary of A) low friction, B) boundary friction, and C) transition numbers.**

## Conclusion

Our results show that Stribeck curves can be used as a tool to understand TMJ disc lubrication. The changes we observed based on anatomic location and sliding direction can be used to explore the effect of friction on TMJ disc decay or dislocation at different stages. Future studies can begin to explore new treatment options and use the Stribeck curve to better understand the frictional behavior of the TMJ.

## Acknowledgements

This work was supported by the Cornell Center for Materials Research funded through NSF grant (DMR 1460428 and DMR - 1719875).

## References

- [1] M. S. Detamore and K. A. Athanasiou, “Structure and function of the temporomandibular joint disc: Implications for tissue engineering,” *J. Oral Maxillofac. Surg.*, vol. 61, no. 4, pp. 494–506, Apr. 2003.
- [2] B. K. Zimmerman *et al.*, “Role of interstitial fluid pressurization in TMJ lubrication.,” *J. Dent. Res.*, vol. 94, no. 1, pp. 85–92, Jan. 2015.
- [3] E. D. Bonnevie, L. Barito, M. Aldridge, L. Wang, D. L. Burris, and X. L. Lu, “Frictional Coefficient of TMJ Disc and Condylar Cartilage,” in *ASME 2012 Summer Bioengineering Conference, Parts A and B*, 2012, p. 295.

# Temperature and Resistance Characterization Device for Magneto-thermal Microscopy

Rajeh Alsaadi<sup>1</sup>, Isaiah Gray<sup>2</sup>, Gregory D. Fuchs<sup>2</sup>

<sup>1</sup>Department of Materials Science and Engineering, The Pennsylvania State University, University Park, University Park, PA 16808, United States

<sup>2</sup>Department of Applied and Engineering Physics, Cornell University, Ithaca, NY 14853

**Abstract-** We developed an experimental set-up to measure local change in temperature based on change in resistance. The set-up helps a new microscopy technique based on anomalous Nernst effect. A pulsed laser generates a thermal gradient perpendicular to the local magnetization, which results in voltage drop. Having a full profile of the thermal gradient is critical for this microscopy. Thermal gradient can be known by local change in temperature induced by laser.

## INTRODUCTION

Our group has developed a magneto-thermal microscopy technique to image magnetic dynamics at the nanoscale, based on magneto-thermal effects<sup>1</sup>. In magnetic metals, we use the anomalous Nernst effect, in which a thermal gradient produces a local electric field perpendicular to the local magnetization:

$$\mathbf{E}(\mathbf{x},t) = -N \nabla T(\mathbf{x},t) \times \mu_0 \mathbf{M}(\mathbf{x},t),$$

where  $N$  is the anomalous Nernst coefficient,  $\mu_0$  is the permeability of free space,  $\nabla T(x,t)$  is the thermal gradient and  $M(x,t)$  is the local magnetization. We apply local thermal gradients in the by focusing a pulsed laser to 700 nm spot and scan over the magnetic metal (figure 1).

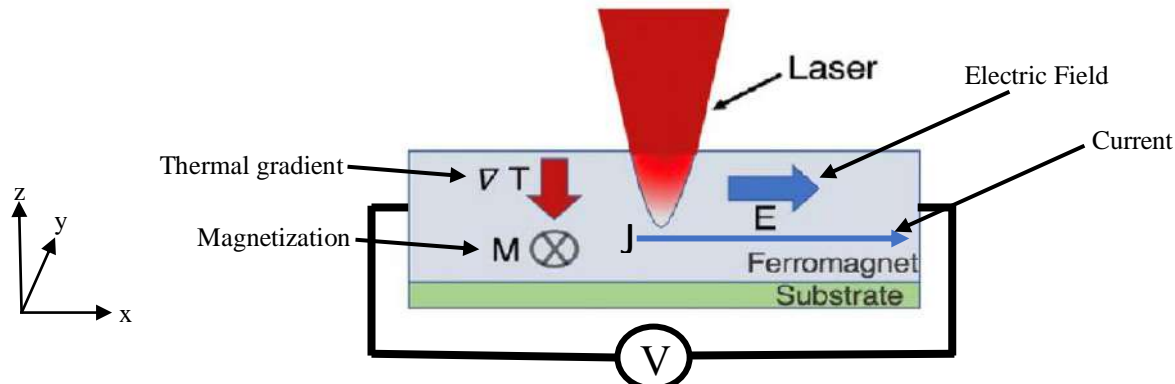


Figure 1. Diagram of anomalous Nernst effect

The electric field creates a voltage drop proportional to the in-plane magnetization component perpendicular to the voltage contacts. As shown in figure 1, the applied thermal gradient in z-direction produces voltage in x-direction perpendicular to the local magnetization in y-direction. The voltage is represented by this equation:

$$V = \alpha M_y \nabla T_z,$$

where  $\alpha$  contains the material-dependent Nernst coefficient and the geometrical constant.

The resulting voltage does not indicate the magnitude of thermal gradient and the material's Nernst coefficient; we have to figure them out in order to make the measurement more quantitative to measure the magnetization. To address this issue, we shine the laser and apply a current along the x-axis. The laser-induced heating will increase local resistance and thus result in change of measured voltage. The combined voltage is represented by:

$$V = \alpha M_y \nabla T_z + \beta J \Delta \rho(T),$$

where  $\beta$  is a geometrical constant,  $J$  is the current density and  $\Delta \rho(T)$  is resistivity. We have two terms in our combined voltage equation that depend on change of temperature,  $\nabla T_z$  and  $\Delta \rho(T)$ . We want to know the change in temperature locally to solve for our two unknowns.

The thermal gradient is the derivative of temperature with respect to position, as shown figure 2. We used a finite element simulation program, COMSOL, to simulate laser heating profile of iron cobalt boron (FeCoB) capped with ruthenium (Ru). We simulated a 4 nm thick FeCoB capped with 4 nm Ru film with skin depth of 30 nm of laser, shown in figure 2. As shown in figure 2, we can have a very close linear approximation of thermal gradient by taking temperature derivate with respect to time,  $\nabla T(x,t) \approx \Delta T / t$ . However, we are not sure how much the laser is heating up the material.

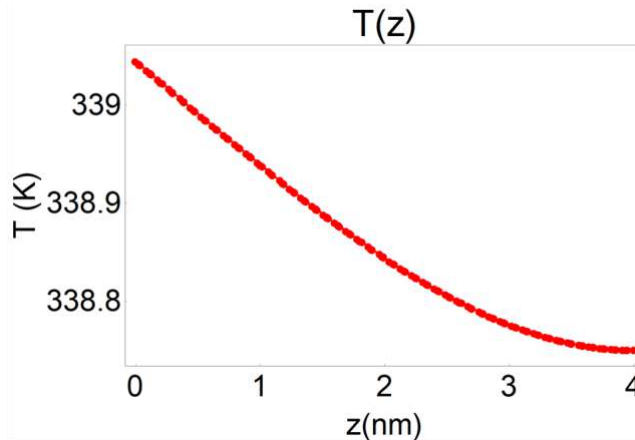


Figure 2. Simulation of change in temperature of FeCoB thin film

Quantifying the change in temperature induced by the laser is crucial in our microscopy because we have two unknown terms,  $\nabla T_z$  and  $\Delta\rho(T)$ , that depend on it. To find change in temperature, we will determine the relationship between resistance and temperature, and by knowing change in resistance produced by laser, we would know change in temperature locally. Therefore, we are motivated to design and build a set-up that measures resistance as a function of temperature.

## DESIGN

### *Schematic*

As shown in figure 3, we place our magnetic sample, FeCoB, on a printed circuit board (PCB) that is connected to a resistance measurement device. We heat our magnetic sample using a resistive heater that heats up the PCB and thus the sample. The sample is connected to gold pads on the PCB by wire bonding contacts on sample to them (figures 4-5). A temperature sensor is placed on top of the PCB to measure temperature.

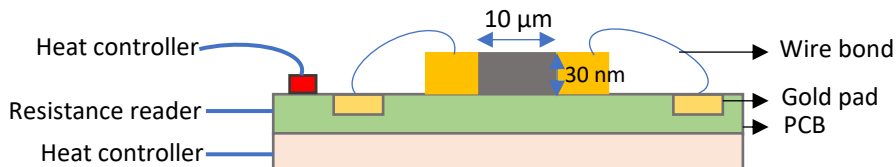


Figure 3. Design of interior connections

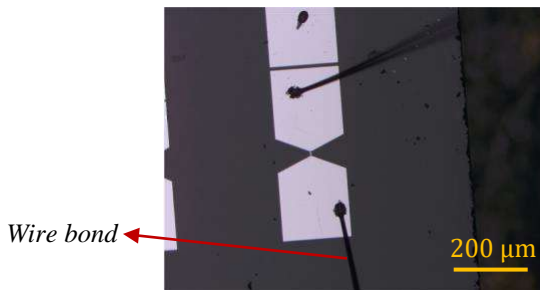


Figure 4. Wire bonding

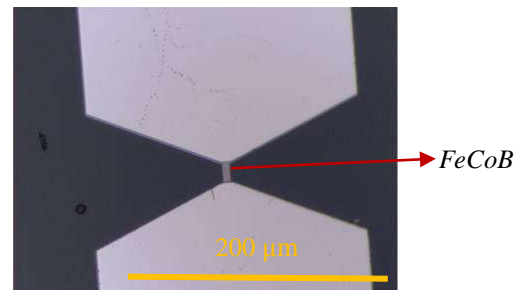


Figure 5. A  $10 \times 40 \mu\text{m}$  FeCoB connected to contacts

## *Requirements and Assembly Precautions*

We have requirements to maintain to make the device functional and practical. We need our device to be in a container that holds vacuum to insure having the same temperature on the surface of the PCB. The PCB should be able to resist high temperature (about 100 Celsius degrees). The PCB has to be removable to place it on wire bonding equipment. In addition, the container should have ports that connect inside parts to the exterior measurement equipment. We have to test electrical connection at each step to prevent any electrical shortening or interference.

## *Interior Parts Design*

Interior parts are shown in figure 6. We have the PCB at top in contact to a copper piece beneath it. The role of copper piece in here is to uniformly distribute the heat to the PCB. A resistive heater is located underneath the copper piece. We then added a plastic piece to avoid direct contact of this stack to the container to prevent heating it up. Finally, we have an aluminum piece that has screw holes to hold all parts together. This stack of pieces is attached to the container by a double-sided Kapton tape that will function at high temperatures.

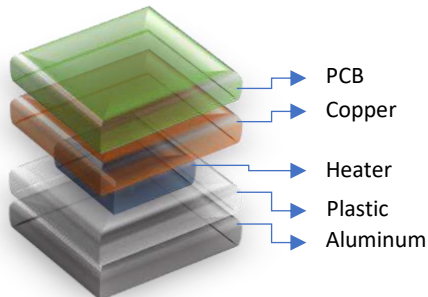


*Figure 6. Interior parts model*

We then deigned a model of the interior of the box, shown in figures 7-8, using Autodesk Inventor. The model contains the location of internal parts and the sizes of screw holes, cable ports and vacuum fittings holes.

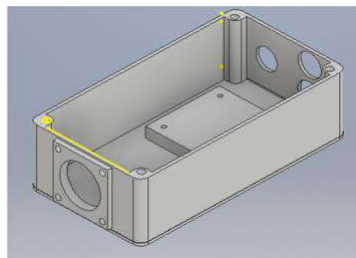


*Figure 7. Container model*

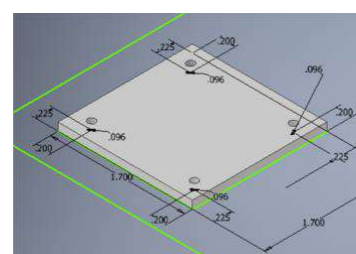


*Figure 8. Aluminum piece model*

### *PCB and Resistance Connection*

We designed a 1.5 "×1.55 " PCB, shown in figure 9, that has 8 gold pads. The PCB has an empty area in the center to place samples and the temperature sensor. We used thermal paste on the sensor to insure good contact to the PCB. We connected all pads to a female header sets on top of the PCB that accepts a removable male header in which we would be able to take off the PCB for wire bonding. The male header is connected to a circular plug that accepts a cable that goes to a breakout box, shown in figure 10, for resistance measurements. The breakout box has 8 pin ports for the 8 PCB pads. The breakout box allows user to pick desired pads to use. The breakout box is connected to Keithley 2100 for resistance measurements.

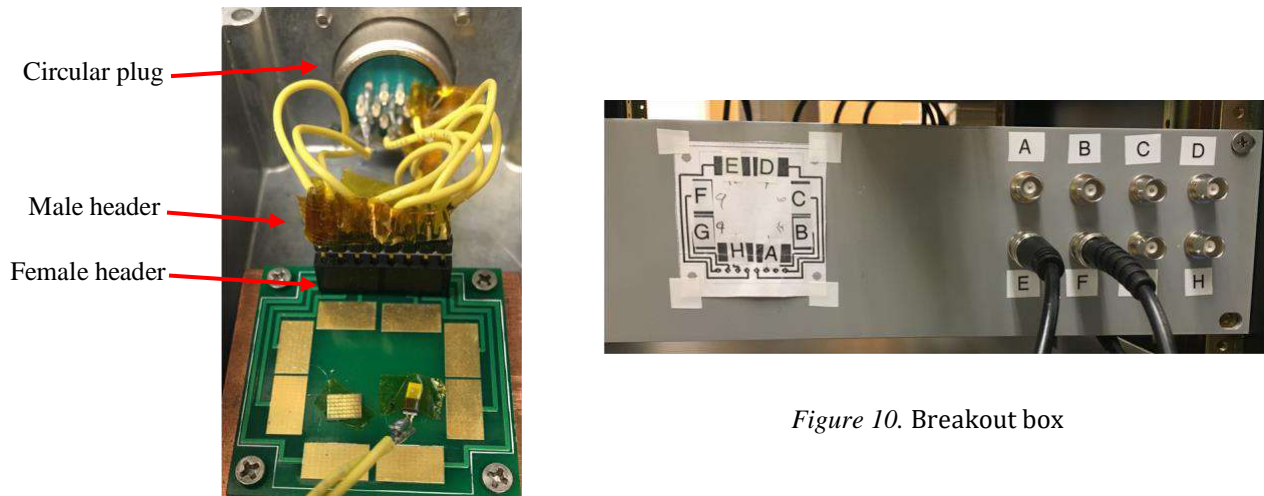


Figure 9. PCB and its connections

### *Heater, Sensor and Vacuum Connections*

We connected the heater and temperature sensor, shown in figure 11, to a similar circular plug that is connected to Thorlabs TC200 for heating and temperature measurements. We have 2 holes for vacuum, one for pulling air and the other for breaking vacuum (figure 12).

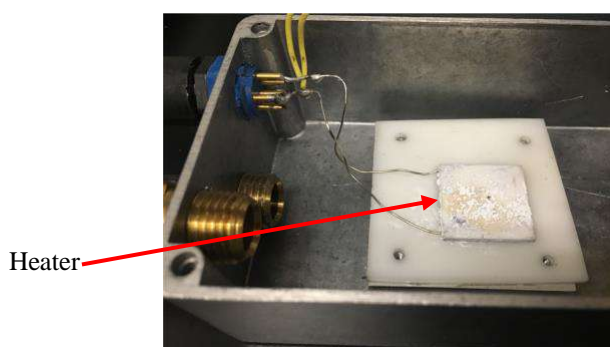


Figure 11. Heater connection

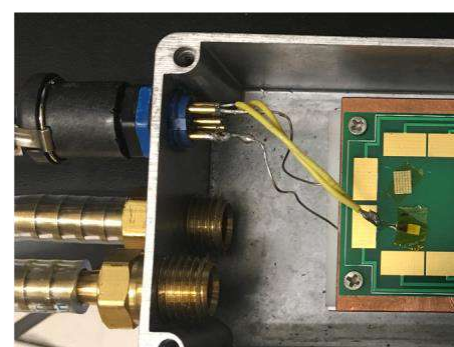


Figure 12. Vacuum connections

## Programming

We now have the device set and ready to function. We used LabVIEW to control the measurements set-up and acquire data. We made a program, shown in figure 13, that allows user to enter a desired heating temperature and time to reach this temperature. We programmed the instrument to take 4 resistance measurements each second and calculate the mean and standard deviation to determine the value and uncertainty, respectively. We also added a plot in the program to observe the resistance and temperature relationship as the device keep measuring data to detect if the device is working or not.

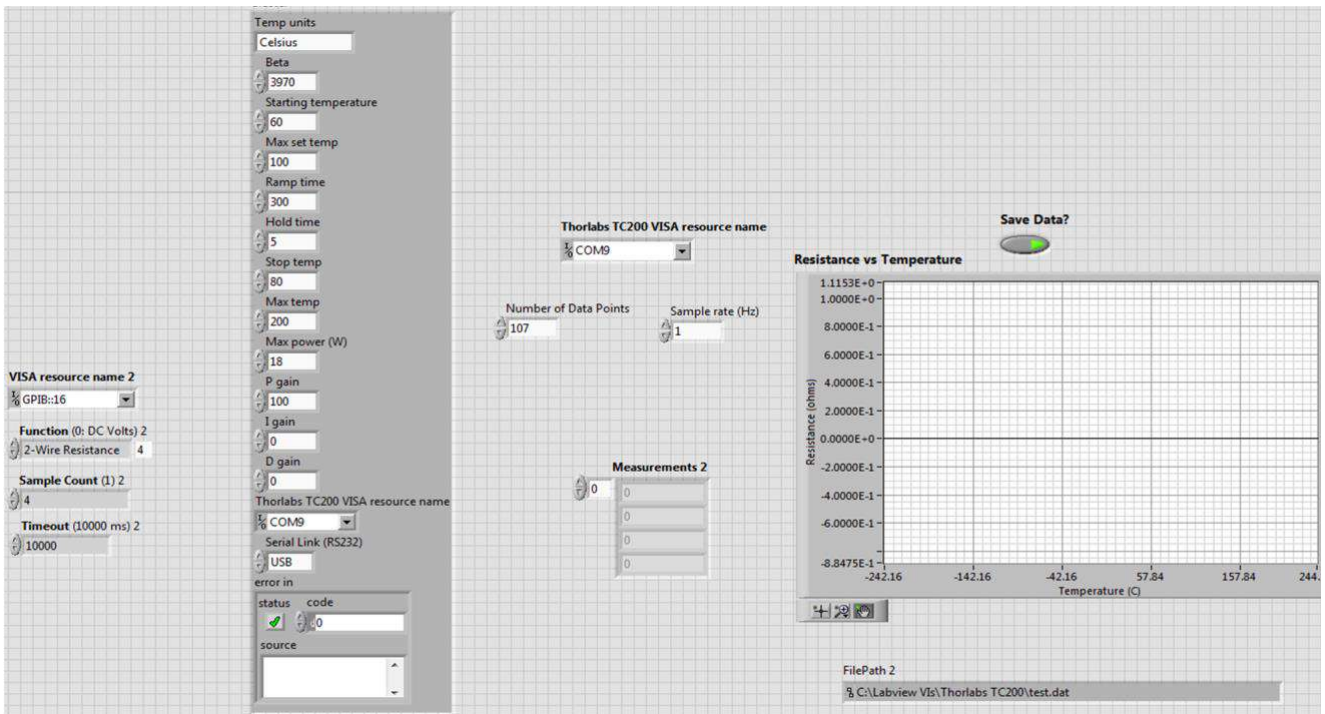


Figure 14. LabVIEW program

## RESULTS

The final product is shown in figure 14.

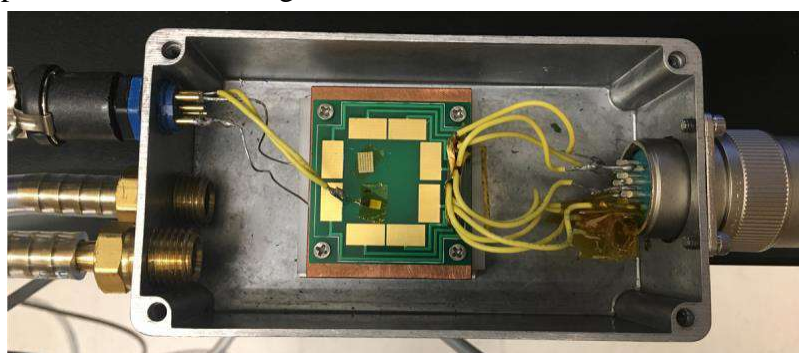


Figure 14. Final product

We took measurements of iron cobalt boron to test the functionality of our device. We expect to have linear relationship between resistance and temperature. We heated up our sample from 24 °C to 74 °C in 300 seconds. We obtained a linear function as shown in figure 15.

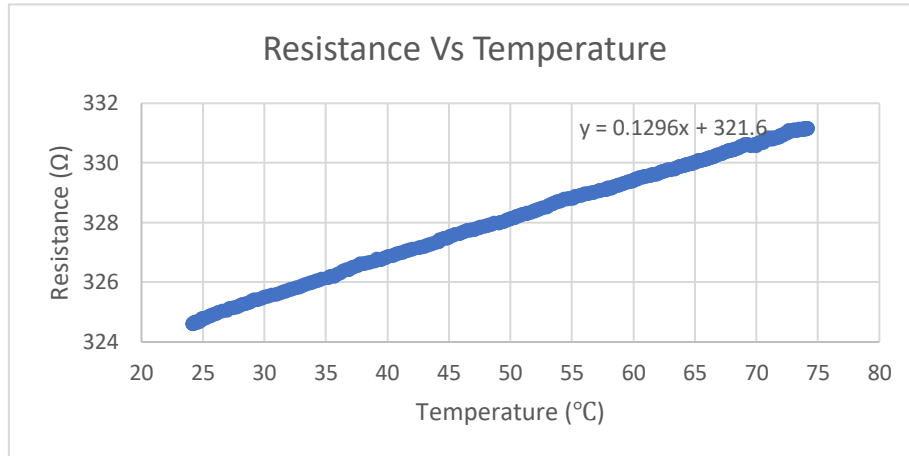


Figure 15. Resistance and temperature relationship

## CONCLUSION

We developed an experimental characterization set-up for resistance and temperature measurements. The set-up helps our new magneto-thermal microscopy technique based on anomalous Nernst effect. We shine a focused laser to a magnetic metal that produces local thermal gradient, which induces voltage. The thermal gradient that depends on change of temperature locally caused by laser. The voltage produced by laser increases local resistance and thus temperature. Our set-up finds the relationship between resistance and temperature and is able to measure change in temperature based on change in resistance. We ran an experiment on FeCoB and observed what is expected, a linear relationship between resistance and temperature.

## ACKNOWLEDGMENT

I would like to thank Dr. Gregory Fuchs for having me in his group, and Isaiah Gray for his heavily support and mentorship during the period of this project. I would also thank Albert Park for his help and all members of Fuchs group. This project was supported by CCMR.

## **REFERENCES**

- [1] J.M. Bartell, D. H. Ngai, Z. Leng, and G. D. Fuchs. Toward a table-top microscope for nanoscale magnetic imaging using picosecond thermal gradients. *Nat. Commun.* 6, 8460 (2015).

# Spin-Torque Transfer Magnetic Random Access Memory Utilizing Films with Perpendicular Magnetic Anisotropy

Aaron Coe<sup>1,2</sup>, Jonathan Gibbons<sup>2</sup>, Arnab Bose<sup>2</sup>, and Dan Ralph<sup>2</sup>

<sup>1</sup>Bethel University, Saint Paul, Minnesota

<sup>2</sup>Cornell Center for Materials Research, Cornell University, Ithaca, New York

(Dated: August 8, 2018)

A magnet with the characteristic of perpendicular magnetic anisotropy (PMA) or out-of-plane magnetization will enable desirable thermal stability for STT-MRAM cells at a scale below 50 nm. This research investigated growing ferromagnetic materials with PMA using dysprosium, cobalt, magnesium oxygen and iron-cobalt-boron, utilizing DC magnetron sputtering. The resulting samples did display PMA. However, the PMA was weaker than reported by other groups. Additionally, MgN was explored to determine if its peculiar magnetic ordering produces nonstandard torques and was found to produce standard torques at room temperature.

## I. INTRODUCTION

Modern computers use a hierarchy of memory types for storing data long term and for active use. Because different memory types provide different advantages, the use of multiple types of memory in a single computer is needed. Random Access Memory (RAM) is used by the computer to store data that it accesses constantly. When a program is run, the information related to that program is stored in the computer's RAM. If this data was stored in main memory (hard drive disks, solid state drives, etc), the computer would not be able to access the data as quickly and programs would run a few orders of magnitudes slower. Instead main memory functions as a storage place to store data long term (saving files) and to store any data that cannot fit in RAM. The memory types used in RAM also cannot be used effectively in main memory without a significant increase in energy usage, cost, and risk if the computer loses power. The memory types used in RAM are volatile they require constant refreshing to keep memory and they lose all data when the power is lost [1]. These memory types are more expensive than hard drive storage. To make a 1 Terabyte (TB) main memory storage out of RAM memory types would cost over \$10,000.

Spin-Torque Transfer Magnetic Random Access Memory (STT-MRAM) may provide the capability for read and write times comparable to dynamic random-access memory (DRAM) and static random-access memory (SRAM), common memory types used in RAM, while providing the non-volatility of a hard drive [2]. If RAM is replaced with STT-MRAM, a computer could be powered off with programs running and save that state. Then when the computer is powered on, it will boot up with those programs running. There would be no need to start up the operating system, except for freeing dynamically allocated memory, making boot times faster than computers with Solid State Drives (SSDs). If main memory were replaced with STT-MRAM, the cost of a program reading or writing to main memory could be reduced by a few orders of magnitude. Programs would be able to run faster and work with more data in this case.

MRAM uses a ferromagnetic layer, known as the free layer, to store the memory bit. The direction of the magnetization of this layer determines whether the bit is a one or a zero. Initially, magnetic switching of the free layer was done by applying an external magnetic field by flowing current through wires to induce a field. However, when the system was scaled down, the current requirements became too large and the external field was found to affect bits other than the one meant to be switched [3, 4].

Spin-torque transfer (STT) is another technique used for switching the direction of the free layer. This method does not suffer from the same problems as external field switching such as power and scaling. Spin-torque transfer utilizes the spin of electrons and the properties of ferromagnetic materials to create torques that cause the magnet to precess and eventually flip magnetization directions [3–5]. Currently, EVERSPIN Technologies sells STT-MRAM based memory up to 256 Mb as an alternative RAM memory type. They claim their units are comparable to DRAM which has access times around 10 ns (extremely fast compared to hard drive disk access time of a few milliseconds) [2]. STT-MRAM is still in its infancy commercially and the size of a bit will need to be scaled down before it can truly compete with other memory types. Unfortunately, thermal energy becomes a problem for most STT-MRAM designs when bit sizes fall below 50 nm [3, 4]. The following investigation explores using ferromagnetic layers with out-of-plane magnetization for a new generation of STT-MRAM.

## II. SPIN-TORQUE TRANSFER MAGNETIC RANDOM ACCESS MEMORY

Electron spin is an intrinsic property of electrons. While the electron does not actually spin (being a point particle), it does carry angular momentum. Ferromagnetic materials contain a net spin polarization. Therefore, there is a net direction for the electrons' spin which means that there is a net field generated by their spinning, giving rise to a net field in ferromagnetic materials.

Ferromagnetic materials prefer to keep their net spin, which means when a current of non-spin polarized electrons flow through a ferromagnet, the spin direction of the electrons will be reoriented to align with the field of the ferromagnet. But if the spin direction of electrons is being changed, then the angular momentum must go somewhere which happens to be into the magnetization. The magnetization will apply a torque on the electrons and the electrons will apply a torque on the magnetization [5]. For charge currents, there is no change in the magnetization direction but for a spin polarized current, there is a net torque on the magnetization which can cause it to change direction.

STT-MRAM utilizes magnetic tunnel junctions (MTJs) shown in Fig 1. The fixed layer is used to generate the spin current (a spin polarized charge current in this case but it can also be purely spin current with no net charge movement). A spin current can be generated by flowing charge current through the fixed layer and into the free layer. The fixed layer will act as a filter for the spin of the electrons creating a net spin and therefore a spin current which flows into the free layer [3, 6]. However, this technique creates heat through joule heating and at maximum efficiency of momentum transfer between spin and magnetization is limited. This is because a single electron carries a single electron's worth of charge and angular momentum so the greatest ratio between momentum imparted and the charge of the electron is  $\frac{\hbar}{2e}$

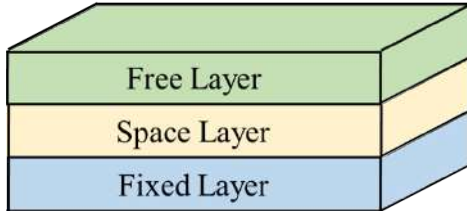


FIG. 1. The free layer is where the bit state of a 1 or 0 is stored. The spacer layer acts as a barrier to keep the fixed layer and free layer from magnetically coupling (one layer cannot be flipped without flipping the other layer) and allows for tunneling between the fixed layer and free layer. Additionally, the fixed layer is used to generate the desired spin current for switching and reading the state of the free layer.

Another method for generating spin current is through the spin Hall effect (SHE). When charge current flows through a conductive material with large spin-orbit coupling, pure spin current will start to flow in a direction perpendicular to both the charge current and the spin direction (Fig 2) [7, 8]. For a non-spin polarized charge current, half the electrons with spin in-plane but perpendicular to the direction of the charge current, will flow upwards out of the film toward the free layer for a non-ferromagnetic conductive material. Limitations on the use of the SHE include that it is observable only in materials with large spin-orbit coupling and the size of the spin current generated through the effect is small

[6]. For magnetic switching, SHE's advantages outweigh its disadvantages because it is not limited by the ratio mentioned earlier and it is used in this investigation for analyzing material properties.

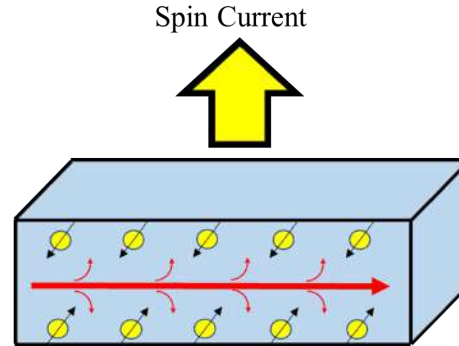


FIG. 2. Illustration of spin current generation through the SHE. As current flows to the right, in the plane of the page, electrons with spins in and out of the page flow downwards and upwards respectively.

When charge current is passed through the fixed layer, a spin current is generated that tunnels into the free layer producing torques on the magnetization. These torques are known as anti-damping torques and along with the equilibrium torques (caused primarily by the Oersted field produced by the charge current) will cause the magnetization to precess [9]. The anti-damping torque will cause greater and greater precession which will result in flipping with a sufficiently large torque [5].

The magnetization direction can be measured utilizing tunneling magneto resistance (TMR). Because magnets are spin polarized, there are more states available for specific spins. If spin current is passed through with direction that is parallel (P) to the magnetization, then there will be relatively low resistance because there are many states available. If spin current with direction anti-parallel (AP) to the magnetization is passed through, there will be relatively large resistance [5, 6]. Performing this measurement requires little current and values of the TMR ratio (Eq 1) of over 1000% have been measured [4].

$$\text{TMR Ratio} = \frac{R_{AP} - R_P}{R_P} \quad (1)$$

The TMR Ratio defines the change in resistance for spin polarized current flowing into a magnetic layer for AP and P orientations.

Research on STT-MRAM devices has primarily focused on free and fixed layers with in-plane magnetization [3–5]. However, in-plane magnets have low thermal stability. Thermal energy can cause the magnetization of a material to flip which is a problem if STT-MRAM is to be non-volatile. The energy needed to flip from one magnetization to another is defined by the energy barrier ( $E_b$ ) between the two desired orientations. The commercial requirement for long-term storage requires a ten year

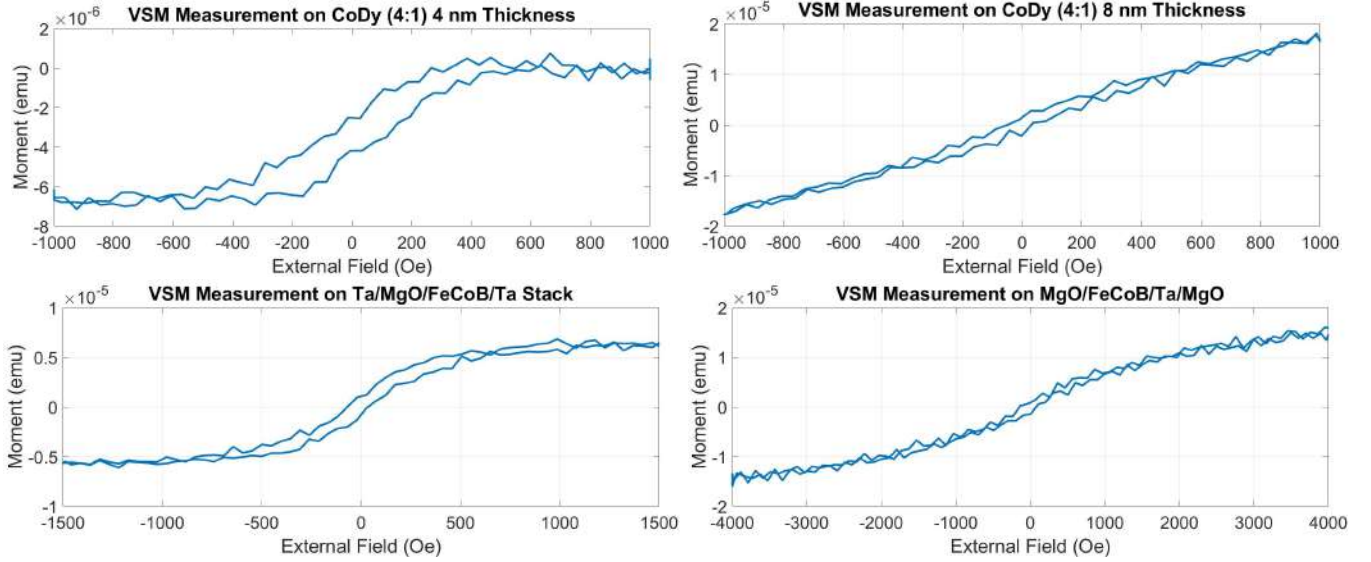


FIG. 3. VSM measurements on potential PMA samples. The 4 nm CoDy and Ta/MgO/FeCoB/Ta stack display signs of PMA not found in the 8 nm CoDy or MgO/FeCoB/Ta/MgO samples.

interval to pass before it is possible for magnetization to flip due to thermal energy; MTJ stacks with in-plane magnets do not meet this requirement [3, 4]. This is because it is relatively easy for the magnetization to rotate in the plane of the free layer. The smaller a bit can be made, the more information can be stored. When STT-MRAM utilizing in-plane ferromagnets are scaled below 50 nm, the thermal instability becomes a problem. Using elliptical shapes for the device can increase the thermal stability but this fix is insufficient below 22 nm [3].

Using a magnet with perpendicular magnetic anisotropy (PMA), out-of-plane magnetization, for the free layer will provide the desired thermal stability for scaling below 50 nm. However, the anti-damping torques used for switching the in-plane free layer were in-plane. For an out-of-plane free layer, an out-of-plane anti-damping torque would be needed to flip the magnetization. This will require a different fixed layer to generate spin currents that will apply the needed torques. Novel materials such as MgN could be explored to determine whether they generate out-of-plane anti-dampening torques. A fixed layer with PMA that is exchanged biased with an antiferromagnetic layer may also provided the needed torques.

### III. FERROMAGNETIC THIN FILMS WITH PERPENDICULAR MAGNETIC ANISOTROPY

A fixed layer with PMA cannot be used by itself to induce torques on the free layer. This is because the net spin, used to switch the free layer, points out of the material's plane. SHE will then create a spin current that flows perpendicular to the current and spin direction which will be in the plane of the fixed layer so these

spins will not reach the free layer. In order to utilize a fixed layer with PMA, its magnetization must have some in-plane component allowing the spin current to flow diagonally upward. This can be done with an external field.

It was found by Ref [10], that an antiferromagnetic material could be used for exchange biasing the fixed layer of an MTJ and allow for tuning of the spin current flowing into the free layer. By placing the antiferromagnetic material below the fixed layer in the stack then heating past the Néel temperature with an external field applied, the top layer of the antiferromagnet will align with the external field and will remain in this state after returning to room temperature. This magnetization is weak and has only a noticeable effect a few nanometers above the surface enough for tilting the magnetization of the fixed layer downwards but having no observable effect on the free layer.

This investigation attempted to grow ferromagnetic materials with PMA using a mixture of Dysprosium (Dy) and Cobalt (Co) and a stack of Iron Cobalt Boron ( $Fe_{60}Co_{20}B_{20}$ ) and Magnesium Oxide (MgO). CoDy layers with ratios of 1:4, 1:3, and 30:70, respectively, were grown with material thicknesses of 4 nm and 5 nm. Additionally, a film of thickness 8 nm was grown with a ratio of 1:4. All CoDy samples were grown over and capped with 1.5 nm of Tantalum (Ta). The following stacks of FeCoB and MgO were grown: Ta(5)/FeCoB(1)/MgO(1.8)/Ta(1) and MgO(1.5)/FeCoB(1)/Ta(1.5)/MgO(3). Number in parenthesis dictates thickness in nanometers. All films were grown using DC magnetron sputtering. After growth the MgO, FeCoB, and Ta stacks were annealed at 260 °C for one hour. All PMA measurements were performed using vibrating sample magnetometer (VSM) measurements. This measurement is done by applying

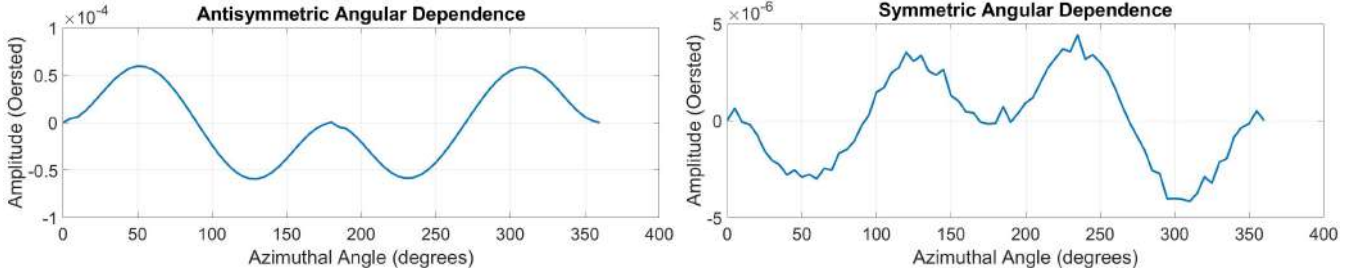


FIG. 4. ST-FMR measurements on MgN sample grown on silicon crystal lattice. Shape of symmetric and antisymmetric components follow  $A * \sin(\theta)^2 * \cos(\theta)$ .

an external magnetic field perpendicular to the sample's plane and measuring the magnetic moment. Samples with observable hysteresis curves will have PMA.

The results from the VSM measurements are shown in Fig 4. The 4 nm thick CoDy sample displayed signs of PMA while the 8 nm thick sample did not. However, the width of the hysteresis curve for the 4 nm thick sample is small. After literature review, it was found that the films grown may have been too thick. Other researchers were able to create PMA films with DyCo stacks on the scales of a nanometer or less. It is reported that interface effects give rise to PMA and thicker films can cover up this effect [11]. The sample grown in this investigation has a much smaller hysteresis curve compared to the samples grown in Ref [11]. Films of similar thickness to those reported in Ref [11] will be grown in the future.

The Ta/MgO/FeCoB/Ta stack did display signs of PMA while the MgO/FeCoB/Ta/MgO either does not display signs of PMA or displays signs of weak PMA. Now that materials with PMA have successfully been grown, the next step to be undertaken will be to make the MTJ devices outlined earlier.

#### IV. SAMPLES WITH MAGNESIUM NITROGEN

MgN is of interest because of its peculiar magnetic ordering. It was obtained from Chang-Beom Eoms group at the University of Wisconsin-Madison researching spin torque in novel material structures. The Ralph group was asked to perform characterization of the samples produced in hope that this material may be able to generate nonstandard torques when current is passed through. A layer of Py serves as the sensor layer for measurements.

Spin-Torque Ferromagnetic Resonance (ST-FMR) measurements, a standard technique used to discern the torques and spin hall angle (ratio between spin current and charge current), was used to characterize the torques being produced from the spin current generated from MgO. This measurement technique works by applying an RF current to the sample and scanning and external magnetic field. Measuring the mixing voltage will produce the signal seen in Fig 5. This signal is composed of a symmetric and antisymmetric lorentzian. If the field is

scanned multiple times with the external field at different angles with respect to the sample, an angular dependence for the symmetric and antisymmetric components can be found. The shape of the angular dependence of the components determines what torques were present.

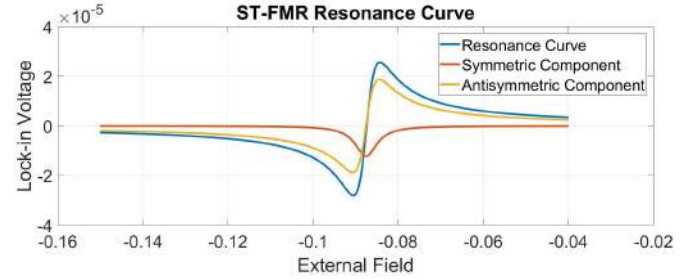


FIG. 5. Example ST-FMR signal in blue. This signal is composed of a symmetric lorentzian (yellow) and an antisymmetric lorentzian (red) component. The angular dependence of these components, with respect to external field and the sample, will determine the torques present.

Fig 3 shows the ST-FMR data for our MgN samples. The torques generated from the spin current are found in the symmetric component which has the shape of  $A * \sin(\theta)^2 * \cos(\theta)$ . Given this shape, there are no nonstandard torques being generated from MgN. Further ST-FMR measurements with MgN will be taken at different temperatures because MgN will have transitions in magnetic ordering at different temperatures.

#### V. CONCLUSION

Films with PMA were successfully grown. In the future, samples similar to Ref [11] will be made to determine if stronger PMA can be obtained. Once strong PMA values have been found, MTJ devices utilizing CoDy for the fixed layer and the Ta/MgO/FeCoB/Ta stack for the free layer will be fabricated. The CoDy films will be used for the free layer because it has lower resistivity so more charge current will flow through it allowing more spin current to be generated.

Additionally further characterization of MgN will continue. Because MgN has transitions in magnetic order-

ing at different temperatures, ST-FMR measurements for different temperatures will be performed to see if any of these other orderings produce nonstandard torques.

## VI. ACKNOWLEDGMENTS

This work was facilitated by Dr. Dan Ralph, Laboratory of Atomic and Solid State Physics, at Cornell

University with mentorship from Jonathan Gibbons and Arnab Bose.

This work was supported by the Cornell Center for Materials Research with funding from the Research Experience for Undergraduates program.

This work made use of the Cornell Center for Materials Research Shared Facilities which are supported through the NSF MRSEC program and the Center for Nanomaterials and Engineering and Technology.

- 
- [1] Alex Ryckman Mellnik. *Measurements of Spin Torques generated by Topological Insulators and Heavy Metals*. A Dissertation of Cornell University, (2015).
  - [2] *STT-MRAM Products*. Everspin Technologies.
  - [3] L. Thomas, G. Jan, J. Zhu, H. Liu, Y. J. Lee, S. Le, R. Y. Tong, K. Pi, Y. J. Wang, D. Shen, R. He, J. Haq, J. Teng, V. Lam, K. Huang, T. Zhong, T. Torng, and P. K. Wang. *Perpendicular Spin Transfer Torque Magnetic Random Access Memories with High Spin Torque Efficiency and Thermal Stability for Embedded Applications*. Journal of Applied Physics **115**, 172615 (2014).
  - [4] S. Bhatti, R. Sbiaa, A. Hirohata, H. Ohno, S. Fukami, S. N. Piramanayagam. *Spintronics based random access memory: a review*. Materials Today, 20 (2017).
  - [5] D. C. Ralph and M. D. Stiles. *Current Perspectives: Spin Transfer Torques*. Journal of Magnetism and Magnetic Materials, 320 (2008).
  - [6] J. Gibbons. *Measurements of Spin Torques due to Reorientable Anomalous Hall Spin Current* A Dissertation of Cornell University, (2018).
  - [7] A. Hoffmann. *Spin Hall Effects in Metals*. IEEE Transactions on Magnetics **10**, 49 (2013).
  - [8] F. Hellman, A. Hoffmann, Y. Tserkovnyak, G. Beach, E. E. Fullerton, C. Leighton, A. H. MacDonald, D. C. Ralph, D. A. Arena, H. A. Dürr, P. Fischer, J. Grollier, J. P. Heremans, T. Jungwirth, A. V. Kimel, B. Koopmans, I. N. Krivorotov, S. J. May, A. K. Petford-Long, J. M. Rondinelli, N. Samarth, I. K. Schuller, A. N. Slavin, M. D. Stiles, O. Tchernyshyov, A. Thiaville, B. L. Zink. *Interface-induced phenomena in magnetism*. Reviews of Modern Physics, 89 (2017).
  - [9] N. R. Reynolds *Controlling Spin Orbit Torques through Strong Correlation*. A Dissertation of Cornell University, (2018).
  - [10] J. D. Gibbons, D. MacNeill, R. A. Buhrman, and D. C. Ralph. *Reorientable Spin Direction for Spin Current Produced by Anomalous Hall Effect*. Physical Review Applied **9**, 064033 (2018).
  - [11] Z. S. Shan and D. J. Sellmyer. *Magnetism of Rare-Earth Transition-Metal Nanoscale Multilayers. I. Experiments on Dy/Co, Dy/Fe, and Tb/Fe*. Physical Review B **16**, 42 (1990).
  - [12] A. E. Freitag and A. R. Chowdhury *Effect of Interface on Magnetic Anisotropy of Fe/Tb Multilayers: Mössbauer Effect Study*. Journal of Applied Physics **82**, 5039 (1997).

# Novel Transfer Technique for Metasurfaces to the Tip of an Optical Fiber

Natalie Cummings<sup>1</sup>, Gennady Shvets<sup>2</sup>, Steven He Huang<sup>2</sup>, and Shourya Dutta Gupta<sup>3</sup>

<sup>1</sup>Department of Materials Science and Engineering, The Pennsylvania State University, State College, PA 16802

<sup>2</sup>Department of Applied and Engineering Physics, Cornell University, Ithaca, NY 14850

<sup>3</sup>Department of Materials Science and Metallurgical Engineering,  
Indian Institute of Technology Hyderabad, Telangana 502285, India

We use a sacrificial copper layer to separate gold and PMMA from its substrate. Then, using a new take on transfer printing, we transfer the surface to PDMS, from which the surface can be applied to the tip of the optical fiber. The process eliminates the need for specialized equipment and excessive processing time while producing a comparable end result. Most of the work was performed with a bulk gold film, but some preliminary tests were performed with a metasurface.

## I. INTRODUCTION

Metasurfaces, which are comprised of metal features designed to manipulate the movement and behavior of light, hold the key to the next generation of biosensors. These surfaces can be tuned to very spectrally narrow wavelengths of light [1]. This means that these surfaces can be used to identify the resonance peaks of proteins or other molecules, even in trace amounts. Although other similar technologies exist, they are incompatible with the current gold standard biosensors. Another potential advantage is the possibility for remote sensing. With the aid of the optical fiber, substances can be analyzed from a reasonable distance. By combining metasurfaces with optical fibers, we can create a remote sensing platform that would be compatible with existing biomedical devices.

The problem with this grand idea is the adhesion of the metasurface to the tip of the optical fiber. There have been a wide variety of proposed solutions, but each has their own drawbacks. FIB can be used to machine the pattern directly onto the fiber, but its small size is a challenge, and the surface can become inadvertently doped with gallium ions [2]. These inconsistencies can interfere with the carefully tailored plasmonic effects of the metasurface. In addition, this method is neither time- nor cost-effective. Other proposed solutions are the decal transfer, [3] nanoskiving, [4] and "transfer printing" [5] techniques. These improve upon direct machining of the optical fiber by producing the metal features on a sacrificial substrate, and then transferring the metasurface onto the fibers tip.

The solution we seek to provide is one that combines aspects of "decal transfer", "nanoskiving", and "transfer printing", and which can be completed quickly and efficiently.

Nanoskiving requires highly specialized equipment. The desired metasurface is created in epoxy, coated in the desired metal, encased in more epoxy, and then sliced into thin sheets using an ultramicrotome. After all those steps, the thickness of slices often varies, and some slices become unusable. Especially due to the low availability of ultramicrotomes, this process can become exceedingly

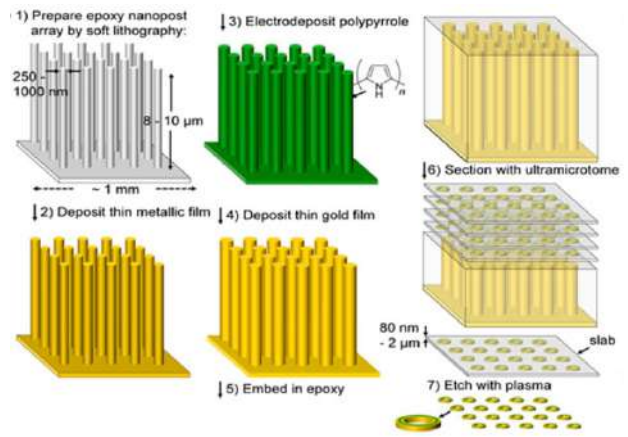


FIG. 1. Diagram showing the nanoskiving process.[4] The ultramicrotome, not pictured, is a highly specialized piece of equipment which is still subject to frequent error.

difficult. Despite its problems, its idea of a film holding together the metasurface was one we wanted to incorporate into our process.

The current decal transfer process is complicated and lengthy. A specialized thiol-ene film must be produced and cured, and then many steps lead to the final transfer of the metasurface to the tip of the fiber. Some of these steps require specialized equipment, such as a stereoscope. The film itself must be produced in-lab from its constituent chemicals, leaving a lot of room for human error. In addition, many parts of the process involve separating one layer from another, and require lengthy waiting times as those sections separate. Even so, the idea of a material which would be sticky enough to pick up the metasurface, but not so sticky to interfere with the final transfer was a great one.

Transfer printing uses some flexible substrate to aid in the transfer of features. There are three kinds of transfer printing; "additive transfer", "subtractive transfer", and "deterministic assembly". [5] Classic PDMS stamps fall under the realms of additive and subtractive transfers. A medium which can selectively pick up certain features is the goal of deterministic assembly. These techniques can be relatively quick and easy, and so we seek to modify

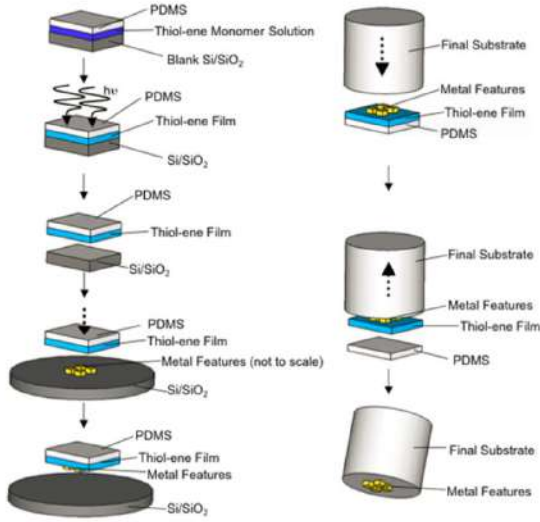


FIG. 2. Diagram showing the Thiol-Ene Decal Transfer process.[3] In addition to the need to synthesize the thiol-ene film, this process has numerous steps and requires a substantial amount of time.

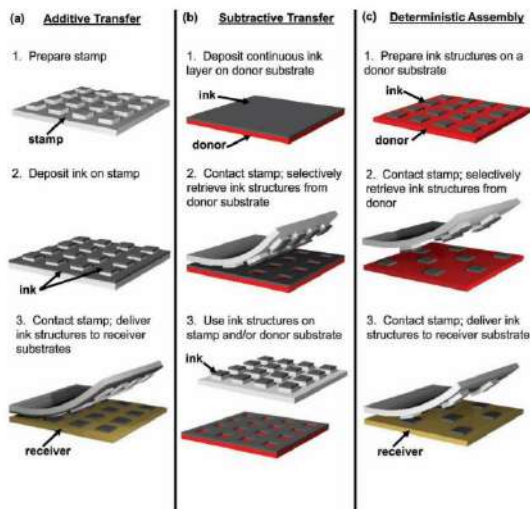


FIG. 3. Diagram showing the three different types of transfer printing.[5] There are strong similarities between these techniques, but each performs the transfer in a slightly different manner. The method most similar to our new approach is Deterministic Assembly. However, our PDMS "stamp" cannot choose features selectively, but rather must pick up all features.

one of these methods to simplify it even further.

Our new process seeks to reduce the difficulty and length of these processes, as well as maintaining or improving their results. By using common, easily available chemicals and tools, we seek to create a practical method for the transfer of metasurfaces to the tip of an optical fiber, which requires neither unreasonable equipment nor

unreasonable amounts of time.

A biological sensor which can identify and observe molecules is a big step forward, but it will likely never see the light of day if its manufacturing cannot be simplified into a commercially feasible process. The advances we have made pave the way for further simplification of our process.

## II. METHODS

In order to optimize our process, we began the process with multimode, glass-clad silica fiber (Thor Labs FG200LEA). This fiber has a core of  $\sim 200 \mu\text{m}$ , a cladding of  $\sim 220 \mu\text{m}$ , and an acrylate coating of  $\sim 320 \mu\text{m}$ .

We adapted the thiol-ene "decal transfer" procedure detailed in "A Technique to Transfer Metallic Nanoscale Patterns to Small and Non-Planar Surfaces". Briefly, this procedure uses a chemically reproducible thiol-ene film to adhere to the metal features. Later, this film is removed via oxygen plasma. This leaves the surface on the tip of the optical fiber. The synthesis of the thiol-ene film adds a significant amount of time and steps to an already complicated process, though.

To shorten the process, we sought to eliminate the need for the thiol-ene film altogether, instead subbing in a different, more ubiquitous polymer (495 PMMA A4) in a more efficient manner. Our process begins with the fabrication of the surface. We evaporate a thin ( $200 \text{ nm}$ ) layer of copper, then a  $10 \text{ nm}$  chromium adhesion layer onto a CaF<sub>2</sub> substrate. Next, a gold layer ( $70 \text{ nm}$ ) is evaporated onto the chromium layer. Beneath the copper layer is a thicker calcium fluoride substrate for support. After the surface is finished, it is spin-coated with one layer of PMMA. This holds the surface together in later steps, but is not overly attracted to the gold (both important characteristics). To cure the PMMA, we bake it at  $90^\circ\text{C}$  for 3 minutes, then at  $170^\circ\text{C}$  for 19 minutes, and at  $90^\circ\text{C}$  again for another 7 minutes.

Next, we scratch the PMMA film in two places on the substrate, so that the etchant will be able to seep under the PMMA and remove all of the sacrificial copper layer. We place small, "L" shaped scratches on opposite corners of the sample. With the scratches complete, we place the sample in copper etchant (CE-200), which separates the surface and PMMA from the copper and silicon. This process takes 2.5 hours, after which the copper has been completely etched away. The PMMA and surface will not delaminate after this step, though. The sample should be gently rinsed and dried before the next step. If the scratches are placed poorly, or the rinsing and drying is too intense, the film can wrinkle or fold, in some cases destroying the surface.

After the etch is complete, we clean a piece of cured Sylgard 184 Silicone Elastomer PDMS to prepare it for transfer. We apply pressure to the PDMS, and when we remove it, it takes the gold surface with it. Although pressure is important to ensure that the surface transfers

to the PDMS, excessive pressure will crack the calcium fluoride substrate, so caution must be taken. Then, we simply turn over the PDMS, readying it for contact with the fiber.



FIG. 4. An image of the PDMS after the surface has been transferred. Small, circular defects can be observed around the surface. These are a result of the transfer to the fiber. The "L" shaped defect in the bottom left hand corner is from the scratch in the PMMA. The other scratch was in the top right hand corner, and part of it can still be observed in the sample.

In preparation for the transfer, fiber samples are cleaved and stripped, with a maximum angle of 2.0 degrees.

To transfer the surface, we press the tip of the fiber onto the PDMS at a 90 degree angle, allowing them to connect and applying gentle pressure for ten seconds. This orientation and pressure are essential to the connection of the fiber and the surface. Care must also be taken not to wiggle the fiber too much during the connection, as this tends to move some of the surface from the tip of the fiber to its sides. Also important to take into consideration is the potential of the fibers to break. If the pressure applied is too great or the application is done at an improper angle, the fiber tends to snap.

After the surface has been successfully transferred to the fiber, oxygen plasma removes the PMMA layer from the original fabrication. An Anatech oxygen plasma etcher was used for this process, at the descum setting. We used a power of 300 W for 40 minutes, with 220 oxygen and 20 nitrogen. After removing the PMMA film, we noticed that the fibers seemed to have retained their previous level of coverage.

### III. RESULTS AND DISCUSSION

Our process took several iterations to reach this level of success. We began with samples of gold evaporated onto

a chromium layer on a glass substrate. A slow etchant rate and a tendency for the PMMA to remain adhered to the substrate ruled out this method. We moved next to similar samples, but with copper on the glass substrate, and an adhesion layer of chromium between the copper and gold.

After this setup provided quicker etching times but still had problems with delamination, we moved to a new solution. Using Kapton tape, we were able to remove clear sections of the gold and PMMA. While effective for removing the features, this method did not facilitate the transfer, even when defects such as small holes were added to aid in the process. The tape was simply too sticky, and the gold wasn't attracted enough to the tip of the fiber to retain its adhesion during periods of mechanical stress. In addition, the Kapton proves very difficult to separate from the surface, even before contact with the fiber. Acetone will remove some of the adhesive, but the tape still fails to separate from the gold and PMMA.

Our PDMS solution managed to solve this problem because it serves as a less sticky transfer medium. It adheres to the gold and PMMA well enough to remove it from the substrate, but is not so attracted that the fiber cannot remove the surface. We faced some issues initially when determining the ideal manner in which to transfer from the PDMS to the tip of the fiber. Many different methods of application result in very patchy covering of the fiber's tip, especially around the edges or excluding the middle. Clearly, these types of results don't ensure full coverage of the fiber's core, and as such would not be usable as sensing devices.

The ability to use PDMS in this capacity is important mainly for two reasons. Firstly, it works consistently and easily; after a bit of practice the process of transferring the surface to the fiber's tip becomes simple. Secondly, PDMS is a readily available, easy to use polymer. We used a very standard recipe, which is simple to produce. This is vast improvement from the thiol-ene film which not only obscures multiple separate chemicals, but also for the user to mix them in the right proportions to successfully synthesize the film.

In order to view the tips of the fibers after the transfers and removal of the PMMA film, we utilized the Thermo Scientific Nicolet Continuum Infrared Microscope, with the 10x objective lens. We needed to ensure that the fiber was angled directly toward the lens, so we devised a technique to keep the fiber upright and in place on the microscope slide. First, another piece of PDMS is needed. The shape is not important, but it must not be so small that it can fall through the hole in the center of the microscope's slide. Next, we used a small biopsy punch to create a small hole through the piece. The fiber (non-coated end first) can be threaded through the PDMS, and both can be positioned on top of the slide. To ensure a lack of movement, we secured the PDMS in place with double sided tape.

We observed that this method resulted in the nearly complete coverage of the tip of the optical fiber. In ad-



FIG. 5. An image of the setup for microscopy. The PDMS supports the fiber, keeping it at a favorable angle for imaging with the microscope. The double-sided tape ensures that, as the stage moves, the fiber and PDMS do not move with it.

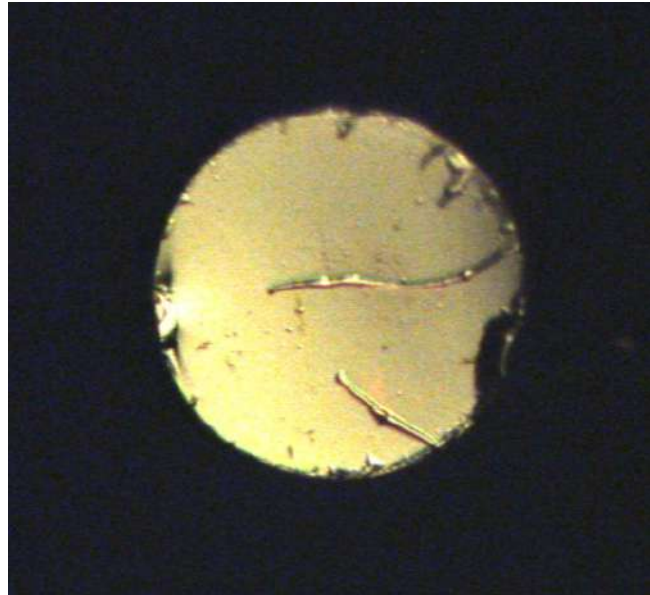


FIG. 6. An image of the fiber's tip after oxygen plasma. It can be seen that nearly the entire tip of the fiber is covered in gold.

on the transfer of bulk gold surfaces, at the end of the research session we were able to transfer one metasurface to PDMS, with good results. Transferring the metasurface to the fiber proved more difficult, but was possible, however a lack of time prevented the perfection of the technique. In the following image, the metasurface (although poorly aligned) can be seen on the fiber's tip.

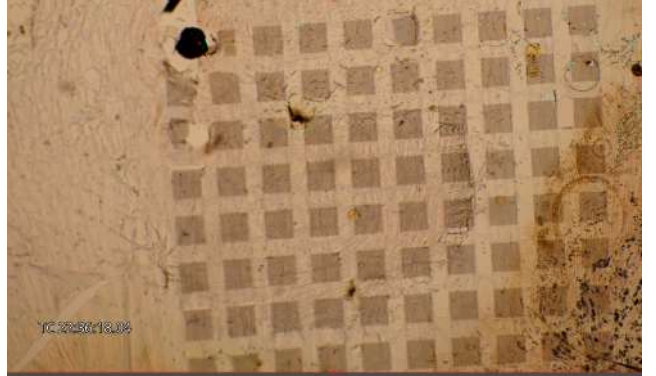


FIG. 7. An image of the PDMS after the transfer of the metasurface. Each square is a 50x50 array of gold nanofeatures. The chromium adhesion layer and the PMMA are still present. It was imaged through the PDMS using an inverted optical microscope.



FIG. 8. An image of the fiber tip after the transfer of the metasurface. The poorly aligned metasurface can be seen on the lower half of the fiber's tip. This may not be an exemplary transfer, but it points to the potential of the method.

#### IV. CONCLUSION

Our experiments have shown that our new copper-based process has the potential to be an effective transfer method. Time constraints meant that a final metasurface-to-fiber transfer process could not be perfected, but what we have learned can be extrapolated toward this conclusion.

We know that the copper etchant is much more efficient than the chromium etchant, etching away the sacrificial layer in around 2 to 2.5 hours. We also know that, although the PMMA layer does not delaminate as we had anticipated, we can use the PDMS to remove

unbesmirched sections of gold and polymer. If the fiber is connected at the correct angle and pressure, we notice that the rate of transfer is very high and expect that these results would carry through to a gold metasurface in place of a solid golden surface.

This same principle of utilizing PDMS doesn't need to change as the process iterates toward the final product; the final chalcogenide fiber will be of a similar size to the fiber we tested, and thus should behave in a similar way when picking up the metasurface.

This process can decrease the time and effort needed to transfer metasurfaces to the tips of optical fibers. The current available methods, thiol-ene film transfer and nanoskiving, have numerous steps requiring specialized equipment, but our method, after fabrication, is much simpler. With a spinner, a chemical hood, and some PDMS, our method can be executed. In addition, once this process has been established, any metasurface could be transferred. Whether we are using an array specialized for proteins or one tuned to an entirely different wavelength, they all ought to be able to be placed onto the tip of a fiber using our method.

Additionally, one transfer to PDMS can result in many transfers to fiber tips. Since the PDMS removes large sections of the surface and the tips only remove small pieces, this method is quite efficient. One round of fabrication can provide for numerous samples, while probably taking a similar amount of time to machining the surface directly onto the tip of one fiber. This principle, in general, speaks to the efficacy of our method. The techniques are not so revolutionary, the process does not take pages to explain. Instead, the simplicity improves the process, leading to better efficiency and an easier process.

### A. Future Work

As this process continues to develop, there are multiple steps which can be taken to improve it. First and foremost is the perfection of the transfer technique. For our preliminary tests with metasurfaces, we used a micrometer stage, an inverted microscope, a fiber holder, and a lot of double-sided tape to create a makeshift device which would regulate the connection of the fiber and the metasurface. With more practice, we will learn exactly how the sample should be aligned, as well as the distance the fiber needs to press down in order to optimally connect with the metasurface.

Also important is the improvement of the adhesion of the gold metasurface (and the chromium adhesion layer) to the tip of the fiber. As of now we are unsure whether or not the fiber would survive a submersion in water. Some ideas to improve the adhesion include annealing the fiber or evaporating a thin layer of silicon onto the surface.

Next, the metasurface we transferred was scaled up, and we used a silica fiber. For its final application, a smaller metasurface and a chalcogenide fiber should be used. Although we don't anticipate significant deviation in results when making these changes, it is still important to consider how they may affect the process. A smaller metasurface means that the transfer process will need to be even more precise, and the chalcogenide fiber may behave differently when picking up the metasurface from the PDMS.

Once the process for the final metasurface and fiber has been streamlined, we will test the fiber for its intended usage: biological sensing. Whether or not the device can successfully identify spectral identities of proteins will determine whether or not further changes to the process need to be made.

Although we may not have reached the final stages of this project, we are confident that our work has laid a solid foundation for a more cost- and time-effective method for transferring metasurfaces to the tip of an optical fiber. With some more work along this vein, we are confident that this method has the potential to simplify the transfer process, opening the doors for minimally invasive yet precise biosensors and countless other applications.

### V. ACKNOWLEDGEMENTS

The author would like to thank Gennady Shvets, Steven He Huang, and Shourya Dutta Gupta. Thank also to the CNF and its staff (especially Aaron Windsor and Jerry Drumheller). This work was performed in part at the Cornell NanoScale Facility, a member of the National Nanotechnology Coordinated Infrastructure (NNCI), which is supported by the National Science Foundation (Grant ECCS-1542081). Of course, a huge thank you to the CCMR REU program, especially Rebecca Broome and Nevjinder Singhota. The CCMR REU program is supported by the NSF MRSEC program (DMR-1719875) and the REU Site program (DMR-1063059).

- 
- [1] Wu, Chihhui, Alexander B. Khanikaev, Ronen Adato, Nihal Arju, Ahmet Ali Yanik, Hatice Altug, and Gennady Shvets. "Fano-resonant Asymmetric Metamaterials for Ultrasensitive Spectroscopy and Identification Of molecular Monolayers." *Nature Materials* 11, no. 1, **69-75** (2011).
- [2] Yu, Nanfang, and Federico Capasso. ["Optical Metasurfaces and Prospect of Their Applications Including Fiber Optics."] *Journal of Lightwave Technology* 33, no. 12, **2344-2358** (2015).
- [3] Smythe, Elizabeth J., Michael D. Dickey, George M. Whitesides, and Federico Capasso. ["A Technique to Transfer Metallic Nanoscale Patterns to Small and Non-

- Planar Surfaces.”] ACS Nano 3, no. 1, **59-65** (2009).*
- [4] Lipomi, Darren J., Ramses V. Martinez, Mikhail A. Kats, Sung H. Kang, Philseok Kim, Joanna Aizenberg, Federico Capasso, and George M. Whitesides. [”*Patterning the Tips of Optical Fibers with Metallic Nanostructures Using Nanoskiving.*”] Nano Letters 11, no. 2, **632-36** (2010).
- [5] Carlson, Andrew, Audrey M. Bowen, Yonggang Huang, Ralph G. Nuzzo, and John A. Rogers. [”*Transfer Printing Techniques for Materials Assembly and Micro/Nanodevice Fabrication.*”] Advanced Materials 24, no. 39 **5284-318** (2012).

# Characterization of Scanning Superconducting Quantum Interference Devices (SQUIDs)

Rebecca Davis<sup>1</sup>, Rachel Resnick<sup>2</sup>, David Low<sup>2</sup>, Professor Katja Nowack<sup>2</sup>

<sup>1</sup>Department of Physics and Engineering, West Virginia Wesleyan College, Buckhannon,  
WV 26201

<sup>2</sup>LASSP, Cornell University, Ithaca, NY 14853

**Abstract-** Detecting small magnetic fields is crucial to various fields, including submarine detection, brain signal scanning, and fundamental science research. Superconducting Quantum Interference Devices (SQUIDs) are highly sensitive magnetic field detectors. However, to detect the lowest fields possible, it is desirable to reduce noise in the SQUID. Here we characterize the noise of SQUIDs specifically designed for scanning. We implement a procedure to tune the SQUIDs to have optimal noise performance. We further study the effect of a damping resistor added to a SQUID circuit and find that it impacts the hysteretic properties and resonances of the SQUIDs.

---

## I. Introduction

SQUID designs have been described in many places in the literature [1]. SQUID magnetometers allow for the measurement of small magnetic fields. This makes them suitable for applications such as neuroscience, military defense, and fundamental science. SQUIDs have been used both to measure the magnetic field activity of the brain and to detect the magnetic field signals emitted by submarines. Fundamentally, these devices function by outputting a measurable voltage signal in response to an input magnetic flux. The resultant voltage signal allows for classification of material properties such as superconductivity; for example, the superconducting transition could be identified using this method.

The SQUIDs used in our lab have several components including a field coil, modulation (mod) coil, pickup loops, shunt resistors and Josephson junctions. An input current is sent through the mod coil. This

generates magnetic flux in the superconducting loop, thus changing the output voltage. The output voltage can then be displayed on current-voltage (IV) curves for analysis. Josephson junctions are the core of these devices. They are comprised of two superconducting layers with a thin insulating layer in between. Here, we use Niobium (Nb) as a superconductor with an insulating aluminum oxide layer. Junctions interrupt the superconducting loop to modulate the input signal in response to magnetic flux. Temperatures as low as ~9K are needed for Nb to superconduct and we perform our measurements at ~4K. Superconductivity can be observed through voltage measurements of the SQUID. Figure 1 shows a diagram of our SQUIDs.

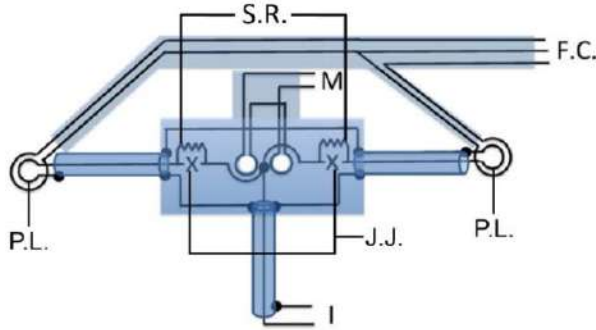


**Figure 1.** A schematic of our SQUIDS including the field coil (F.C.), modulation coil (M), Josephson Junctions (J.J.), shunt resistor (S.R.) and pickup loop (P.L). [4]

An important component are the resistors ( $R$ ) that shunt the Josephson junction as visible in Figure 1 and Figure 2a. These determine whether or not the SQUID is hysteretic through the quantity defined by Eq. (1).

$$\beta_c = \frac{2\pi}{\phi_0} (I_c R^2 C) \quad (1)$$

$I_c$  denotes the critical current

$R^2$  denotes Shunt Resistance

$C$  denotes capacitance

$\phi_0$  denotes the magnetic flux quantum

When  $\beta_c < 1$ , hysteresis will not occur. When  $\beta_c \geq 1$ , the SQUIDs begin to exhibit hysteretic properties [3]. For our application, hysteretic SQUIDs are not desirable because they switch randomly between two different states. From Eq. (1), it is apparent that higher shunt resistor values result in higher  $\beta_c$  values. Considering this, selection of the resistor values allow for control over the hysteretic properties of the SQUIDs.

Another less controlled component of the SQUID is parasitic capacitance, which is present due to our specific design as shown in Figure 1. The parasitic capacitance causes

resonances in the SQUID [2]. It has been theorized that adding a damping resistor (See Figure 2b), in addition to the shunt resistors, can alter these resonances [5] and through that, can improve the noise performance. We therefore tested SQUIDs with and without damping resistors, as seen in Figure 2a and Figure 2b.

The SQUIDs we are testing are fabricated by Hypres [6], all with varying shunt resistors and with and without a damping resistor.

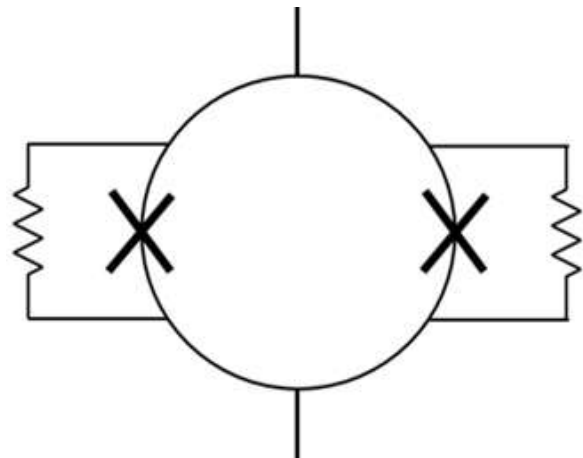


**Figure 2a.** SQUID with shunt resistors and without a damping resistor.

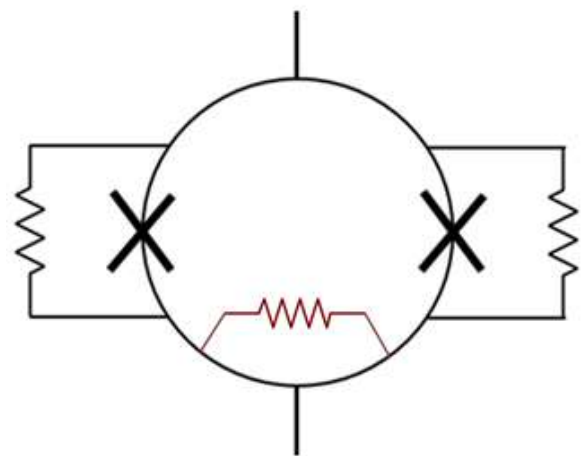
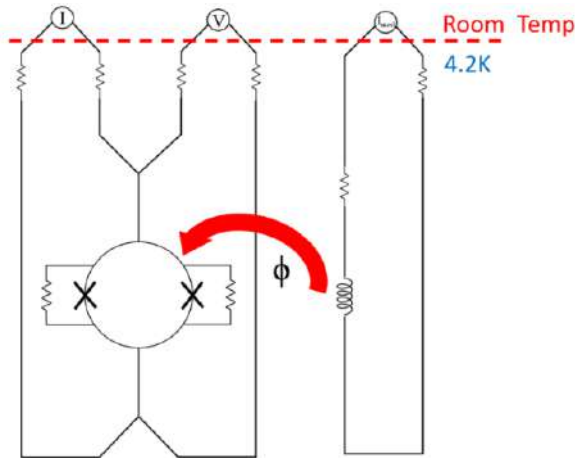


**Figure 2b.** SQUID with shunt resistors and a damping resistor

## II. Methods

### A. Process of IV Measurement

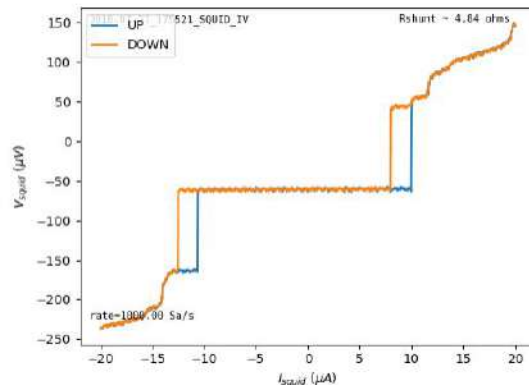
To take IV measurements, a current must run through the SQUID. Figure 3 shows the general setup for IV testing. The red dashed line signifies the helium Dewar in which our SQUIDS are placed during testing to cool to 4.2 K. Current is sent through the mod coil which then generates a magnetic field that threads magnetic flux into the SQUID, seen by the red arrow.



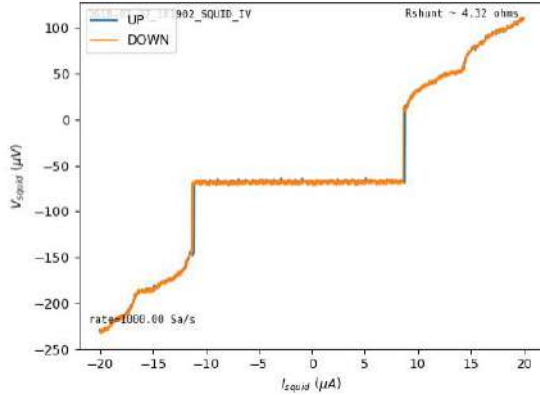
**Figure 3.** Diagram of 4 point IV system. Current is sent through the SQUID to generate a voltage. Current is sent through the mod coil which generates magnetic field. This magnetic field then threads into the superconducting loop of the SQUID to create magnetic flux.

Using Python, the lab can remotely control the current and read the resulting voltage across the SQUID to record IV characteristics of the SQUID. This IV process allows us to observe crucial characteristics of the SQUID, such as when it superconducts below the critical current and the hysteretic properties.

Hypres scanning SQUIDs with 8 ohm shunt resistors (R8 SQUIDs) were used to compare properties of the SQUID. These SQUIDs were expected to be hysteretic given their high resistor values. Multiple sets of damped and non-damped R8 SQUIDs were tested and we observed that the addition of a damping resistor decreased the hysteretic properties. Figure 4a shows the IV measurements for a SQUID that is not damped. The portions of the graph in which the orange and blue traces do not coincide clearly show the hysteretic characteristic of the SQUID. The blue line is measured with current increasing from low to high [UP] and the orange line is measured with current decreasing from high to low [DOWN]. Meanwhile, Figure 4b shows the IV measurements for a different SQUID containing a 4 ohm damping resistor in addition to the 8 ohm shunt resistors. This SQUID is not hysteretic.



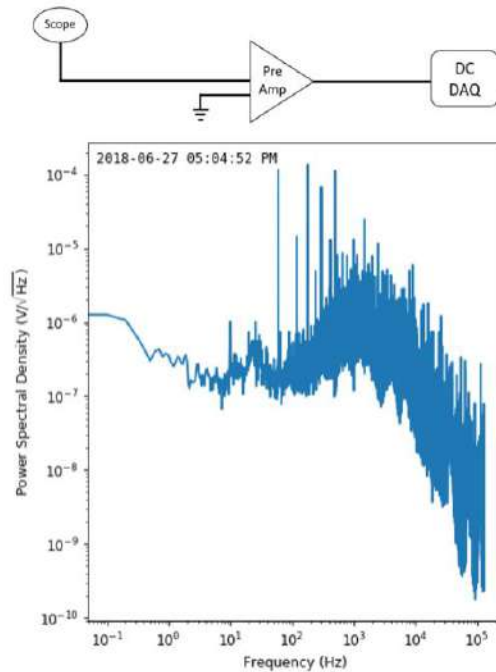
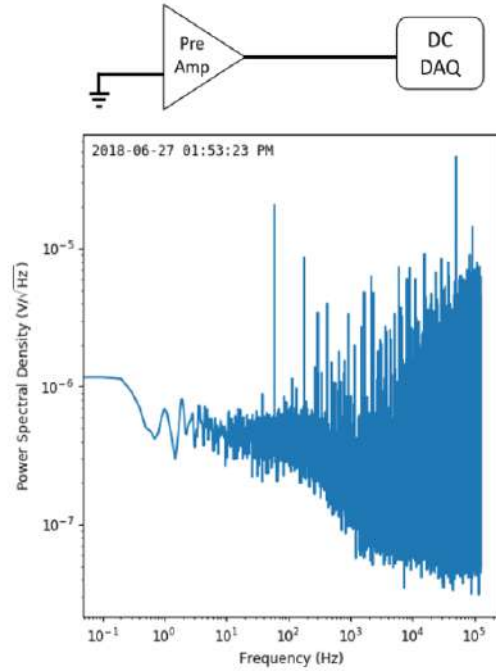
**Figure 4a.** IV measurement of non-damped SQUID with 8 ohm resistor.



**Figure 4b.** IV measurement of damped SQUID with 8 ohm resistor and 4 ohm damping resistor.

### B. Noise Background Measurements

For this project we needed to measure the noise of our SQUIDs. It is important to first check the background noise produced by our experimental setup including an oscilloscope, a data acquisition card (DAQ) and a preamplifier. To check the system, a series of tests were conducted to determine where the majority of the noise signal was originating. The diagrams for the tests are shown in Figure 5.



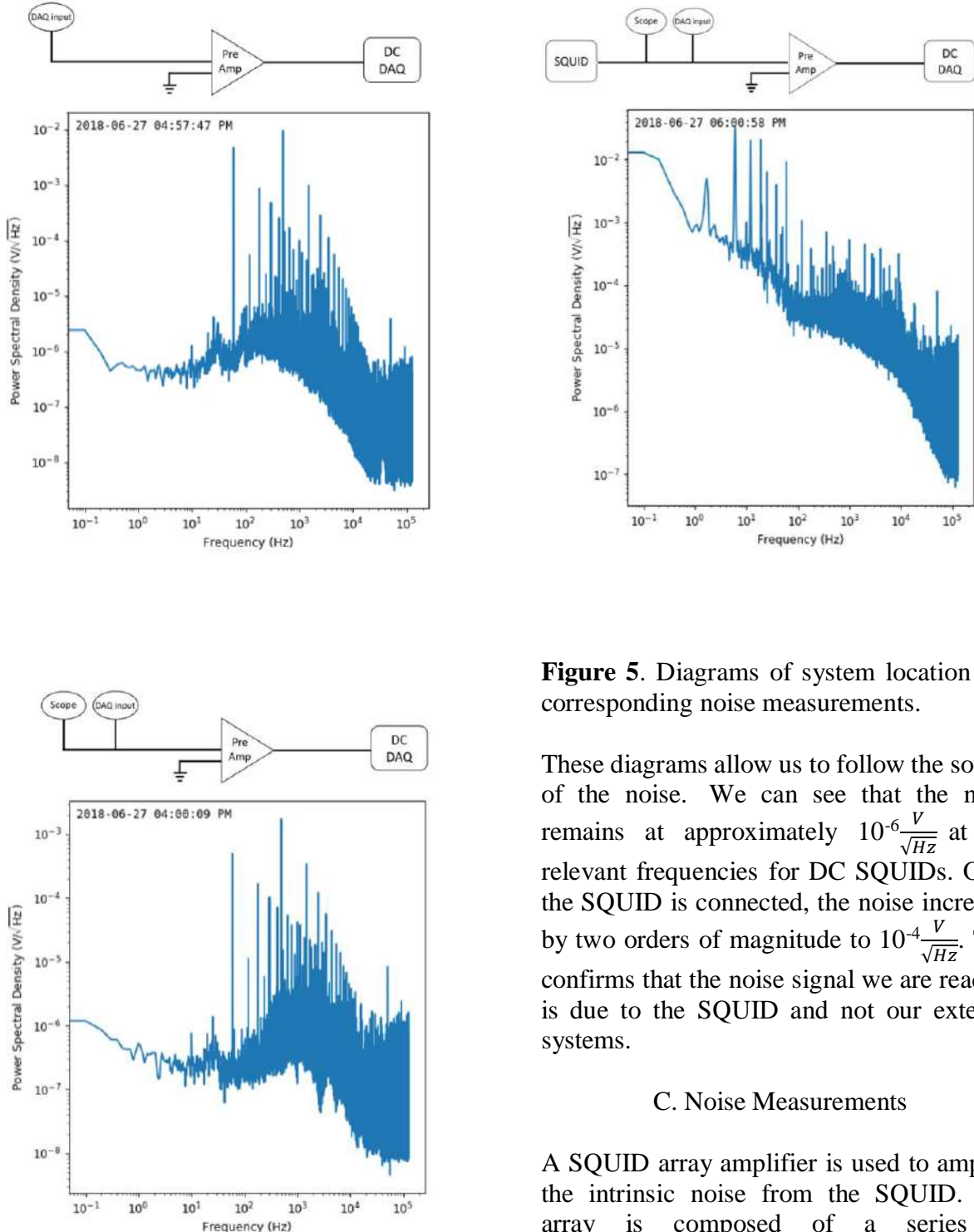


**Figure 5.** Diagrams of system location and corresponding noise measurements.

These diagrams allow us to follow the source of the noise. We can see that the noise remains at approximately  $10^{-6} \frac{V}{\sqrt{Hz}}$  at the relevant frequencies for DC SQUIDs. Once the SQUID is connected, the noise increases by two orders of magnitude to  $10^{-4} \frac{V}{\sqrt{Hz}}$ . This confirms that the noise signal we are reading is due to the SQUID and not our external systems.

### C. Noise Measurements

A SQUID array amplifier is used to amplify the intrinsic noise from the SQUID. The array is composed of a series of SQUIDs. Variations in the current passing through the SQUID are amplified by the array. The current through the SQUID changes due to intrinsic noise and due to changes in magnetic flux through the

SQUID. The amplifier is important for our experiments since our SQUIDs generally have noise on order of  $\mu\phi_0$  which must be amplified in the cold in order to be detected at room temperature. Figure 6 shows the components of the experimental set-up. The entire system is an amplifier for the SQUID shown in Figure 6.

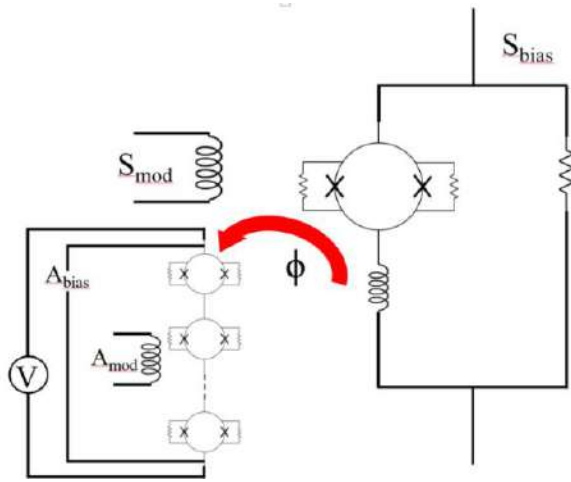


**Figure 6.** Diagram of array system. The array consists of 30 SQUIDS in series, inside of a magnetic shield. The array has a bias current as well as a voltage readout. The SQUID also is measured through a bias current and voltage readout. An array amplifies the noise signal of the SQUID.

We find that the noise performance of the SQUID depends on the available tuning parameters: the current applied to the circuit ( $S_{bias}$ ) and a flux offset ( $S_{mod}$ ). We have implemented a procedure in which we measure the noise as a function of these tuning parameters and then sort through all of the collected data to find the optimum tuning parameter for the SQUID. This gives us the lowest possible noise signal for a given SQUID. An example of an optimal noise spectrum is shown in Figure 7.

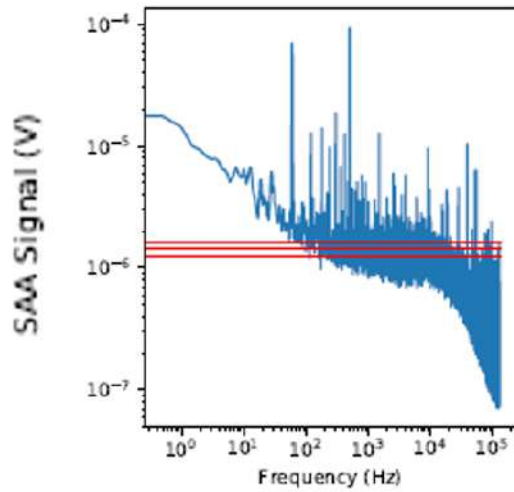


**Figure 7.** R8 non-damped SQUID noise measurement graph. The noise measured in this graph is  $1.44 \frac{\mu\phi}{\sqrt{Hz}}$ .

A noise generally around  $1 \frac{\mu\phi}{\sqrt{Hz}}$  can be classified as a good SQUID that will be able to take accurate magnetic field measurements of a sample. It is crucial to carry out these tests to find the best signal-to-noise ratio of SQUIDS to use for scanning samples.

### III. Results and Discussion

The focus of the study included IV and noise measurements of 8 ohm shunt resistor SQUIDS. We found that damped SQUIDS exhibit significantly less hysteresis and that resonances in the SQUID changed. We further have implemented a procedure to find the optimum noise performance for a given SQUID. Future work will investigate the impact of the damping resistors on the noise performance.

Moving forward, we plan to repeat testing to obtain more data points for both damped and non-damped SQUIDS. A greater number of data points will allow us to determine whether a correlation exists between resistance values and noise performance. If it is found that the addition of a damping resistor also decreases the noise present

within a SQUID, researchers would be encouraged to use damped SQUIDs to obtain more accurate measurements.

[6] SQUIDS & SQIFs. (2011, July 06). Retrieved from <https://www.hypres.com/squids-sqifs/>

## V. Acknowledgements

I would like to thank the CCMR program at Cornell University for allowing me to conduct research this summer. I would also like to thank the NSF for funding me and allowing me to be immersed in academia.

More specifically, I would like to thank Dr. Katja Nowack, David Low, Rachel Resnick and the rest of the Nowack lab for their expertise throughout these ten weeks and for allowing me to use their equipment.

## References

- [1] Clarke, J., & Braginski, A. I. (2004). *The SQUID handbook*(Vol. 1, Fundamentals and Technology of SQUIDs and SQUID Systems). Weinheim: Wiley-VCH.
- [2] Hilbert, C., & Clarke, J. (1985). Measurements of the dynamic input impedance of a dc SQUID. *Journal of Low Temperature Physics*, 61(3-4), 37-262.
- [3] Huber, M. E., Koshnick, N. C., Bluhm, H., Archuleta, L. J., Azua, T., Björnsson, P. G., Moler, K. A. (2008). Gradiometric micro-SQUID susceptometer for scanning measurements of mesoscopic samples. *Review of Scientific Instruments*, 79(5), 053704.
- [4] Kirtley, J. R., Paulius, L., Rosenberg, A. J., Palmstrom, J. C., Holland, C. M., Spanton, E. M., . . . Moler, K. A. (2016). Scanning SQUID susceptometers with sub-micron spatial resolution. *Review of Scientific Instruments*, 87(9), 093702.
- [5] Knuutila, J., Ahonen, A., & Tesche, C. (1987). Effects on DC SQUID characteristics of damping of input coil resonances. *Journal of Low Temperature Physics*, 68(3-4), 269-284.

# A differential current cutoff method for the electrochemical fabrication of gold tips for magneto-thermal microscopy

Jamie Holber,<sup>1</sup> Chi Zhang,<sup>2</sup> and Gregory Fuchs<sup>2</sup>

<sup>1</sup>Department of Physics, Brown University, Providence, RI 02912

<sup>2</sup>Department of Applied and Engineering Physics, Cornell University, Ithaca, NY 14853

The magnetic imaging of a ferromagnet is important to the development of spintronics. Magneto-thermal microscopy is one such method of magnetic imaging. The resolution of the microscopy is dependent on the size of the heat source used in the microscopy. A very sharp gold plasmonic antenna could provide a solution to high resolution imaging. The sharpness of the tip is essential to high quality microscopy. In this report we study a new method to produce a sharp gold tip using electromagnetic etching.

## I. INTRODUCTION

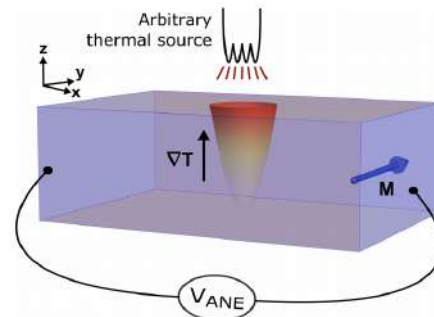
Recently there has been increasing interest in the field of spin-based devices, or spintronics. Spintronics relies on precise control of the magnetic moment throughout the entirety of a material<sup>7</sup>. Finding ways to control the magnetic moments relies on microscopy that can observe magnetic phenomenon at the nanoscale. One method of measuring the magnetic moment is by applying a thermal source in the Z direction to the ferromagnetic material and measuring the voltage across the material in the Y direction as in Figure 1a. The thermal source causes a heat gradient through the Z direction of the sample, which interacts with the magnetization in the Y direction to produce a voltage,  $V_{ANE} \propto |\nabla T \times M|$ . Given the thermal source and by measuring the voltage, we can calculate the magnetization at each position in the Y axis. The resolution of magnetization across the Y axis is roughly equal to the diameter of the thermal source at the point of contact with the ferromagnet.

Traditionally, a laser has been used as the thermal source. However, using light limits the resolution to a few hundred nanometers, due to the diffraction-limited focal resolution<sup>7</sup>. Our group simulated a new technique using a gold plasmonic antenna of sub-100 nm diameter. A light is shined on the conical antenna exciting the surface plasmon polaritons, as shown in Figure 1b. When the apex of the antenna is within a few nm of the surface of the ferromagnet there is electromagnetic loss in the sample creating a heat gradient. The FWHM of the electromagnetic loss grows with apex radius at 0.95 nm/nm for apex radii below 30 nm, and grows with apex radius at 3.73 nm/nm for apex radii above 30 nm<sup>7</sup>. The tip radius is therefore crucial to the resolution of the magneto-thermal microscope.

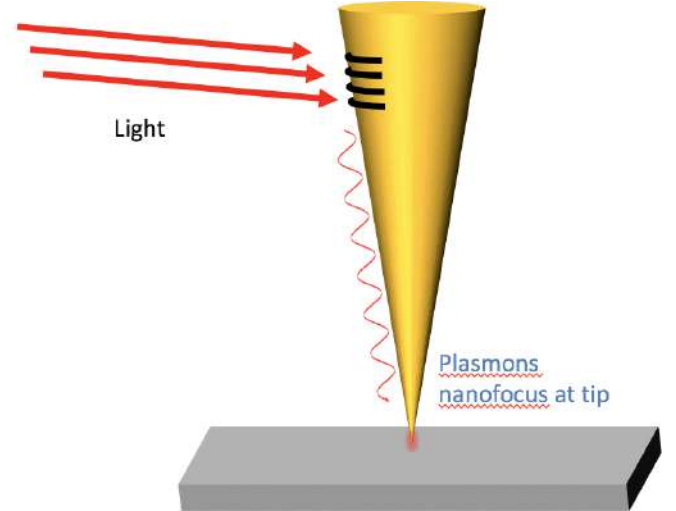
There have been at least 10 different techniques used to produce metallic tips for use such fields as electron microscopy, field ion microscopy, scanning tunneling microscopy<sup>4</sup>, and Raman spectroscopy. However, reliable and cost effective methods are still being explored. Some explored techniques are mechanical cutting<sup>2,5</sup>, ion milling<sup>5</sup>, grinding<sup>8</sup>, beam deposition<sup>8</sup>, and using a field ion microscope in a vacuum<sup>2</sup>,

One of the most practical and reliable methods for tip

production is electrochemical etching<sup>1–5</sup>. A fast control method is imperative in order to create a sharp tip. This project compares two control methods for stopping the current: a homemade differential cutoff loop, and a preset cutoff current.



(a) The thermal gradient,  $\nabla T$ , produced by a thermal source interacts with the magnetization of the ferromagnet to produce a voltage<sup>7</sup>.



(b) Magneto-thermal microscopy with a gold tip as a heat source

FIG. 1: Magneto-thermal microscopy

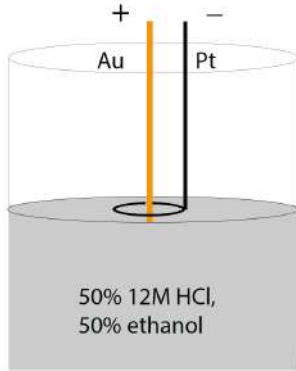


FIG. 2: Diagram of the setup for preparing the gold tip.

## II. EXPERIMENT

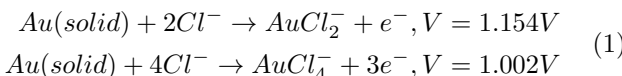
### A. Preparation of Tips

A gold wire of 0.05 mm is used to create the tips. The wire is cut into pieces approximately 1 inch in length. These pieces are then annealed at 800 C for 8-10 hours. They are then cooled at 0.5 C/min to 300 C, then cooled at 40 C/min to 50 C, before being allowed to naturally cool to room temperature.

### B. Electrochemical Etching

The gold tips are etched in a solution of 50% 12M HCl, and 50% ethanol. There are other possible solutions, but the advantage of HCl is that it is non-toxic and has a low etching voltage<sup>2</sup>(~2 V). The setup used is shown in Figure 2. The gold wire is immersed several millimeters in the solution and a 500  $\mu$ m platinum wire is placed on the surface of the solution with the voltage applied across them.

The electrochemical etching is governed by several redox reactions, shown below with their potential thresholds<sup>3</sup>. The gold atoms at the surface are dissolved, the rate being determined by the voltage applied. The gold atoms are dissolved more quickly at the surface because there is a higher concentration of Cl<sup>-</sup>.



In this project, the tip is formed in two steps. A threshold voltage is found based on the minimum in the IV curve. Etching below the threshold voltage creates a smooth tip, but not very sharp. Etching above the threshold yields a very sharp tip, but is not as smooth. The first step is with a voltage about 0.1 V below the threshold, and the second step is with a voltage about 0.1 V above the threshold. By using the lower voltage

we create a longer smooth tip, then applying the high voltage creates a sharp tip at the end.

This project relies on the 'drop-off' method. When the diameter of the wire at the interface is sufficiently small, the weight of the immersed wire exceeds the tensile strength of the necked region and the lower part of the wire will break and fall<sup>4</sup>. At the point of falling, the current applied to the wire drops significantly, and the tip is at its sharpest point. If a voltage continues to be applied then the wire will continue to be etched and will start to become more dull. An important part of the method is to stop the voltage through the wire as quickly as possible (ideally in the range of several hundred nanoseconds). There are two main approaches. One approach is setting a cutoff current, and if the current drops below this point, the power supply will be shut off. The other approach is monitoring the current, and shutting off the system when the differential current decreases.

### C. Preset Current Cutoff

The current method used in our lab to etch relies on a Keithley, which both supplies voltage to the gold wire, and measures the current across the wire. Labview controls the Keithley, dictating the voltage output and monitoring the current input. When the current drops to the preset cutoff (0.005 A), labview will shutdown the Keithley's output and etching will cease. The problem with this method is that between the current dropping, the Keithley has to measure the current, relay the information to the computer, which sends information back to the Keithley, before the power is shut off. This delay is likely several ms and means the tips are not as sharp as they could be.

### D. Differential Current Cutoff

A second method for shutting off the current is to use a homemade differential current cutoff circuit shown in Figure 3a based off of the circuit described by Anwei et al<sup>4</sup>. When the lower part of the wire drops, the current through the wire will drop as well. We then expect to see a large drop in the dI/dt curve, as shown in Figure 4. We can utilize this spike to shut off the system.

The circuit consists of a current to voltage converter, a differentiator, a comparator, and a D type flip flop(latch). The current to voltage converter is an op-amp circuit, shown in Figure 3b, while the passive differentiator is shown in Figure 3c. We decided to use an op-amp as a comparator instead of an actual comparator, because the op amp was more reliable. The latch is a D type positive edge triggered flip flop where the output of the comparator goes to the clock input of the flip flop.

First the current is converted to voltage, as shown in Figure 3b, where  $V_{out} = -RI_{in}$ . Then the differentiator takes the derivative of the input voltage, so

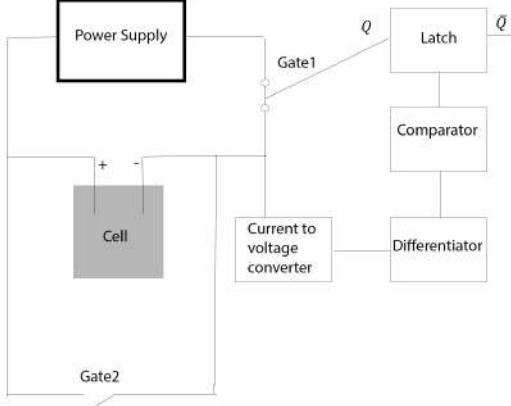
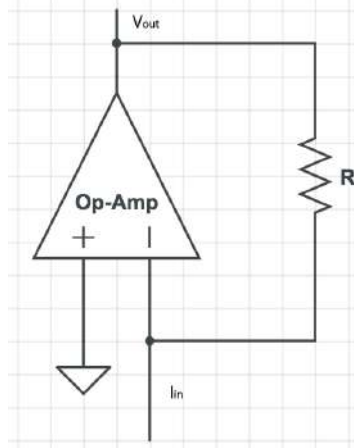
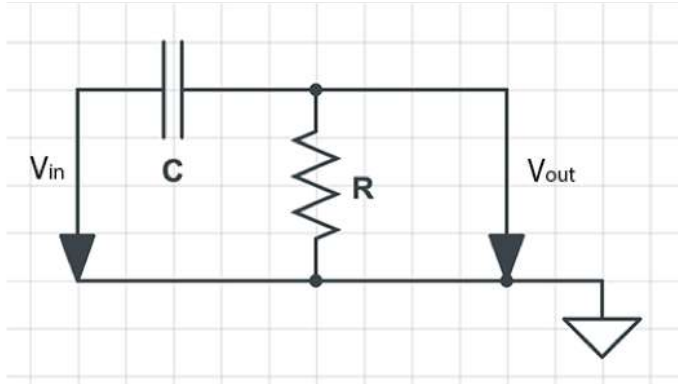
(a) Diagram of the differential current cutoff<sup>6</sup>.(b) Diagram of the current to voltage converter<sup>5</sup>.(c) Diagram of the differentiator<sup>5</sup>.

FIG. 3: The differential cutoff circuit

$V_{out} = RC \frac{dV_{in}}{dt}$ .  $V_{out}$  of the differentiator is approximately equal to zero except when the lower part of the wire drops, when  $V_{out} \approx -0.2$  V. The two inputs to the comparator are  $V_{out}$  and ground. When  $V_{out}$  is larger than

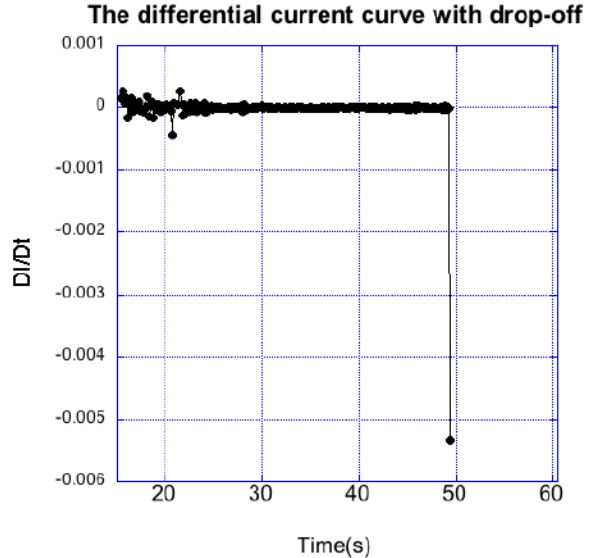


FIG. 4: Plot of the derivative of current with respect to time for a sample tip

ground the comparator's output is low (~0.030). When  $V_{out}$  is smaller than ground the comparator outputs a high voltage (~3.9) and triggers the flip flop so that  $Q$  becomes high and  $\bar{Q}$  becomes low. The flip flop output is ~0.135 for low outputs and ~4.5 for high outputs. The  $Q$  and  $\bar{Q}$  are applied to the base of PNP transistors. For PNP transistors, if the base input is <0.7 then the transistor operates as a closed gate, otherwise the transistor operates as an open gate.

Before the current drops Gate 1 is closed and Gate 2 is open. Once the current drops, Gate 1 opens and Gate 2 closes. The opening of Gate 1 causes current to stop flowing through the system. Any residual current should go through Gate 2, instead of the cell, because gate 2 is closed and will have a much lower resistance. The time delay of the circuit is determined by the two op-amps (<100 ns), the flip flop (40 ns) and the transistor (75 ns). The circuit is expected to have a delay time of less than 500 nm and be much faster than using an ammeter and computer, and therefore would be expected to make sharper tips.

## E. Imaging

We used a Focused Ion Beam (FIB) to image the tips we etched. We first had to remove the tip from the cell, from Figure 3a, with tweezers. We then had to glue the tip to a sapphire substrate slide. We next transferred the slides to a SEM sample holder. Copper was then glued on top of the tips for grounding during imaging. The slides could then be imaged. This process is very tricky

and often tips are broken during one of the steps.

### III. RESULTS

#### A. Testing

Once setting up the circuit we first tested to make sure that when there was a drop in current, the circuit responded and the current was cut off. To test this we replaced the cell portion of the setup, Figure 3a with a resistor of a similar resistance to model the stage of etching before the drop off point. We then dropped the voltage, which in turn decreases the current across the circuit, which approximates what would happen at the drop off point. Even though the voltage does not actually drop in the real etching, the voltage across the cell would increase in proportion to the rest of the circuit because of the increase in resistance in the cell.

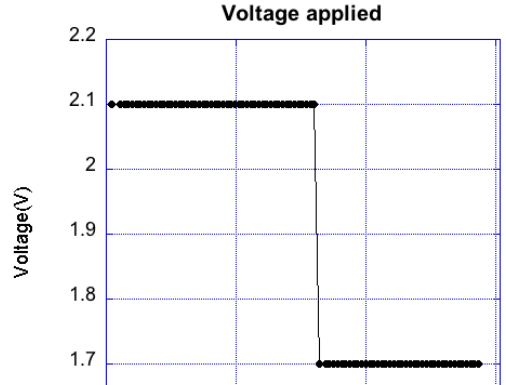
We used the computer to apply a voltage across the resistor and circuit and had the voltage switch from 2.1 V to 1.7 V after a few seconds, shown in Figure 5a. We then used the circuit in the off position as the control to compare against the circuit in the determine if the circuit works. With the circuit off, the current decreases from  $\sim 0.006$  to  $\sim 0.004$  A as shown in Figure 5b. When the circuit is on, the circuit decrease from  $\sim 0.006$  to  $\sim 0$  A, shown in Figure 5c. The decrease in current due to the voltage decreasing as shown in Figure 5b leads to the circuit opening gate 1 and closing gate 2. The current does not completely reach 0, but drops to  $\sim 10^{-11}$  A. We used a normal switch, but a high quality more expensive switch would likely cause the current to be completely cut off.

This testing shows that the circuit is capable of cutting off the current to near-zero and given the parts used could be significantly faster than the computer at responding to a change in current.

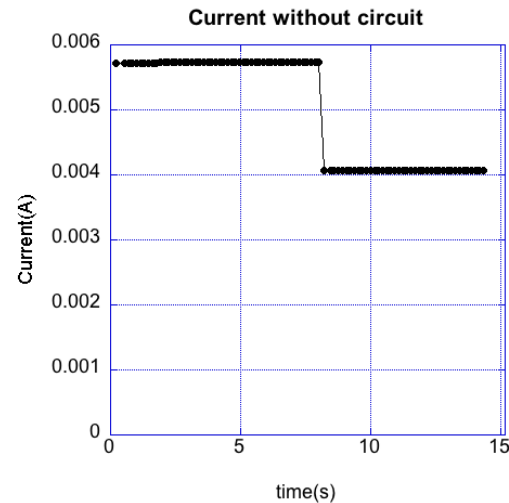
#### B. Etching

We etched gold wires using both the preset current method, with a computer monitoring the current and controlling the power supply, and the differential current cutoff method. The best tip produced with the preset current method is shown in Figures 6a and 6b and is about 75 nm across. The smallest gold tips in the literature are about 10 nm, and many are below 50 nm<sup>4</sup>. In the past we have produced smaller tips, but most are 50 nm or larger.

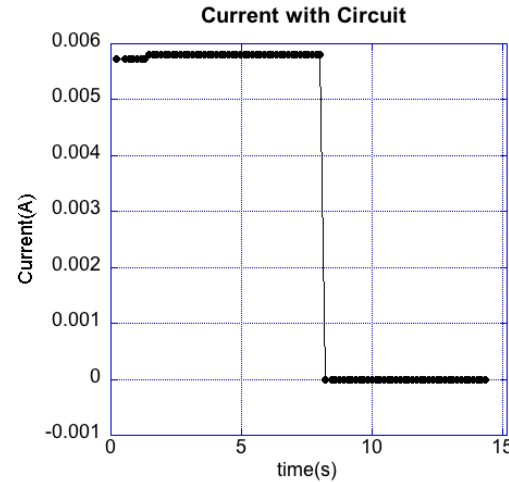
We also etched using the circuit in addition to the computer method. We still used the preset cutoff so that when the current was cutoff the power supply was shut off automatically. We found that the current measured changed significantly when the circuit was introduced to the system. In addition the current increased when the voltage increased with the circuit but decreased when the



(a) The voltage applied to the system to test the circuit

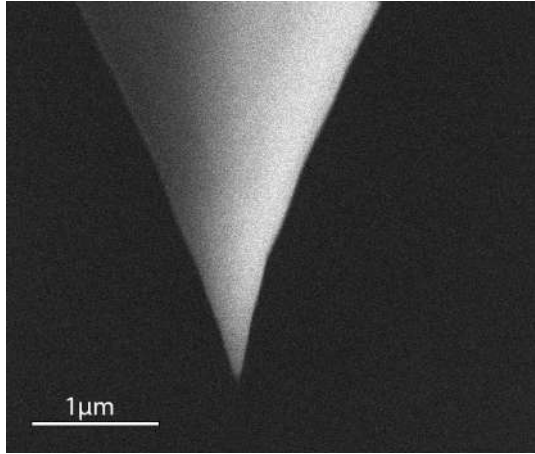


(b) How the current responds to the change in voltage without the circuit

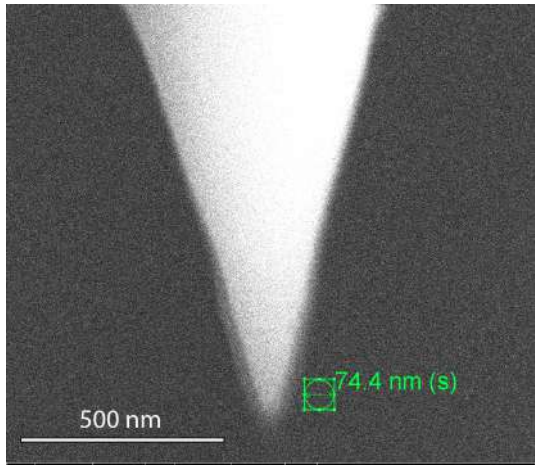


(c) How the current responds to the change in voltage with the circuit

FIG. 5: The results from testing the circuit



(a)



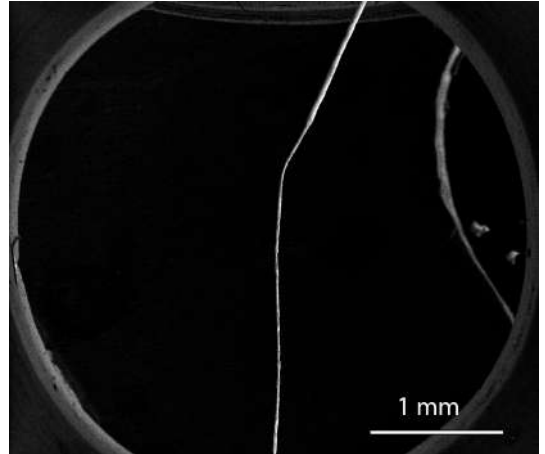
(b)

FIG. 6: Tip produced using preset current cutoff method

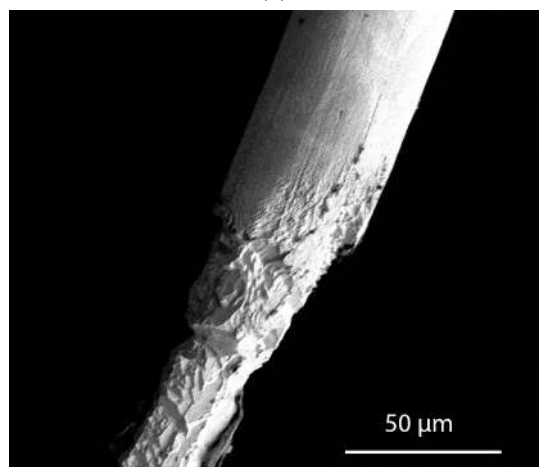
voltage increased for the computer method. The decrease in the current is due to the increased resistance throughout the system. We found that the closed gate and the path through it had a lot higher resistance than what was assumed. The change in the relationship of current and voltage is assumed to be due to the fact that the wire was being etched in the preset current cutoff method, and the wire was hardly etched in the differential current cutoff method.

The gold tip for the differential current cutoff is shown in Figures 7a and 7b. In Figure 7a you can see that there is a thinner part of the wire and a thicker part. The thinner part of the wire was in the acid and the thicker part was in the air. This implies that the drop-off point did not happen when the circuit cutoff the current. Instead, there was probably a smaller decrease in current that was enough to trigger the flip-flop. The circuit ended up being too sensitive to small changes in current.

To correct for the sensitivity there could be a change in the resistors for the current to voltage converter and the



(a)



(b)

FIG. 7: Tip produced using differential current cutoff method

differentiator. An increase in the resistor for the current to voltage converter, and a decrease in the resistor for the differentiator would both make the circuit less sensitive. In addition, ground was used as the other input for the comparator because the output of the differentiator must be significantly below zero for the comparator to output the high voltage. Instead, an additional power supply could be used to compare, which could also solve the problem.

In addition to the over-sensitivity, the wire does not etch much with the voltages we have been using. In Figure 7b, it is clear even after etching for about 66 s, the wire near the interface between the air and water is barely etched, due to the addition of the circuit. There will need to be further testing to determine if there is a different optimal voltage, or if the wire will need to be etched for much longer.

#### IV. CONCLUSION

From the testing it is clear that with better switches, the differential circuit cutoff method is a viable method to cutoff the current more quickly than using a computer to monitor the current. However, we need to solve the problem of oversensitivity and to find the optimal voltages to apply to the gold wire. With a faster cutoff time we could make gold tips that are less than 25 nm<sup>4</sup> creat-

ing a much more accurate magneto-thermal probe.

#### V. ACKNOWLEDGEMENTS

I would like to thank the entire Fuchs group, especially Professor Gregory Fuchs and Chi Zhang for their mentorship. This work was supported by the Cornell Center for Materials Research with funding from the NSF MRSEC program (DMR-1719875) and the REU Site program (DMR-1063059).

- [1] M. Lopes, T. Toury, M. L. De La Chapelle, F. Bonaccorso, and P. G. Gucciardi, Rev. Sci. Instrum. 84, 073702 (2013).
- [2] B Ren, G Picardi, and B Pettinger. Review of Scientific Instruments 75, 837 (2004); doi: 10.1063/1.1688442
- [3] J. J. Lingane, Journal of Electroanalytical Chemistry (1959), vol. 4, no. 6, pp. 332-342, 1962.
- [4] Boyle MG, Feng L, Dawson P. Safe fabrication of sharp gold tips for light emission in scanning tunneling microscopy. Ultramicroscopy 2008;108:558-66.
- [5] L Anwei, H Xiaotang, L Wenhui, J Guijun. Review of Scientific Instruments 68, 3811 (1997); doi: 10.1063/1.1148032
- [6] Simpson, R. E. (1987). Introductory electronics for scientists and engineers. Boston: Allyn and Bacon. pp. 133, 428
- [7] J Karsch, J Bartell, and G Fuchs. APL Photonics 2, 086103 (2017); <https://doi.org/10.1063/1.4998757>
- [8] Y. Khan, H. Al-Falih, Y. Zhang, T. K. Ng, and B. S. Ooi, Rev. Sci. Instrum. 83, 063708 (2012).

# 3D Printing Porous Monoliths in Microfluidic Device to be Used in Protein Separation

Saman Khorasi<sup>1</sup>, Jen-Yu Huang<sup>2</sup>, Tobias Hanrath<sup>3</sup>

**Abstract:** Protein separation in a microfluidic device is a relatively novel idea. The ability to confine the separation process to a micrometer scale allows for fewer resources to be used and almost instantaneous results which would be useful in clinical settings where small samples need to be tested. In this study, we use a microfluidic device composed of a body polydimethylsiloxane (PDMS) rested upon a transparent microscope glass slide. Ultraviolet light (UV) patterns provided by a digital light processing printer are shined into a microfluidic channel that is filled with a zirconia-based ink. The reaction of the ink and UV light produces a highly porous monolith. The high surface area means more active sites can be created for the separation process. Through analyzing many results, we were able to determine the optimal size of the images being projected and the ideal concentration of zirconia in the ink to produce the highest resolution images possible. Future work involves redesigning the microfluidic chip with a UV transparent backing and figuring out a mechanism to print even smaller images to allow for a finer separation process. Nonetheless, the methods development discussed in this paper shows promising results for the field of small-scale protein separation.

## Introduction:

Previously, various methods of protein separation have allowed us to analyze the functions of proteins and their applications in various fields. This multi-step process, although effective, requires a high volume of resources and is time consuming [1]. The most common approach of protein separation, column chromatography, requires a tedious column preparation and when applied to the micro scale, it is not as efficient [2]. By scaling down the process using a microfluidic device, we are able to confine the separation and use a fraction of the reagents and energy. An alternative method of protein separation uses stationary phases such as monoliths, [2] which can be successfully scaled down to the micro level.

These monoliths have a higher surface area, yielding more active sites for separation to take place. Previous studies have used silica beads, whose surfaces have been tagged with binding agents to separate proteins [1]. However, it can be difficult to control the precise location of these beads within the channel due to the high pressure of the liquid passing through the device. Furthermore, the beads have a limited surface area, which restricts the number of active sites that would be used for protein separation. These silica beads have been held in place using a gel to prevent them from moving during the flowing process, but this gel can restrict the flow of the protein solution due to its low surface area [1]. By having a stationary porous monolith inside a microfluidic channel, one would be able to efficiently and

---

<sup>1</sup> Georgia Institute of Technology, School of Material Science and Engineering, Atlanta, Georgia

<sup>2</sup> Cornell University, Department of Chemical and Biomolecular Engineering, Ithaca, New York

<sup>3</sup> Cornell University, Department of Chemical and Biomolecular Engineering, Ithaca, New York

effectively separate proteins in comparison to previous methods.

In this work, we use a 3D printer to control where we want to print images in the microfluidic channels that would be used in protein separation. We tested multiple types of shapes and sizes before finding the optimal arrangement that was to be used. By using a resin based with a high porous material and confining it in a channel, we are able to increase the number of active sites, thus increasing the efficiency of protein separation and minimizing the number of resources to do so.

## Experimental section:

The microfluidic device that we used contains parallel, micrometer sized channels. The channel design is etched onto a wafer using photolithography.

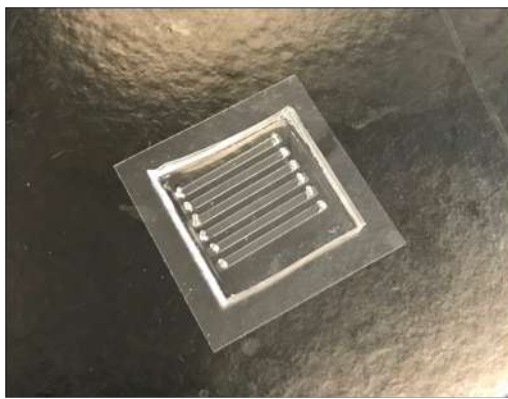


Figure 1: Microfluidic device that was used throughout the experimental procedure

Polydimethylsiloxane (PDMS) is poured on top of this design and allowed to cure. This polymer layer is then bonded to a glass slide or any other sturdy, clear platform. Small holes are punctured at the opening and closing of each channel and small tubes are

attached to these holes to allow for the liquid to flow through.

After the device was made, we formulated the ink that would be used in the printing process. Zirconia crystal was combined with a small amount of photo initiator (PI) and a solvent. This solution was sonicated for 5 minutes and then purged with nitrogen for 3 minutes to remove any oxygen that would inhibit the reaction. Prior to printing, the images were designed in PowerPoint. The slide that would be projected had a black background with the images being white.

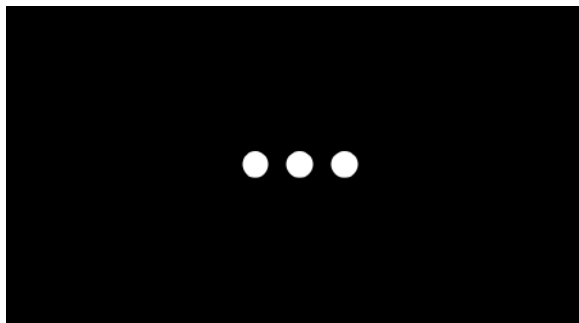


Figure 2: Example of what the projected slide looked like.

In order to print, a device was hooked up to the DLP printer that would contain the slides that were to be projected. The printer was turned on and the image was allowed to project onto the platform. The microfluidic device was then lined up with the image, making sure that the image was projecting into one channel.

The ink was loaded into the channels and reacted with the UV light for 10-15 minutes. After the reaction was completed, the remaining ink was pushed out of the channel with a syringe. The channel was then rinsed with toluene to remove any existing ink. Methanol was then added to prevent the images inside from drying or cracking.

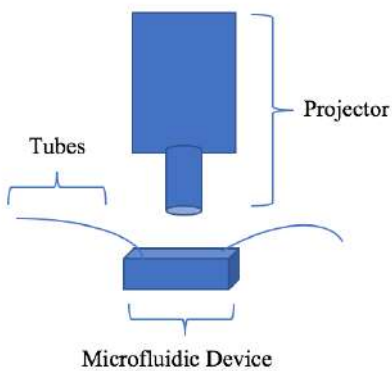


Figure 3: Set up of the microfluidic device and projector during the experiments.

## Results:

After the samples were covered in methanol, they were taken to a high-power microscope to get measurements. For every 1 centimeter that was drawn on the computer, 2.5 millimeters was projected. From this conversion, an image size was estimated. The actual image, when examined, was actually smaller than what was estimated.

Size on the Computer	Theoretical Size (um)	Actual Size Printed (um)
4.3 mm	1075	843
3.5 mm	875	668
3.8 mm	950	716
1.5 mm	375	311
1.25 mm	312.5	285
1.0 mm	250	190

Figure 4: Table of the predicted sizes of the samples versus the actual size that was printed out.

The resolution of the images was also not as clear and defined as we had predicted it to be. When using commercial resin to test which

shapes would print the best in the channels, we found that shapes that had minimal edges such as circles or triangles were more successful in holding to their true shape than shapes with more edges such as stars.

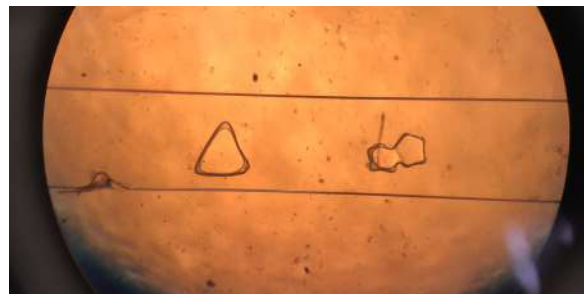


Figure 5: Sample of a microfluidic channel. The image with fewer edges (triangle) printed better than the images with more edges (stars).

Nonetheless, even those images were not as defined as we expected them to be. Furthermore, for the channels that contained small images of only 1-2 millimeters, the reaction took place very slowly or the ink did not react at all.

## Discussion:

Since the resolution of the images was not up to par with what was expected, we changed our approach for printing. The channels were closer to the glass slide than they were to the surface of the PDMS so we decided to shine the UV light through the glass slide.

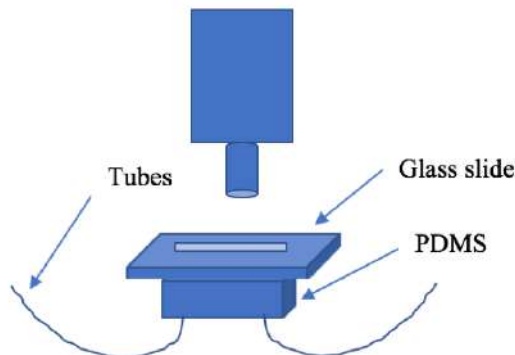


Figure 6: Proposed bottom to top printing method to achieve better resolution.

However, when this theory was tested out, it was not successful. We found that although the glass slide was very thin, it had a lower transmittance for UV light than the PDMS did. We reverted back to the old method of printing from the top down, through the layer of the PDMS. We tried reducing the thickness of the layer of PDMS as well so that the projected light was as close to the channels as possible. But, the needles that attached the tubes to the device would not stay connected to the channels and as a result, it was very difficult to flow liquid through them. Nevertheless, the resolution of the images can still be improved. In the next step of this experiment, the glass slide will be replaced with either quartz or TPX RT 18, both of which have a higher transmittance than PDMS. Doing so could yield higher resolution images and a shorter reaction period.

Another solution that was proposed to produce better images was to increase the concentration of zirconia in the ink. It was noted that each subsequent time the ink from the same batch was used, the reaction would take longer to complete. We hypothesized that by increasing the concentration of zirconia, there would be more ligands to connect and create a stable network, which would create a more defined image. In the formulation of this new ink, we noticed that the same amount of solvent that was used previously was not sufficient enough to completely dissolve the increased amount of zirconia crystals. Rather than increase the amount of solvent and lower the concentration of the overall ink, the solvent was changed to toluene. Toluene was better able to dissolve all the zirconia crystals and did not lower the concentration of the ink. As a result, we were able to use the same sample of ink multiple times and get consistent results.



Figure 7a: Image with initial zirconia concentration.

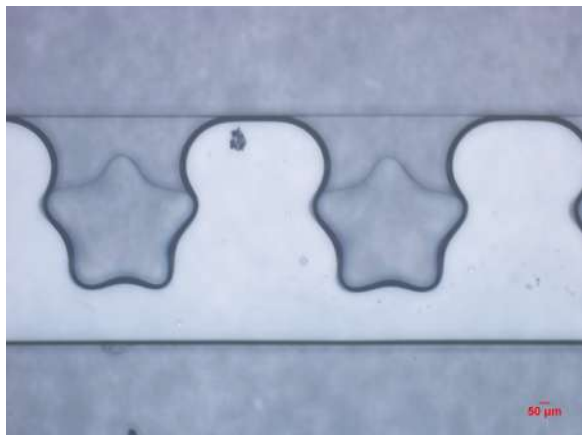


Figure 7b: Image after doubling the concentration of zirconia

Now that a printing method and ink formula had been finalized, the next step was figuring out which pattern of images would be best for the protein separation process. We knew from our test with the commercial resin that images with minimal edges printed the best. As a result, we decided to create an array of circles. Since the zirconia ink has a high surface area, we wanted to have as many circles in the array as possible so that more proteins could be separated in one experiment. Each circle was 1 millimeter in diameter and the columns of circles were

separated by 2.75 millimeters. We discovered earlier that small images took a long time to react or did not react at all. To solve this, we placed a larger image next to the array of circles that would initiate the reaction. This image still had room on all sides for the liquid to pass through so that the separation process could occur

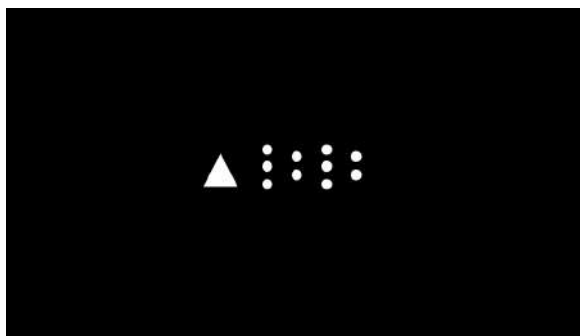


Figure 8: Proposed array design that is to be used in protein separation

The circles printed almost true to size with an expected size of 250 nanometers and an actual size of 220 nanometers.

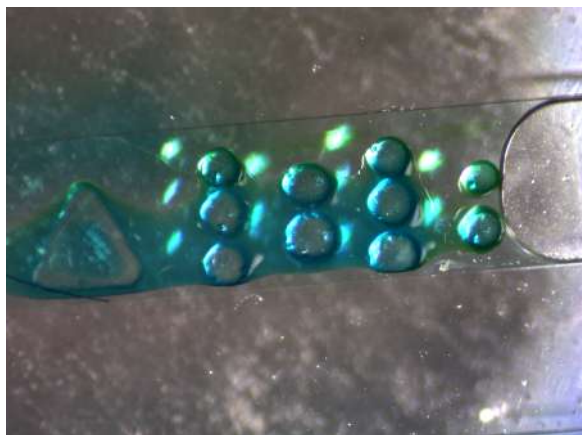


Figure 9: The actual array that was printed in the microfluidic channel. The blue methanol dye proves that liquid is able to get in between the crevices of the array and into the pores of the actual material.

## Conclusions:

In summary, the most efficient printing method that we discovered involved using the top down printing approach and doubling the zirconia concentration in the ink. Furthermore, if small images were to be printed in the channel, a larger image should be placed inside the same channel to initiate the reaction. This method that we developed is the next step in small scale protein separation. The ability to pattern any device with a highly porous monolith means that the method can be implemented in various applications.

The next step in this project is to test the array in actually separating proteins. After the array is finished printing and rinsed with toluene, a solution will be flowed through to create active separation sites in the pores of the monolith. Following this, a protein solution will be inserted into the channel to be separated.

## Acknowledgements:

This work was supported in part by the Cornell Center for Materials Research with funding from the Research Experience for Undergraduates program. I would also like to thank the Hanrath Lab for hosting me and Jen-Yu Huang for being my mentor this summer.

## References:

- [1] Sarkar, A., Hou, H. W., Mahan, A. E., Han, J., & Alter, G. (2016). Multiplexed Affinity-Based Separation of Proteins and Cells Using Inertial Microfluidics. *Scientific Reports*, 6(1). doi:10.1038/srep23589
- [2] Rodríguez-Ruiz, I., Babenko, V., Martínez-Rodríguez, S., & Gavira, J. A. (2018). Protein separation under a

microfluidic regime. *The Analyst*, 143(3),  
606-619. doi:10.1039/c7an01568b

# Magnetic Handshake Materials

Richard Liebert<sup>1,2</sup>, Edward Esposito<sup>2,3</sup>, Ran Niu<sup>2,3</sup>, Sloane Amato<sup>2</sup>, and Itai Cohen<sup>2,3</sup>

<sup>1</sup>Northeastern University, Boston, Massachusetts

<sup>2</sup>Cornell Center for Materials Research, Cornell University, Ithaca, New York

<sup>3</sup>Laboratory of Atomic and Solid State Physics, Cornell University, Ithaca, New York

Self-assembly is a useful technique for constructing complex objects at the nano- and microscale. We aim to develop magnetic materials capable of self-assembling, with the ultimate goal of creating microscale building blocks that allow easy programming and manipulation of the self-assembly process. Using magnets as the driving components in our system is ideal due to the long-range nature of magnetic forces, as well as the relative ease with which they can be designed and their ability to function well on both the macroscale and microscale. While past work on microscale magnetic self-assembly has focused on components featuring simple dipole-dipole interactions, we intend to explore the interactions of complex magnetic patterns (“handshakes”) at the microscale.

## I. INTRODUCTION

Self-assembly is the process by which particles will spontaneously arrange themselves into ordered structures with little external direction. Self-assembly is widely employed in nature, especially in biological processes such as protein synthesis. With the ever-growing push for smaller and smaller technologies straining current small-scale manufacturing techniques, self-assembly processes have received interest and study as a possible nanoscale manufacturing technique with broad potential applications. Due to their ability to function well at both the macroscale and nanoscale, magnetic forces are especially promising as potential drivers of self-assembly. In this paper, we study a macroscale system that is analogous to systems we hope to study at the microscale. Physical vibrations caused by a shaker in this work are analogous to thermally exciting a system at the nano- or microscale. Past work, such as that by Stambaugh et al. [1,2] has shown that by mechanically “thermalizing” systems of magnetic particles, reversible self-assembly into ordered structures can be observed as well as self-segregation behaviors between particles featuring attractive forces of different magnitudes. However, this and other past work (such as that by Ilievski and Whitesides et al. [3], Pál et al. [4], and Hageman et al. [5]) has focused only upon simple dipole-dipole magnetic interactions. We seek to explore particle systems featuring complex magnetic patterns which allow for many types of interactions. We hope that this allows us to not only recreate those reversible self-assembly and self-segregation behaviors previously shown but to allow for myriad complex ways to program, manipulate, and control the self-assembly process itself. Ultimately, we intend for this macroscale study to lay the groundwork for more novel research to be done at the nano- and microscale using nanofabrication and lithography techniques at the Cornell NanoScale Science and Technology Facility (CNF).

## II. MATERIALS AND METHODS

### A. Particles

Our objective was to design self-assembling building blocks with complex patterns of magnets that allow for different types of interactions. We used cylindrical, rare earth (Neodymium) magnets 1/16” in diameter and 1/8” in height, dropped into four holes forming a square in a laser-cut cylinders of acrylic 9mm in diameter and 1/8” tall. Since these “particles” each featured a 4x4 array of magnets, there are four unique patterns possible (everything else can flip or rotate to one of these) which we have arbitrarily color-coded white, green, blue, and red as shown in Fig. 1.

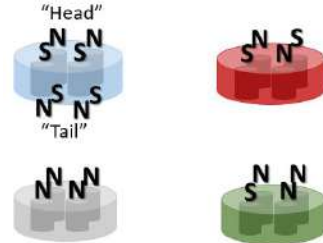


FIG. 1. The four types of particles, color coded.

Particles are attracted to those of the same type most strongly in a “head-to-tail” orientation in which the circular surfaces of two cylinders line up face to face with one another, however same-type bonds vary in strength for each particle type. For example, the strongest bond is that between two white particles, the next strongest is between two green, followed by blue, and the weakest bonds are between red particles. Magnets are held in place in their acrylic disks using super glue, and each complete disk was spray painted according to our color coding scheme. With the particles in this configuration, the formation of the weaker “incorrect” bonds, in which two pieces of different types bond together or pieces of the same type bond in a non head-to-tail orientation was

possible due to the raw strength of the interactions between the magnets when their bare surfaces are exposed. To decrease the strength of the magnetic interactions so that incorrect bonding configurations could reliably be broken in our apparatus, we glued a single 1/16" tall cylinder of acrylic with the same diameter as our disks onto the top and bottom of each disk, covering the exposed area of the magnets. After extensive prototyping, it was determined that these 1/16" "spacers" were the optimal size to allow the correct same type head-to-tail bonding to initiate a self-assembly process without enabling incorrect bonds that were too strong to be easily broken in our apparatus.

## B. Apparatus

After fabricating our self-assembling pieces, we began our experimentation by putting a homogeneous mixture of the blue pieces into a transparent, acrylic box 4" in height and 6" by 6" in length and width. This box was then screwed on top of a Brüel & Kjaer Vibration Exciter type 4809 (shaker) (soon to be replaced with the more powerful type 4808), with a Teflon cylinder acting as a spacer between the box and the shaker. This shaker vibrated with varying amplitude and frequency. We fed the shaker energy via a Brüel & Kjaer Power Amplifier type 2718 (soon to be replaced by the more powerful type 2719) where wattage and thus vibration amplitude could be controlled. The amplifier in turn received input from a BK Precision 3011B Sine Function Generator on which we could control signal frequency. The shaker was clamped down onto a table to prevent movement. A Logitech webcam placed on a tripod pointing down towards the apparatus was used to capture video and images at specific intervals for some experiments. This complete apparatus is shown in Fig. 2.

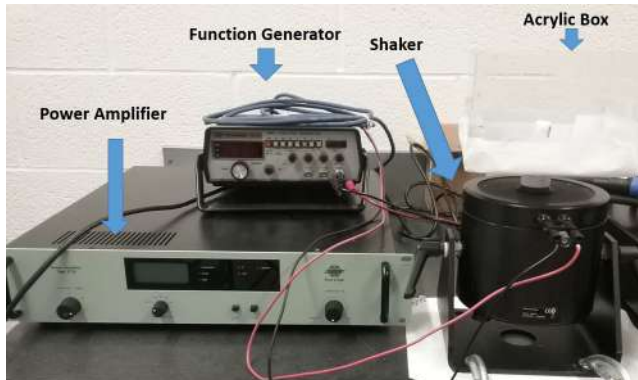


FIG. 2. Our apparatus.

## C. Experimentation

Upon providing power to the shaker and changing the amplitude and frequency of the vibrations, the particles were observed to bond together as predicted, self-assembling into long chains consisting of many blue particles bonded head to tail into a single long cylinder, analogous to a polymer. At some especially low amplitudes, these self-assembled chains would interact with one another by sticking together side by side, since there exists a mild attractive force between particles horizontally in certain orientations. The size of these chains of particles varied but at low amplitude settings they would reach as large as about 20 particles, a large enough chain to stretch across an entire dimension of the box side to side, while they were sometimes as small as two particle "dimers", and most chain sizes fell somewhere in between. A comprehensive study of the distribution of chain sizes has not yet been conducted. As amplitude rose and the particles bounced up and down, these chains eventually began to break up as particles at either end of a chain saw their bonds broken due to collisions of increasing intensity with the bottom surface and walls of the box. In addition, chains of pieces would sometimes split at some point midway across due to a collision, which resulted in either two smaller chains then moving independently or in the shattering of the entire length of the chain into independent particles with no bonds, "monomers". Upon further exploration of this change in behavior, we learned that at low amplitudes virtually all of the particles would ultimately end up in a chain bonded with at least one neighbor while at high amplitudes virtually every particle would become and remain independent and bonds would not be sustainable. We determined that it would be beneficial to study this change in behavior as analogous to a phase transition; hereafter, states where the dominant behavior of particles is forming and maintaining bonds will be referred to as "solid", while states where the dominant behavior is to break bonds and fly around independently will be referred to as "gaseous". Examples of snapshots taken of a system of red particles in the gaseous and solid states are shown in Fig. 3. The transition to a gaseous state was observed

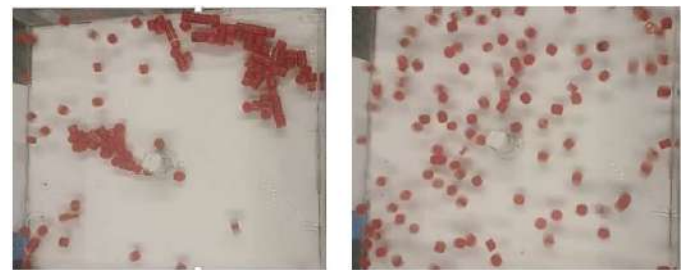


FIG. 3. Snapshots of a system of red particles in the solid phase (left) and the gaseous phase (right).

to happen most easily at frequencies between about 20

and 40 Hz. At frequencies lower than this, our particles would stay flush with the bottom of the box regardless of amplitude, while at frequencies above this range the particles would not experience powerful enough collisions to break bonds. This is likely because they did not have time to respond to the extremely fast oscillations and did not bounce very high as a result. For the purposes of these experiments we decided to set frequency at 30 Hz moving forward, since we were interested in investigating changes in this self-assembly behavior in relation to the acceleration experienced by the particles and considered frequency to be a minor detail of our setup.

### III. RESULTS AND DISCUSSION

Once we had determined through qualitative observation that a phase transition exists, the next logical step was to quantitatively define those phases. To do this, we ran experiments in which a system of particles began at a high amplitude, gaseous phase and then were “cooled” to a lower amplitude solid phase very quickly, while recording snapshots at 8 Hz using the webcam. The webcam pictures were analyzed by manually counting the number of particles that experienced any bonding with neighbors (were part of chains) or did not at all (were monomers) in specific frames. We plotted the fraction of pieces that were monomers labeled as the gaseous fraction and the remaining portion of pieces as the solid fraction as a function of time. When the final amplitude setting is low enough, the system will reach an equilibrium with greater than 90% of the particles in the solid state, with most of the transition activity occurring in the first five seconds, as shown in Fig. 4. On the other

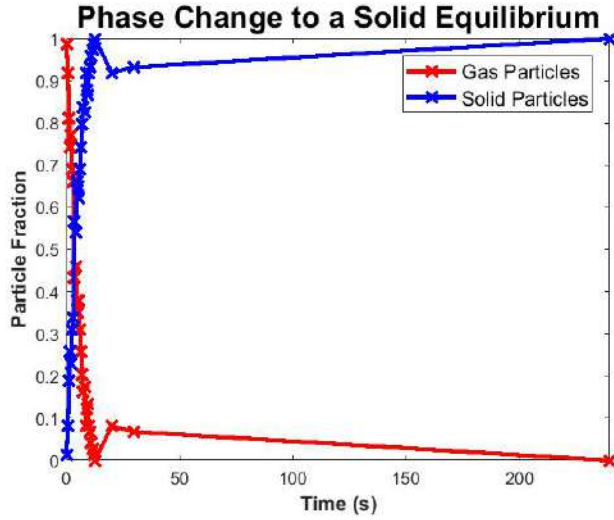


FIG. 4. Reaching an equilibrium in the solid state.

hand, when the system is cooled to an amplitude that is very close to the gaseous region, it will reach an equilibrium where there are significant numbers of particles in

both the gaseous and solid state, as shown in Fig. 5. This

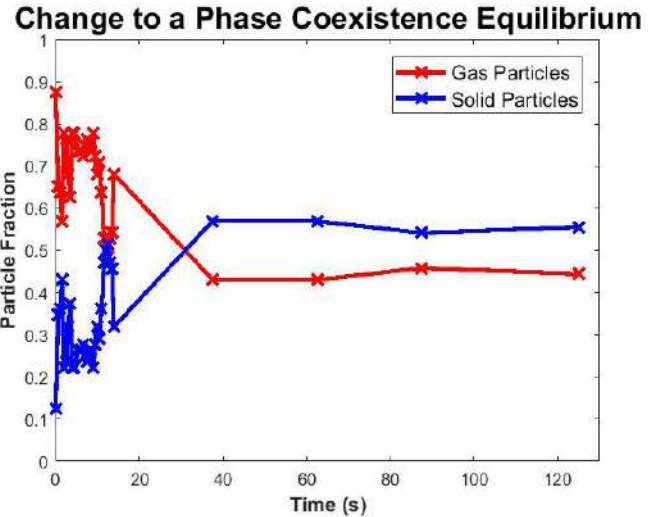


FIG. 5. Reaching an equilibrium where solid and gaseous phases coexist.

demonstrates that the threshold between the two states is not clear-cut, and there exists some phase transition region in which gaseous and solid behavior coexisted in equilibrium. Based on our data, we determined that the system was definitely in the solid phase if at least 90% of the particles had at least one bond and was gaseous if at least 90% had no bonds, while describing everything in between as a transition state. The significant size of the coexistence region presents a number of interesting possibilities for better controlling self-assembly processes by allowing us to cause such a reaction to only partially complete. Subsequently, we changed various parameters in an attempt to manipulate this phase transition, starting by increasing the number of particles in the box thus increasing the area fraction of our system. By doing this, it appeared that a higher amplitude was required in order to initiate the phase transition. Seeking to better understand this relationship, we ran various tests and constructed a “phase diagram” of the system of blue particles in Fig. 6. The lower line in this graph represents the beginning of the coexistence region and the upper line represents the end of it. Above the coexistence region is the gaseous phase, and below it lies the solid phase. The y-axis is in units of  $gs$  ( $9.81 \text{ m/s}^2$ ) of maximum acceleration experienced by the box, which is proportional to amplitude, while the x-axis is in units of particles in the box (essentially area fraction of the system). Values of  $g$  are logical to compare since accelerations below a single  $g$  should theoretically be counteracted by gravity and fail to result in any motion of the particles. Currently, values of  $g$  are approximate relying on a relationship between wattage provided to the speaker and resultant amplitude that was studied manually using a ruler. In the future, we hope to use an accelerometer that we do not yet possess to accurately measure maximum acceleration

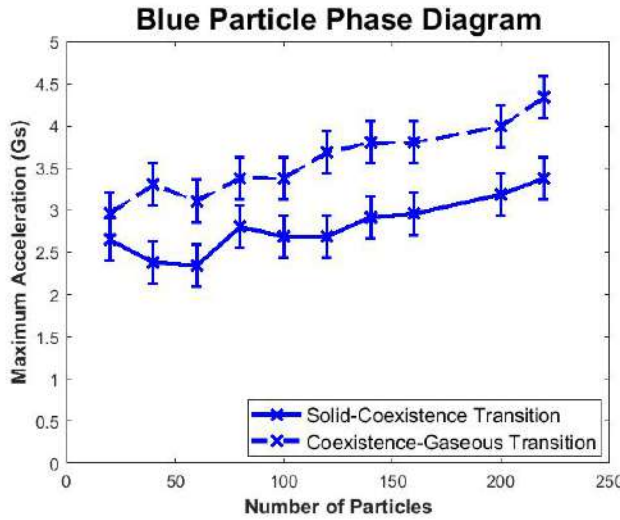


FIG. 6. “Phase Diagram” of blue particles.

in each experiment. The approximately linear relationship shown should be investigated further in the future at higher orders of magnitude with respect to number of particles (area fraction), since this relationship could have powerful implications when fabricating thousands or millions of these on the nano- and microscale. Since up until now we have only used the blue particles, we next tried these same experiments with the red particles (green and white particles could not be broken up by our current apparatus), resulting in the graph shown in Fig. 7 (points represent the approximate middle point of the phase coexistence region, calculated using the mean of the bottom and top of points of said region).

This graph shows that each type of particle has a unique phase transition line related to the strength of the bonds it forms. Up to this point, our experiments had

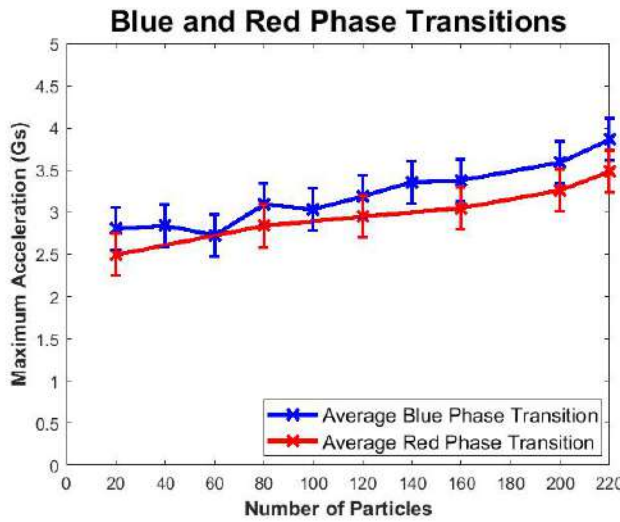


FIG. 7. Phase Diagram of blue and red pieces).

exclusively investigated homogeneous mixtures where all of the particles were of the same type. Our naïve expectation was that particles of different types will interact with each other minimally when put together and display independent phase transitions. To test this, we mixed red and blue particles at a fixed particle number and mapped the phase transition of each particle type with different ratios of each in the mixture, as shown in Fig. 8. Once again, the data points represent the

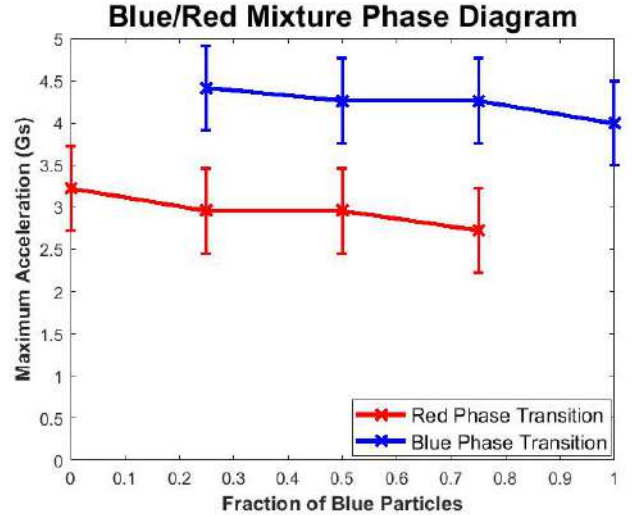


FIG. 8. Phase Diagram of a heterogeneous red/blue mixture with variable composition and constant area fraction.

approximate midpoint of the coexistence region. Our results here suggest that the phase transition of particles in heterogeneous mixtures is virtually the same as it is when particle types are alone, suggesting that they do not interact with particles of a different type much and that whatever interactions exist across types are insufficiently strong to affect same type interactions. In addition, our naïve expectation regarding independent phase transitions was actually proven correct, as at settings between the two phase transition curves all the blue particles would settle into a solid state while red particles remained gaseous. This constitutes both a self-segregation behavior and an avenue through which we may be able to control the order of a self-assembly process. Another way in which we tried to manipulate the phase transition was by applying a magnetic field to the box. Since our particles are magnetic, it intuitively makes sense to investigate the effects of magnetically perturbing them. Upon waving a magnet outside the box with my hand while the speaker was active, we observed that particles in the region being affected by the magnetic field were able to form bonds even at amplitude settings that would typically induce the gaseous phase. We believe that this is because particles will all be arranged in the same orientation by the magnetic field, which means that bonds are more likely to form since particles are biased towards an orientation in which collisions are more likely to result in

new bonds. We have not yet been able to take thorough data on how this changes the phase transition since we have not yet constructed an apparatus capable of applying a uniform magnetic field to the entire box. Another layer of complexity can be added to the system with the introduction of “Janus particles”, which have different magnetic patterns on each side (Fig. 9), resulting in different strength bonds being formed on each side of the particle. This results in a number of interesting prop-

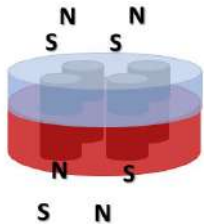


FIG. 9. A red/blue “Janus particle”.

erties that can be observed qualitatively. For instance, since they have a different bond strength on each side, the phase transition happens at a different point for each side. This means that at some higher amplitude setting Janus particles might begin sticking together in twos as the stronger bonding site becomes active, while at a much lower amplitude those dimers begin to actually bond together and create longer chains as the weaker bonding site becomes active. Thorough data on this has not been taken either yet, due mostly to how time consuming and difficult the creation of Janus particles is. It is worth noting that when constructing a Janus particle, the specific orientation of each magnet is more relevant than when creating standard particles since one pole of each magnet is embedded within the disk, where the interactions it can experience with external particles are minimal. In addition, while the Janus particles in Fig. 9 show the two magnetic patterns directly on top of each other, it is possible to rotate either one of these patterns any number of degrees relative to the other before applying glue, introducing even more possible configurations for these particles. This effectively means that for each combination of two particle types, there exist many possible distinct Janus particle configurations each with slightly different bonding strengths and properties. Determining which orientations are ideal to mass produce for our work remains an ongoing process.

#### IV. FUTURE DIRECTIONS

This project is still in early exploratory stages, and as such there is a wealth of work that should be done in

the future. Firstly, exploring pieces with new geometries and different arrays of magnets should be investigated in a few different ways. By introducing larger arrays of magnets, it is possible that we can create more and more distinct bond strengths, which in turn could lead to an entire spectrum of phase transitions that allow precise control of the order of bonding in a self-assembly process. In addition, introducing magnets both in and out of the plane perpendicular to each other could allow for more complex three dimensional shapes, or potentially for the encoding of information in one plane while bonds in another plane form a backbone analogous to a DNA structure. Prototyping of particles like these is already underway and early results seem promising. Secondly, expanding upon our work with Janus particles to see if we can actually create a “controlled polymerization” reaction whereby chain size can be controlled accurately by changing the applied power may be an important direction for further work. Exploratory work in this area has led us to believe that with many more Janus particles this may be possible, and it could represent yet another promising way to influence the self-assembly process. Thirdly, we do intend to eventually bring all of this work into the nanoscale at the CNF with the help of collaborators in the McEuen group, which is where we hope true breakthroughs in nanotechnology will emerge.

#### V. CONCLUSION

We have shown that magnetic self-assembly systems featuring complex arrays of magnets at bonding sites successfully presents many new ways to manipulate and control the self-assembly process at the macroscale. In the future, we hope to further explore the unique behaviors and possibilities these systems enable and to replicate this work on the micro- and nanoscale.

#### VI. ACKNOWLEDGEMENTS

Thank you to the entire Cohen group, especially to Professor Itai Cohen for welcoming me into their laboratory. Special thanks to Edward (Ted) Esposito for his superb mentorship and guidance, as well as to Ran Niu and Sloane Amato for all of their help this summer. This work was supported by funding from the NSF MRSEC program (DMR-1719875) and the REU Site program (DMR-1063059).

[1] J. Stambaugh, Z. Smith, E. Ott, and W. Losert, Phys. Rev. E 70, 031304 (2004).

[2] J. Stambaugh, K. V. Workum, J. F. Douglas, and W. Losert, Phys. Rev. E 72, 031301 (2005).

- [3] F. Ilievski, M. Mani, G. M. Whitesides, and M. P. Brenner, Phys. Rev. E 83, 017301 (2011).
- [4] G. Pál, F. Kun, I. Varga, D. Sohler, and G. Sun, Phys. Rev. E 83, 061504 (2011).
- [5] T. A. G. Hageman, P. A. Löthman, M. Dirnberger, M. C. Elwenspoek, A. Manz, and L. Abelmann, J. Appl. Phys. 123, 024901 (2018).

# Synthesis of TEMPO- and TIPNO-based Alkoxyamines to be Used as Initiators for Controlled PMMA Polymerizations

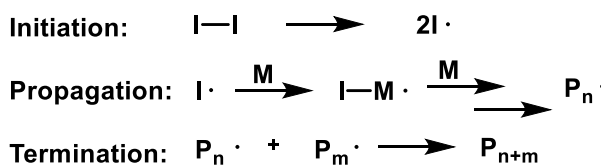
Erin E. Meyers, Renee J. Sifri, Scott W. Spring, and Brett P. Fors

**ABSTRACT:** Scientists are currently investigating ways to polymerize methyl acrylate (MA) and methyl methacrylate (MMA) using an external stimulus to gain control of polymer molecular weight and dispersity, thereby enhancing polymeric properties. Previous work on chemically initiated Nitroxide-Mediated Polymerizations (NMP) and Atom Transfer Radical Polymerizations (ATRP) have allowed PMMA and PMA to be synthesized in a controlled manner. However, finding new methods that entail the use of an external stimulus to initiate polymerization is of great interest and high regard, as it creates potential for starting and stopping a polymerization at any given time by simply adding or removing the external stimulus. In this project, we have developed ways to synthesize various ester-derived alkoxyamines that could be used as initiators for a photocontrolled radical polymerization. These alkoxyamines were successfully synthesized, but polymerization studies need to be pursued in further detail before this mechanism can be supported.

## Introduction

Poly(Methyl Methacrylate), or PMMA, is a polymer that is found in every-day materials, commonly in the form of Plexiglas®, and can be used in a variety of structures and technologies surrounding us. PMMA is transparent and durable, making it useful for a myriad of applications such as aquarium “glass”, airplane windows, and structural layers of electronics. With a relatively high glass transition temperature range ( $T_g$ ) of 100 °C to 130 °C, PMMA is utilized for its glassy state properties such as high resistance to heat and physical stress in standard human environments.<sup>1</sup>

Free radical polymerizations are a common method of PMMA synthesis in industry due to its one batch setup.<sup>2</sup> This reaction consists of three steps: 1) initiation, 2) propagation, and 3) termination (*Scheme 1*).



*Scheme 1. General Free Radical Polymerization Mechanism*

One key issue that accompanies large-scale radical polymerization is the potential for runaway reactions. The termination step is the portion of the reaction that is typically uncontrolled in these exothermic, free radical polymerizations and can create problems when a polymerization is not properly temperature-regulated. If excess heat is applied to the reaction system, more radicals will form, increasing the rate of the reaction, and releasing more heat. This can lead to explosions in an industrial setting, creating hazards for workers and equipment in a plant. Additionally, these reactions produce a broad range of molecular weight chains as a result of an uncontrollable termination step, affecting the overall properties of the final material. This can potentially reduce the quality of the product for certain applications.

New methods are currently being researched in order to control radical polymerizations, allowing for the ability to stop and start polymer growth through the use of external stimuli. This can include factors such as light and electric current. A few examples of these controlled polymerization methods include Atom-Transfer Radical Polymerization (ATRP), Reversible-Addition Fragmentation Chain Transfer Polymerization (RAFT), and Nitroxide-Mediated Radical Polymerization (NMP). Primary research is being directed toward utilizing these particular mechanisms with external stimuli.

We are working to build upon these precedented mechanisms for polymerization control by modifying a photocontrolled ATRP of methyl acrylate (MA) and methyl methacrylate (MMA) via the use of a reducing photocatalyst developed by Fors and Hawker (*Figure 1*).<sup>3</sup> Unlike Hawker's use of a reducing photocatalyst, we aim to formulate a reaction that will undergo an oxidative pathway to initiate polymerization. By using an ester-derived alkoxyamine initiator, we hope to produce an alkyl radical initiator through homolytic cleavage for the synthesis of controlled PMA and PMMA (*Figure 3*).

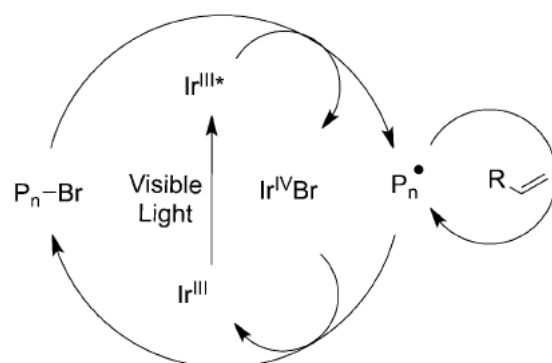


*Figure 1. Previously Developed Controlled Living Polymerization of PMMA by Fors and Hawker*

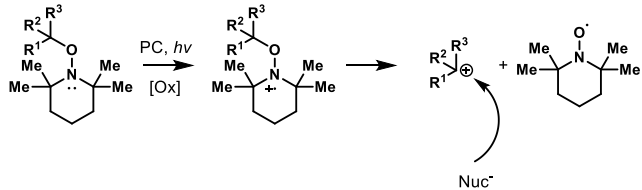


**Figure 2.** Previous work developed by Rob Knowles, which uses an oxidizing photocatalyst to initiate mesolytic cleavage of alkoxyamine to form an alkyl cation which can be subjected to nucleophilic attack.<sup>4</sup>

Inspired by the work of Rob Knowles (Figure 2), we envision that, with the appropriate oxidizing photocatalyst, the alkoxyamine can be oxidized and then homolytically cleave to form an ester radical and oxidized TEMPO cation (Figure 3). This ester radical can then proceed as an initiator for the radical polymerization of MA and MMA. An ester-derived alkoxyamine should force homolytic cleavage to form the radical on the alpha carbon due to resonance stability.

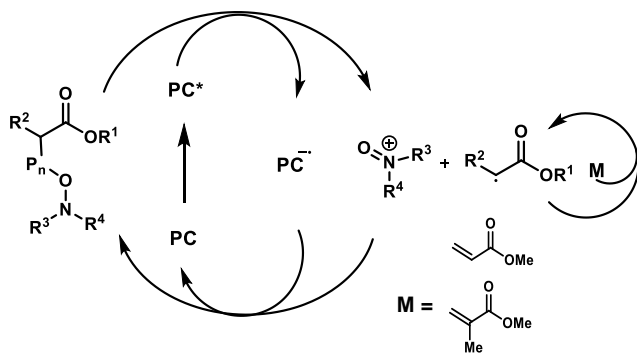


**Figure 3.** Proposed Mechanism for Controlled PMA & PMMA Polymerizations

The first step to creating this modified, controlled mechanism is to synthesize an initiator compatible with this PMMA polymerization. We want to use two nitroxyl radicals, 2,2,6,6-Tetramethylpiperidine 1-oxyl (TEMPO), and 2,2,5-Trimethyl-4-phenyl-3-azahexane-3-nitroxide (TIPNO), which are commonly used in universal initiators for other polymerizations. These nitroxyl radicals are stable and persistent as a result of their sterically-protective groups, so they will be the optimal nitroxyl radicals to screen first for finding the best reaction conditions.<sup>5</sup> The following reactions were performed for screening.

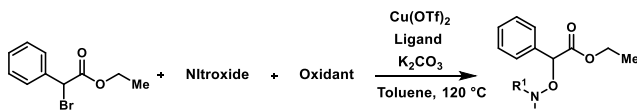


**Figure 4.** Reaction Scheme with Cu Catalyst

Nitroxide	Oxidant	Ligand	Yield (%)
TEMPO	Aniline	PMDTA	40
TEMPO	Aniline	Bpy	<5
TEMPO	Et <sub>3</sub> N	PMDTA	61
TEMPO	Cu (0)	PMDTA	54
TIPNO	Et <sub>3</sub> N	PMDTA	<5

**Table 1.** Screening different variables with Cu Catalyst

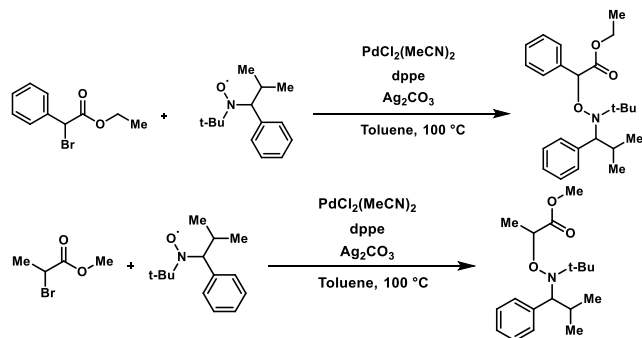


**Figure 5.** Reaction Schemes with Pd Catalyst

## Procedure

### Synthesis of TEMPO- and TIPNO-based Initiators using Cu Catalyst

All alkoxyamine synthesis reactions were prepared in a flame-dried Schlenk bomb with a stir bar. The bomb was flushed with nitrogen gas and solid material (TEMPO = 2 equiv, K<sub>2</sub>CO<sub>3</sub> = 2 equiv, and Cu(OTf)<sub>2</sub> = 0.04 equiv) was added under positive pressure of nitrogen gas. The liquid material was added through a septum via needle syringe ( $\alpha$ -bromo-ester = 1 equiv, Sacrificial oxidant = 1 equiv, PMDTA = 0.04 equiv, TIPNO = 1.2 equiv). Dry toluene was obtained through an alumina column solvent system under an argon atmosphere. The Schlenk bomb was recapped with a stopper and the contents were degassed by the freeze-pump-thaw method three times. The reaction was placed in a 120 °C oil bath and left to react overnight (~20 hours). A liquid-liquid extraction was performed using diethyl ether three times. The organic layer was washed with brine and dried with sodium sulfate. The solvent was then evaporated off using a rotary evaporator. Purification methods varied for each reaction setup, but a column was required to remove excess TEMPO from the reaction material. Typically, a column in silica gel was run with 20% diethyl ether and 80% hexanes solvent system. The product was characterized using proton nuclear magnetic resonance (<sup>1</sup>H-NMR) with deuterated chloroform and Direct Analysis in Real Time Mass Spectrometry (DART-MS).

## Synthesis of TIPNO-based Initiators using Pd Catalyst

Solid material ( $\text{PdCl}_2(\text{MeCN})_2 = 0.05$  equiv, dppe = 0.1 equiv,  $\text{Ag}_2\text{CO}_3 = 1$  equiv) was added into a flame-dried Schlenk bomb containing a stir bar within the Unilab MBraun nitrogen atmosphere glovebox. The flask was sealed off with a stopper and pumped out of the glovebox. The flask was connected to the Schlenk line and the outside joint was purged and backfilled three times. A septum replaced the stopper under positive nitrogen gas pressure and the remaining reaction components were added (TEMPO = 2 equiv, TIPNO = 1.2 equiv,  $\alpha$ -bromo-ester = 1 equiv, toluene = 4 mL). Reaction flask was degassed by freeze-pump-thaw method three times. The flask was flushed with an atmosphere of  $\text{N}_2$  and was placed in a 100 °C oil bath. The same workup procedure as the Cu catalyst reactions was followed for the Pd catalyst reactions, except ethyl acetate was used to perform extractions. The product was characterized using  $^1\text{H-NMR}$  with deuterated chloroform and DART-MS.

### Polymerization Trials

Poly(methyl acrylate) polymerization trials were carried out in the glovebox. 1.11 mmol (0.1 mL, 100 equiv) of methyl acrylate and 0.022 mmol (2 equiv) was added into each reaction vial in 0.27 mL acetonitrile (4.11 M). The following oxidizing agents were added to each of the vials (4 equiv): Tris(4-bromophenyl) ammonium hexachloroantimonate (TBPA), Hantzsch ester, ammonium cerium (IV) nitrate (CAN), 2,3-Dichloro-5,6-dicyano-p-benzoquinone (DDQ), Tris(1,10-phenanthroline) iron (II) hexafluorophosphate, and ferrocenium hexafluorophosphate. Each vial was left to react for 22 hours. Aliquots of each reaction were diluted in tetrahydrofuran and run through the gel permeation chromatography (GPC) instrument to check for polymer growth.

We initially wanted to screen for chemical oxidizing agents to see if we could form a polymer before we started adding in photocatalysts. No polymer was reported directly from the propionate initiator, but we discovered that CAN was able to polymerize methyl acrylate alone. Additional polymerizations can be run in the future using different oxidizing agents or different alkoxyamine derivatives. A different monomer, such as methyl methacrylate, could also be used as well.

### Results and Discussion

When synthesizing the different TEMPO- and TIPNO-based alkoxyamines, we focused on two different catalyst conditions. First, we worked with the copper triflate catalyst, trying different ester materials and sacrificial oxidants to increase yields. The reaction containing ethyl  $\alpha$ -bromophenylacetate and triethylamine had the best results with a yield of 61% and easy purification due to UV visibility via thin layer chromatography (TLC). This reaction did not produce a side product, unlike other Cu-catalyzed TEMPO reactions, which was determined to be a result of a reaction between toluene and TEMPO (Figure 6).<sup>6</sup>

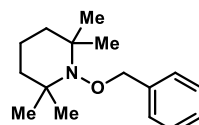


Figure 6. TEMPO and Toluene Reaction Side Product

The palladium catalyst conditions did not produce this particular side product. The propionate-TIPNO reaction produced the best results with this method, having a yield of 38%. This reaction was not successful with the ethyl  $\alpha$ -bromophenylacetate.

We were able to see promising results with this polymerization mechanism through cyclic voltammetry (CV) with the help of Cara Gannett from the Abruna Group at Cornell University. The oxidative-reduction potential of TEMPO-propionate was tested by CV in DCM using an Ag/Ag<sup>+</sup> electrode (Figure 7). From the first cycle (blue line), we can see that TEMPO-propionate is oxidizing near +1.7 V, which suggests formation of the oxoammonium ion and the radical that is essential for the proposed polymerization mechanism. This data gives us insight of the initiator's capability to be oxidized by an excited photocatalyst. We also noticed that it is a slightly reversible process as a reducing peak appeared near +1.4 V when the current was decreased, indicating that the alkoxyamine is not fully cleaving. The reducing peak near +0.8 V could be the further reduction of the oxoammonium ion to form TEMPO. The second cycle (orange line) shows the appearance of a small peak near +0.9 V, which could be an indication of the now cleaved TEMPO<sup>+</sup> molecule becoming oxidized to its radical form. This suggests a favorable mesolytic cleavage, showing promise for future polymerization attempts.

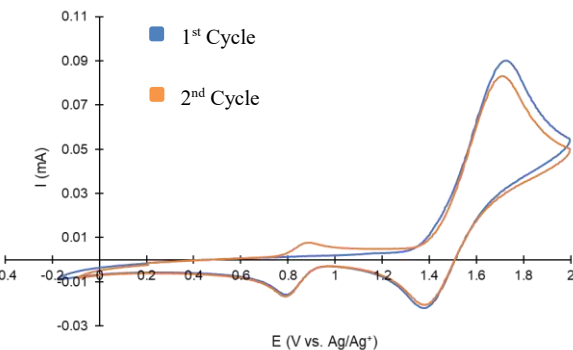
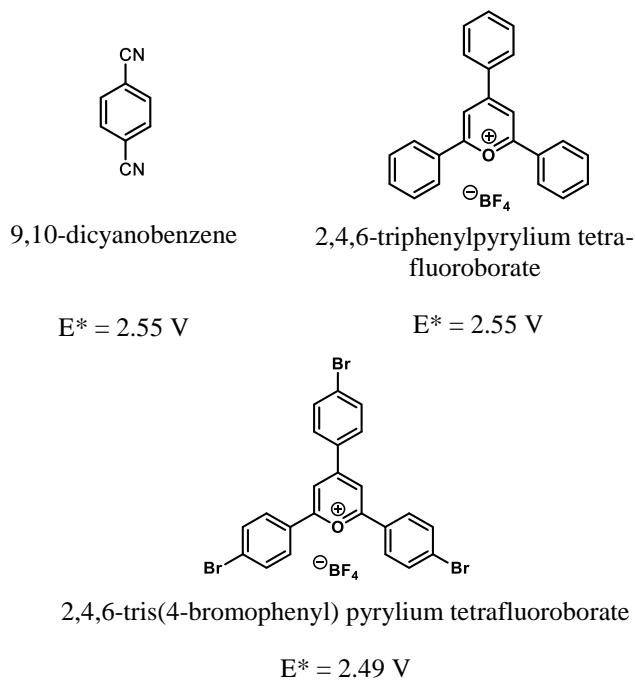


Figure 7. CV of TEMPO-propionate initiator

### Conclusion

We were able to successfully synthesize TEMPO-phenylacetate with the copper catalyst conditions and TIPNO-propionate with the palladium catalyst conditions, producing appreciable yields. Although we were not successful creating polymer with TEMPO-propionate as the initiator, further screenings need to be performed for suitable chemical oxidants and photocatalysts. We will need to find a compound that has noticeable oxidizing ability. Some potential oxidizing photocatalysts could be 9,10-

dicyanobenzene, 2,4,6-triphenylpyrylium tetrafluoroborate, and 2,4,6-tris(4-bromophenyl) pyrylium tetrafluoroborate (*Figure 8*).



**Figure 8.** Potential Oxidizing Photocatalysts

Additional polymerizations need to be performed with different alkoxyamine initiators as well, including TEMPO-phenylacetate, TEMPO-isobutyrate, and the TIPNO derivatives. Other sterically-protected nitroxyl groups can be tested as well, such as 1,1,3,3-tetramethylisoindolin-2-ol (TMIO) and 1,1,3,3-tetramethylisoindolin-2-ol (PROXYL) due to their radical stability.<sup>7</sup> The next step in our project is to continue finding optimal conditions for polymer formation in order to have potential polymerization controllability.

## Acknowledgements

I would like to thank Professor Brett Fors for offering me the opportunity to work in his lab for the summer, as well as Renee Sifri for her stellar mentorship throughout the CCMR REU. Additional thanks to the Fors Group members for welcoming me in as a member of the lab. A special thanks to the CCMR REU program for making this experience possible.

## Funding

This work was supported by the NSF under the award number CHE-1752140. Additionally, this work made use of the NMR Facility at Cornell University and is supported, in part, by the NSF under the award number CHE-1531632.

## References

1. *Polymer Reviews* **2015**, 55:4, 678-705.
2. Winola L. Rasmussen. Novel Carbazole Based Methacrylates, Acrylates, and Dimethacrylates to Produce High Refractive Index Polymers. Ph.D. Dissertation, Virginia Polytechnic Institute and State University., Blacksburg, VA, 2001.
3. *Angew. Chem. Int. Ed.* **2012**, 51, 8850-8853
4. *Angew. Chem. Int. Ed.* **2016**, 55, 9969 –9973
5. Yun Ma. Nitroxides in Mechanistic Studies: Ageing of Gold Nanoparticles and Nitroxide Transformation in Acids. Ph.D. Dissertation, University of York, York, United Kingdom, 2010.
6. *J. Am. Chem. Soc.* **1999**, 121, 3939-3943
7. Daniel Keddie. The Synthesis of Novel Profluorescent Nitroxide Probes. Ph.D. Dissertation, Queensland University of Technology, Brisbane, Australia, 2008.

# Covalent Immobilization of Proteins on Electrospun Nanofibers for Biosensor and Biomedical Applications

Matthew Molinaro<sup>1</sup>, Mesbah Najafi<sup>2</sup>, Michael Delaney<sup>3</sup>, Margaret W. Frey<sup>2</sup>

1 Department of Biomedical Engineering, University of Florida, Gainesville, FL 32611, USA  
2 Department of Fiber Science and Apparel Design, Cornell University, Ithaca, NY 14853, USA  
3 Chemical and Biomolecular Engineering Department, Cornell University, Ithaca, NY 14853, USA

**Abstract:** In this work, plasma treatment was used to functionalize the surface of electrospun poly(lactic acid) (PLA) nanofibers for protein immobilization. To achieve this, the effect of various plasma treatment parameters such as voltage and time on the chemical structures of the nanofibers fabrics was studied. Methylene blue adsorption analysis was used to characterize the surface chemistry of the nanofibers. Protein binding to the nanofibers surface was examined by static and dynamic adsorption tests. BSA was used as a model protein for this study. The adsorption tests were also conducted on poly(vinyl alcohol)/poly(methyl vinyl ether-alt-maleic anhydride) (PVA/PMA) nanofibers for comparison. Oxygen plasma treatment effectively created carboxylic acid functional groups on the surface of the PLA fibers. The data also showed that a dynamic binding of protein to PLA via bioconjugation chemistry yielded the best results in terms of maximizing specific covalent binding and minimizing non specific adsorption. Static binding of protein led to high levels of nonspecific binding for both PLA nanofibers and PVA/PMA. Covalent binding of proteins on nanofibers can allow for high sensitivity biosensing thanks to high surface area and porosity of nanofiber fabrics. The results obtained widen the biomedical applications of PLA.

**Keywords:** nanofibers, poly(lactic acid) PLA, oxygen plasma treatment, proteins, biosensor , electrospinning

---

## 1. Introduction

Biosensor devices are critical to successful biochemical research and diagnostics [1]. Biomarkers (proteins, peptides, hormones, etc.) levels can change in relation to disease state and pharmaceutical intervention. Highly sensitive quantification is an essential part of research and accurate diagnoses [2]. Enzyme linked immunosorbent assay (ELISA) is a common method for quantifying biomolecules [2,3]. ELISA typically involves physical adsorbing an antigen or antibody to a flat plastic surface then the successive administration of antibodies, target biomolecules, and signal producing species. For example, a sandwich ELISA involves the immobilization of an antibody on a flat surface followed by the administration of antigen containing solution. This solution is then washed away and another antigen binding antibody known as the secondary antibody is administered. An antibody linked to a signal producing species (i.e. enzyme) is then bound to the secondary antibody. Finally, the substrate for the enzyme is added and the absorbance of the resulting solution can be taken and compared to standards to quantitatively estimate the concentration of a particular biomolecule [2]. One of the main issues with this ELISA method is the physical adsorption of an antigen or antibody to a flat surface. This can lead to loss of function, leaching of biomolecule from the surface, and inconsistent distribution [2,3]. One possible solution to this problem is through the use of nanofibers (NFs). NFs have large surface area, porous structure, and good mechanical properties [1-4]. Additionally, polymer NFs can under go a variety of

surface modifications including and not limited to plasma treatment, chemical modification, and polymer grafting [1-3, 5-9]. These properties make NFs good candidates for biomolecule immobilization.

Electrospinning of NFs has gained increasing popularity over the decades for its ease of processing and quality of fibers produced [5]. Electrospinning involves using a high voltage source connected to a syringe extruding a conductive polymer solution and a grounded collector plate. The high voltage draws out fibers between the syringe tip and the collector plate. Typically, NFs collect as a woven mat. The properties of the collected NF mat can be altered by changing the extrusion speed of the solution, voltage of the power source, distance between the syringe needle and the collector, and the concentration of polymer in the solution [10]. Figure 1 illustrates the basic set up for an electrospinning operation.

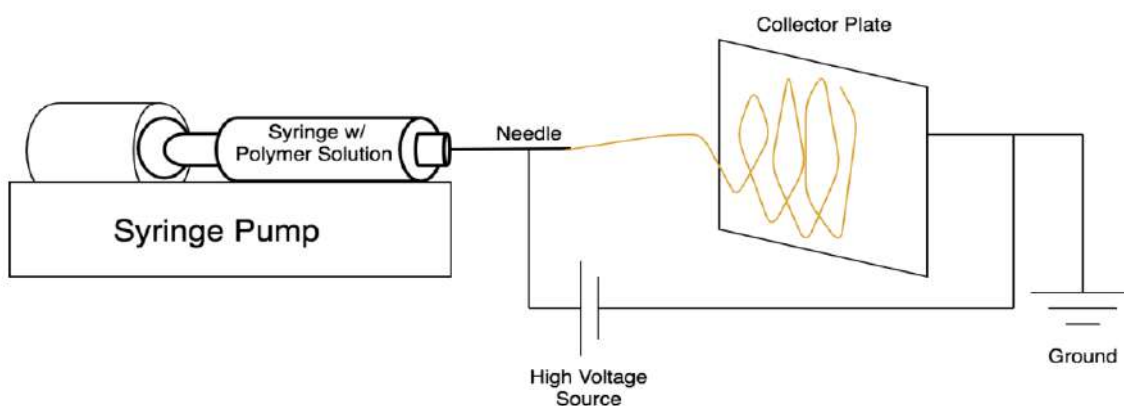


**Figure 1.** Scheme of electrospinning process

Electrospun NFs have been used in a variety of purposes including advanced ELISA, protein capture, microbe capture, and tissue engineering [2,4, 6-9,11]. Hosseinzadeh et al. [2] covalently attached antibodies to polyethersulfone NF meshes and was able to gain higher intensity ELISA signals when compared to traditional methods. The higher intensity signals lead to higher sensitivity assays. Najafi et al. [4] utilized charged electrospun NF meshes for the selective binding of proteins based on electrostatic properties. Matlock-Colangelo [11] covalently bound antibodies to NFs for the capture of *E. coli* cells. Schofer et al. [9] bound RGD peptides to biocompatible NFs for the growth and differentiation of stem cells.

PLA is a biodegradable and biocompatible natural polyester [14]. PLA can be fashioned into NFs via electrospinning [1,3,6-10,14,15]. PLA contains no free carboxyl groups in its intrinsic form. In order to introduce carboxyl groups on PLA NFs, oxygen plasma treatment can be performed to modify the surface of the NFs [6,7,9]. Previously hydrophobic PLA NFs become more hydrophilic after plasma treatment [6,7,9,15]. This chemical change is indicative of the addition of carboxyl groups. The PLA NFs activated by the plasma can now participate in the formation of the semi-stable amine reactive sulfo-NHS ester. PLA modified with surface protein can have application ranging from biosensing to tissue engineering [6,7,9,15]. Biosensing could simply be the isolation of amine presenting species as well as utilizing of interactions such as the well studied biotin-avidin interaction [15]. The avidin protein can be bound to the NF and then the NFs could be used to filter out or isolate biotinylated species. PLA's biocompatibility and biodegradability have made its NFs applicable for bone tissue engineering, stem cell engineering, and cartilage tissue engineering [6,7,9,16].

Another promising multi-functional polymer NF system is the PVA/PMA blend. Similar to PLA,

PVA/PMA blends can be electrospun into NF fabrics [4,11]. The PVA portion of this blend makes the fibers extremely hydrophilic [4]. The highly hydrophilic nature will allow water based solutions to easily travel through the porous NF structure giving dissolved molecules in the solution better opportunity to bind to the fibers or functional groups on the fibers [4,11,15]. Additionally, the PMA portion of the fibers contains anhydride groups that can be hydrolyzed to form carboxyl groups [4]. These carboxyl groups can be reacted with sulfo-NHS/EDC chemistry to allow the fibers to bind proteins covalently. PVA/PMA has been used to electrostatically sort proteins and covalently bind microbe antibodies for selective capture [4,11]. Ideally the PVA/PMA fibers, with their intrinsic hydrophilic nature, will be good candidates for enhanced biosensing applications as well as protein filtration and purification.

In this study, we examined the use of bioconjugation chemistry on NFs for the binding of proteins. Specifically, 2 polymer NF systems were investigated. The first being PLA and the second being a PVA/PMA blend. PVA/PMA presents carboxyl groups without plasma treatment and will be used to compare results of plasma treated PLA. Both polymer systems were modified with sulfo-NHS/EDC bioconjugation chemistry. Sulfo-NHS/EDC bioconjugation allows for the cross linking of amide presenting species with carboxyl presenting species [12]. Sulfo-NHS/EDC chemistry has been applied to the crosslinking of proteins to NFs, functionalization of nanoparticles, and creation of immunoassays [2, 9,13,12]. The bioconjugation works by binding EDC to a carboxyl group forming a reactive o-acylisourea ester. Sulfo-NHS can then be reacted with the ester to form a semi-stable amine reactive sulfo-NHS ester which can then react with amine groups, commonly present on proteins [12]. Figure 2, inspired by Vashist, diagrams the chemical reactions that take place during sulfo-NHS/EDC conjugation on NFs.

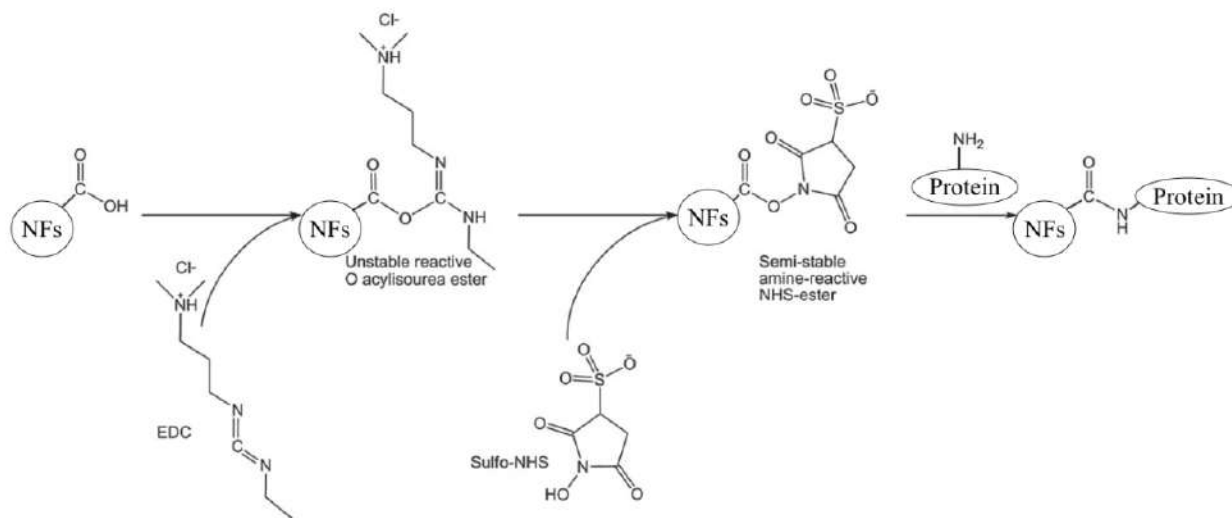


**Figure 2.** Sulfo-NHS and EDC conjugation reaction

## 2. Materials and Methods

### 2.1. Materials:

PLA 4043D (MW: 150 KD) was purchased from NatureWorks (Blair, NE, USA). Hydrolyzed PVA (MW: 78 KD) was purchased from Polysciences, Inc (Warrington, PA, USA). PMA (MW: 216 KD), Triton X-100 (p-tertiary-octyl polyethyl alchol), and Bovine Serum Albumin-fluorescein isothiocyanate conjugate were purchased from Sigma-Aldrich (St. Louise, MO, USA). 2-(N-morpholino)ethanesulfonic acid hemisodium salt (MES) was purchased from Sigma-Aldrich. Sulfo-NHS

and EDC were purchased from ThermoFisher Scientific (Rockford, IL, USA). Anhydrous Dimethylformamide (DMF) and phosphate buffered saline (PBS) salt were purchased from Sigma-Aldrich.

## 2.2 Formation of Electrospinning solutions

PLA was dissolved in DMF at 70 °C at 22 wt% PLA for at least an hour before spinning. PVA/PMA was prepared similar to methods from our previous work [4]. In summary, PVA was dissolved in deionized (DI) water and heat treated at 95 °C for 4 hours. PMA was also dissolved in DI-water and heat treated at 95 °C for 4 hours. The PVA/PMA solutions were mixed with mass ratio of PVA/PMA of 80/20 (w/w). Triton X-100 was added to the polymer solution to relieve surface tension. The mass ration of X-100/DI-water was 0.5/99.5 (w/w).

## 2.3 Electrospinning

PLA spinning dope was heated up to 70 °C. The solution was drawn into a 10 ml glass syringe. The spinning dope's temperature was maintained by a homemade ceramic heater that encapsulated the syringe. Additionally, a heat gun (Master Appliances Corp., Racine, WI, USA) heated the extrusion needle. A 21-gauge metal needle was used to extrude the polymer solution. A high voltage power source (Gamma High Voltage Research) supplied a 11 kV potential difference between the needle and a 3.5cm by 3.5cm copper collecting plate. The needle tip and plate were placed 10 cm apart. A programmable pump (Harvard Apparatus, Holliston, MA, USA) extruded polymer from the syringe at 10 uL/minute. Fibers were spun for 20 minutes. PVA/PMA dope was spun in a similar fashion. The dope was loaded into a plastic syringe and spun at room temperature. A 18 kV voltage was supplied, the distance from the needle tip to collector was 20 cm, and the solution feed rate was 0.5 ml/h. These NFs were spun for 3 hours.

## 2.4 Plasma Treatment

PE-100 Benchtop Plasma System (Plasma Etch, Carson City, NV, USA) was used for plasma treatment of PLA nanofibers. Oxygen plasma treatment was performed at 0.2 mbar pressure and 100, 200, and 300 watts for 3 minutes. The oxygen feed rate was 50 cc/minute.

## 2.5 Methylene Blue Dye Binding

A methylene blue dye binding assay was performed to estimate the carboxyl content of plasma treated PLA fabrics. Methylene blue dye has a single positive charge and should interact with carboxyl groups in a 1:1 molar fashion. For the experiment, a 20 mg/ml (ppm) methylene blue dye solution in DI-water is created. An equal volume of .1M borate buffer (pH = 8.4) is created and mixed with the dye solution (final concentration of 10 ppm). Each fabric piece ranging from 3 – 10 mg is placed in 10 ml of 10 ppm dye solution and incubated for 1 hour. After the incubation, supernatant from the fabric/dye solution was extracted and absorbance at 664 nm is taken to determine the amount of dye bound to the fabrics. This dye binding experiment was performed on untreated PLA, 100 watts, 200 watts, and 300 watt plasma treated PLA (3 minutes each). The results of the binding are normalized to mg of dye bound per gram of fabric.

## 2.6 Sulfo-NHS/EDC Chemistry

Plasma treated PLA NFs were incubated .1M Sulfo-NHS and .1M EDC in an MES buffer (pH = 5.4). The fabrics incubated for 90 minutes at room temperature before they were washed with a PBS solution. PVA/PMA fibers naturally produce carboxyl groups so sulfo-NHS/EDC chemistry can be done

on these fibers without any plasma modification.

## 2.7 Static BSA-FITC Binding

PLA fabrics that have been plasma activated (150 watts) and treated with sulfo-NHS/EDC chemistry were incubated in a .2 mg /ml BSA-FITC PBS (pH = 7.4) solution for 20 hours at ~8°C. Supernatant solution was obtained and absorbance at 494nm was measured using a PerkinElmer Lambda 35 UV/VIS spectrometer (Waltham, MA, USA) to determine the concentration of protein in the solution. Fabrics are then placed into filter holders and washed with pH 10 PBS at .2 ml/min for 50 minutes. Fabrics were then stored in the fridge at 4 °C until fluorescent images of the fibers could be obtained.

PVA/PMA fabrics had a different static adsorption. Fabrics were treated with sulfo-NHS/EDC chemistry and then incubated in .2 mg/ml BSA-FITC PBS (7.4) solution for 3 hours at room temperature (~21°C). Supernatant solution was obtained and absorbance at 494 nm was taken to determine the mass of protein bound to the fabrics. Fabrics were then placed in filter holders and washed with pH 10 PBS at .2 ml/min for 50 minutes. Fabrics were then stored in the fridge at 4°C until fluorescent images of the fibers could be obtained.

As inspired by Najafi et al. [4], Adsorption capacity ( $Q_p$ ) will be defined as mg of protein bound per gram of fabric. This can be determined by the following equation:

$$Q_p = V (0.2 - C_s) / m$$

Were V being the volume (ml) of the protein solution the fabrics incubated in,  $C_s$  is the protein concentration (mg/ml) of the supernatant after the incubation period, and m is the mass (g) of the dry fabric.

## 2.8 Dynamic BSA-FITC Binding

PLA fabrics were additionally submitted to dynamic binding procedure. Sulfo-NHS/EDC treated fabrics were placed in filter holders and then had BSA-FITC solution run through them to initiate the covalent binding. .2 mg/ml BSA-FITC PBS solution was run through the fabrics at .05 ml/min for 1 hour. Fabrics were then washed with pH 10 PBS solution at .05 ml/min for 1 hour. The fabrics were then stored in the fridge at 4°C until fluorescent images could be obtained.

## 2.9 Confocal Fluorescent Imaging

The binding of BSA-FITC to the fibers was examined using a Zeiss 710 Confocal microscope (Carl Zeiss, Stockholm, Sweden). Fluorescent images were captured by using an excitation wavelength of 488nm and emission spectra of 510-530nm to produce the images. Some images have been enhanced using the contrast function on ImageJ™ open source software (National Institutes of Health, Bethesda, MD, USA).

# 3. Results and Discussion

## 3.1 Effectiveness of Plasma

Figure 3 shows the methylene blue dye binding capacity of PLA and plasma treated PLA at various voltages. According to the data, plasma treated fabrics bind significantly more methylene blue dye than non plasma treated fabrics. Considering the methylene blue interaction is electrostatic, it can be assumed that it is a negatively charged carboxyl group that is interacting with the positively charged dye molecule. It can also be seen that as one increases the energy of the plasma the amount of dye binding increases. This implies that higher energy plasma can create more carboxyl groups on the surface of the

NFs. The data shows that 200 watt plasma treatment raises the dye adsorption by more than 2 mg/g over 150 watt and 100 watt treatments. It should also be noted, that fabrics treated at higher plasma energy became more brittle and prone to fracture. This change in mechanical properties is likely due to increased chain breaking from the plasma treatment. Lastly, the chemical change cause by oxygen plasma treatment can be subjectively seen in figure 4. This image shows a plasma treated fabric that appears to be solvated in an aqueous solution compared to an untreated fabric that has maintained its hydrophobic character and floats on top of the solution.

### Methlyene Blue Dye Binding

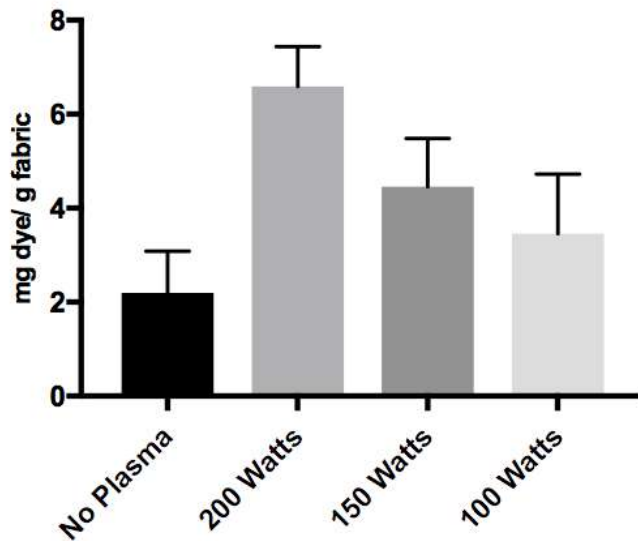


**Figure 3.** Carboxyl quantification of PLA NFs via methylene blue dye binding for various plasma treatment voltages for 3 minute treatment with 50 cc/min oxygen infusion.

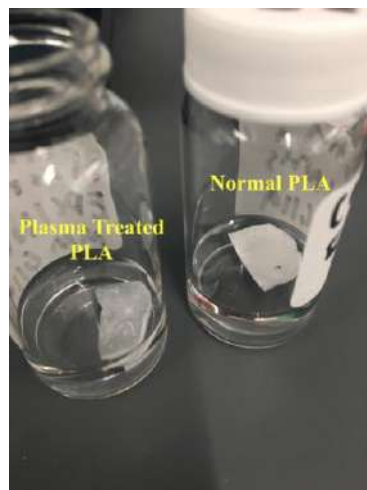


**Figure 4.** Image of plasma treated (left) and untreated PLA (right) fabrics in aqueous solutions

### 3.2 Static BSA-FITC Binding

Quantitative results for BSA-FITC binding yielded peculiar results. Figure 5 implies that untreated PVA/PMA fibers bind more protein than fibers treated with sulfo-NHS/EDC chemistry. Clearly there is some significant nonspecific binding occurring likely due to PVA/PMA's ability to participate in hydrogen bonding. The reason for the discrepancy between the sulfo-NHS/EDC treated fabric and the control group may be due to a decrease in surface charge. As the sulfo-NHS/EDC reacts with fibers, it decreases the number of carboxyl groups that may be interacting with the protein. However, further experimentation is needed to explicitly determine the cause of the adsorption difference. As for PLA fabrics, Figure 6 shows that plasma treated and sulfo-NHS/EDC treated fabrics bound more protein than untreated PLA. There is no statistically significant difference between plasma treated fabrics and fabrics that had plasma and sulfo-NHS/EDC treatment. Because of this, we cannot determine whether any specific covalent binding is occurring. Qualitative data shows minimal differences in protein binding. Figure 7 shows fluorescent microscopy images of PVA/PMA fabrics under various treatments along with static binding procedure. Fibers can be seen in both however this is minimal if any difference in the brightness of the fabrics. This indicates a similar protein content on the surface of the fabrics. Similar results were seen for PLA fabrics (figure 8). The static binding method may not be optimal due to this high propensity for non-specific adsorption.

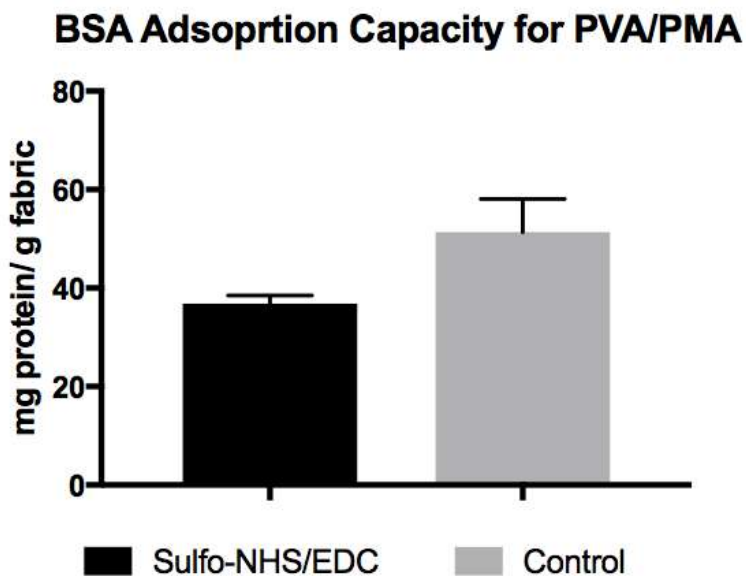


**Figure 5.** BSA-FITC Static Binding on PVA/PMA fibers treated with sulfo-NHS/EDC chemistry and control (untreated)

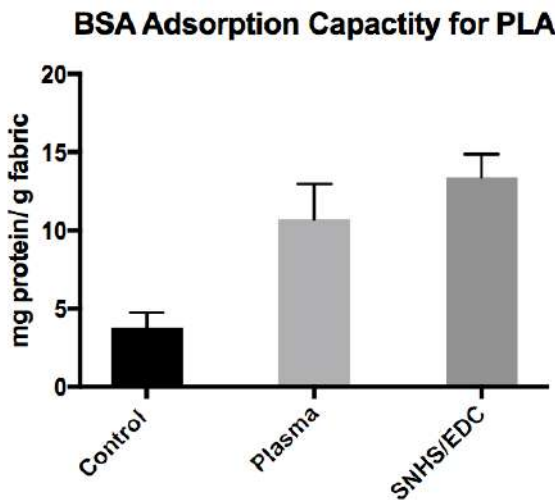


**Figure 6.** BSA-FITC Static Binding on PLA fibers treated with plasma only (150 watt, 3 minutes), plasma and sulfo-NHS/EDC, and a control (untreated).

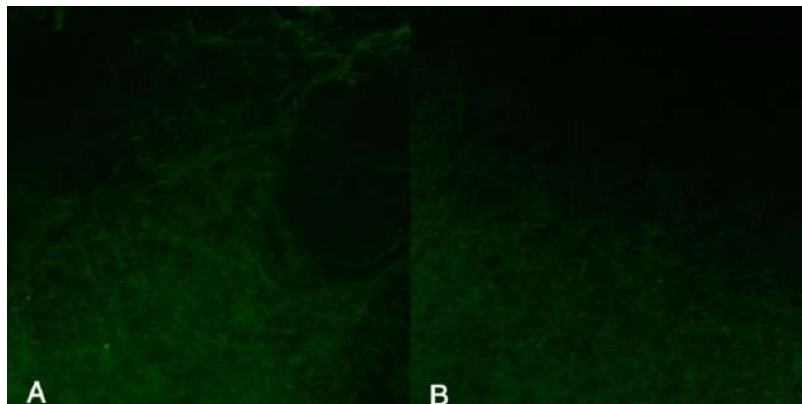


**Figure 7.** Confocal fluorescence images of PVA/PMA treated with sulfo-NHS/EDC (A) and untreated (B) after static BSA-FITC binding and PBS wash.

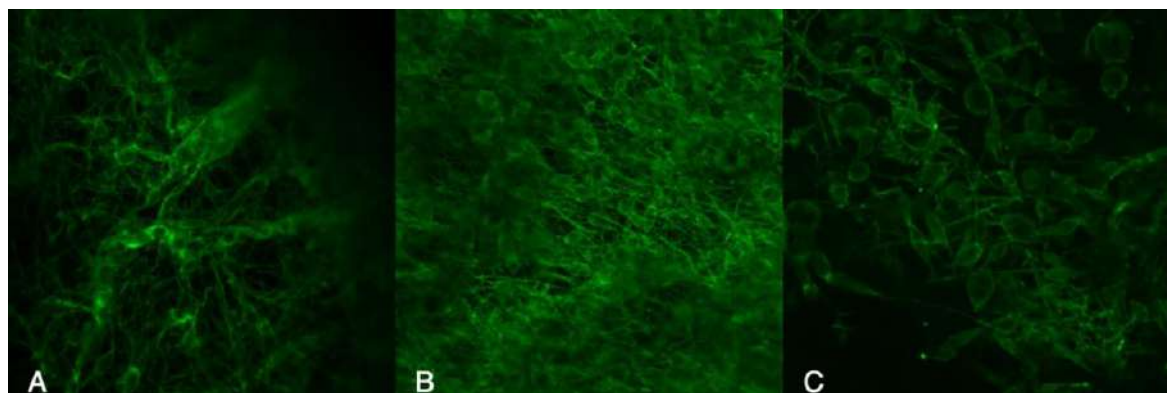


**Figure 8.** Confocal fluorescence images of PLA untreated (A), plasma treated (B), and treated with plasma and sulfo-NHS/EDC chemistry (C) after static BSA-FITC binding and PBS wash

### 3.3 Dynamic BSA-FITC Binding

The dynamic binding of BSA-FITC to PLA NFs appears to be more successful than both the static binding onto PVA/PMA and PLA. Specifically, the dynamic binding procedure provided bettered washing of nonspecifically bound protein and more specific covalent binding. This could be due to optimal washing conditions and minimization of nonspecific binding. Figure 9 shows that the PLA fabrics that receive sulfo-NHS/EDC treatment after plasma have brighter fibers than all of the other groups show. This is indicative of there being more protein bound on the fibers. Fibers can be seen in the other groups however this is likely baseline fluorescence noise from the fibers themselves. In the image of the PLA fibers that weren't treated with plasma, sulfo-NHS/EDC, or BSA-FITC, the fiber outlines can be seen. The images for plasma treated with BSA-FITC and untreated PLA with BSA-FITC show fibers that are no brighter than plain PLA. The additional green spots could be due to aggregated denatured protein or dust particles on the slides.

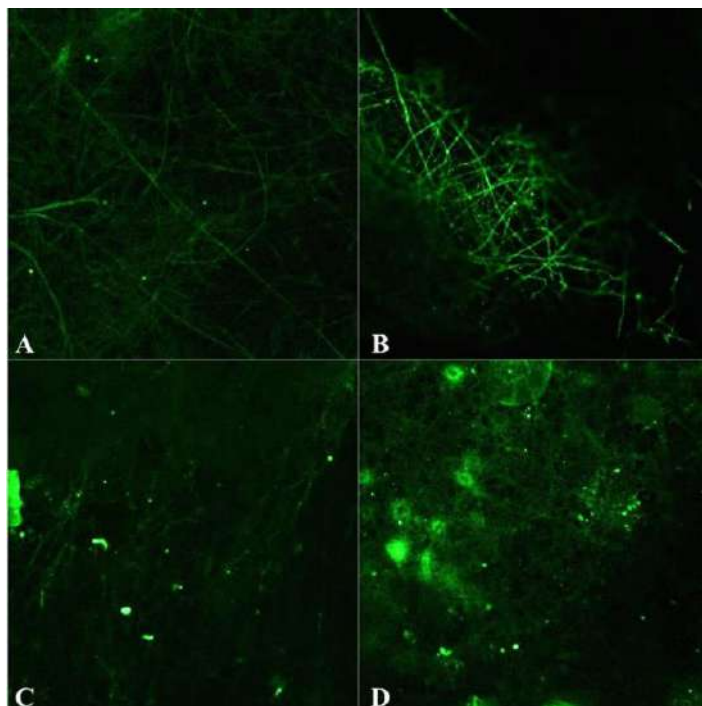


**Figure 9.** Confocal fluorescence images of PLA (A), PLA treated with plasma, sulfo-NHS, and dynamic BSA-FITC binding procedure (B), PLA treated with plasma and dynamic BSA-FITC binding procedure (C), and PLA treated only with dynamic BSA-FITC binding procedure (D).

## 4. Conclusion

In this work, covalently binding of proteins to various electrospun NFs was investigated. PLA NFs received oxygen plasma treatment to chemically modify the surface of the NFs. The data showed that dynamic binding of protein to PLA NFs with sulfo-NHS/EDC chemistry allowed for the covalent binding of proteins to the NFs. The dynamic binding method limited nonspecific adsorption better than the static binding method. Additionally, plasma treated PLA fibers showed increase carboxyl content which increased the hydrophilicity of the fibers. The increase in hydrophilicity allows for better diffusion of analytes dissolved in aqueous solution. This makes the fibers especially well suited for biosensor applications. PVA/PMA fibers appear to have a high level of non-specific adsorption with the protein and may need additional modification to limit this key flaw before these fibers can be used in practical

applications. Future studies could be performed to optimize the covalent binding of protein while limiting nonspecific adsorption. Different solution feed rates for dynamic protein binding could be explored as well as different washing conditions. Additionally, experiments could be run to determine why static binding increases nonspecific adsorption relative to the dynamic binding. The results of this project present a material that can be used in a variety of applications. The enhanced PLA fibers could be applied to increase sensitivity and reliability of biosensors and create protein functionalized tissue engineering scaffolds.

## References

- 1) Prabhu, P. Nanofibers for Medical Diagnosis and Therapy Handbook of Nanofibers. 2018, 1-37 DOI: 10.1007/978-3-319-42789-8\_48-1
- 2) Mahmoudi, M.; Soudi, S.; Soleimani, M.; Hosseinzadeh, S.; Esmaeili, E.; Vossoughi, M. Efficient protein immobilization on polyethersulfone electrospun nanofibrous membrane via covalent binding for biosensing applications *Mater Sci Eng C Mater Biol Appl* **2016**, 58, 586-94 DOI: 10.1016/j.msec.2015.09.007
- 3) Sapountzi, E.; Braiek, M.; Chateaux, J. F.; Jaffrezic-Renault, N.; Lagarde, F. Recent Advances in Electrospun Nanofiber Interfaces for Biosensing Devices *Sensors* **2017**, 17, 1887 DOI: 10.3390/s17081887
- 4) Najafi, M.; Chery, J.; Frey, M.W. Functionalized Electrospun Poly(Vinyl Alcohol) Nanofibrous Membranes with Poly(Methyl Vinyl Ether-Alt-Maleic Anhydride) for Protein Adsorption *Materials* **2018**, 11(6), 1002 DOI:10.3390/ma11061002
- 5) Kim, D.; Herr, A.E. Protein immobilization techniques for microfluidic assays *Biomicrofluidics* **2013**, 7(4):041501 DOI: 10.1063/1.4816934
- 6) Jacobs, T.; Declercq, H.; De Geyter, N.; Cornelissen, R.; Dubruel, P.; Leys, C.; Beaurain, A.; Payen, E.; Morent, R. Plasma surface modification of polylactic acid to promote interaction with fibroblasts *J Mater Sci Mater Med* **2013**, 24(2), 469-78 DOI: 10.1007/s10856-012-4807-z
- 7) Chen, J.P.; Su, C.H. Surface modification of electrospun PLLA nanofibers by plasma treatment and cationized gelatin immobilization for cartilage tissue engineering *Acta Biomater* **2011**, 7(1), 234-43 DOI:10.1016/j.actbio.2010.08.015
- 8) Xia, Y.; Boey, F.; Venkatraman, S.S. Surface modification of poly(L-lactic acid) with biomolecules to promote endothelialization *Biointerphases* **2010**, 5(3), 32-40 DOI: 10.1116/1.3467508
- 9) Paletta, J.R.; Bockelmann, S.; Walz, A.; Theisen, C.; Wendorff, J.H.; Greiner, A.; Fuchs-Winkelmann, S.; Schofer, M.D. RGD-functionalisation of PLLA nanofibers by surface coupling using plasma treatment: influence on stem cell differentiation *J Mater Sci Mater Med* **2010**, 21(4), 1363-9 DOI: 10.1007/s10856-009-3947-2
- 10) Reinholt, S.J.; Sonnenfeldt, A.; Naik, A.; Frey, M.W.; Baeumner, A.J. Developing new materials for paper-based diagnostics using electrospun nanofibers *Anal Bioanal Chem* **2014**, 406(14), 3297-304 DOI: 10.1007/s00216-013-7372-5
- 11) Matlock-Colangelo, L.; Coon, B.; Pitner, C.L.; Frey, M.W.; Baeumner, A.J. Functionalized electrospun poly(vinyl alcohol) nanofibers for on-chip concentration of *E. coli* cells *Anal Bioanal Chem* **2016**, 408(5), 1327-34 DOI: 10.1007/s00216-015-9112-5
- 12) Vashist, S.K. Comparison of 1-Ethyl-3-(3-Dimethylaminopropyl) Carbodiimide Based Strategies to Crosslink Antibodies on Amine-Functionalized Platforms for Immunodiagnostic Applications *Diagnostics* **2012**, 2(3), 22-33 DOI: 10.3390/diagnostics2030023
- 13) Bartczak, D.; Kanaras, A.G. Preparation of Peptide-Functionalized Gold Nanoparticles Using One Pot EDC/Sulfo-NHS Coupling *Langmuir* **2011**, 27(16), 10119-23 DOI: 10.1021/la2022177
- 14) Ikada, Y.; Tsuji, H. Biodegradable polyesters for medical and ecological applications *Macromol. Rapid Commun.* **2000**, 21(3), 117-32 DOI: 10.1002/(SICI)1521-3927(20000201)21
- 15) González, E.; Sheperd, L.M.; Saunders, L.; Frey, M.W. Surface Functional Poly(lactic Acid)

Electrospun Nanofibers for Biosensor Applications *Materials* **2016**, 9(1), 47 DOI: 10.3390/ma9010047

- 16) Narayanan, N.; Jiang, C.; Uzunalli, G.; Thankappan, S.K.; Laurencin, C.T.; Deng, M. Polymeric Electrospinning for Musculoskeletal Regenerative Engineering *Regen. Eng. Transl. Med.* **2016**, 2, 69-84 DOI: 10.1007/s40883-016-0013-8

# Organic molecule as a cathode material for Li-ion batteries

Joshua Reyes Morales<sup>1</sup>, Cara Gannett<sup>1</sup>, Héctor Abruña<sup>2</sup>

Cornell University, Abruñas Electrochemistry Laboratory

*Abstract: Modern society has begun to utilize more energy sources to meet our growing energy needs. One of the most used sources are the batteries where the majority are from Lithium. Some of the problems with these batteries include that the synthesis of inorganic materials leads to the production of toxic substances for the environment and these materials are expensive. Due to this, the use of organic materials has been considered as they are mostly non-toxic, low cost and their structure can be modified to change the properties of these materials to obtain a better performance of the batteries. In this work, this approach was carried out in a molecule derived from phenothiazine since it is known that its structure can be modified through synthetic means to obtain different properties that can be turned to optimize the performance of these batteries. Several molecules were characterized to identify the redox peaks of the polymer so that the stability of the active material could then be studied. Cyclic voltammetry studies of the polymer revealed a degradation process which could be slowed using different solvent systems and cycling through only the first two redox couples. From these studies, it appears that the third oxidation state is largely the case of the degradation in the polymer.*

## 1. Introduction

The rapid rise of technology in the modern world has led to an increased demand for energy and a need for more sources to provide it. This energy is used to power technology like cars, cellphones, and computers. One energy source used most is batteries, that most of them are made of Li-ion batteries. Batteries are not an energy source, they are a form of energy storage. Most commercial Li-ion batteries utilize inorganic materials, which store energy through a change of oxidation state of the metal [1]. The best inorganic material for Li-ion battery is LiFePO<sub>4</sub> because has high cyclability and non-toxic nature. However, this material works at low potential of 3.4 V [2]. Additionally, the material is expensive and its synthesis tends to release toxic metals into the environment [1]. Because of these problems, scientists are pursuing other materials to be used in Li-ion batteries.

There is an interest on organic materials because are low cost, benign to environment and the synthesis of these materials can be modified to tune chemical structure which in turn will change properties like solubility, capacity, energy density

and others. The ideal battery would have a long lifetime, low cost, and be benign to the environment. Typical capacities for commercial batteries are around 150 mAhg<sup>-1</sup>.

Capacity is the maximum amount of charge that a material can hold per gram. If the material it's dissolved in the solution of the battery, is going to be troublesome because if there is a miss of the material, the battery is going to lose capacity. There is a relationship that is:

$$C_{\text{theor}} = \frac{nF}{(3.6)(MW)}$$

where n is the number of electron transferred, F is the Faraday constant, and MW is the molecular weight of the active material. Ideally, an organic material would be capable of multiple electron transfer and would possess a low molecular weight to obtain a high capacity.

The material studied here is a derivative of phenothiazine. Phenothiazine has been used for pharmaceutical purposes. One of the most known derivatives of this molecule is methylene blue. In recent research there is been an interest in using

derivatives of phenothiazine as an active material for Li-ion batteries. Some phenothiazine derivatives exhibit an oxidation potential of 3.9 V vs Li/Li<sup>+</sup>, which is 500 mV higher than that of LiFePO<sub>4</sub> [2]. Its chemical structure has been previously modified for pharmaceutical purposes, providing an existing knowledge base for modifying the structure for use as a battery material. For these reasons, a phenothiazine derivative is promising for a new cathode electrode material that exhibits high capacity, high redox potential and high cyclability [2].

## 2. Methodology

### 2.1. Sample preparation

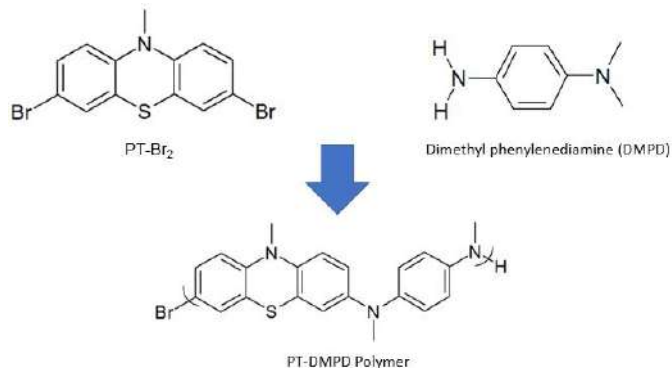
The polymer and other phenothiazine derivatives were previously synthesized by collaborators in the Fors group. The synthesis involved Buchwald-Hartwig cross-coupling of 3,7-dibromo-N-methylphenothiazine with dimethyl phenylenediamine, and is outlined in Scheme 1.

For electrochemical tests, the phenothiazine small molecules were prepared by dissolution into solution of 0.1M tetrabutylammonium perchlorate (TBAP) in acetonitrile (MeCN) at a 1 mM concentration. The polymer is insoluble and was prepared for electrochemical testing as a slurry. The slurry was prepared with a ratio of 3:6:1 of active material: Super P: polyvinylidene difluoride binder dissolved in 1.0 mL of N-Methyl-2-pyrrolidone (NMP). 2  $\mu$ L of the slurry were then drop cast onto the surface of a polished glassy carbon working electrode with a diameter of 3 mm and dried under a heat lamp to evaporate the NMP.

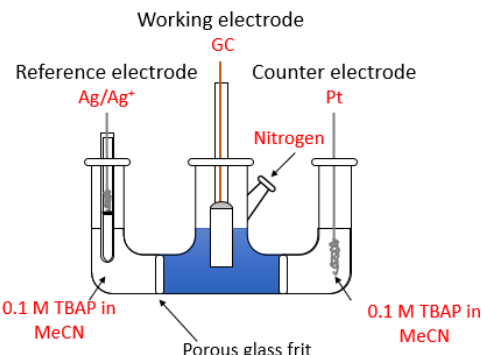
### 2.2. Characterization

To understand the chemical behavior of this polymer a series of small molecules were studied to compare the electrochemical chemical response using cyclic voltammetry. To identify the different peaks of the polymer the peak shifts of the phenothiazine small molecule derivatives were used to deduce which heteroatom gave rise to which response. The degradation process of the polymer was studied in different solvents two different solvents, nitrobenzene (NB) and propylene carbonate (PC). Electrochemical characterization was carried out by cyclic voltammetry. The working electrode was a glassy carbon with a diameter of 3mm,

reference electrode of Ag/Ag<sup>+</sup> and a counter electrode of platinum. The electrochemical cell is depicted in Scheme 2. The solutions were purged with nitrogen to remove oxygen from the solvent. The scan rate used was 20 mV/s, unless otherwise noted.



Scheme 1. PT-DMPD polymer



Scheme 2. Electrochemical Cell

## 3. Results and Discussion

### 3.1. Characterization

To understand the response in the cyclic voltammetry experiments of the polymer, the CV response from different phenothiazine derivatives were compared to observe the redox potential shift relative to one another. In figure 1, the voltammogram of phenothiazine is shown. The first peak is the oxidation of the nitrogen group and the third is due to the sulfur group. In an attempt to obtain results which better match those seen in literature, where the second peak is not observed, the molecule was tested in an argon glove box (Figure 2). In an inert atmosphere, the second peak disappeared, which it is attributed to likely being due to the use of the MeCN which is kept in the glovebox and likely has fewer impurities.

To understand better the polymer behavior, the potential of the oxidation peak from the nitrogen of the phenothiazine was compared with the one of the PT-Br<sub>2</sub> (Figure 3). The redox potential was observed to shift to higher potentials with the attached bromines and methyl group. Bromine groups have an effect on the electrochemical behavior of a molecule due to their electron withdrawing nature. The bromine atoms withdraw electronic density from the nucleus of the molecule and make it more difficult to oxidize the nitrogen group, shifting the peaks to higher potentials [3].

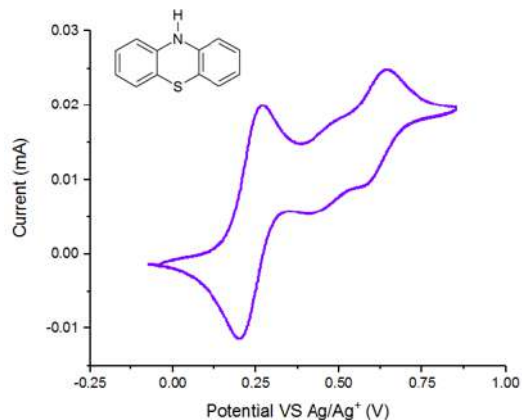


Figure 1. Phenothiazine Cyclic Voltammetry

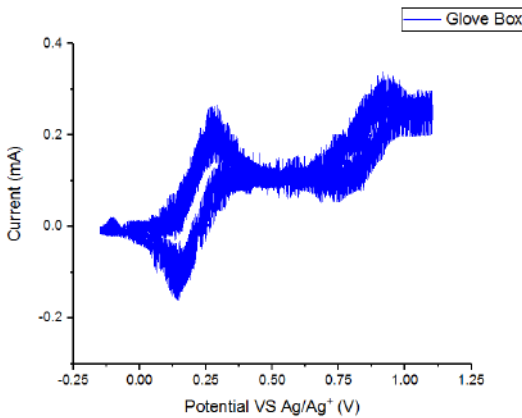


Figure 2. Phenothiazine characterization, glove box

After the characterization of PT and PT-Br<sub>2</sub>, two more phenothiazine derivatives were characterized. Figure 3a and 3b show the cyclic voltammograms (CV's) of PT-(Ani)<sub>2</sub> and PT-N(Me)<sub>2</sub>. The CV's show similar behavior, but with a shift in the oxidation potential. All of the peaks of the PT-N(Me)<sub>2</sub> have been shifted to more negative potential. The explanation for this is because methyl groups are more electro-donating than the benzene groups, so it's easier to oxidize the nitrogen with the methyl groups. To know which redox peak corresponds to which heteroatoms in the

molecules, we compared the magnitude of the shift of each of the peaks in these two CV's. It was observed that the first peak and the third peak shifted by about 150 mV, while the second peak only shifted around 50 mV. The most affected group by the electro-donating effect of the methyl groups will be the atoms that are directly linked to the methyl or benzene group. From this logic, we can infer that the nitrogen in the center of the molecule, will be less effected by the electron donating effect of the methyl groups, and its redox peak will shift the least. From this, we correlated this nitrogen giving rise to the second peak in the CV response. The first and the third peak then arise from the nitrogen atoms with the attached methyl/benzene groups. Although the two nitrogen's originally start out equivalent in the neutral molecule, once one is oxidized, the chemical environment of the other becomes different and more difficult to oxidize, as described by percolation theory. One will be oxidized first and the second will then be oxidized at a higher potential.

When obtaining the voltammograms of the different molecules, the characterization of the polymer was obtained by comparing the data. Figure 3d shows the cyclic voltammogram of the polymer. It has three main peaks that are labeled. The results of determining which peaks correspond to which heteroatom from the small molecule studies have been extended to the polymer response. We assume that the peaks in the polymer arise from the same heteroatoms which they were correlated to in the small molecules. The small peaks between peak two and peak three is related to one of the main peaks. It is known that polymers are chains of monomers with n monomer units. The monomers near the start of the polymer chain will feel an effect from the bromine atom which begins the polymer chain. As observed with the small molecule, the electron withdrawing effect will shift the redox potential of a group to more positive potentials. These small peaks then arise from the phenothiazine units at the beginning of the polymer chain, which are shifted anodically from this electron withdrawing effect. We do not observe a peak from the sulfur atom like we did in the phenothiazine molecule. A possible reason why the redox peaks of the sulfur group was not observed is because it appears at a high potential where the electrolyte solution is unstable.

### 3.2. Degradation Process Study

To know if a material can be used for batteries

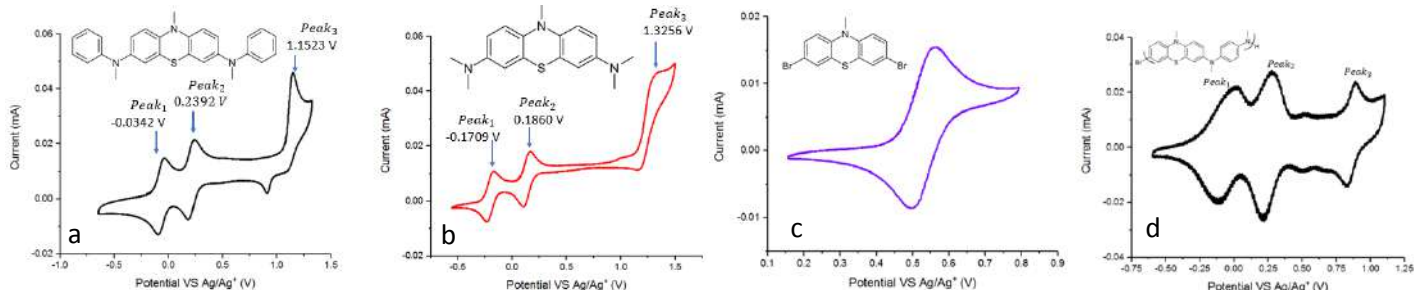


Figure 3. (a) PT-N(Me)<sub>2</sub>, (b) PT-(Ani)<sub>2</sub>, (c) PT-(Br)<sub>2</sub> and (d) PT-DMPD Polymer

the stability of it must be studied. The stability of the sample was studied by cycling the polymer through all three of its redox peaks ten times (Figure 4a). It was found that the first and third peak of the polymer started to decay rapidly, but the second one decreased more slowly, although a small shift in its potential also occurred. Isopotential points where observed in the cycling which indicates that there is some form of a conversion occurring in the polymer. A possible explanation to this problem may be due to the nucleophilic activity of the solvents. The same process was repeated using different solvents with less nucleophilic activity like NB (Figure 4b) and PC (Figure 4c). In these two cases the peaks all started to decrease uniformly, unlike what was observed in the MeCN. The sample run in the PC had the fastest decrease in its peaks. The sample in NB was observed as the most stable and least nucleophilic in this case. The normalized peak current was plotted versus the number of cycles for each of the samples to fairly compare the results in all three solvents (Figure 4d).

This stability test in the different solvents was repeated, but with cycling the polymer only through the first two redox couples. This was done to observe if the +3 oxidation state of the polymer was making the active material unstable. Figure 5 shows the stability of the polymer in the different solvents. Comparing the results with those performed when cycling through all three states, it can be clearly observed that the polymer is much more stable. With this, it is considered that the third oxidation state is linked to the degradation process of the polymer. These results show that this material would be suitable as a battery material if the potential range is limited to the second oxidation state.

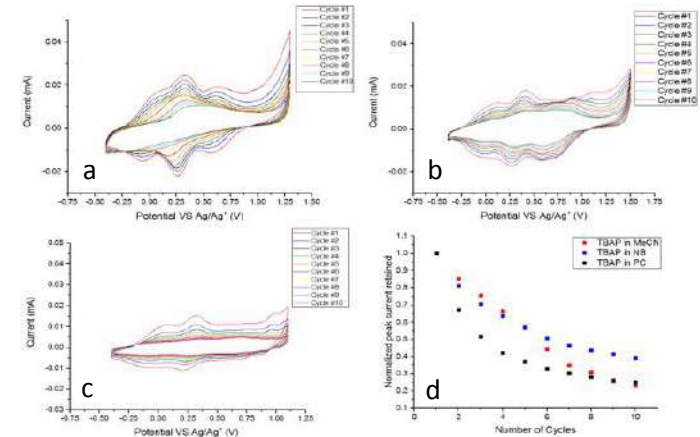


Figure 4. Degradation process test in different solvents like (a) MeCN, (b) NB and (c) PC. The graph (d) is the comparison of the first current peak of each of the first three graphs.

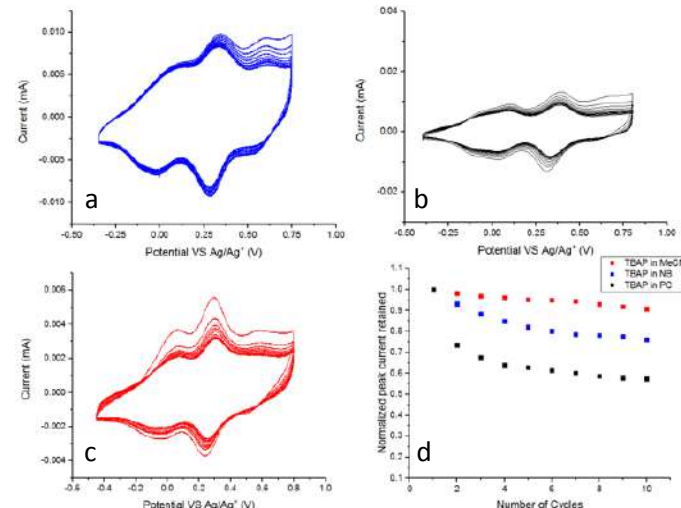


Figure 5. Degradation process test in different solvents only going through the first two peaks. The solutions were (a) MeCN, (b) NB and (c) PC. The graph (d) is the comparison of the first current peak of each of the first three graphs.

## Conclusions

Organic materials are promising for electrochemical storage. The most stable performance was observed when cycling only the first two peaks in all solvents. In the case of the two peaks the most stable solvent used was the acetonitrile. Further experiments will be testing the

solubility of the material in different solvents and studying a related polymer featuring a protecting group in hopes of preventing degradation and enabling all three oxidation states to be stably accessed.

### Acknowledgments

This project is supported by the Cornell Center for Material Research REU Program. Thanks to this program for the opportunity to be at Cornell University doing research. Thanks to Brian for Fors group in Cornell for the synthesis of the active material and the small molecule. Special thanks to Cara Gannet who has been the person with whom have worked during the summer. Another person who is thanked is Dr. Abruña for allowing to work in his research laboratory with his group.

### References

[1] Schon TB, McAllister BT, Li P and Seferos DS. 2016. The rise of organic electrode materials for energy storage. *Chem. Soc. Rev.* 45: 6345-6404.

[2] Godet-Bar T, Lepretre JC, Le Bacq O, Sanchez JY, Deronzier A and Pasturel A. 2015. Electrochemical and ab initio investigations to design a new phenothiazine based organic redox polymeric material for metal-ion battery cathodes. *Phys. Chem. Chem. Phys.* 17: 25283-25296.

[3] Bejan A, Shova S, Damaceanu MD, Simionescu BC, and Marin L. 2016. Structure-Directed Functional Properties of Phenothiazine Brominated Dyes: Morphology and Photophysical and Electrochemical Properties. *Cryst. Growth Des.* 16: 3716–3730.

[4] Elgrishi N, Rountree KJ, McCarthy BD, Rountree ES, Eisenhart T and Dempse JL. 2018. A Practical Beginner's Guide to Cyclic Voltammetry. *J. Chem. Educ.* 95: 197–206.

[5] Nitta N, Wu F, Lee JT and Yushin G. 2015. Li-ion battery materials: present and future. Elsevier Ltd. 18: 1369-7021.



# Phase Transitions in Sodium Ion Batteries Upon Charging and Discharging

Malia Okamura<sup>1</sup>, Daniel Weinstock<sup>2</sup>, Andrej Singer<sup>2</sup>

<sup>1</sup>Department of Materials Science and Engineering, Carnegie Mellon University, Pittsburgh, PA 15289

<sup>2</sup>Department of Materials Science and Engineering, Cornell University, Ithaca, NY 14853

---

**ABSTRACT:** Lithium Ion Batteries (LIB's) are commonly utilized in technology and energy storage, however, Sodium is much more abundant than Lithium, and can potentially offer improved battery function and faster kinetics [1]. Analysis of Synchrotron X-ray diffraction scans of a charging and discharging Sodium Ion Battery (NIB) gives information about the particles in the battery and how they behave during charging and discharging. From the results, it is concluded that there is a phase transformation upon charging and discharging. More interestingly, some of the particles in the battery are proven to exhibit two phases in a single particle.

---

## I. MOTIVATION

Cell phones, electric vehicles, and most rechargeable devices are popular nowadays, and there is a high demand for electric energy storage. Lithium ion batteries (LIB's) are utilized in all these devices [1]. The battery is very successful and researchers are constantly studying how to improve this battery [1]. Despite the success of the LIB, it is not practical to limit research to lithium. It is not considered an abundant element, and is unevenly distributed throughout the earth [1]. Because of this fact, it is moderately expensive and not easy to obtain.

Sodium on the other hand, is considered one of the most abundant elements in the earth's crust, as shown in Figure 1 [1]. It is found in the ocean and in many known minerals [1]. In addition, it is easy to synthesize and it is a low cost

element [2]. Sodium is also the most similar to lithium of the alkali metals in mass and in size [1].

---

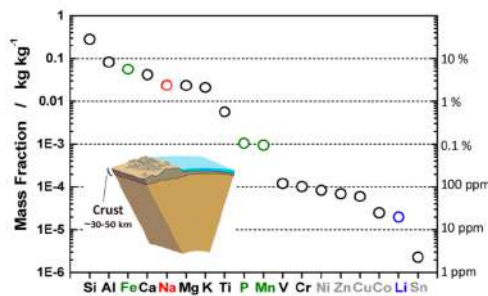


**Figure 1:** Elemental abundance in the Earth's crust.  
Figure from [1]

---

In addition, the structures, components, and systems are similar [1]. Due to these findings, NIB's are an ideal replacement for LIB's. The bigger ionic radius of sodium allows for an increase in the flexibility of the

material design, which is an advantage over LIB's [1]. NIB's can also potentially offer faster kinetics because of its smaller diffusion activation energy [1]. In addition, sodium's higher ionic conductivity leads to increased battery performance [1]. These are some of the many reasons why NIB research is important.

## II. INTRODUCTION

The material the Singer Lab utilizes in the NIB is called layered P2-Na<sub>x</sub>[Ni<sub>1/3</sub>Mn<sub>2/3</sub>]O<sub>2</sub> where x is a number between zero and 1/3 depending on its charged state [2]. As the battery becomes charged, the sodium ions are removed. This material is potentially a good low-cost NIB cathode [2]. The structure of the different materials can be of P2 or O3 type [2]. The letter (P or O) refers to the site that the ion occupies (prismatic or octahedral (see Figure 2)) and the following number refers to the number of ion layers in the repeat unit of the structure [1].

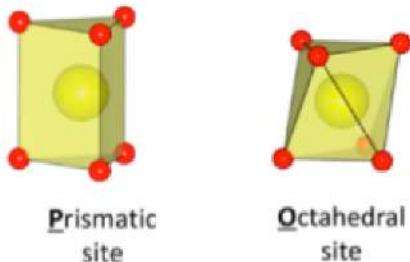


**Figure 2:** Image of Prismatic and Octahedral sites  
Figure from [1]

These different structure types have different stacking sequences as seen in Figure 3 [2].

As sodium ions are removed upon charging, the structure increases its volume due to repulsions [1]. Because of the volume increase, phase transitions occur. This particular material shows a P2 to O2 phase transition seen in Figure 3 upon charging above 4.2 volts (V) [2]. Once the concentration of sodium reaches  $\frac{1}{3}$ , the O2 phase becomes more stable [2]. This phase transition was also shown to be reversible

upon discharging [2]. A voltage versus time graph shows three plateaus, which indicates that there is three phase transitions and therefore there are two more stable intermediate phases apart from P2 and O2 [2]. However, phase transitions are not wanted as they cause slow nucleation and defect formation [4].

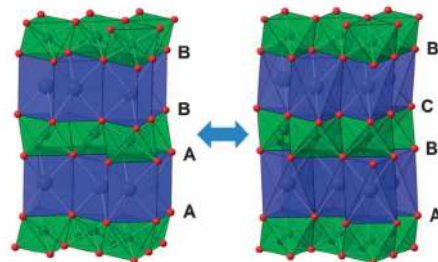


**Figure 3:** P2 structure (left) and O2 structure (right)  
Figure from [2]

## III. EXPERIMENTAL

To prepare the battery sample, a small opening was created in the center of the coin cell, and then sealed with Kapton film to allow the x-rays to penetrate the battery material [4]. The Kapton that is used to seal the opening does not affect the electrochemical performance of anything [4]. The sample was then mounted, and the detector was set to a specific  $2\theta$  value and a certain distance d away from the detector [4]. The sample was irradiated with 15-kilo electron volts (keV) photon energy while rocking the sample back and forth (see Figure 4).

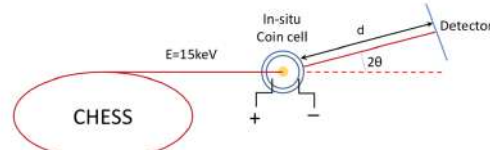


**Figure 4:** Schematic setup of the experiment  
Figure from [6]

The rocking of  $\theta$  (back and forth) allows for a full 2D image of the Bragg peak. Portions of the Debye-Scherrer rings for different planes are recorded on a charge-coupled

device (CCD) [4]. We expect to see the 002 (highest intensity), the 004, and maybe the 100 planes diffract [2]. Once these images are obtained, Matlab was used to extract information from the 4D data set. There are many “cubes” of data according to the number of scans. The dimensions are  $2\theta$ ,  $\theta$ , and  $\chi$  illustrated in Figure 5. By stacking and extracting data, we are able to see the many peaks, and observe their movement and behavior.

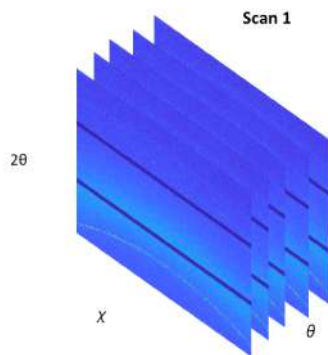


**Figure 5:** 4D Data set

There were four sets of data used in data analysis as seen in Table 2, each sample run with a different  $2\theta$  values, and with different charging rates. From the resulting data, Matlab was used to extract useful information about the Bragg peaks of the 002 ring.

**Table 1:** Recorded data

Sample	Charging Rate	$2\theta$
B2_S7 charging	C/10	11.29
B2_S7 discharging	C/10	11.29
B2_S9 full scan	C/3	11.79
B3_S10 full scan	C/10	11.79

#### IV. RESULTS

First, looking at the average images of the 002 Debye-Scherrer ring portion scan after scan, a phase transition is clearly visible. There is first only a presence of one

ring, and then it splits into two, indicating a phase transition upon charging.

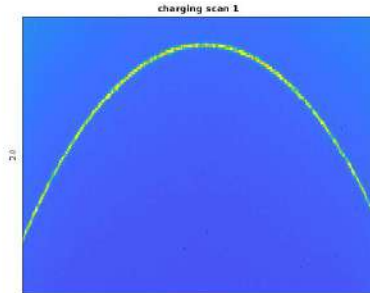


**Figure 6:** 002 ring in scan one. One phase present

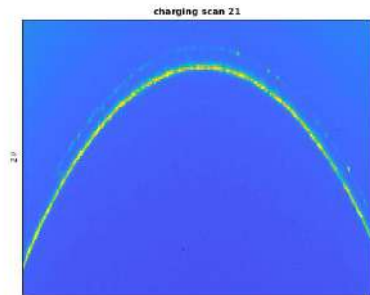


**Figure 7:** 002 ring in scan 21. Two phases present

After retrieving these images, the rings were flattened, and averaged over  $\chi$  to create a line scan. As seen in Figure 7, it is easier to see the phase transition and when it occurs.

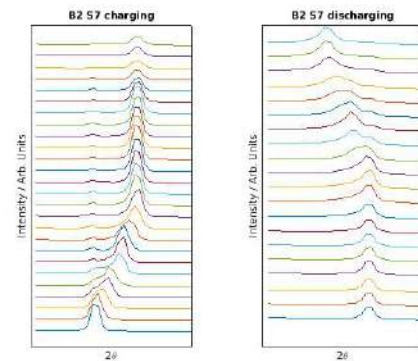


**Figure 8:** Line scan of flattened rings showing the phase transition upon charging and discharging.

In order to obtain information about the peaks and to determine if the two phases exist in a single particle or two separate particles, the 2D Bragg peak is needed. All images from one scan that were rocked in theta were stacked, and the portion of the block that both rings are present was extracted and averaged into one 2D image. This process was done over all the scans.

Now, looking at specific peaks gave information about each particle. Using a peak finding program, and creating a line scan of each peak along  $2\theta$  showed if there was two phases present in a single particle. If there were two phases present, there should be two intensity peaks at the same  $2\theta$  values as the two flattened rings. If only one phase is present, there would only be one peak, and the  $2\theta$  value it is at corresponds to that phase.

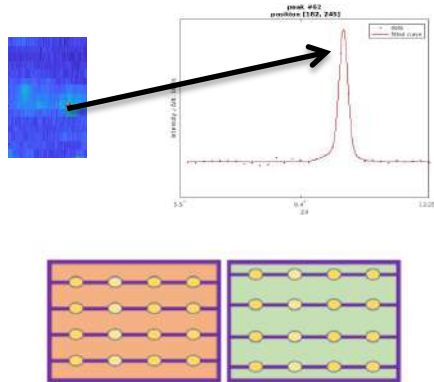


**Figure 9:** Peak coming from a particle with one phase present

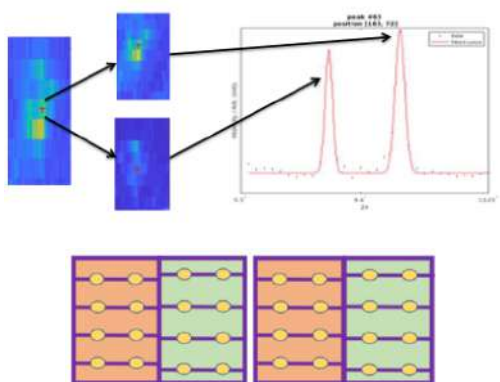


**Figure 10:** peak coming from a particle with two phases present

To prove that these peaks come from the same particle and it's not just a coincidence that they overlap, the relationship of  $\theta$  and  $2\theta$  comes in handy. Due to the  $d$  spacing of each phase and assuming the planes of the two different phases are parallel, the relationship between  $\theta$  and  $2\theta$  is half. In other words, the shift in  $\theta$  should equal half the shift in  $2\theta$ .

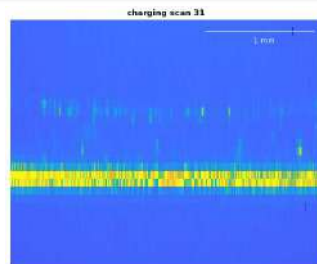


**Figure 11:** Flattened rings showing shift in  $2\theta$

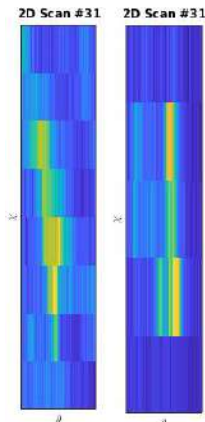


**Figure 12:** Peaks found on the two rings at the same location

The shift in  $2\theta$  was calculated by use of geometry. The distance between the two rings is known as well as the distance between the sample and the detector. This allowed for calculation of the shift in  $2\theta$ . To determine the theta value of each peak, the peak image was averaged over  $\chi$ , and the highest intensity position was considered the theta value of the peak. Comparing the values, for the peaks in Figure 11, the shift in the  $2\theta$  value was  $.21^\circ$  and the shift in the  $\theta$  values was  $.1^\circ$ . The ratio of these values is 2.1, which is close to double. Some other peaks exhibited this ratio but they are all slightly off. This is because there is some

# Effect of Glycation Time on Rheological Properties of Collagen Gels for Extrusion Bioprinting

Marcos R. Rodríguez<sup>1</sup>, Nicole Diamantides<sup>2</sup>, Lawrence J. Bonassar<sup>2</sup>

<sup>1</sup>Department of Chemical Engineering, University of Puerto Rico – Mayagüez

<sup>2</sup>Meinig School of Biomedical Engineering, Cornell University

**Abstract:** Collagen is a promising bioink for extrusion bioprinting due to its inherent biocompatibility and temperature-dependent gelation. The rheological properties of collagen solutions before, during and after gelation dictate their printability and utility however, some collagen gel crosslinking methods introduce cytotoxicity. Previous studies demonstrated that crosslinking through non-enzymatic glycation enhances collagen gel mechanics while maintaining the viability of encapsulated cells. The goal of this study is to determine the effect of glycation time on rheological properties of collagen gels. Results showed that glycation time was non-linear and improved post-gelation storage modulus and gelation rate. Optimal results were seen after 5-7 days of glycation while additional glycation time delayed gelation and decreased mechanical performance.

## 1. Introduction:

Extrusion bioprinting is the process by which a material (usually a gel) is extruded in a layer by layer method to build 3D constructs. These gels serve as tissue constructs and have a certain degree of geometric complexity. Collagen is a promising bioink for extrusion bioprinting because collagen has a gelation process which develops a branched fiber network, forms the main structural component of the extra-cellular matrix, and has inherent biocompatibility. The rheological properties (i.e., storage modulus, gelation rate, and crossover time) of collagen bioinks before, during and after gelation dictate their printability [3] and utility. Crosslinking methods have been employed to improve the rheological properties of collagen gels however, some of these methods introduce cytotoxicity [3]. Based on previous studies, the non-enzymatic glycation of collagen with ribose enhances collagen gel mechanics while maintaining the viability of encapsulated cells [2]. This is likely due to the formation of advanced glycation end products (AGEs) [2] which crosslink collagen fibers during gelation. We propose the use of this technique to enhance the mechanical properties of collagen bioinks while maintaining cell viability. The goal of this study is to determine the effect of glycation time on the key rheological properties of collagen gels used in bioprinting, including the storage modulus before and after gelation, crossover time and gelation rate of the collagen gels with the purpose of identifying an optimal glycation period.

## 2. Materials and Methods:

### 2.1 Collagen Bioink Formulation

Type I collagen was extracted from rat tails and solubilized in 0.1 % acetic acid at 150 mL/g [3]. The collagen solution was then centrifuged at 9000 rpm for 90 minutes at 4 °C [3]. The supernatant was collected, frozen overnight at -80 °C and lyophilized for 5 days.

Lyophilized collagen was reconstituted in 0.1 % acetic acid at 15 mg/mL. Stock collagen was mixed with a 250 mM ribose solution to induce glycation and stored at 4 °C for 5, 7, 9, 14 or 21 days.

### 2.2 Rheological Characterization

The solution was tested with a TA Instruments DHR3 rheometer using a 25 mm parallel plate geometry. For this process the collagen-ribose solution was neutralized with a working solution containing 1X PBS, 10X PBS and NaOH [1], transferred to the base of the plates, and examined in oscillatory mode at 0.1 Hz with a 0.5 % strain and 1 mm gap for 5 minutes at 4 °C followed by 30 minutes at 37 °C wherein gelation occurs [2]. Glass coverslips previously treated with polyethylenimine (PEI) and glutaraldehyde were attached to the rheometer's plates to prevent the gels from slipping during testing [3]. The mean storage modulus at 4 °C (before gelation) and 37 °C (after gelation), the gelation rate and the crossover time were acquired.

## 3. Results:

Glycation with ribose lowered pre-gelation storage modulus (Figure 1A) and delayed gelation time (Figure 1D) when compared to control runs (no-ribose) which exhibited  $1.3 \pm 0.2$  Pa and  $1.9 \pm 0.1$  minutes respectively. The 7 day glycation gels showed the largest pre-gelation storage modulus of the glycation periods with  $1.1 \pm 0.2$  Pa (Figure 1A) and the shortest crossover time with  $3.2 \pm 0.4$  minutes (Figure 1D). The 7 day glycation period along with the 5 day exhibited the largest post-gelation storage modulus (Figure 1B) with  $3668.0 \pm 317.2$  Pa and  $3713.0$  Pa, respectively. The 7 day samples also resulted with the highest gelation rate (Figure 1C) with  $27.9 \pm 1.4$  Pa/s. Glycation time after 9, 14 and 21 days decreased storage modulus before and after gelation. These glycation

periods also reported the slowest gelation rate and crossover time.

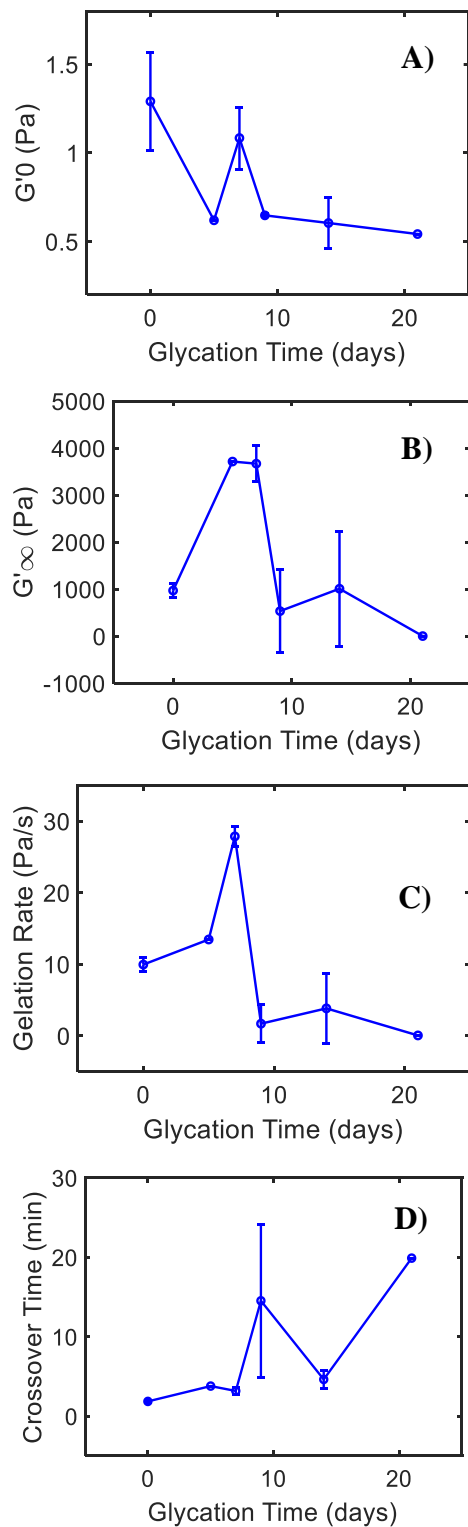


**Figure 1.** Rheology tests results showing rheological properties of collagen solutions such as a) pre-gelation storage modulus, b) post-gelation storage modulus, c) gelation rate and d) crossover time as a function of glycation time. Results represent averages

and standard deviation (error bars) of the tests within each glycation time.

#### 4. Discussion:

The effect of glycation time was non-linear, with optimal results seen after 5-7 days, while additional glycation time delayed gelation and decreased mechanical performance. Glycation introduces two competing factors into the collagen gel, the intermediaries formed during the glycation process (i.e., ribose, Schiff base, Amadori product, etc.) and AGEs. The intermediaries likely increase the solubility of the collagen which lowers the viscosity and hinders gelation. This is a deterrent for the gelation phenomena and is most likely responsible for delayed gelation and worsening pre-gelation storage modulus. Meanwhile, the AGEs aid the crosslinking of the collagen during gelation and is most likely responsible for the increase in post-gelation storage modulus and gelation rate for 5 and 7 day glycation times in comparison to the control runs.

#### 5. Conclusions:

Glycation improved the post-gelation storage modulus and gelation rate due to formation of AGEs and subsequent crosslinking. The effect of glycation time was non-linear, with optimal results seen after 5-7 days, while additional glycation time delayed gelation and decreased mechanical performance.

#### 6. Acknowledgements:

This work was supported by CCMR with funding by the NSF MRSEC program (DMR-1719875) and REU Site program (DMR-1063059).

#### 7. References:

- [1] Rhee, S., ACS Biomater. Sci. Eng., 2016, 2, 1800-1805
- [2] Roy, R., J. Orthop. Res., 2008, 26, 1434-1439.
- [3] Diamantides, N., Biofabrication, 2017, 9, 03410

error to take into consideration. There is still some lingering background noise, and the peak shapes are funky, so the determination of the theta value of the peak is a bit off. Nonetheless, this ratio proves that the two peaks come from the same particle, and it is not a coincidence that these two peaks happen to be in the same position. This proves that there are two phases present within this single particle.

## V. CONCLUSION

In Conclusion, a phase transition is observed upon charging and discharging for this sodium ion battery as shown by the ring splitting in Figures 6 and 7. There are some particles that show peaks in both phases meaning that some single particles contain two stable phases.

## ACKNOWLEDGEMENTS

This research was supported by the Cornell Center for Materials Research and the National Science Foundation. Special thanks to the Singer Lab, my mentor Daniel Weinstock, and my Professor Andrej Singer for a great research experience.

## REFERENCES

- [1]. Naoaki Yabuuchi, Kei Kubota, Mouad Dahbi, Shinichi Komaba, “Research Development on Sodium-Ion Batteries”, Chemical

- Reviews, November 2014, pg. 11636-11682
- [2]. DaeHoe Lee, Jing Xu, Ying Shirley Meng, “An advanced cathode for Na-ion batteries with high rate and excellent structural stability”, Phys. Chem. Chem. Phys., 2013, 15, 3304-3312
- [3]. Barnes, Paul, et al. “Powder Diffraction.” Structure Refinement III: Rietveld in Practice, pd.chem.ucl.ac.uk/pdnn/diff2/kine mat2.htm.
- [4]. Singer, et al. “Nonequilibrium Structural Dynamics of Nanoparticles in  $\text{LiNi}_{1/2}\text{Mn}_{3/2}\text{O}_4$  Cathode Under Operando Conditions”, Nano Lett. 2014, 14, 5295–5300
- [5]. Feng Lin, et al. “Synchrotron X-ray Analytical Techniques for Studying Materials Electrochemistry in Rechargeable Batteries”, Chem. Rev. 2017
- [6]. R. Kumar, H.Hirsh, R.Buock, M.Zhang, D.Weinstock, O.Gorobstov, J.Ruff, Y.S.Meng, A.Singer, Phase Transformations in Sodium Ion-Batteries: in-situ X-ray Diffraction

# Synthesis and Purification of Antimicrobial Oligothioetheramides

Mathias Rodriguez

**Abstract –** As resistance to traditional antibiotics becomes a growing concern, new antibiotics will need to be developed that offer alternative treatment methods and routes.

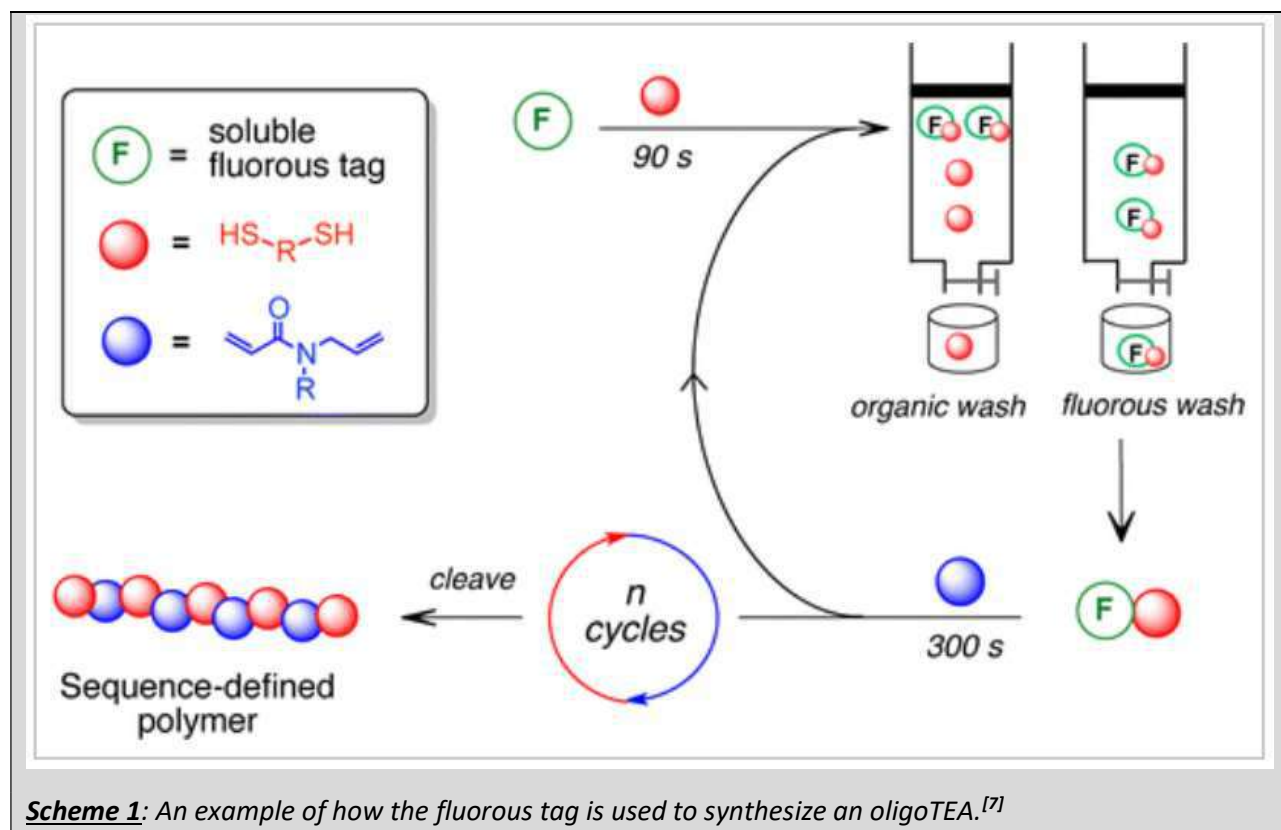
Oligothioetheramides (oligoTEAs) are a new class of oligomers that can be modified to mimic the antibiotic characteristics of antimicrobial peptides. In the synthesis of these oligoTEAs, there are several side products that are generated, which negatively impact the yield of the intended product. Traditionally, purification was performed using fluorous solid phase extraction (FSPE). However, this purification process would decrease the effective yield of oligoTEA synthesis with each successive coupling step – quite notably on the last step. To improve synthesis yield and scalability, a different purification protocol was developed. This new purification protocol utilized sodium hydroxide as the aqueous layer, and dichloromethane (DCM) as the organic layer. Excess 1,3-propanedithiol was deprotonated with NaOH, and successfully removed from the organic layer after a thiol-ene reaction. Excess guanidine monomer was reacted with 3-mercaptopropionic acid (MPA) to form a polar, hydrophilic molecule that would theoretically migrate into the aqueous layer. While the MPA reacted with guanidine monomer, the solution formed an emulsion that could not be removed with brine or sodium bicarbonate. The extraction after the Michael addition will need to be repeated to determine whether the protocol will need to be altered.

## Introduction

Over the past several decades, there have been troubling developments in antibiotic resistance as the lifespan of antibiotic medications are being shortened due to bacteria rapidly evolving to resist such treatments. These challenges are due to several factors, such as insufficient drug discovery by the pharmaceutical industry<sup>[1]</sup>, mismanagement of prescriptions<sup>[2]</sup>, and regulatory concerns<sup>[3]</sup>.

Research into antimicrobial peptides (AMPs) has been one method developed to address antibiotic resistance. AMPs are molecules that are naturally produced by the immune system to combat foreign bacteria<sup>[4]</sup>. While there has been success with AMPs as a new class of antibiotics, there are concerns with regards to proteolytic degradation, serum binding protein sequestration, and cell toxicity<sup>[5]</sup>. However, some such concerns can be addressed by new classes of sequence-defined AMP mimetics such as oligothioetheramides (oligoTEAs).

A critical component of oligoTEA synthesis is a soluble fluorous support (fluorous tag) that is found at the beginning of the peptide. The fluorous tag is a perfluorocarbon alkyl chain that is soluble in many organic solvents, but can be attached to a fluorous solid phase silica column.<sup>[6]</sup> The purpose of the fluorous tag is to be able to separate the synthesized oligomer with a fluorous tag from the excess reactants and catalysts during an extraction.



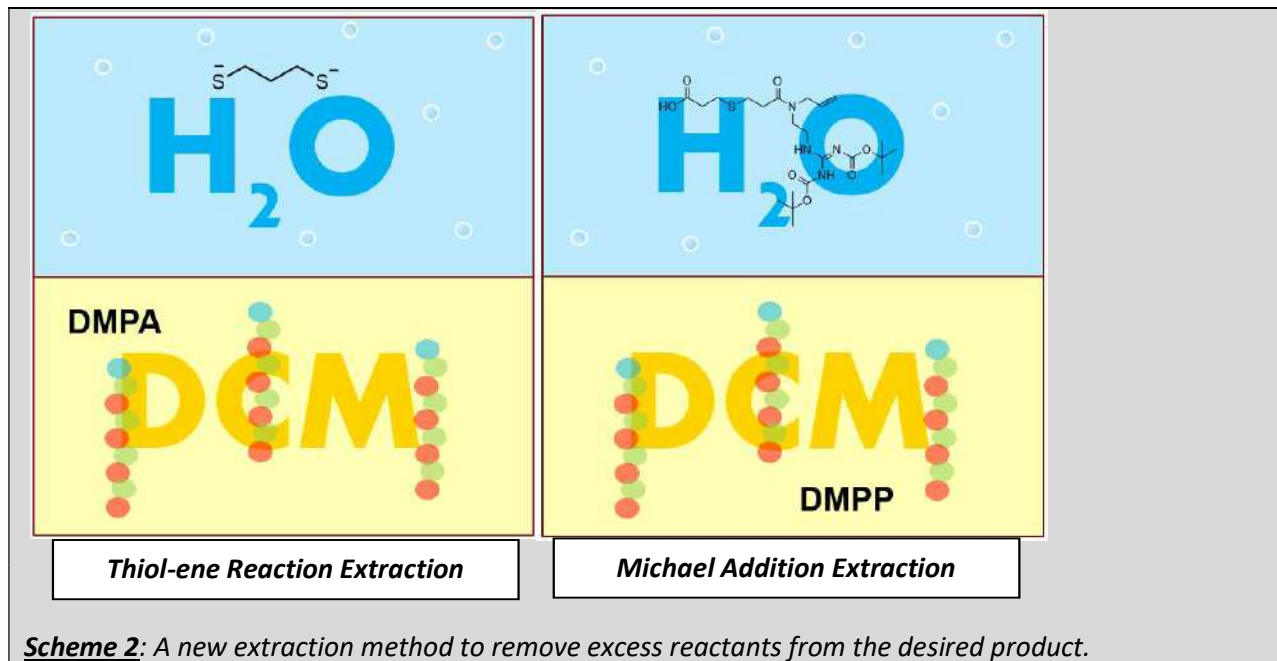
**Scheme 1:** An example of how the fluorous tag is used to synthesize an oligoTEA.<sup>[7]</sup>

The oligomer with a fluorous tag will remain attached to the fluorous solid phase silica column on the fluorous stationary phase while everything else will be washed away during the purification process. The oligomer with a fluorous tag can then be removed from the fluorous silica stationary phase with a different eluent protocol after all undesired organic materials are washed away. The key advantages of performing FSPE involve “homogenous reaction conditions, fast solution phase kinetics, and reaction monitoring via common spectroscopic techniques”.<sup>[6]</sup>

While there are benefits of using a fluorous tag support to demonstrate a proof-of-concept design for oligoTEAs, its advantages do not lend well when attempting to scale up synthesis. Common issues include low yields over multiple purification steps, long purification times per step, lack of scalability beyond the size of the column, and time spent removing water and methanol from the product (water is known to interfere with the coupling of dithiol monomers). Additionally, there would significant cost savings due to no longer needing to use a fluorous tag, which is priced at \$80 per 2 g.

An alternative solution to using a fluorous tag support is performing liquid-liquid phase extractions. This addresses the limitations of solid fluorous phase extraction by shortening the duration of each purification step, increasing the scalability, and reducing the time to remove solvents after purification. While the oligomer would remain in the DCM organic layer, the excess reactants would be separated into the aqueous layer. Using a basic aqueous solution such as NaOH would deprotonate the dithiol used in the thiol-ene reaction, allowing it to move into the aqueous layer. After the Michael addition, the excess guanidine monomer would be

recreated with a highly polar thiol, forming a molecule that would migrate into the aqueous layer as well.



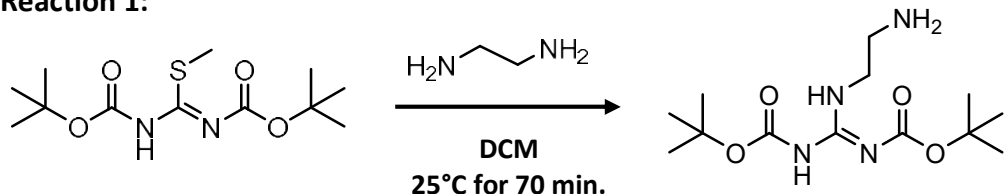
## Methods

### Synthesis of the Fluorous BOC-Protected Allyl Amine

One equivalency of fluororous BOC-ON (with a perfluorocarbon alkyl chain of C<sub>8</sub>F<sub>17</sub>), 1.6 equivalents of allyl amine, and 2.5 equivalents of triethylamine were combined in 10 mL of tetrahydrofuran (THF). The solution was stirred at room temperature overnight. Solvent was removed at reduced pressure. The product was dissolved in methanol, purified using fluororous solid phase extraction, and then verified using nuclear magnetic resonance (NMR)

### Synthesis of Guanidine Monomer

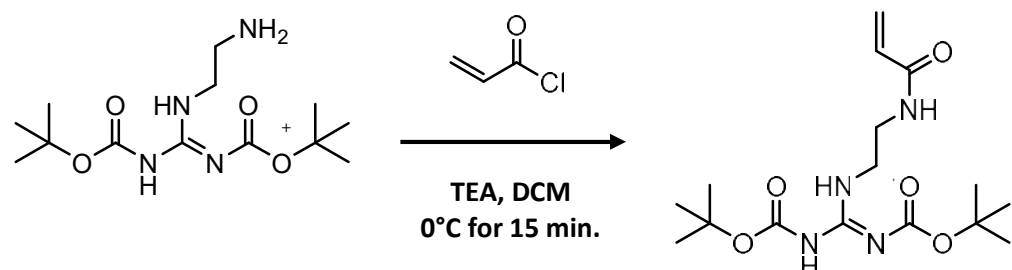
#### Reaction 1:



One equivalency of 1,3-Di-boc-2-methylisothiourea was combined with 2.5 equivalents of ethylenediamine in DCM to form a concentration of 250 mM for 1,3-Di-boc-2-methylisothiourea. This solution was stirred at 25°C for 70 minutes. The organic solution was purified using liquid-liquid phase extraction – it was washed 3x with water, 1x with brine, and

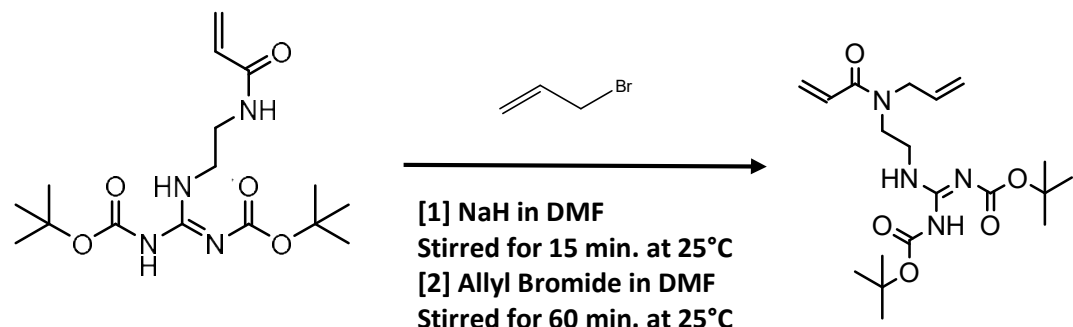
excess water was removed with anhydrous sodium sulfate. DCM was removed using a rotary evaporator.

**Reaction 2:**



The product from **Reaction 1** was solubilized with DCM to create a reaction concentration of 150 mM, and 1.5 equivalents of triethylamine (“TEA”) was added. The reaction was stirred at 0°C for 15 minutes, and then 1.5 equivalents of acryloyl chloride solubilized in 3 mL DCM was added dropwise into the reaction at 0°C for 20 minutes. The reaction was stirred at 0°C for 60 minutes, and then stirred at 25°C for 60 minutes. The reaction was then quenched with water. The solution was purified using liquid-liquid phase extraction – it was extracted 3x with DCM, and the combined organic layers were washed 1x with brine and dried with anhydrous sodium sulfate. The remaining DCM in the organic layer was removed by rotary evaporator to yield the desired product.

**Reaction 3:**



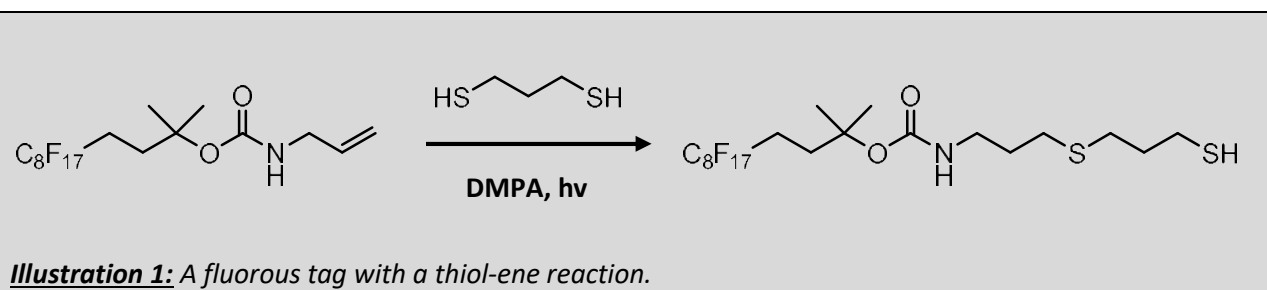
The product from **Reaction 2** was weighed to determine how much dry dimethylformamide (“DMF”) would be needed to create a reaction concentration of 200 mM. One-third of the required DMF was used to solubilize 4 equivalents of sodium hydride (“NaH”). Another one-third of the required DMF was used to solubilize the product from **Reaction 2**. The solubilized NaH was added to the solubilized product from **Reaction 2** and stirred at 25°C for 15 minutes. The remaining one-third of required DMF was used to solubilize 2.5 equivalents of allyl bromide, which was added dropwise at 25°C for 10 minutes. The reaction mixture was stirred at 25°C for 60 minutes, and then quenched with water. The solution was purified using liquid-liquid phase extraction – it was extracted 3x with diethyl ether, and the combined ether layers

were washed 1x with brine and dried with anhydrous sodium sulfate. The remaining diethyl ether in the organic layer was removed by rotary evaporator. The final product, guanidine monomer, was purified using silica column flash chromatography on a gradient of 0-100% ethyl acetate in hexanes.

### *Synthesis and Purification of OligoTEAs*

The synthesis of oligoTEAs was performed by subsequent thiol-ene reactions and Michael additions on a fluorous tag. The product was purified by extraction after each reaction. The synthesis of oligoTEAs was performed on a 10 – 30 mg scale of fluorous tag.

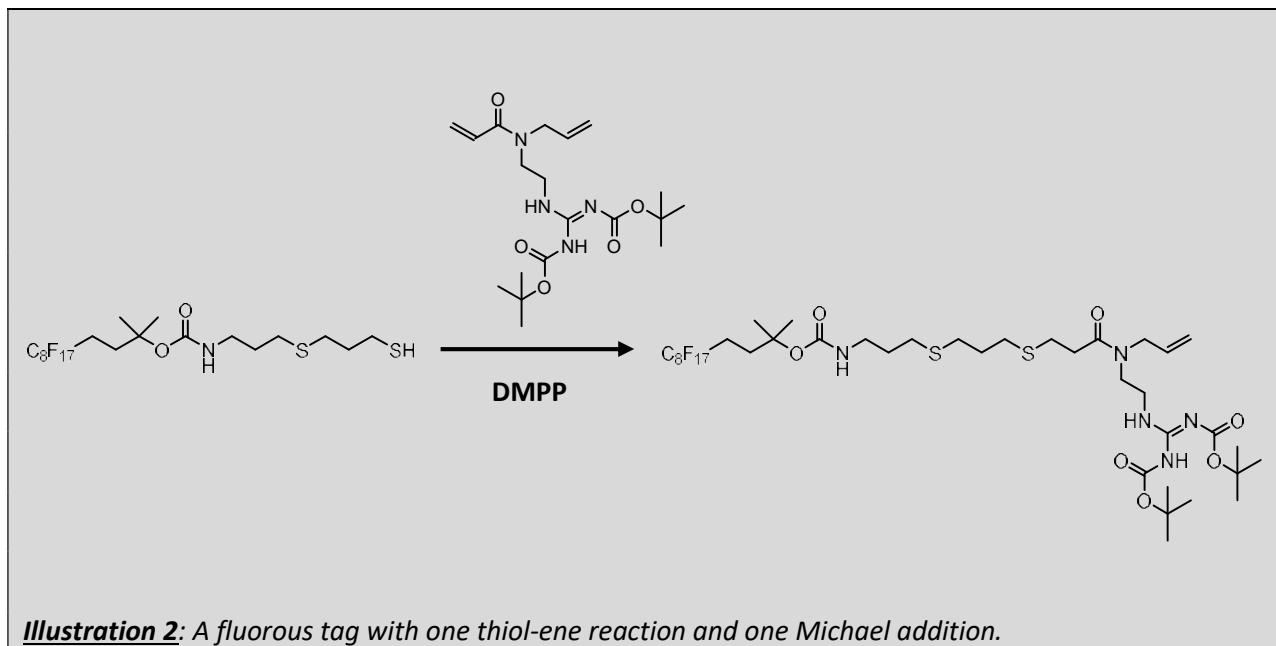
**Thiol-ene Reaction:** One equivalency of fluorous tag was solubilized in methanol (“MeOH”) so that the reaction concentration would be 150 mM. Then, 5 equivalents of 1,3-propanedithiol (“PDT”) and 0.25 equivalents of 2,2-dimethoxy-2-phenylacetophenone (“DMPA”) were added. The reaction was then exposed to three 90-second intervals of ultraviolet light. This created a fluorous tag with a dithiol attached (“FT-T1”).



**Purification After Thiol-ene Reaction:** The FT-T1 product was dried down to remove MeOH, and it was resolubilized in 1 mL DCM. The excess PDT would need to be deprotonated by a base so that the negatively charged excess PDT would move into the aqueous layer. Based upon troubleshooting, the ideal extraction would involve a 1:1 equivalency of 100 mM NaOH to DCM. Thin layer chromatography (“TLC”) was utilized to readily identify whether was a significant amount of PDT remaining in the organic layer. The mobile phase was 100% MeOH, and potassium permanganate was used as the staining agent. Given the relative polarity of the fluorous tag and guanidine monomer as compared to PDT, identification of each component on a stained TLC plate using 100% MeOH were the best parameters ([Figure 4\[A\]](#)). Solvents such as hexane, ethyl acetate, and DCM kept the comparison of fluorous tag, PDT, and product dots close together with not enough separation to discern whether the product contained PDT ([Figure 4\[B\]](#)).

**Michael Addition Reaction:** The thiol-ene reaction was assumed to yield 100% of the theoretical product – This became the new basis for equivalency. Two equivalents of guanidine

monomer and 0.1 equivalents of dimethylphenylphosphine (DMPP) were added to the thiol-ene reaction product and solubilized in methanol to have a reaction concentration of 100 mM. The reaction was stirred at 40°C for one hour. The completion of the Michael addition reaction was confirmed via a 2,2'-dithiodipyridine (DTDP) assay. The DTDP assay measures the extent to which there are primary thiols in a sample. The DTDP assay was performed using 150 µL of 0.1% TEA in dimethyl sulfoxide, 2.5 µL of 12 mM 2,2'-Dithiodipyridine in DMSO, and 1 µL of the sample or blank was combined and mixed for 5 minutes. The blank was MeOH. Next, 5 µL of glacial acetic acid was added to both the sample and blank, and mixed for 5 minutes. Finally, a DTDP assay was performed. The resulting product was a fluorous tag with both one thiol-ene reaction and one Michael Addition reaction ("FT-T1M1").



**Purification after Michael Addition Reaction:** The Michael Addition reaction was dried down to remove MeOH and resolubilized in 1 mL DCM. To remove the excess guanidine monomer, the solution was reacted with 3-mercaptopropionic acid ("MPA") so that the combined product MPA and guanidine monomer ("MPA-GM") would be a hydrophilic molecule that would move into the aqueous phase. Since there was still DMPP catalyst in the product solution, the MPA and guanidine monomer would undergo a Michael Addition reaction as well.

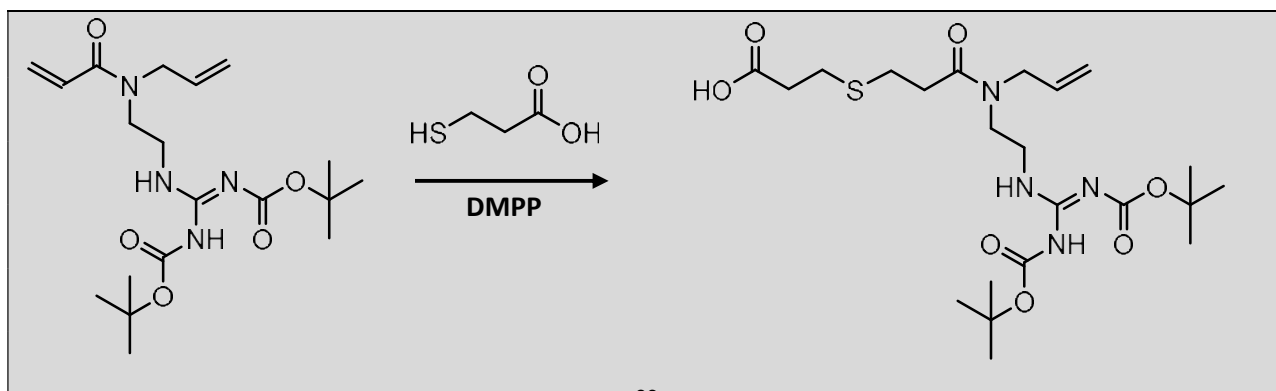
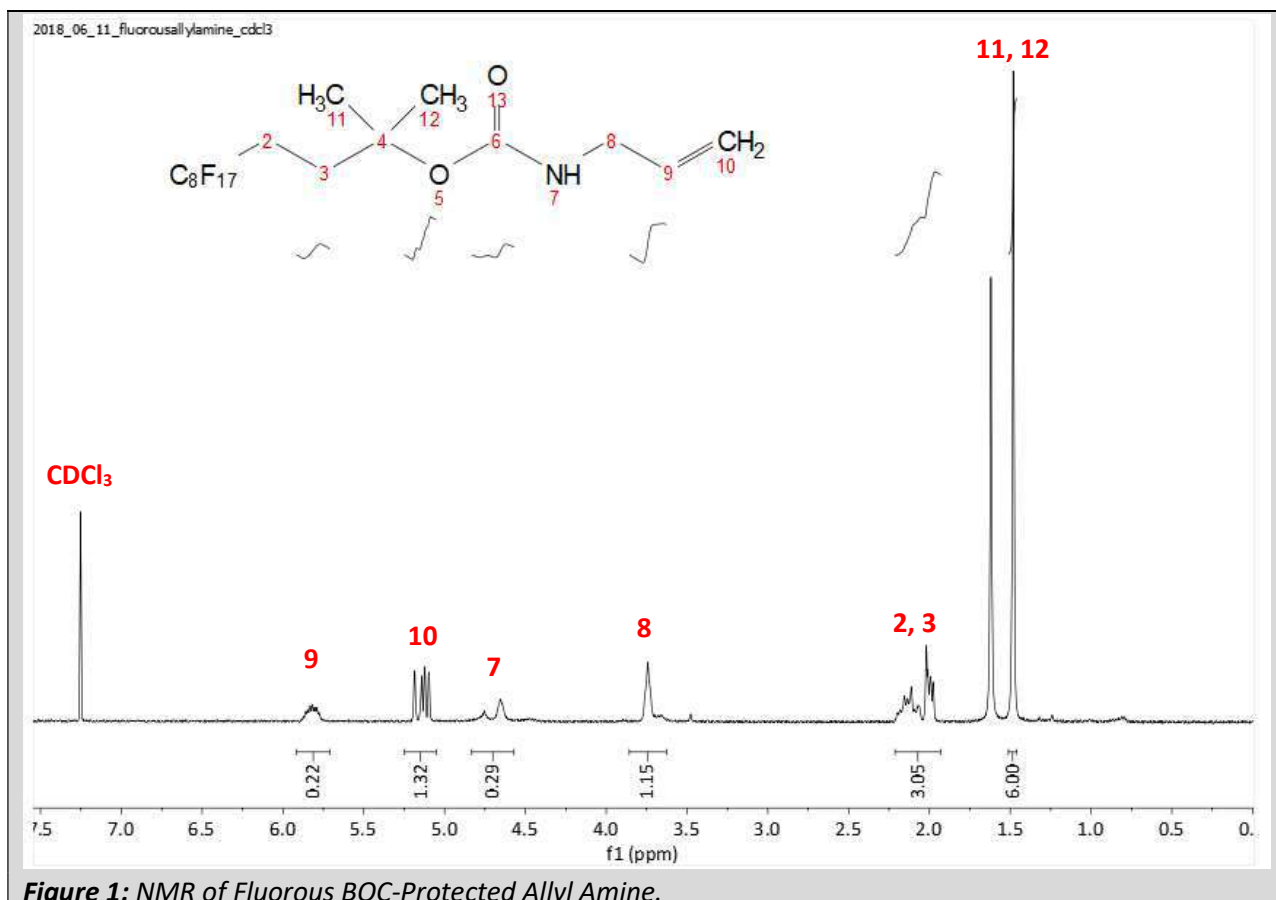


**Illustration 3:** Reacting guanidine monomer with MPA to form a hydrophilic molecule.

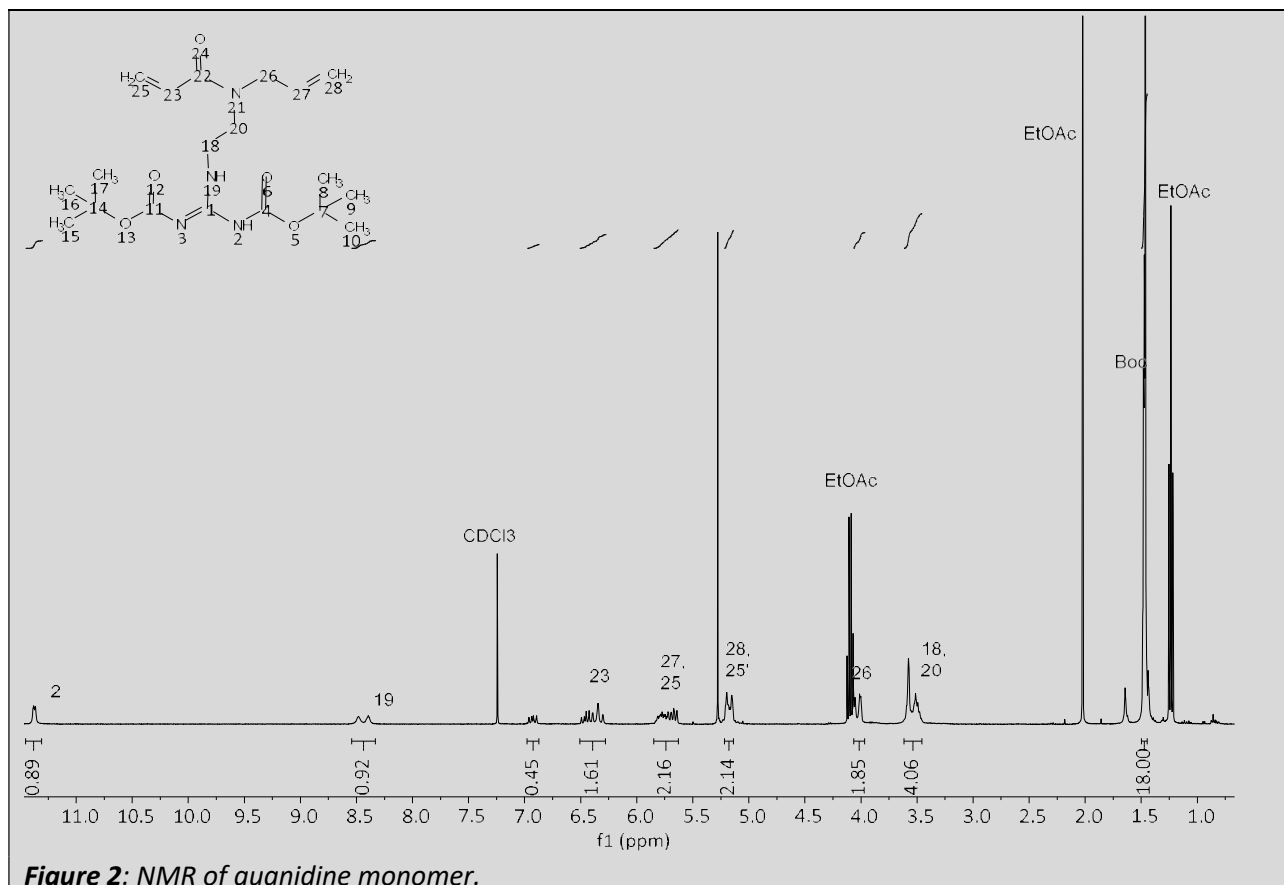
## Results / Discussion

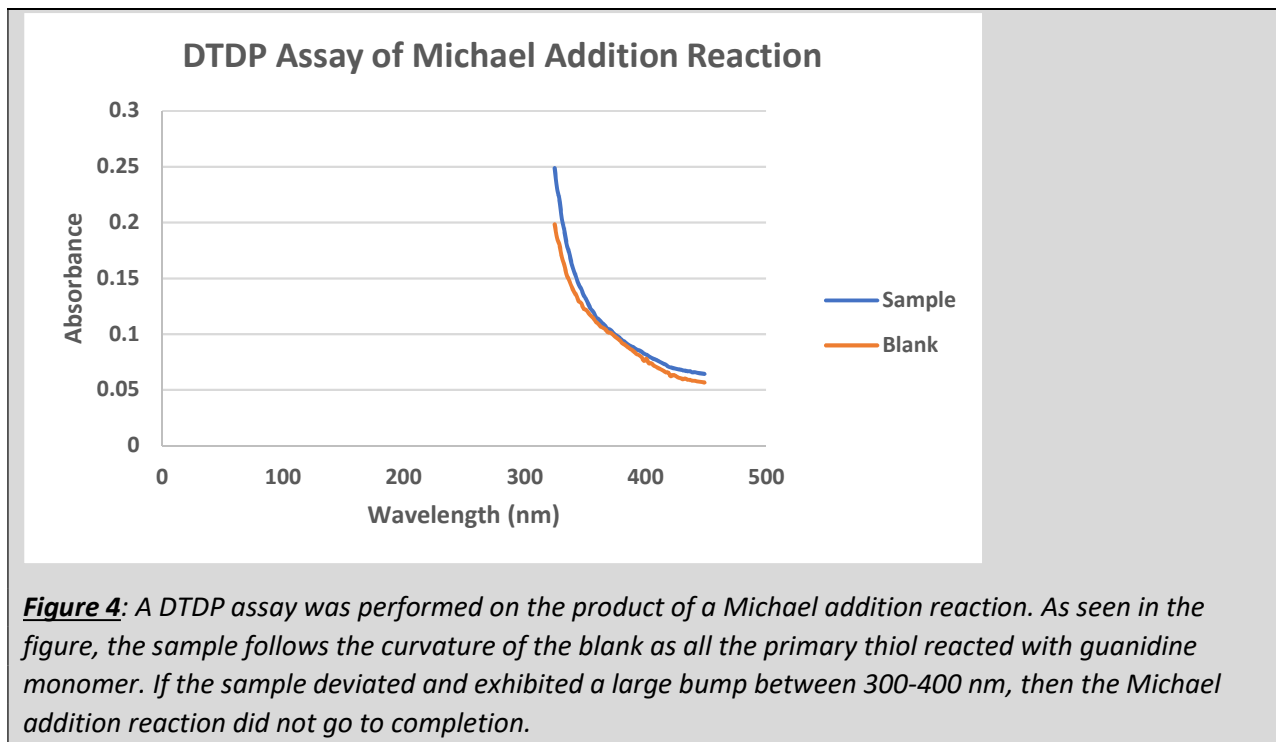
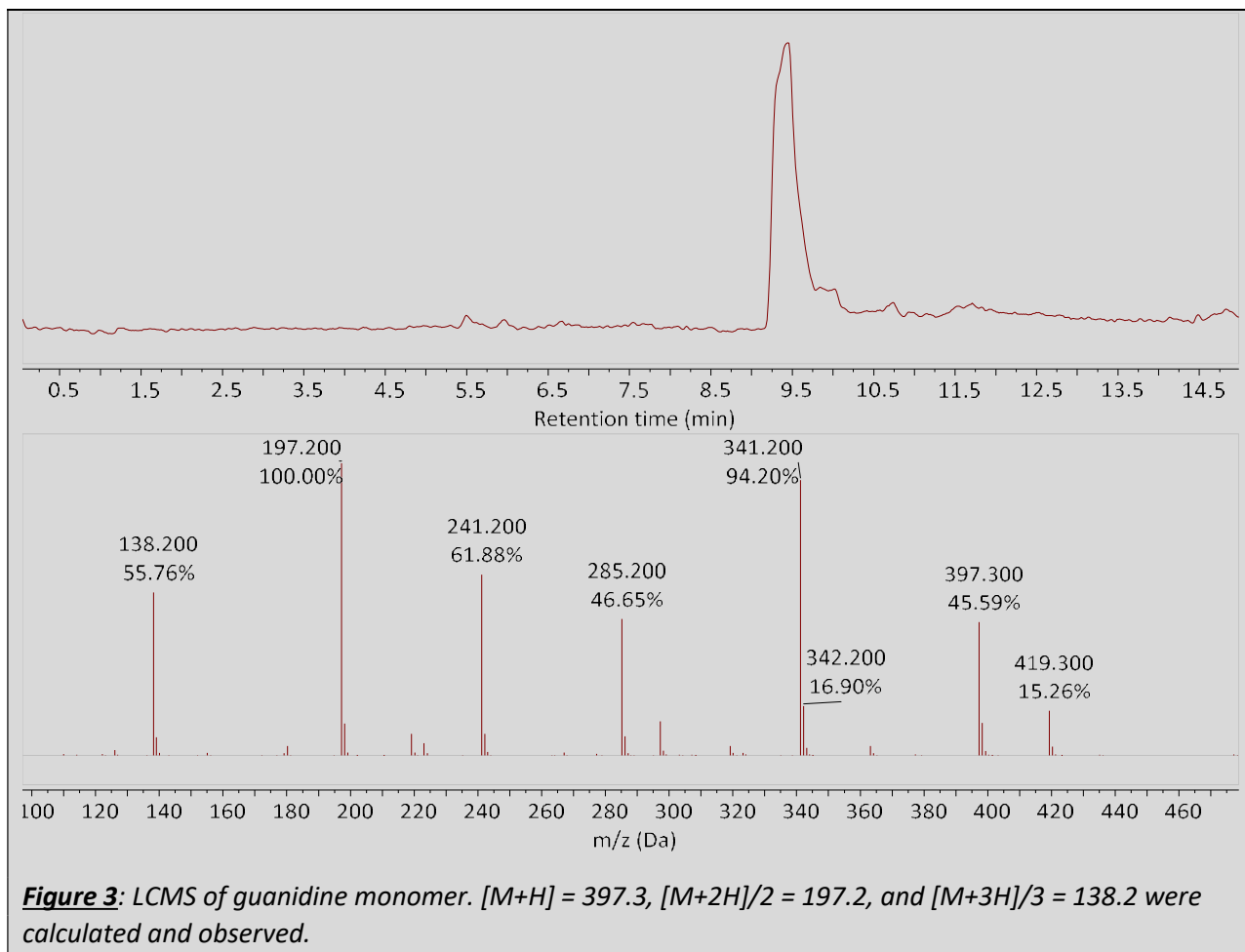
### Reactant and OligoTEA Synthesis

The fluorous tag was synthesized and verified via nuclear magnetic resonance (NMR) ([Figure 1](#)). Guanidine monomer was synthesized and verified using NMR ([Figure 2](#)) and Liquid Chromatography - Mass Spectrometry (“LCMS”) ([Figure 3](#)). A thiol-ene reaction and Michael addition were performed, respectively, to a fluorous tag. The completion of the Michael addition was verified using a DTDP assay ([Figure 4](#)).



**Figure 1:** NMR of Fluorous BOC-Protected Allyl Amine.





### *Extraction after Thiol-ene Reaction*

After five washes at a lower concentration of 10 mM NaOH, a distinguishable amount of PDT remained in the organic layer (**Figure 4[C]**). After two washes of 100 mM NaOH, thin layer chromatography showed that there was no remaining PDT in the organic layer (**Figure 4[D]**). For extractions performed onward, five washes with 100 mM NaOH were used to ensure the complete removal of PDT from the organic layer.

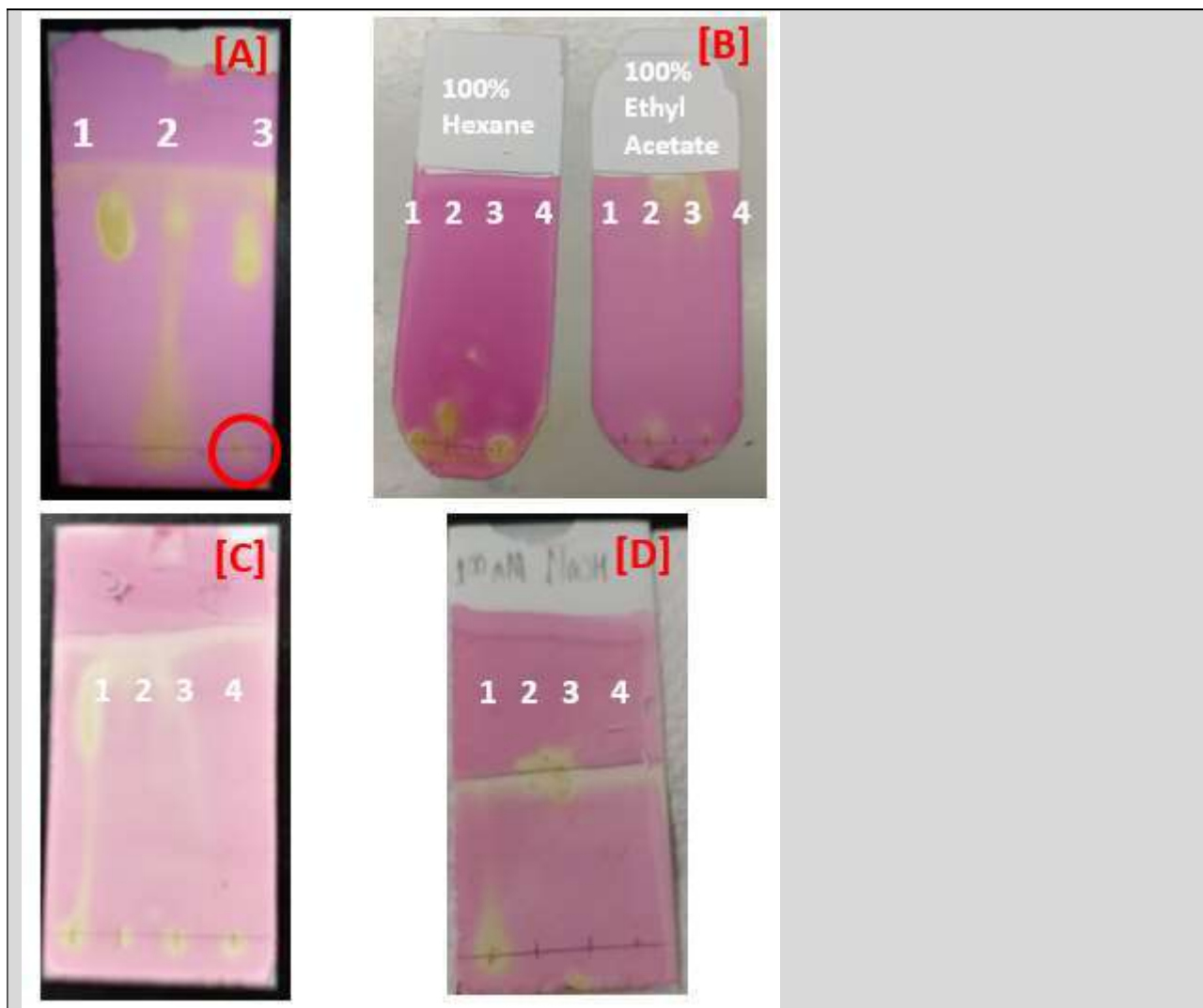


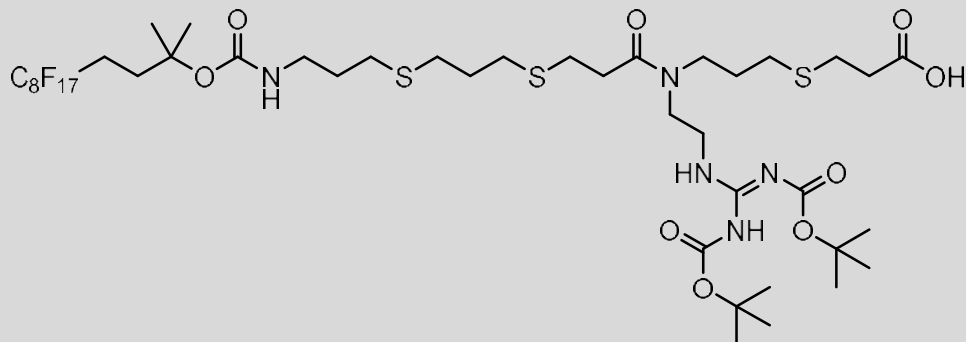
**Figure 4:** Fluorous tag spots were dabbed three times with a 10 mg per 10 mL stock solution. PDT spots were dabbed one time with a 0.1 mg per 10 mL stock solution. DMPA spots were dabbed three times with a 10 mg per 10 mL stock solution. FT-T1 spots, unless otherwise noted, were dabbed three times. **[A]:** TLC was performed on an organic layer after five washes of 100 mM NaOH. 1 is fluorous tag, 2 is PDT, and 3 is FT-T1. Excess PDT exhibits a conspicuously large streak that extends the length of the mobile phase, allowing for a straightforward identification of its presence. The FT-T1 dot on 3 was dabbed 10 times to see if there was any remaining PDT in the product, which can be observed at the beginning of the mobile phase as circled in red. **[B]:** TLC was performed on a purified thiol-ene reaction using fluorous solid phase extraction. 1 is fluorous tag, 2 is PDT, 3 is DMPA, and 4 is FT-T1. The left TLC plate was made using 100% hexane as the mobile phase, and the right TLC plate was made using 100% ethyl acetate as the mobile phase. In both cases, there was not enough vertical separation between each

*dot when compared side-by-side. [C]: TLC was performed on an organic layer of a thiol-ene reaction with 10 mM NaOH. 1 is the product before any washes, 2 is the product after one wash, 3 is the product after three washes, and 4 is the product after five washes. Each dot was dabbed three times. PDT remained after five washes, so the aqueous layer was replaced with 100 mM NaOH. [D]: TLC was performed on an organic layer of a thiol-ene reaction with 100 mM NaOH. 1 is the product after one wash, 2 is the product after two washes, 3 is the product after three washes, and 4 is the product after four washes. Each dot was dabbed three times. There was no noticeable amount of PDT at the beginning of the mobile phase after two washes, but five washes were performed for the reactions to ensure that all PDT was removed.*

#### *Extraction after Michael Addition*

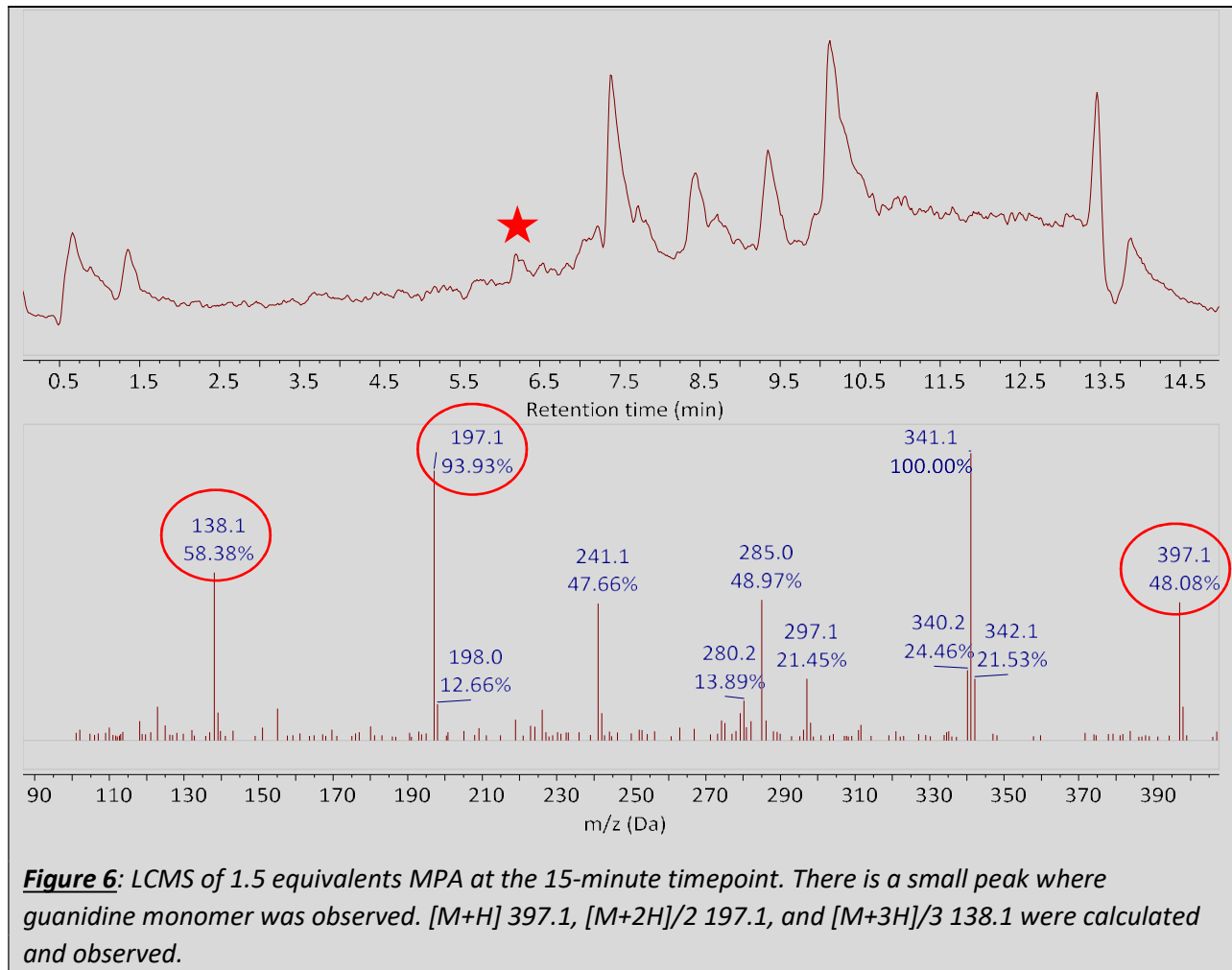
A kinetics study was done using 1, 1.5, 2, and 4 equivalencies of MPA relative to unreacted guanidine monomer, and samples were analyzed using LCMS at timepoints 0, 15, 30, 45, 60, 75, and 90 minutes. This was performed to identify the ideal amount of MPA to react with all the unreacted guanidine monomer from the Michael addition.

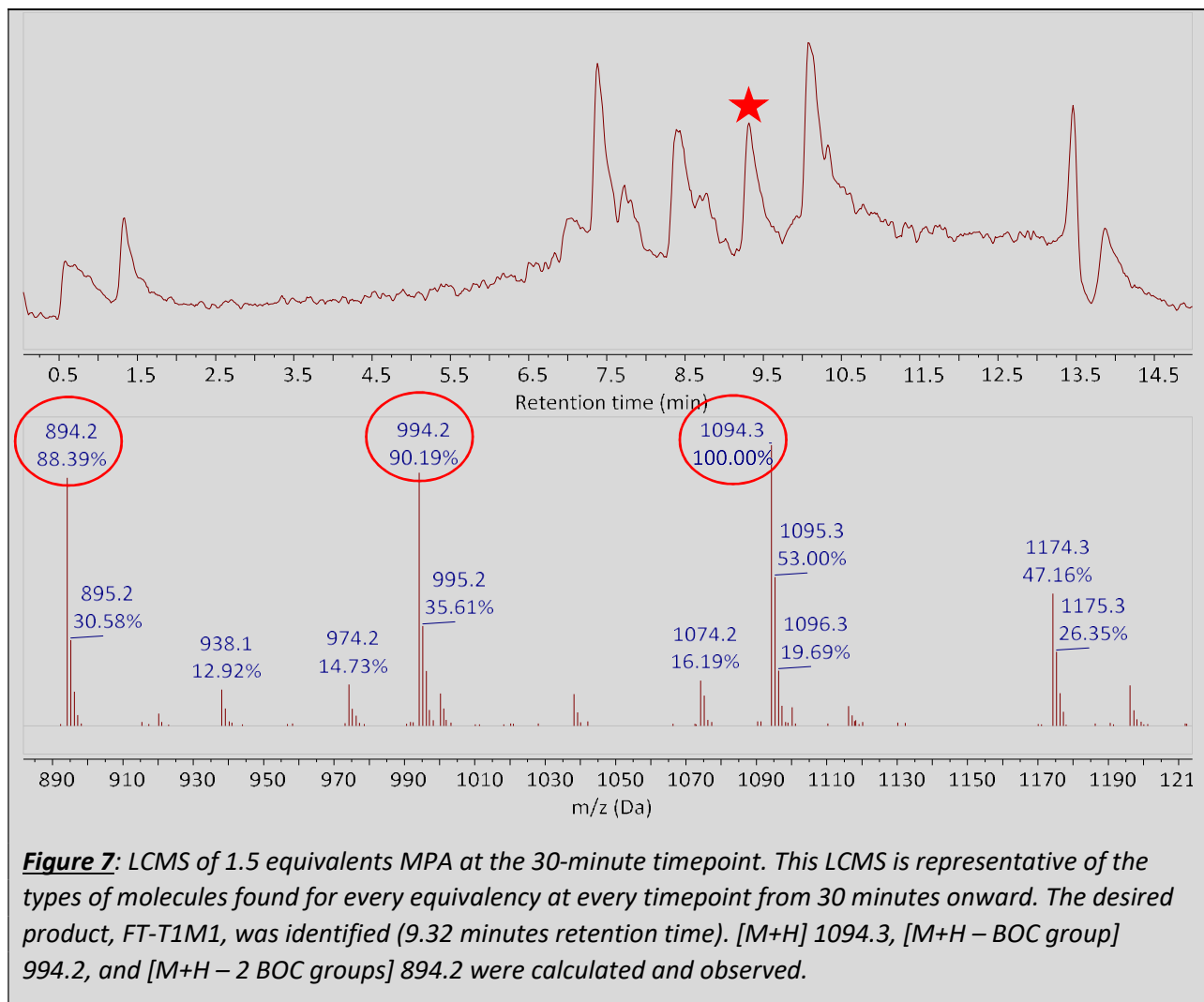
There were two goals that this reaction needed to accomplish: [1] React all the excess guanidine monomer with MPA so that there is no remaining unreacted guanidine monomer in solution; and [2] ensure that the conditions of the reaction do not allow the MPA to react with FT-T1M1 so that the oligomer is “capped” with MPA on the product’s allyl group of the guanidine monomer – This would terminate the oligomer’s ability to grow.

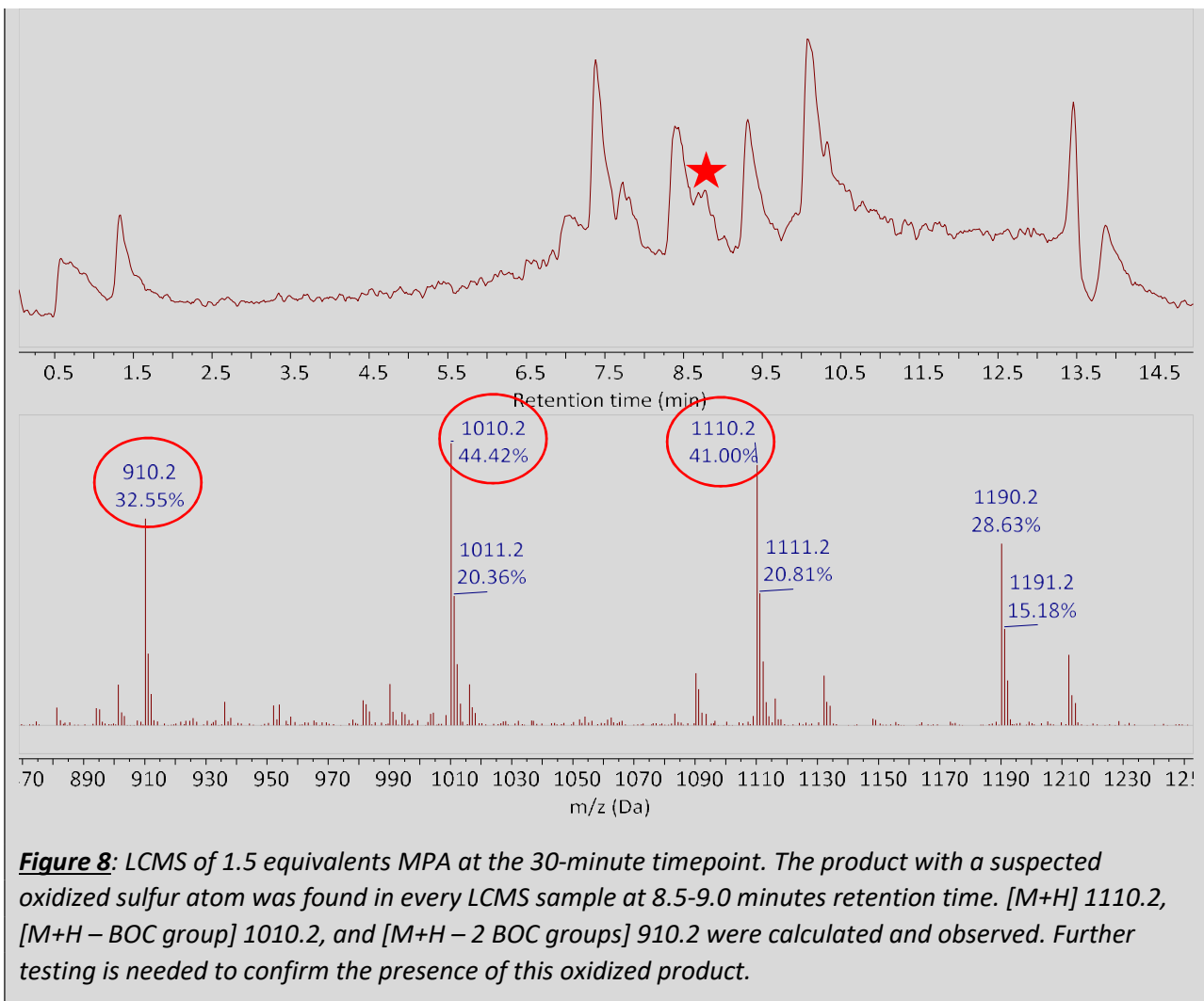


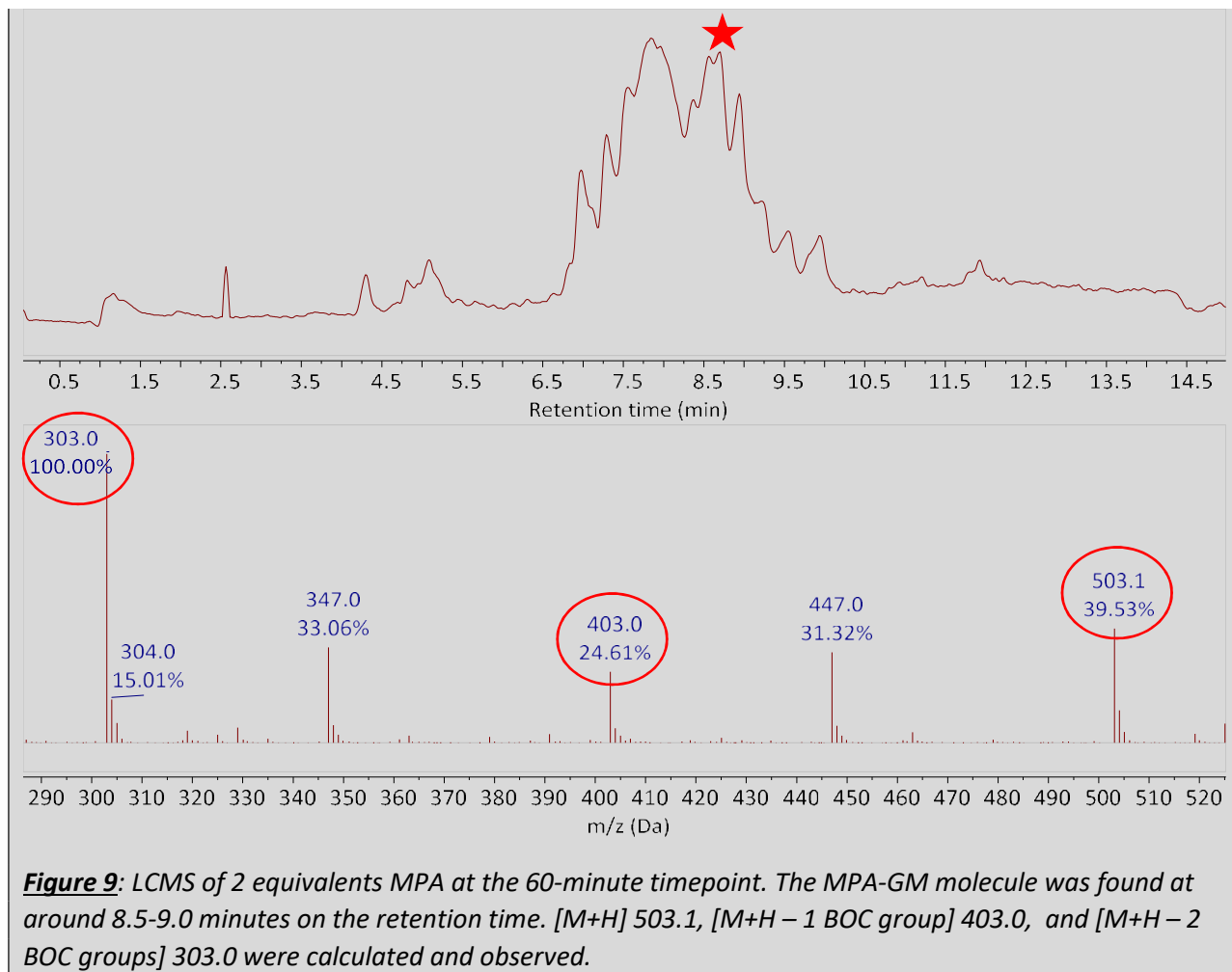
**Illustration 4:** The FT-T1M1 product that reacted with MPA, disabling its ability to grow.

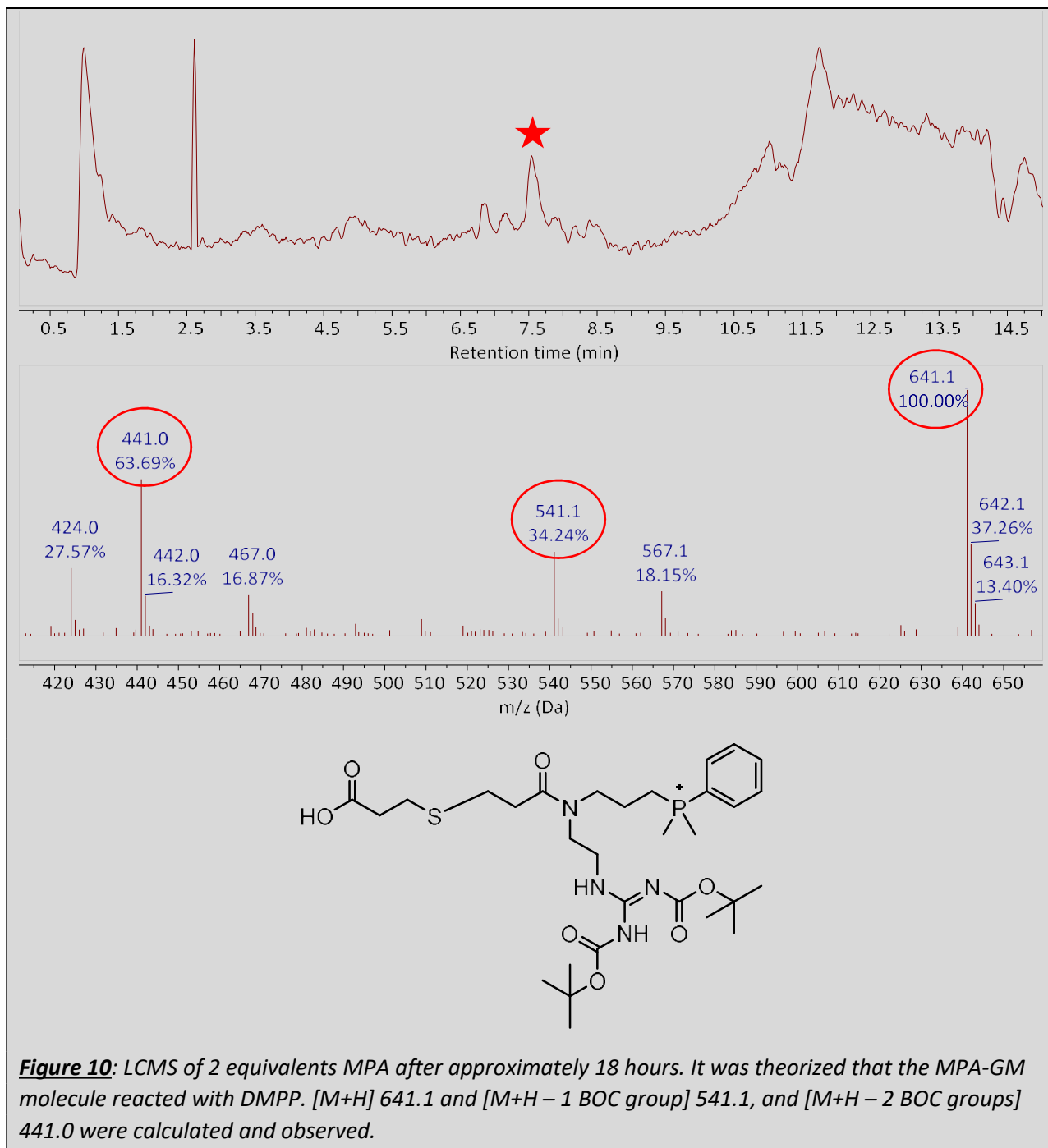
Guanidine monomer was not detected by LCMS analyses after the 30-minute time interval for all conditions tested. At the 15-minute mark for each equivalency, a small peak indicated the presence of guanidine monomer ([Figure 6](#)). None of the equivalencies at any timepoint yielded a “capped” FT-T1M1 product with MPA attached to the allyl group of the guanidine monomer at the end of the oligomer. The desired FT-T1M1 product was observed and confirmed with LCMS at all timepoints ([Figure 7](#)). However, there was another product created with a mass of 1100.3, which is suspected to be the FT-T1M1 product with one of its sulfur atom oxidized ([Figure 8](#)). The MPA-GM molecule was observed and identified as well ([Figure 9](#)). Additionally, it was noted that if the reaction went on for too long, DMPP would react with the MPA-GM molecule as well ([Figure 10](#)).







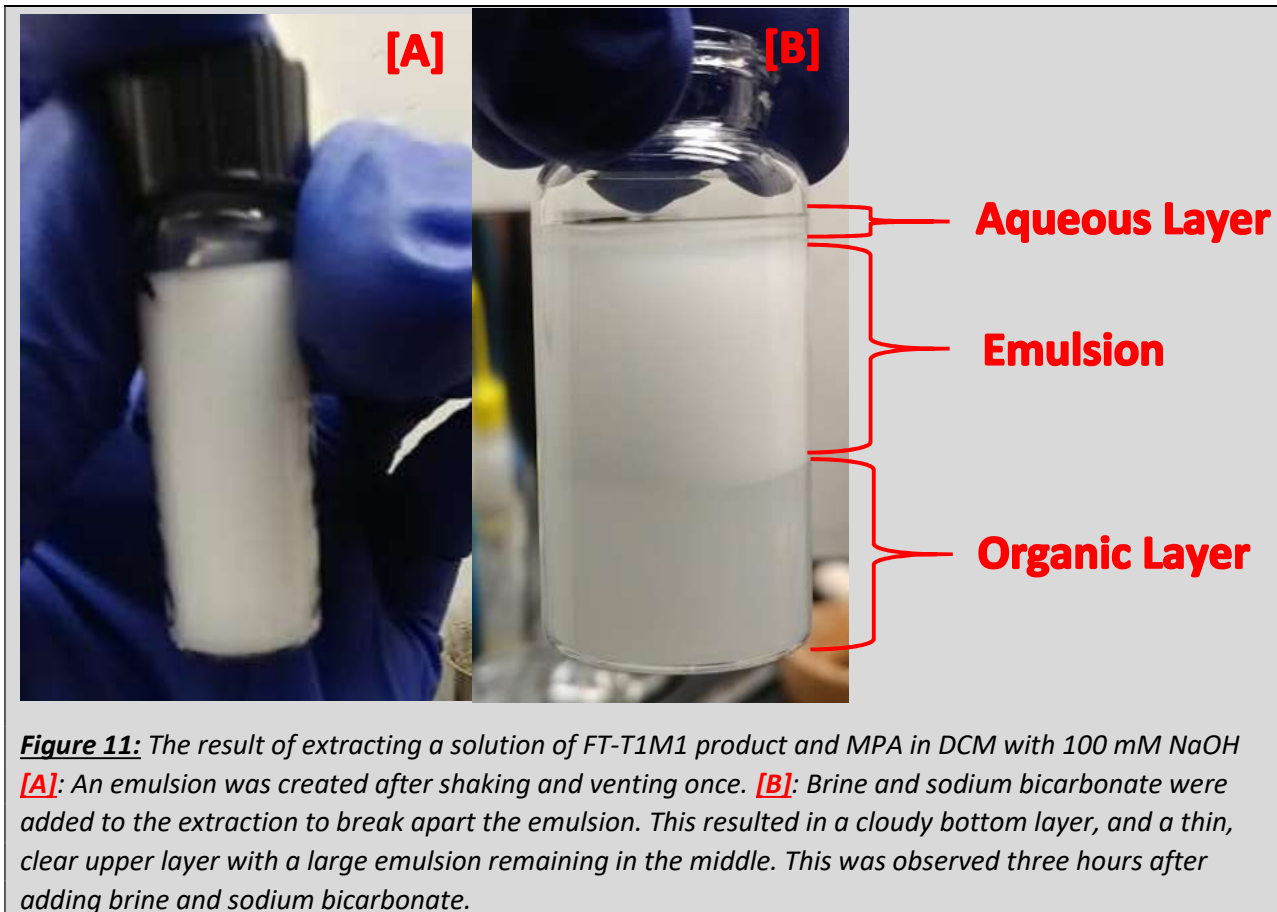




Based upon troubleshooting different equivalencies of MPA compared to unreacted guanidine monomer and different reaction times, the ideal conditions were 2 equivalents of MPA with a minimum reaction time of 30 minutes.

The FT-T1M1 product was reacted with 2 equivalents of MPA to unreacted guanidine monomer and heated to 40°C for 60 minutes. The product was dried down to remove MeOH, and resolubilized in 1mL DCM. Next, an equivalent volume of 100 mM NaOH was used to extract the MPA-GM molecule. Once the solution settled after being shaken, it formed an emulsion

([Figure 11\[A\]](#)). Brine and sodium bicarbonate were added to remove the emulsion, but the emulsion remained ([Figure 11\[B\]](#)).



MPA is well documented in literature as being a stabilizer for nanoparticles<sup>[8]</sup>, surfactants<sup>[9]</sup>, and colloids<sup>[10]</sup>. Attempts to remove the emulsion have yielded modest results ([Figure 11\[B\]](#)).

### Conclusion / Future Work

The extraction of excess PDT from the product after the thiol-ene reaction was a success. Even though it was documented that two washes of 100 mM NaOH removed a majority of the PDT, five washes were performed to ensure that all excess PDT was removed. Furthermore, TLC was successfully used to identify whether the product still contained PDT. It was a straightforward procedure that can be performed immediately after the extraction of a thiol-ene reaction, and can assist in qualitatively assessing the product after each extraction wash. There was notable time savings when using a liquid-liquid extraction method with TLC as compared to a traditionally lengthy FSPE. When PDT remained in the solution when the Michael addition was performed, the guanidine monomer would react with the excess PDT instead of the desired FT-T1 reagent – This would severely limit the growth of the oligomer, and additional amounts of guanidine monomer would need to be used.

The extraction of excess guanidine monomer from the product after the Michael addition needed further test work. LCMS was used to verify that the guanidine monomer would react with MPA, creating a molecule that could be extracted through an aqueous layer. Moreover, the desired product, FT-T1M1, was found in the solution with no remaining guanidine monomer. Also, at no point was a “capped” FT-T1M1 product with MPA found at any equivalency or at any time point. The only notable side product was DMPP reacting with the MPA-GM molecule.

Additional test work would need to be performed to see if the emulsion would be formed again following the same protocol. If the emulsion forms again, possible solutions include centrifuging the solution at a high enough speed to break apart the emulsion, use a less polar thiol molecule than MPA, gently shake the extraction, or try different solvents for the organic layer, such as diethyl ether or methanol.

The protocol for extraction after the Michael addition will need to be retested and resolved before continuing with the synthesis process of oligoTEAs. Questions remain as to how feasible the extraction will be once the oligomer is longer, and whether the growing amount of DMPA and DMPP in the solution will create any byproducts. Further advances in the extraction process may need to include more definitive ways of removing these catalysts as they could cause unforeseen reactions.

## References

- [1] Piddock LJ. The crisis of no new antibiotics—what is the way forward? *Lancet Infect Dis.* 2012;12(3):249–253. <https://www.ncbi.nlm.nih.gov/pubmed/22101066>
- [2] The antibiotic alarm. *Nature.* 2013;495(7440):141. <https://www.ncbi.nlm.nih.gov/pubmed/23495392>
- [3] Centers for Disease Control and Prevention, Office of Infectious Disease Antibiotic resistance threats in the United States, 2013. Apr, 2013. Available at: <http://www.cdc.gov/drugresistance/threat-report-2013>. Accessed August 3, 2018.
- [4] Van't Hof, W., Veerman, E. C., Helmerhorst, E. J., and Amerongen, A. V. (2001) Antimicrobial peptides: properties and applicability. *Biol. Chem.* 382, 597– 619. <https://www.degruyter.com/view/j/bchm.2001.382.issue-4/bc.2001.072/bc.2001.072.xml>
- [5] Hancock, R. E. W. and Sahl, H.-G. (2006) Antimicrobial and host-defense peptides as new anti-infective therapeutic strategies. *Nat. Biotechnol.* 24, 1551– 1557. <https://www.nature.com/articles/nbt1267>
- [6] Matsugi, M.; Curran, D. P. (2004) Reverse Fluorous Solid-Phase Extraction: A New Technique for Rapid Separation of Fluorous Compounds. *Org. Lett.*, 6, 2717. <https://pubs.acs.org/doi/10.1021/o1049040o>
- [7] Porel, M. and Alabi, C. A. (2014) Sequence-Defined Polymers via Orthogonal Allyl Acrylamide Building Blocks. *J. Am. Chem. Soc.* 136, 13162– 13165. <https://pubs.acs.org/doi/10.1021/ja507262t>
- [8] H. Kaczmarek, M. Metzler, K. Wegrzynowska-Drzymalska. (2016) Effect of stabilizer type on the physicochemical properties of poly(acrylic acid)/silver nanocomposites for biomedical applications. *Polym. Bull.*, 73, pp. 2927-2945. <https://link.springer.com/article/10.1007%2Fs00289-016-1617-3>
- [9] Jiménez-Hernández, L & Estévez Hernández, Osvaldo & Hernández, Mayra & Diaz, Jesus & Farías- Sánchez, M & Reguera, E. (2015). 3-mercaptopropionic acid surface modification of Cu-doped ZnO nanoparticles: Their properties and peroxidase conjugation. *Colloids and Surfaces A: Physicochemical and Engineering Aspects.* 489. <https://www.sciencedirect.com/science/article/pii/S0927775715303332?via%3Dihub>
- [10] Marcos Marques da Silva Paula, Helton Jeremias de Souza, Carina Búrigo, Jamile Thön Langbehn, Alice Scarabelot Baesso, Luciano da Silva, Paulo Roberto Paes da Silva, Roberto Benavides, Gabriel Alonso-Núñez, Virginia Collins. (2017) Evaluation of the permeability of silver nanoparticles in polymer films of sulfonated polystyrene-co-acrylic acid. *Colloids and Surfaces A: Physicochemical and Engineering Aspects*, Volume 520, Pages 78-84. <http://www.sciencedirect.com/science/article/pii/S0927775717300961>

# Synthesis of Block Copolymer with Mixed Electronic-Ionic Conductivity

Meg Tetzloff<sup>1,2</sup>, Ziwei Liu<sup>2</sup>, Christopher Ober<sup>2</sup>

<sup>1</sup>Department of Chemical Engineering, Michigan Technological University, Houghton, MI

<sup>2</sup>Department of Materials Science and Engineering, Cornell University, Ithaca, NY

**ABSTRACT:** Copolymers with blocks that exhibit electronic and ionic conductivity have been discovered to be useful for energy harvesting storage, such as in batteries, sensor, etc. However, the current conductivities exhibited by these organic batteries do not rival those of standard batteries. This project has explored the effect of linking various lengths of the ionically conductive poly(di(ethylene glycol) methyl ether methacrylate) homopolymer to a fixed length electronically conductive poly(3-hexylthiophene) homopolymer to determine the optimal ratio between blocks for self-assembly and highest conductivity.

## I. INTRODUCTION

Linking immiscible well-defined polymer blocks with covalent bonds to simultaneously utilize the properties of each block is useful in developing highly engineered materials. A benefit of block copolymers with immiscible blocks is their ability to self-assemble into phase-separated morphologies, so that the blocks align and do not hinder the properties of the other block.<sup>1</sup>

The conjugated regioregular polymer poly(3-hexylthiophene) (P3HT) is an electrically conductive material has been the subject of significant research in recent years due to its use as a flexible organic semiconductor, with current applications including organic photovoltaic cells, light-emitting diodes, and field-effect transistors.<sup>2,3</sup>

Polymers with a high density of ethylene oxide have been found to be ionically conductive.<sup>4</sup> The polymer poly(di(ethylene glycol) methyl ether methacrylate) (PDEOMEMA) is one such molecule that can be synthesized with a good control of

molecular weight and polydispersity using atom transfer radical polymerization (ATRP).<sup>5</sup>

By combining the electronically conductive properties of P3HT with the ionically conductive PDEOMEMA, a block copolymer can be formed that is useful in batteries, which require both of these properties. While a typical battery contains an electrolyte for ion transport and electrodes for electronic conduction, an ordered block copolymer can serve both these functions in a single material that is low-cost, lightweight, and flexible.<sup>6</sup>

The goal of this project is to link a fixed-length P3HT block (with a molecular weight of 8,000) to a variable-length PDEOMEMA block with “click” chemistry in order to optimize the ratio of electronic conductivity to ionic conductivity. This will allow the development of organic batteries with higher conductivities. Creating a PDEOMEMA block with a polydispersity index (PDI) of below 1.4 will allow us to create a uniform

material and more accurately analyze the effect of the chain length on conductivity.

## II. EXPERIMENTAL

### *ATRP of PDEOMEMA Block*

Because of the oxygen sensitivity of the copper catalyst required for ATRP, the reaction needs to occur in an oxygen free environment. In a Schlenk flask, 2-azidoethyl 2-bromo-2-methylpropanoate initiator (1 molar equivalent), di(ethylene glycol) methyl methacrylate (DEOMEMA) monomer (100 molar equivalents for ATRP 1, 3-5; 200 equivalents for ATRP 2) and Fisher Brand anhydrous ethanol were added and the flask was sealed with a rubber septum. Five freeze-pump-thaw cycles were completed and the flask was purged with argon. Cu(I)Br activator (1 molar equivalent) and 2,2'-bipyridine ligand (2 molar equivalents equivalents) were weighed into a second Schlenk flask containing a magnetic stir bar and fitted with a rubber septum. The flask was degassed and purged with argon five times. A cannula transfer was used to transport the contents of the first flask into the second flask. This mixture was stirred in a 60 °C oil bath for varied amounts of time to produce PDEOMEMA polymers of different molecular weights. Variable reaction conditions are summarized in Table 1. The reaction was quenched by opening the flask and allowing air to oxidize the Cu(I) catalyst.

### *Purification of PDEOMEMA*

A 25 mL syringe of neutral alumina was used as a column to remove the copper from the reacted solution. The solution was diluted with THF and allowed to pass through the column, and the THF was removed by rotary evaporation. To further purify the polymer, the solution was placed in a 3.5k MWCO

membrane for dialysis and stirred in anhydrous ethanol for 24 hours to remove unreacted monomer, initiator, and ligand. The solution was then transferred from the membrane to a flask, and ethanol was removed by rotary evaporation and vacuum oven. The polymer was then characterized with Gel Permeation Chromatography (GPC) and Fourier Transform Infrared Spectroscopy (FTIR) analysis.

### *Deprotection of P3HT Block*

The previously prepared P3HT polymer was functionalized with an alkyne end group for use in the click reaction. To keep this alkyne group from reacting with itself in the presence of oxygen, it had been protected with a trimethylsilyl (TMS) group. To remove this group, the molecule was dissolved in anhydrous THF and stirred with 5 molar equivalents of tetra-n-butylammonium fluoride (TBAF) in a flask at room temperature for 2 hours. A rotary evaporator was used to remove the THF. The deprotected P3HT polymer was then precipitated with methanol and filtered gravimetrically, then dried in a vacuum oven.

### *Azide-Alkyne "Click" Reaction*

One molar equivalent of P3HT, 1 molar equivalent of PDEOMEMA, and 2 molar equivalents of N,N,N',N'',N''-pentamethyldiethylenetriamine (PMDETA)

**Table 1:** ATRP molecular weight data.

ATRP 3 yielded no results in GPC analysis likely because it was lost through the dialysis membrane.

ATRP	Reaction Time (hr)	Initiator : Monomer	M <sub>n</sub>	PDI
1	21	1:100	18,000	1.18
2	21	1:200	16,000	1.14
3	4	1:100	-	-
4	8	1:100	8,000	1.12
5	26	1:100	24,000	1.86

ligand were dissolved in anhydrous THF and bubbled with argon for 30 minutes. In a Schlenk flask containing a magnetic stir bar, 2 equivalents of CuI catalyst were degassed and purged with argon five times. A cannula transfer was used to transport the contents of the first flask into the second, and the mixture was stirred in a 40 °C oil bath for 72 hours.

#### Purification of P3HT-*b*-PDEOMEMA

As with the purification of the PDEOMEMA block, a 25 mL syringe of neutral alumina was used as a short column to remove the copper from the solution. The polymer was diluted in THF and passed through the syringe and collected in a flask. The flask was then rotary evaporated to remove the THF, and the polymer was precipitated in methanol. A vacuum pump was then used to dry the polymer. GPC and FTIR were used to analyze the polymer.

### III. RESULTS

Five homopolymer blocks of PDEOMEMA were synthesized, and two were considered feasible for testing as a unique block for the copolymer. ATRP 1 and 4 were used because

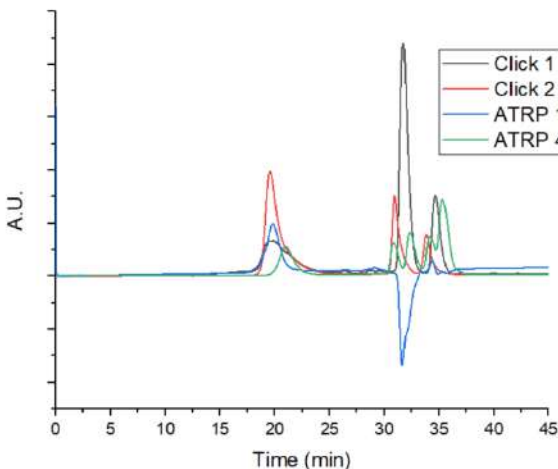


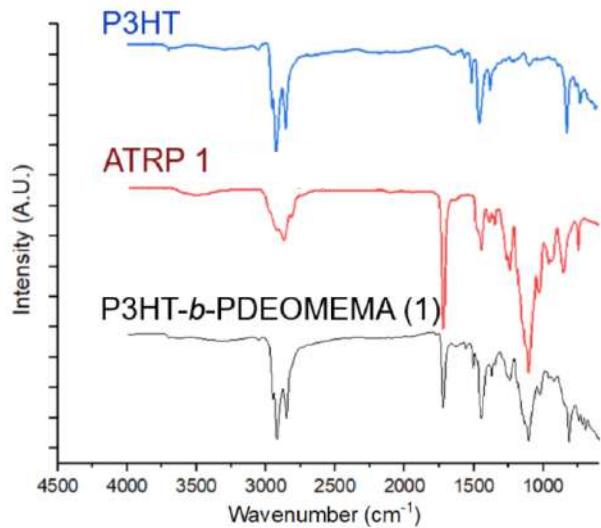
**Figure 1:** GPC curves for PDEOMEMA polymers and P3HT-*b*-PDEOMEMA copolymers

of their widely different molecular weights, their consistency in ratio of reactants, and their sufficiently low polydispersities. The GPC curves can be found in Figure 1 while the molecular weight data for the click reactions can be found in Table 2.

**Table 2:** Click reaction molecular weight data

Click Reaction	ATRP Used	Reaction Time (hr)	M <sub>n</sub>	PDI
1	1	72	14,000	1.36
2	4	72	14,000	1.38

a.)



b.)

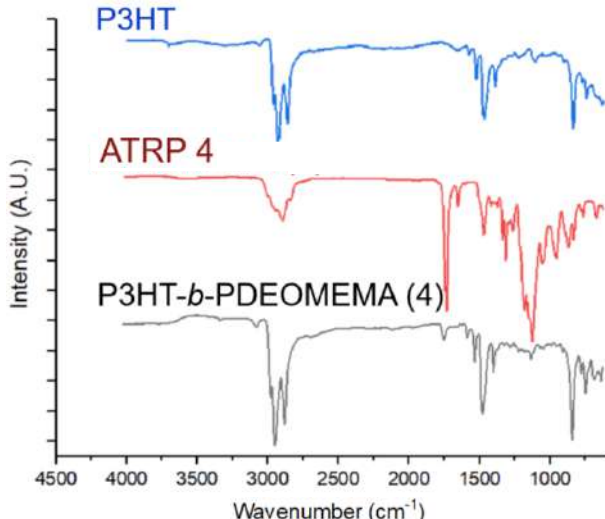


**Figure 2:** FTIR data. a.) Comparison of P3HT and ATRP 1 blocks to P3HT-*b*-PDEOMEMA (1); b.) Comparison of P3HT and ATRP 4 blocks to P3HT-*b*-PDEOMEMA (4)

#### IV. DISCUSSION

The GPC and FTIR results confirm the synthesis of the P3HT-*b*-PDEOMEMA copolymer. While the GPC results for the block copolymer report lower molecular weight averages than one might predict by adding the average molecular weights of each block, the average molecular weight reported was likely skewed to be lower than the weight of the copolymer due to the existence of unreacted homopolymers in the sample.

The carbonyl group present in the PDEOMEMA homopolymer can be seen in both FTIR graphs in the strong peak around  $1750\text{ cm}^{-1}$ . This peak is also present in both block copolymers, which confirms the presence of the PDEOMEMA block. Because the polymer was also able to be precipitated in methanol, we are able to confirm that the P3HT block is present in the macromolecule, because P3HT precipitates in methanol while PDEOMEMA does not. This information coupled suggests that a P3HT-*b*-PDEOMEMA copolymer was synthesized.

To fully test a range of ratios of the two polymer blocks, additional lengths of PDEOMEMA polymers need to be synthesized, especially in molecular weights less than that of the P3HT block, and slightly larger than the P3HT block. In order to purify PDEOMEMA polymers with lower molecular weights, a dialysis membrane with smaller pores is necessary.

In order to analyze the effectiveness of these block copolymers, future analysis needs to be completed. It is important to optimize the electronic and ionic conductivities of the polymer, so both should be taken into account when analyzing the effects of the PDEOMEMA chain length. Atomic force

microscopy can determine the morphology of a spin-coated sample. A well-ordered structure would suggest formation of nanopathways for effective charge transport, while a disordered morphology would likely hinder both conductivities.

#### V. CONCLUSION

Two block copolymers of P3HT and varied lengths of PDEOMEMA were synthesized and characterized with GPC and FTIR analysis. While the conductive and morphological properties of the polymer have not yet been measured, the work done on this project shows potential to create optimized polymers with simultaneous ionic-electronic conductivity that can be useful in solid organic batteries.

#### VI. ACKNOWLEDGEMENTS

This work was supported by the Cornell Center for Materials Research with funding from the NSF MRSEC program (DMR-1719875) and the REU Site program (DMR-1460428). I would like to thank Professor Christopher Ober for welcoming me into his group, and Ziwei Liu for providing me with guidance and mentorship. I would also like to thank CCMR facilities managers and all members of the Ober group for their help. Finally, I would like to thank Jonathan Onorato of the Luscombe group for synthesizing the P3HT for use in this project.

#### VII. REFERENCES

1. Javier, A. E., Patel, S. N., Hallinan, D., Srinivasan, V., Balsara, N. P. Simultaneous Electronic and Ionic Conduction in a Block Copolymer: Application in Lithium Battery Electrodes. *Angewandte Chemie*, **2011**, 42, 10022–10025.

2. P. C. Ewbank, D. Laird, R. D. McCullough in *Organic Photovoltaics*, Wiley-VCH, **2009**, 1 – 55.
3. Obrzut, Jan, and Kirt A. Page. Electrical Conductivity and Relaxation in Poly(3-Hexylthiophene). *Physical Review B*, **2009**, 80.
4. Berthier, C., Gorecki, M., Armand, M. B., Chabagno, J. M., Rigaud, P. Microscopic investigation of ionic conductivity in alkali metal salts-poly(ethylene oxide) adducts. *Solid State Ionics* **11**, 91–96 (1983).
5. Young, R. J.; Lovell, P. A. *Introduction to Polymers*, 3rd ed.; CRC Press: Boca Raton, 2011
6. Gu, Z., Kanto, T., Tsuchiya, K., Shimomura, T., Ogino, K. Annealing Effect on Performance and Morphology of Photovoltaic Devices Based on Poly(3-Hexylthiophene)-b-Poly(Ethylene Oxide). *Journal of Polymer Science Part A: Polymer Chemistry*, **2011**, 49, 2645–2652.

## **Acknowledgements**

Thank you to Professor Alabi, Christine, Jake, Chris, Nana, the Alabi Lab group, and the Cornell Center for Materials Research for their guidance, support, and patience.

# A Comparison of Mapping Variable and Coherent State Instantons

Peter Tomlinson, Binghamton University  
Srinath Ranya, Ananth Lab, Cornell University

August 8, 2018, CCMR REU Program

## Abstract

Mapping variable and coherent state ring polymers are two representations of the path integral discretization of the quantum partition function, which take into account diabatic states. This allows for the study of chemical reactions in the non-adiabatic limit. Both methods use the standard ring polymer path integral representation for nuclear variables, and map discrete states to continuous electronic variables. Python code was written to determine the instanton for the coherent state method, and compared to the mapping variable instanton. Although each are exactly defined, with similar procedures for computing the instanton, the coherent state results were inconsistent with the mapping variable results.

## 1 Introduction

Quantum mechanics provides an accurate picture of nature on its smallest scale, but quantum calculations are computationally expensive. It is only feasible to exactly model the simplest of systems. Quantum calculations scale exponentially with the number of variables, whereas classical calculations scale linearly. Therefore, if an analogous classical formulation can capture quantum phenomena, a quantum system's dynamics may be modeled approximately. Its statistics are modeled exactly.

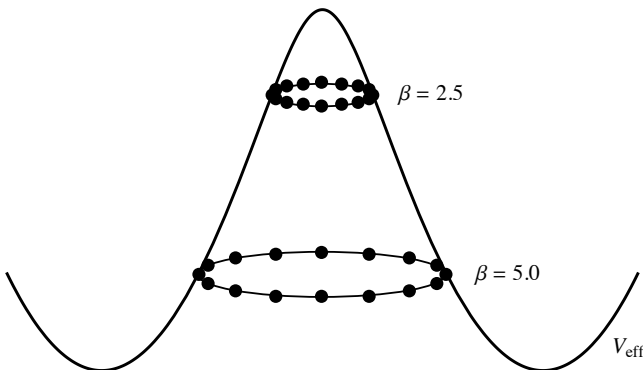


Figure 1: Diagram of ring polymer instantons simulating tunneling through a potential barrier at low temperature ( $\beta = 5.0$ ) and at high temperature ( $\beta = 2.5$ )

Ring Polymer Molecular Dynamics (RPMD) is one approach developed to study nuclear dynamics and quantum effects such as tunneling. In this formulation, path integral discretization creates  $N$  identical copies of a particle, called beads, connected in a ring by springs. This ring polymer simulates tunneling by draping over or wrapping around a potential barrier, similarly to what is shown in figure 1. At higher temperatures and therefore higher energies, the ring polymer contracts and will collapse to a single classical point resting on the potential surface. Modeling the classical trajectory of each bead determines the reaction rate and transition state of a reaction. Specifically, figure 1 illustrates a pair of instantons, which represent the dominant tunneling pathways. [1]

RPMD is an established method for one state systems. [2] It is therefore well suited for adiabatic systems, such as the one shown in figure 2, where the reaction may be approximated to occur on one surface. Mapping variable [3] and coherent state [4] ring polymer molecular dynamics (MV-RPMD and CS-RPMD respectively) are recently developed methods for applying the path integral formalism to multiple state systems. They therefore allow for the study of systems in the non-adiabatic limit. Thus, they show potential for multi-electron reactions, such as in photochemistry. [3] This report compares the derivation and instantons of the mapping variable and coherent state methods.

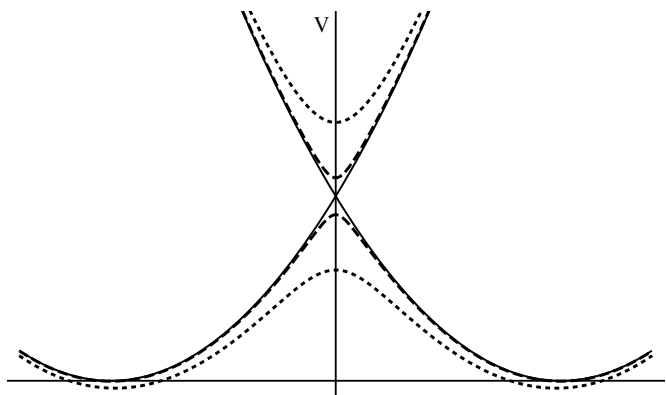


Figure 2: Diabatic states are given by the solid lines, states with weak coupling, in the non-adiabatic limit, are given by the dashed lines, and states with strong coupling, in the adiabatic limit, are given by the dotted lines

## 2 Theory

### 2.1 The Path Integral Ring Polymer

The Hamiltonian for a general  $L$ -level system is given as

$$\hat{H} = \frac{\hat{\mathbf{P}}^2}{2M} + V_0(\hat{\mathbf{R}}) + \sum_{n,m=1}^L V_{nm}(\hat{\mathbf{R}})|n\rangle\langle m|, \quad (1)$$

where  $\mathbf{R}$  and  $\mathbf{P}$  denote the nuclear position and momentum,  $M$  is the nuclear mass,  $V_0(\mathbf{R})$  is the electronic state-independent potential,  $V_{nn}(\mathbf{R})$  is the potential for the  $n$ th electronic state, and  $V_{nm}(\mathbf{R})$  for  $n \neq m$  is the coupling between electronic states. The electronic state potential energy will later be denoted as  $\mathcal{V}(\mathbf{R})$  for simplicity.

We begin the derivation of the ring polymer Hamiltonian with the canonical quantum partition function, given as

$$Z = \text{Tr} [e^{-\beta \hat{H}}], \quad (2)$$

where  $\beta = 1/k_B T$  is the reciprocal temperature.  $\beta$  can also be interpreted as imaginary time, since the transformation  $\beta = it/\hbar$  corresponds to a Wick rotation from the canonical density matrix  $\hat{\rho}(t) = \exp[-\beta \hat{H}]$  to the time evolution operator  $\hat{U}(t) = \exp[-i\hat{H}t/\hbar]$ . [2] Using the Trotter expansion,

$$e^{-\beta \hat{H}} = \lim_{N \rightarrow \infty} [e^{-\beta_N \frac{\hat{\mathbf{P}}^2}{2M}} e^{-\beta_N \hat{V}_0(\hat{\mathbf{R}})} e^{-\beta_N \mathcal{V}(\hat{\mathbf{R}})}]^N, \quad (3)$$

where  $\beta_N = \beta/N$ . Using equation (3) and writing out the trace, the partition function becomes

$$Z = \lim_{N \rightarrow \infty} \int d\mathbf{R} \int d\mathbf{x} \langle \mathbf{R}, \mathbf{x} | [e^{-\beta_N \frac{\hat{\mathbf{P}}^2}{2M}} e^{-\beta_N \hat{V}_0(\hat{\mathbf{R}})} e^{-\beta_N \mathcal{V}(\hat{\mathbf{R}})}]^N | \mathbf{R}, \mathbf{x} \rangle, \quad (4)$$

where  $\mathbf{x}$  and  $\mathbf{p}$  are introduced as electronic position and momentum.

According to the path integral procedure, the identity  $\hat{I} = \int d\mathbf{R} \int d\mathbf{x} |\mathbf{R}, \mathbf{x}\rangle \langle \mathbf{R}, \mathbf{x}|$  is inserted into equation (4)  $N - 1$  times, yielding

$$Z = \lim_{N \rightarrow \infty} \int d\{\mathbf{R}_\alpha\} \int d\{\mathbf{x}_\alpha\} \prod_{\alpha=1}^N \langle \mathbf{R}_\alpha | e^{-\frac{\beta_N \hat{\mathbf{P}}^2}{2M}} | \mathbf{R}_{\alpha+1} \rangle e^{-\beta_N V_0(\mathbf{R}_\alpha)} \langle \mathbf{x}_\alpha | e^{-\beta_N \mathcal{V}(\mathbf{R}_\alpha)} | \mathbf{x}_{\alpha+1} \rangle. \quad (5)$$

The notation  $\int d\{\mathbf{R}_\alpha\}$  represents  $\int d\mathbf{R}_1 \int d\mathbf{R}_2 \cdots \int d\mathbf{R}_N$ . Note that because of the initial trace,  $\mathbf{R}_1 = \mathbf{R}_{N+1}$  and  $\mathbf{x}_1 = \mathbf{x}_{N+1}$ . Now the  $\hat{\mathbf{P}}$  term in equation (5) can be evaluated by inserting  $\hat{I} = \int d\mathbf{P} |\mathbf{P}\rangle \langle \mathbf{P}|$ , and the nuclear momentum is introduced using the Gaussian integral

$$\int d\{\mathbf{P}_\alpha\} \prod_{\alpha=1}^N e^{-\beta_N \mathbf{P}_\alpha^2/2M} = \left( \frac{2\pi M}{\beta_N} \right)^{N/2}. \quad (6)$$

Also, throughout this report we set  $\hbar = 1$ .

The partition function is evaluated as

$$Z \propto \lim_{N \rightarrow \infty} \int d\{\mathbf{R}_\alpha\} \int d\{\mathbf{P}_\alpha\} e^{-\beta_N H_{RP}} I_E \quad (7)$$

where

$$H_{RP} = \sum_{\alpha=1}^N \frac{\mathbf{P}_\alpha^2}{2M} + V_0(\mathbf{R}_\alpha) + \frac{M}{2\beta_N^2} (\mathbf{R}_\alpha - \mathbf{R}_{\alpha+1})^2 \quad (8)$$

and

$$I_E = \int d\{\mathbf{x}_\alpha\} \prod_{\alpha=1}^N \langle \mathbf{x}_\alpha | e^{-\beta_N \mathcal{V}(\mathbf{R}_\alpha)} | \mathbf{x}_{\alpha+1} \rangle. \quad (9)$$

$H_{RP}$  is an established result of the Path Integral Ring Polymer method for single state systems. [2] MV-RPMD [3] and CS-RPMD [4] have been developed to handle multiple state systems, and differ in the way they handle  $I_E$ .

### 2.2 Mapping Electronic States

The Stock-Thoss mapping representation [5] is used in both MV-RPMD and CS-RPMD to be able to express the discrete electronic states in terms of continuous phase space variables  $\mathbf{x}$  and  $\mathbf{p}$ . Under this protocol,  $L$  diabatic electronic states  $|\psi\rangle$  are mapped to  $L$  singly excited harmonic oscillators (SEOs), such that

$$|\psi_n\rangle \langle \psi_m| \rightarrow \hat{a}_n^\dagger \hat{a}_m \quad (10)$$

and

$$|\psi_n\rangle \rightarrow |0_1, \dots, 1_n, \dots, 0_L\rangle = |n\rangle. \quad (11)$$

In this notation,  $|n\rangle$  is the product of  $L$  oscillators with the  $n$ th in first excited state and the remainder in the ground state. The terms  $\hat{a}_n^\dagger$  and  $\hat{a}_m$  are the harmonic oscillator creation and annihilation operators respectively, they are given by

$$\hat{a}_n^\dagger = \frac{\hat{x}_n - i\hat{p}_m}{\sqrt{2}} \quad \text{and} \quad \hat{a}_m = \frac{\hat{x}_m + i\hat{p}_m}{\sqrt{2}}, \quad (12)$$

and obey the commutation rule  $[\hat{a}_n^\dagger, \hat{a}_m] = \delta_{nm}$ .

The projection of an SEO state onto an electronic position state is given by

$$\langle \mathbf{x} | n \rangle = \frac{\sqrt{2}}{\pi^{N/4}} [\mathbf{x}]_n e^{-\frac{1}{2} \mathbf{x}^2}. \quad (13)$$

Coherent states, denoted  $|\mathbf{p}, \mathbf{q}\rangle$  are eigenstates of the annihilation operator. Here,  $\mathbf{q}$  represents the electronic position, and is equivalent to  $\mathbf{x}$ . The projection of an SEO state onto a coherent state is found as

$$\begin{aligned} \langle \mathbf{p}, \mathbf{q} | n \rangle &= \langle \mathbf{p}, \mathbf{q} | \hat{a}_n^\dagger | 0 \rangle = \frac{q_n - ip_n}{\sqrt{2}} \langle \mathbf{p}, \mathbf{q} | 0 \rangle \\ &= \frac{q_n - ip_n}{\sqrt{2}} \int_{-\infty}^{\infty} dx \langle \mathbf{p}, \mathbf{q} | x \rangle \langle x | 0 \rangle \\ &= \frac{q_n - ip_n}{\sqrt{2}} e^{-\frac{1}{4}(\mathbf{q}^2 + \mathbf{p}^2)}, \end{aligned} \quad (14)$$

Likewise

$$\begin{aligned}\langle m|\mathbf{p}, \mathbf{q} \rangle &= \langle 0|\hat{a}_m|\mathbf{p}, \mathbf{q} \rangle = \frac{q_m + ip_m}{\sqrt{2}} \langle 0|\mathbf{p}, \mathbf{q} \rangle \\ &= \frac{q_m + ip_m}{\sqrt{2}} \int_{-\infty}^{\infty} dx \langle 0|x\rangle \langle x|\mathbf{p}, \mathbf{q} \rangle \\ &= \frac{q_m + ip_m}{\sqrt{2}} e^{-\frac{1}{4}(\mathbf{q}^2 + \mathbf{p}^2)}.\end{aligned}\quad (15)$$

### 2.3 Mapping Variable Ring Polymer

MV-RPMD expresses  $I_E$  in phase space by applying Wigner transforms. The Wigner function is given by

$$O(\mathbf{x}, \mathbf{p}) = \int d\Delta\mathbf{x} \left\langle \mathbf{x} - \frac{\Delta\mathbf{x}}{2} \middle| \hat{O} \middle| \mathbf{x} + \frac{\Delta\mathbf{x}}{2} \right\rangle e^{i\mathbf{p}^T \Delta\mathbf{x}} \quad (16)$$

and is used to find the trace of an operator in phase space,

$$\text{Tr}[\hat{O}] = \frac{1}{(2\pi)^L} \int d\mathbf{x} \int d\mathbf{p} O(\mathbf{x}, \mathbf{p}). \quad (17)$$

First, to ensure the projection onto the SEO subspace, insert the diabatic projection operator  $\mathcal{P} = \sum_n |n\rangle \langle n|$  throughout  $I_E$ ,

$$I_E = \int d\{\mathbf{x}_\alpha\} \prod_{\alpha=1}^N \langle \mathbf{x}_\alpha | \mathcal{P} e^{-\beta_N V(\mathbf{R}_\alpha)} \mathcal{P} | \mathbf{x}_{\alpha+1} \rangle. \quad (18)$$

Now, if we define

$$\begin{aligned}\hat{S} &= \mathcal{P} e^{-\beta_N V(\mathbf{R}_1)} \mathcal{P} | \mathbf{x}_2 \rangle \langle \mathbf{x}_2 | \mathcal{P} e^{-\beta_N V(\mathbf{R}_2)} \mathcal{P} | \mathbf{x}_3 \rangle \\ &\quad \cdots \langle \mathbf{x}_N | \mathcal{P} e^{-\beta_N V(\mathbf{R}_N)} \mathcal{P} | \mathbf{x}_1 \rangle,\end{aligned}\quad (19)$$

we can write  $I_E$  as a trace of  $\hat{S}$  over  $\mathbf{x}_1$ ,

$$I_E = \int d\mathbf{x}_2 \cdots \int d\mathbf{x}_N \text{Tr}[\hat{S}]_1. \quad (20)$$

Applying equations (16) and (17),  $I_E$  becomes

$$\begin{aligned}I_E &= \frac{1}{(2\pi)^L} \int d\mathbf{x}_1 \int d\mathbf{p}_1 \int d\Delta\mathbf{x}_1 \int d\mathbf{x}_2 \cdots \int d\mathbf{x}_N \\ &\quad \left\langle \mathbf{x}_1 - \frac{\Delta\mathbf{x}_1}{2} \middle| \hat{S} \middle| \mathbf{x}_1 + \frac{\Delta\mathbf{x}_1}{2} \right\rangle e^{i\mathbf{p}_1^T \Delta\mathbf{x}_1}.\end{aligned}\quad (21)$$

By rearranging  $I_E$  as

$$\begin{aligned}I_E &= \frac{1}{(2\pi)^L} \int d\mathbf{x}_1 \int d\mathbf{p}_1 \int d\Delta\mathbf{x}_1 \int d\mathbf{x}_2 \cdots \int d\mathbf{x}_N \\ &\quad \langle \mathbf{x}_2 | \mathcal{P} e^{-\beta_N V(\mathbf{R}_2)} \mathcal{P} | \mathbf{x}_3 \rangle \cdots \langle \mathbf{x}_N | \mathcal{P} e^{-\beta_N V(\mathbf{R}_N)} \mathcal{P} | \mathbf{x}_1 + \frac{\Delta\mathbf{x}_1}{2} \rangle \\ &\quad \langle \mathbf{x}_1 - \frac{\Delta\mathbf{x}_1}{2} | \mathcal{P} e^{-\beta_N V(\mathbf{R}_1)} \mathcal{P} | \mathbf{x}_2 \rangle e^{i\mathbf{p}_1^T \Delta\mathbf{x}_1},\end{aligned}\quad (22)$$

and redefining  $\hat{S}$  as

$$\begin{aligned}\hat{S} &= \mathcal{P} e^{-\beta_N V(\mathbf{R}_2)} \mathcal{P} | \mathbf{x}_3 \rangle \cdots \langle \mathbf{x}_N | \mathcal{P} e^{-\beta_N V(\mathbf{R}_N)} \mathcal{P} | \mathbf{x}_1 + \frac{\Delta\mathbf{x}_1}{2} \rangle \\ &\quad \langle \mathbf{x}_1 - \frac{\Delta\mathbf{x}_1}{2} | \mathcal{P} e^{-\beta_N V(\mathbf{R}_1)} \mathcal{P},\end{aligned}\quad (23)$$

$I_E$  can be written as

$$\begin{aligned}I_E &= \int d\mathbf{x}_1 \int d\mathbf{p}_1 \int d\Delta\mathbf{x}_1 \\ &\quad \int d\mathbf{x}_3 \cdots \int d\mathbf{x}_N \text{Tr}[\hat{S}]_2 e^{i\mathbf{p}_1^T \Delta\mathbf{x}_1},\end{aligned}\quad (24)$$

and equations (16) and (17) can again be applied. Repeating this process a total of N times yields

$$\begin{aligned}I_E &= \frac{1}{(2\pi)^{LN}} \int d\{\mathbf{x}_\alpha\} \int d\{\mathbf{p}_\alpha\} \int d\{\Delta\mathbf{x}_\alpha\} \\ &\quad \prod_{\alpha=1}^N \left\langle \mathbf{x}_\alpha - \frac{\Delta\mathbf{x}_\alpha}{2} \middle| \mathcal{P} e^{-\beta_N V(\mathbf{R}_\alpha)} \mathcal{P} \middle| \mathbf{x}_{\alpha+1} + \frac{\Delta\mathbf{x}_{\alpha+1}}{2} \right\rangle e^{i\mathbf{p}_\alpha^T \Delta\mathbf{x}_\alpha}.\end{aligned}\quad (25)$$

Using a high temperature approximation, define an  $\mathcal{M}(\mathbf{R})$  matrix with elements given by

$$\mathcal{M}_{nm} = \langle n | e^{-\beta_N V(\mathbf{R})} | m \rangle \quad (26)$$

where

$$\mathcal{M}_{nm} = \begin{cases} e^{-\beta_N V_{nm}(\mathbf{R})} & n = m \\ -\beta_N V_{nm}(\mathbf{R}) e^{-\beta_N V_{nm}(\mathbf{R})} & n \neq m \end{cases}. \quad (27)$$

By making use of this notation and equation (13), equation (25) is written

$$\begin{aligned}I_E &\propto \int d\{\mathbf{x}_\alpha\} \int d\{\mathbf{p}_\alpha\} \int d\{\Delta\mathbf{x}_\alpha\} \\ &\quad \prod_{\alpha=1}^N \left( \mathbf{x}_\alpha - \frac{\Delta\mathbf{x}_\alpha}{2} \right)^T \mathcal{M}(\mathbf{R}_\alpha) \left( \mathbf{x}_{\alpha+1} + \frac{\Delta\mathbf{x}_{\alpha+1}}{2} \right) \\ &\quad \exp \left[ \sum_{\alpha=1}^N i\mathbf{p}_\alpha^T \Delta\mathbf{x}_\alpha - \frac{1}{2} \left( \mathbf{x}_\alpha + \frac{\Delta\mathbf{x}_\alpha}{2} \right)^2 \right. \\ &\quad \left. - \frac{1}{2} \left( \mathbf{x}_{\alpha+1} - \frac{\Delta\mathbf{x}_{\alpha+1}}{2} \right)^2 \right].\end{aligned}\quad (28)$$

Simplifying the exponent yeilds

$$i\mathbf{p}_\alpha^T \Delta\mathbf{x}_\alpha - \mathbf{x}_\alpha^2 - \frac{1}{4} \Delta\mathbf{x}_\alpha^2, \quad (29)$$

and completing the square gives

$$-\frac{1}{4} ((\Delta\mathbf{r}_\alpha - 2i\mathbf{p}_\alpha)^2 + 4\mathbf{x}_\alpha^2 + 4\mathbf{p}_\alpha^2). \quad (30)$$

Substituting the exponent back into equation (28) and using the fact that for a product of matrices  $ABCD = \text{Tr}[D \otimes ABC]$ ,

$$\begin{aligned}I_E &\propto \int d\{\mathbf{x}_\alpha\} \int d\{\mathbf{p}_\alpha\} \int d\{\Delta\mathbf{r}_\alpha\} \\ &\quad \text{Tr} \left[ \prod_{\alpha=1}^N \left( \mathbf{r}_\alpha - \frac{\Delta\mathbf{r}_\alpha}{2} \right) \otimes \left( \mathbf{r}_\alpha + \frac{\Delta\mathbf{r}_\alpha}{2} \right)^T \mathcal{M}(\mathbf{R}_\alpha) \right] \\ &\quad \exp \left[ -\frac{1}{4} \sum_{\alpha=1}^N (\Delta\mathbf{r}_\alpha - 2i\mathbf{p}_\alpha)^2 + 4\mathbf{x}_\alpha^2 + 4\mathbf{p}_\alpha^2 \right].\end{aligned}\quad (31)$$

Now with the substitution  $\mathbf{u}_\alpha = \Delta\mathbf{r}_\alpha - 2i\mathbf{p}_\alpha$ ,

$$I_E \propto \int d\{\mathbf{x}_\alpha\} \int d\{\mathbf{p}_\alpha\} \exp \left[ -\sum_{\alpha=1}^N \mathbf{x}_\alpha^2 + \mathbf{p}_\alpha^2 \right] \\ \int d\{\mathbf{u}_\alpha\} \text{Tr} \left[ \prod_{\alpha=1}^N \left( \mathbf{x}_\alpha + i\mathbf{p}_\alpha + \frac{\mathbf{u}_\alpha}{2} \right) \right. \\ \left. \otimes \left( \mathbf{x}_\alpha - i\mathbf{p}_\alpha - \frac{\mathbf{u}_\alpha}{2} \right)^T \mathcal{M}(\mathbf{R}_\alpha) \right] \exp \left[ -\frac{1}{4} \sum_{\alpha=1}^N \mathbf{u}_\alpha^2 \right]. \quad (32)$$

By expanding equation (32),

$$I_E \propto \int d\{\mathbf{x}_\alpha\} \int d\{\mathbf{p}_\alpha\} \exp \left[ -\sum_{\alpha=1}^N \mathbf{x}_\alpha^2 + \mathbf{p}_\alpha^2 \right] \\ \int d\{\mathbf{u}_\alpha\} \text{Tr} \left[ \prod_{\alpha=1}^N (\mathbf{x}_\alpha + i\mathbf{p}_\alpha) \otimes (\mathbf{x}_\alpha - i\mathbf{p}_\alpha)^T \right. \\ \left. - \frac{1}{2} (\mathbf{x}_\alpha + i\mathbf{p}_\alpha) \otimes \mathbf{u}_\alpha^T + \frac{1}{2} \mathbf{u}_\alpha \otimes (\mathbf{x}_\alpha + i\mathbf{p}_\alpha)^T \right. \\ \left. - \frac{1}{4} \mathbf{u}_\alpha \otimes \mathbf{u}_\alpha^T \mathcal{M}(\mathbf{R}_\alpha) \right] \exp \left[ -\frac{1}{4} \sum_{\alpha=1}^N \mathbf{u}_\alpha^2 \right], \quad (33)$$

the integral in  $\mathbf{u}_\alpha$  can be evaluated by comparison with the Gaussian integrals  $\int_{-\infty}^{\infty} e^{-ax^2} dx = (\frac{\pi}{a})^{1/2}$ ,  $\int_{-\infty}^{\infty} xe^{-ax^2} dx = 0$ , and  $\int_{-\infty}^{\infty} x^2 e^{-ax^2} dx = \frac{1}{2} (\frac{\pi}{a^3})^{1/2}$ . This gives

$$I_E \propto \int d\{\mathbf{x}_\alpha\} \int d\{\mathbf{p}_\alpha\} \exp \left[ -\sum_{\alpha=1}^N \mathbf{x}_\alpha^2 + \mathbf{p}_\alpha^2 \right] \\ \text{Tr} \left[ \prod_{\alpha=1}^N \left( (\mathbf{x}_\alpha + i\mathbf{p}_\alpha) \otimes (\mathbf{x}_\alpha - i\mathbf{p}_\alpha)^T - \frac{1}{2} \mathcal{I} \right) \mathcal{M}(\mathbf{R}_\alpha) \right]. \quad (34)$$

Now inserting  $I_E$  back into equation (7), we have

$$Z \propto \lim_{N \rightarrow \infty} \int d\{\mathbf{R}_\alpha\} \int d\{\mathbf{P}_\alpha\} \int d\{\mathbf{r}_\alpha\} \int d\{\mathbf{p}_\alpha\} e^{-\beta_N H_{MV}} \quad (35)$$

where

$$H_{MV} = \sum_{\alpha=1}^N \left[ \frac{\mathbf{P}_\alpha^2}{2M} + V_0(\mathbf{R}_\alpha) + \frac{M}{2\beta_N^2} (\mathbf{R}_\alpha - \mathbf{R}_{\alpha+1})^2 \right. \\ \left. + \frac{1}{\beta_N} (\mathbf{x}_\alpha^2 + \mathbf{p}_\alpha^2) \right] - \frac{1}{\beta_N} \ln |\text{Re}[\text{Tr}[\mathbf{\Gamma}]]|, \quad (36)$$

and

$$\mathbf{\Gamma} = \prod_{\alpha=1}^N \left( (\mathbf{x}_\alpha + i\mathbf{p}_\alpha) \otimes (\mathbf{x}_\alpha - i\mathbf{p}_\alpha)^T - \frac{1}{2} \mathcal{I} \right) \mathcal{M}(\mathbf{R}_\alpha). \quad (37)$$

## 2.4 Coherent State Ring Polymer

The CS-RPMD derivation begins by writing  $I_E$  as a trace over  $\mathbf{x}$  by removing the identities from equation (9)

$$I_E = \int d\mathbf{x}_1 \langle \mathbf{x}_1 | \prod_{\alpha=1}^N e^{-\beta_N \mathcal{V}(\mathbf{R}_\alpha)} | \mathbf{x}_1 \rangle \quad (38)$$

$$= \text{Tr} \left[ \prod_{\alpha=1}^N e^{-\beta_N \mathcal{V}(\mathbf{R}_\alpha)} \right]. \quad (39)$$

Using the Taylor expansion  $e^x = \sum_{n=0}^{\infty} x^n / n!$ ,

$$I_E = \text{Tr} \prod_{\alpha=1}^N \left[ 1 - \beta_N \sum_{n,m} V_{nm}(\mathbf{R}_\alpha) \hat{a}_n^\dagger \hat{a}_m + \mathcal{O}(\beta_N^2) \right], \quad (40)$$

and the commutation relation  $[\hat{a}_m, \hat{a}_n^\dagger] = \delta_{mn}$ ,

$$I_E \approx \text{Tr} \prod_{\alpha=1}^N \left[ 1 - \beta_N \sum_{n,m} V_{nm}(\mathbf{R}_\alpha) (\hat{a}_m \hat{a}_n^\dagger - \delta_{mn}) \right]. \quad (41)$$

Inserting the identity over coherent states,

$$\hat{I} = \left( \frac{1}{2\pi} \right)^L \int d\mathbf{p} d\mathbf{q} |\mathbf{p}, \mathbf{q}\rangle \langle \mathbf{p}, \mathbf{q}|, \quad (42)$$

$N$  times gives

$$I_E \propto \int d\{\mathbf{p}_\alpha\} \int d\{\mathbf{q}_\alpha\} \text{Tr} \prod_{\alpha=1}^N \left[ |\mathbf{p}_\alpha, \mathbf{q}_\alpha\rangle \langle \mathbf{p}_\alpha, \mathbf{q}_\alpha| \right. \\ \left. - \beta_N \sum_{n,m} V_{nm}(\mathbf{R}_\alpha) (\hat{a}_m |\mathbf{p}_\alpha, \mathbf{q}_\alpha\rangle \langle \mathbf{p}_\alpha, \mathbf{q}_\alpha| \hat{a}_n^\dagger - \right. \\ \left. \delta_{mn} |\mathbf{p}_\alpha, \mathbf{q}_\alpha\rangle \langle \mathbf{p}_\alpha, \mathbf{q}_\alpha|) \right] \quad (43)$$

and since coherent states are eigenstates of  $\hat{a}^\dagger$  and  $\hat{a}$ ,

$$I_E \propto \int d\{\mathbf{p}_\alpha\} \int d\{\mathbf{q}_\alpha\} \\ \text{Tr} \prod_{\alpha=1}^N \left[ |\mathbf{p}_\alpha, \mathbf{q}_\alpha\rangle \langle \mathbf{p}_\alpha, \mathbf{q}_\alpha| \left( 1 - \beta_N \sum_{n,m} V_{nm}(\mathbf{R}_\alpha) \right. \right. \\ \left. \left. \left( \frac{1}{2} [\mathbf{q}_\alpha + i\mathbf{p}_\alpha]_m [\mathbf{q}_\alpha - i\mathbf{p}_\alpha]_n - \delta_{mn} \right) \right) \right]. \quad (44)$$

Using the fact that for a product of matrices  $ABCD = \text{Tr}[D \otimes ABC]$ , and inserting the diabatic projection operator  $\mathcal{P} = \sum_n |n\rangle \langle n|$ ,

$$I_E \propto \int d\{\mathbf{p}_\alpha\} \int d\{\mathbf{q}_\alpha\} \\ \prod_{\alpha=1}^N \left[ \sum_n \langle \mathbf{p}_\alpha, \mathbf{q}_\alpha | n \rangle \langle n | \mathbf{p}_{\alpha+1}, \mathbf{q}_{\alpha+1} \rangle \left( 1 - \beta_N \sum_{n,m} V_{nm}(\mathbf{R}_\alpha) \right. \right. \\ \left. \left. \left( \frac{1}{2} [\mathbf{q}_\alpha + i\mathbf{p}_\alpha]_m [\mathbf{q}_\alpha - i\mathbf{p}_\alpha]_n - \delta_{mn} \right) \right) \right]. \quad (45)$$

By equations (14) and (15),

$$I_E \propto \int d\{\mathbf{p}_\alpha\} \int d\{\mathbf{q}_\alpha\} \prod_{\alpha=1}^N [(\mathbf{q}_\alpha - i\mathbf{p}_\alpha)^T (\mathbf{q}_{\alpha+1} + i\mathbf{p}_{\alpha+1})] \exp \left[ \sum_{\alpha=1}^N -\frac{1}{4} (\mathbf{q}_\alpha^2 + \mathbf{p}_\alpha^2 + \mathbf{q}_{\alpha+1}^2 + \mathbf{p}_{\alpha+1}^2) - \beta_N \sum_{n,m} V_{nm}(\mathbf{R}_\alpha) \left( \frac{1}{2} ([\mathbf{q}_\alpha]_m [\mathbf{q}_\alpha]_n + [\mathbf{p}_\alpha]_m [\mathbf{p}_\alpha]_n) - \delta_{mn} \right) \right], \quad (46)$$

which can be rewritten as

$$I_E \propto \int d\{\mathbf{p}_\alpha\} \int d\{\mathbf{q}_\alpha\} \text{Tr} \left[ \prod_{\alpha=1}^N [(\mathbf{q}_\alpha + i\mathbf{p}_\alpha) \otimes (\mathbf{q}_\alpha - i\mathbf{p}_\alpha)^T] \right] \exp \left[ \sum_{\alpha=1}^N -\frac{1}{2} (\mathbf{q}_\alpha^2 + \mathbf{p}_\alpha^2) - \beta_N \text{Tr} \left[ \mathcal{V}(\mathbf{R}_\alpha) \left( \frac{1}{2\hbar} (\mathbf{q}_\alpha \otimes \mathbf{q}_\alpha^T + \mathbf{p}_\alpha \otimes \mathbf{p}_\alpha^T) - \mathcal{I} \right) \right] \right]. \quad (47)$$

Now inserting  $I_E$  back into equation (7), we have

$$Z \propto \lim_{N \rightarrow \infty} \int d\{\mathbf{R}_\alpha\} \int d\{\mathbf{P}_\alpha\} \int d\{\mathbf{p}_\alpha\} \int d\{\mathbf{q}_\alpha\} e^{-\beta_N H_{CS}} \quad (48)$$

where

$$H_{CS} = \sum_{\alpha=1}^N \left[ \frac{\mathbf{P}_\alpha^2}{2M} + V_0(\mathbf{R}_\alpha) + \frac{M}{2\beta_N^2} (\mathbf{R}_\alpha - \mathbf{R}_{\alpha+1})^2 + \frac{1}{2\beta_N} (\mathbf{q}_\alpha^2 + \mathbf{p}_\alpha^2) + \text{Tr} \left[ \mathcal{V}(\mathbf{R}_\alpha) \left( \frac{1}{2} (\mathbf{q}_\alpha \otimes \mathbf{q}_\alpha^T + \mathbf{p}_\alpha \otimes \mathbf{p}_\alpha^T) - \mathcal{I} \right) \right] - \frac{1}{\beta_N} \ln \left| \text{Re}[\text{Tr}[\Gamma]] \right| \right], \quad (49)$$

and

$$\Gamma = \prod_{\alpha=1}^N (\mathbf{q}_\alpha + i\mathbf{p}_\alpha) \otimes (\mathbf{q}_\alpha - i\mathbf{p}_\alpha)^T. \quad (50)$$

## 2.5 Alternate Coherent State Form

A different derivation involving coherent states involves performing the trace in equation (39) over coherent states, so that

$$I_E = \int d\mathbf{p} \int d\mathbf{q} \langle \mathbf{p}, \mathbf{q} | \prod_{\alpha=1}^N e^{-\beta_N \mathcal{V}(\mathbf{R}_\alpha)} | \mathbf{p}, \mathbf{q} \rangle. \quad (51)$$

Then by inserting  $N-1$  coherent state identities, similarly to the path integral procedure, we obtain

$$I_E = \int d\{\mathbf{p}_\alpha\} \int d\{\mathbf{q}_\alpha\} \prod_{\alpha=1}^N \langle \mathbf{p}_\alpha, \mathbf{q}_\alpha | e^{-\beta_N \mathcal{V}(\mathbf{R}_\alpha)} | \mathbf{p}_{\alpha+1}, \mathbf{q}_{\alpha+1} \rangle. \quad (52)$$

By expanding the exponential,

$$I_E \approx \int d\{\mathbf{p}_\alpha\} \int d\{\mathbf{q}_\alpha\} \prod_{\alpha=1}^N \langle \mathbf{p}_\alpha, \mathbf{q}_\alpha | \left[ 1 - \beta_N \sum_{n,m} V_{nm}(\mathbf{R}_\alpha) \hat{a}_m^\dagger \hat{a}_n \right] | \mathbf{p}_{\alpha+1}, \mathbf{q}_{\alpha+1} \rangle, \quad (53)$$

and by distributing the states through each term and inserting  $\mathcal{P}$ ,  $I_E$  becomes

$$I_E \approx \int d\{\mathbf{p}_\alpha\} \int d\{\mathbf{q}_\alpha\} \prod_{\alpha=1}^N \langle \mathbf{p}_\alpha, \mathbf{q}_\alpha | \mathcal{P} | \mathbf{p}_{\alpha+1}, \mathbf{q}_{\alpha+1} \rangle \left[ 1 - \beta_N \sum_{n,m} V_{nm}(\mathbf{R}_\alpha) [\mathbf{q}_\alpha - i\mathbf{p}_\alpha]_m [\mathbf{q}_{\alpha+1} + i\mathbf{p}_{\alpha+1}]_n \right]. \quad (54)$$

Carrying out the derivation as before, we find

$$H_{CS} = \sum_{\alpha=1}^N \left[ \frac{\mathbf{P}_\alpha^2}{2M} + V_0(\mathbf{R}_\alpha) + \frac{M}{2\beta_N^2} (\mathbf{R}_\alpha - \mathbf{R}_{\alpha+1})^2 + \frac{1}{2\beta_N} (\mathbf{q}_\alpha^2 + \mathbf{p}_\alpha^2) + \frac{1}{2} \text{Tr} \left[ \mathcal{V}(\mathbf{R}_\alpha) (\mathbf{q}_\alpha \otimes \mathbf{q}_{\alpha+1}^T + \mathbf{p}_\alpha \otimes \mathbf{p}_{\alpha+1}^T) \right] - \frac{1}{\beta_N} \ln \left| \text{Re}[\text{Tr}[\Gamma]] \right| \right], \quad (55)$$

and

$$\Gamma = \prod_{\alpha=1}^N (\mathbf{q}_\alpha + i\mathbf{p}_\alpha) \otimes (\mathbf{q}_\alpha - i\mathbf{p}_\alpha)^T. \quad (56)$$

## 2.6 Multi-State Instantons

The instanton configuration is the first-order saddle point of the effective potential. [7] This is well established and is predicted to be true for multiple electronic states as well.

## 3 Implementation Details

The same procedures were used for both the Mapping Variable and Coherent State cases. Although for

the mapping variable case, a version of the Hamiltonian was used which did not include the electronic momentum,

$$H = \sum_{\alpha=1}^N \left[ \frac{\mathbf{P}_\alpha^2}{2M} + V_0(\mathbf{R}_\alpha) + \frac{M}{2\beta_N^2} (\mathbf{R}_\alpha - \mathbf{R}_{\alpha+1})^2 + \frac{1}{\beta_N} \mathbf{x}_\alpha^2 \right] - \frac{1}{\beta_N} \ln |\Gamma| \quad (57)$$

where

$$\Gamma = \prod_{\alpha=1}^N \mathbf{x}_\alpha^T \mathcal{M}(\mathbf{R}_\alpha) \mathbf{x}_{\alpha+1}. \quad (58)$$

In each case, the effective potential was taken to be the Hamiltonian, neglecting the nuclear kinetic energy term and the electronic-state independent potential ( $V_0$ ). The potential, its gradient, and its hessian were written in Python. The potential was minimized using the l-bfgs-b algorithm from `scipy.optimize`, [6] using an approximate gradient. The resulting values for  $\mathbf{R}_\alpha$  and  $\mathbf{x}_\alpha$  (and  $\mathbf{p}_\alpha$  for the Coherent State case) were then used to compute the hessian of the effective potential. The eigenvalues and eigenvectors were computed by `numpy.linalg.eigh`.

The electronic state populations for each bead were found from the electronic position and momentum variables, using a Wigner Estimator. For the Mapping Variable formulation, the populations were calculated from

$$[\mathbf{x}_\alpha]_n^2, \quad (59)$$

since it was not written to include electronic momentum variables. For the Coherent State formulation, the populations were found using

$$\frac{[\mathbf{x}_\alpha]_m^2 + [\mathbf{p}_\alpha]_m^2}{\sum_n [\mathbf{x}_\alpha]_n^2 + [\mathbf{p}_\alpha]_n^2}. \quad (60)$$

Our model used the two state potential

$$\mathcal{V} = \begin{bmatrix} \frac{1}{2}M\omega^2(r+5)^2 & \Delta \\ \Delta & \frac{1}{2}M\omega^2(r-5)^2 \end{bmatrix}. \quad (61)$$

Where  $M = 2$  and  $\omega = 1$ . The non-adiabatic limit corresponds to when  $\Delta \rightarrow 0$ , we found the instanton for the adiabatic case (high coupling,  $\Delta = 0.8$ ) and for the non-adiabatic case (low coupling,  $\Delta = 0.01$ ). We also varied the reciprocal temperature between  $\beta = 2.5$  and  $\beta = 5.0$ . Our initial guesses for the optimization were

$$R_\alpha = \cos(2\pi\alpha/N), \quad (62)$$

$$[\mathbf{x}_\alpha]_1 = [\mathbf{p}_\alpha]_1 = \sqrt{\frac{e^{-\beta_N V_{11}}}{e^{-\beta_N V_{11}} + e^{-\beta_N V_{22}}}}, \quad (63)$$

and

$$[\mathbf{x}_\alpha]_2 = [\mathbf{p}_\alpha]_2 = \sqrt{\frac{e^{-\beta_N V_{22}}}{e^{-\beta_N V_{11}} + e^{-\beta_N V_{22}}}}. \quad (64)$$

## 4 Results and Discussion

The path integral representation is exact in the limit of  $N \rightarrow \infty$ , so as we increase the number of beads, we expect the instanton to converge to a single configuration. This is observed early on in the mapping variable case, as figure 3 shows convergence for  $\beta = 2.5$  at  $N = 128$ . The coherent state case however, for the same parameters, has still not converged by  $N = 512$ , as shown in figure 4.

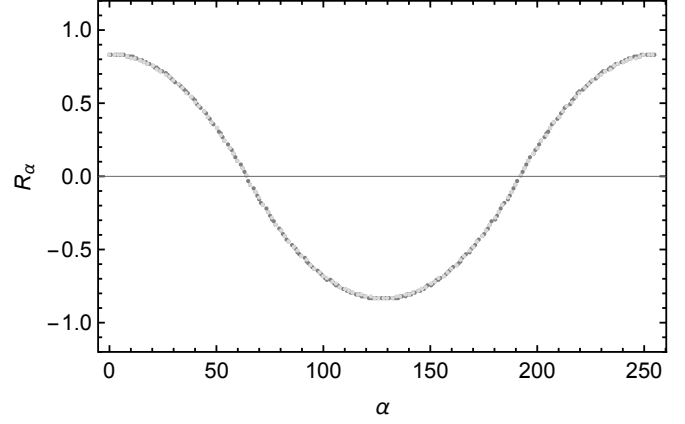


Figure 3: Nuclear bead positions for the  $H_{MV}$  potential with  $\beta = 2.5$  and  $\Delta = 0.8$  for  $N = 128$  (light gray) and  $N = 256$  (gray)

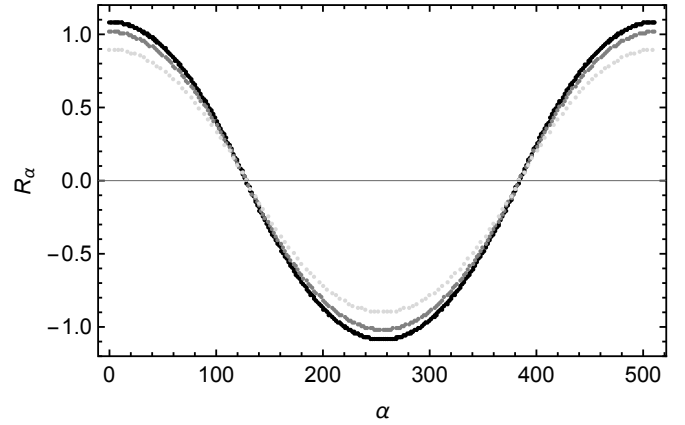


Figure 4: Nuclear bead positions for the  $H_{CS}$  potential with  $\beta = 2.5$  and  $\Delta = 0.8$  for  $N = 128$  (light gray),  $N = 256$  (gray), and  $N = 512$  (black)

For the coherent state case with  $\beta = 5.0$ , convergence occurred quickly figure 5 shows that the instanton has converged by  $N = 128$ . The bead positions for this case flatten out when they reach -5 and 5, accumulating in the bottom of the potential wells given in equation (55). It was observed that all CS instantons which stretched to the bottom of the wells (those with  $\beta > 5.0$ ) converged. This suggests that the minimizing algorithm is finding this position to be a strong minimum. If the frequency of the initial guess is doubled (so that the ring polymer

is draped over the barrier twice, with an initial guess of  $R_\alpha = \cos(4\pi\alpha/N)$ , then the coherent state  $\beta = 5.0$  case no longer converges, and its amplitude begins growing as the number of beads increases. With two cycles,  $\beta = 5.0$  is now behaving more like  $\beta = 2.5$ , as can be seen in figure 6. This is expected because below certain temperatures (above some  $\lambda\beta_c$ ), the instanton folds back on itself  $\lambda$  times. [7]

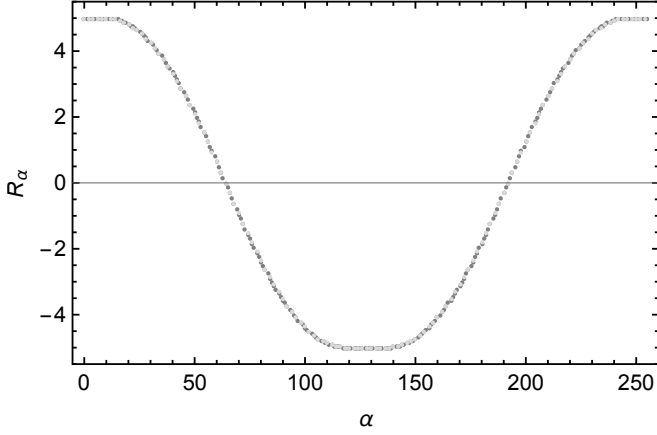


Figure 5: Nuclear bead positions for the  $H_{CS}$  potential with  $\beta = 5.0$  and  $\Delta = 0.8$  for  $N = 128$  (light gray) and  $N = 256$  (gray)

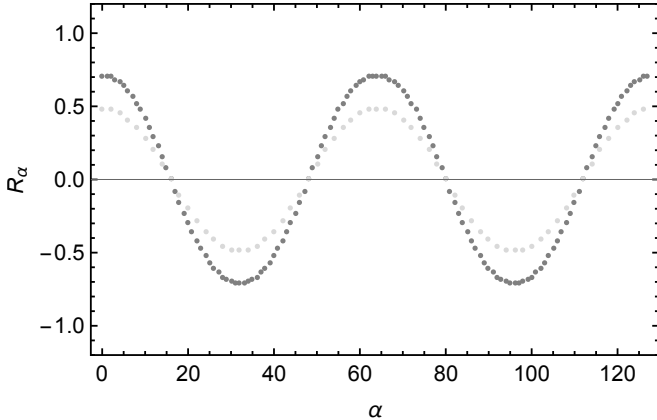


Figure 6: Nuclear bead positions for the  $H_{CS}$  potential with an initial guess of  $R_\alpha = \cos(4\pi\alpha/N)$ ,  $\beta = 5.0$  and  $\Delta = 0.8$  for  $N = 64$  (light gray) and  $N = 128$  (gray)

The CS instantons are also consistently greater than the MV results, at a high enough bead count, as is illustrated in figure 7 and 8. And by comparing the scales on those two figures, it is confirmed for both CS and MV instantons that the amplitude decreases with increasing temperature (decreasing  $\beta$ ). The results for the alternate CS Instanton however, with  $\beta = 2.5$  and  $\Delta = 0.8$ , given in figure 9 were less than the corresponding MV instanton by  $N = 256$ . Though at that point, like the original CS Instanton, it has yet to converge. So it is possible

that when it does converge, it will be close to the MV instanton.

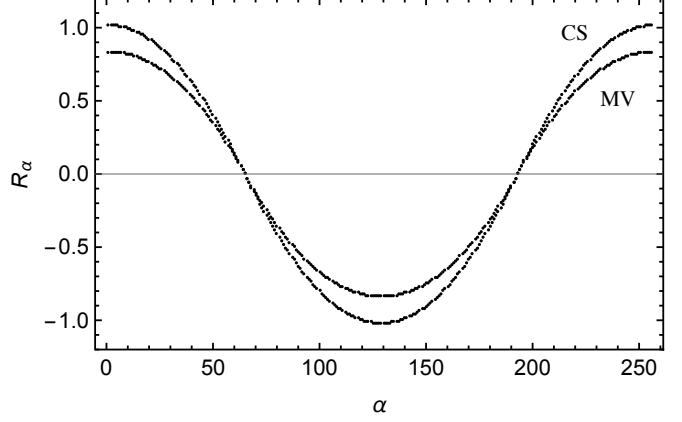


Figure 7: Nuclear bead positions for both the  $H_{CS}$  potential and the  $H_{MV}$  potential, with  $\beta = 2.5$  and  $\Delta = 0.8$  for  $N = 256$

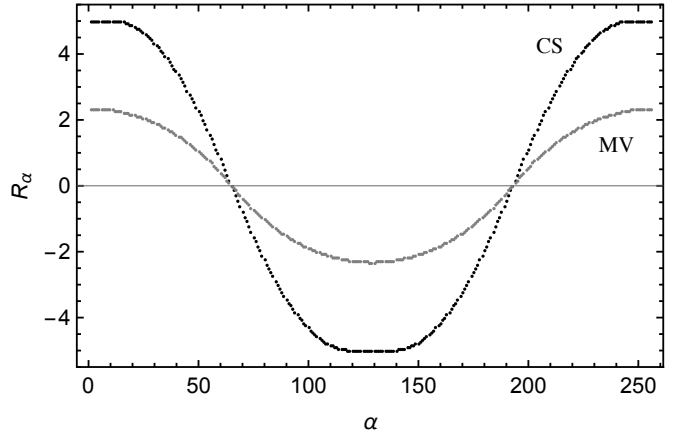


Figure 8: Nuclear bead positions for both the  $H_{CS}$  potential and the  $H_{MV}$  potential, with  $\beta = 5.0$  and  $\Delta = 0.8$  for  $N = 256$

The populations for the two cases are much more similar than the bead positions are. It is shown in figure 10 the beads closest to a given state have a population of approximately 1 for that state and 0 for the other. The beads in the middle each have a population of about 0.5, so it experiences an equal influence from both states. Some of the populations wrinkle up a bit before switching between 0 and 1. These parts of the curves are shown in 11. The transition appears to become smoother in both the mapping variable and coherent state populations for lower temperatures (increasing  $\beta$ ) and lower coupling between states (decreasing  $\Delta$ ).

## 5 Conclusions and Future Work

The nuclear ring polymer Hamiltonian was derived and used as a starting spot for deriving the mapping vari-

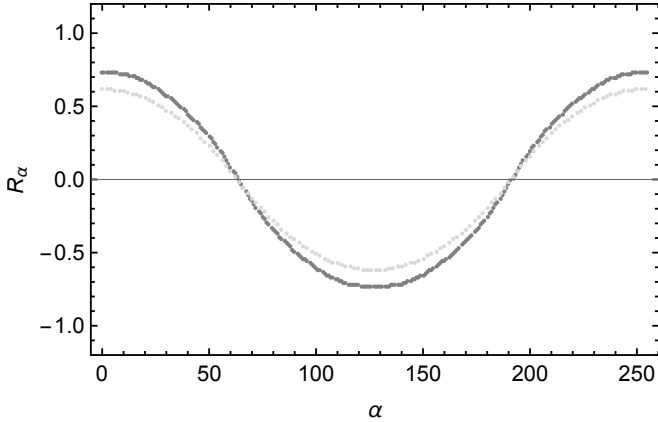


Figure 9: Nuclear bead positions the alternate  $H_{CS}$  potential, with  $\beta = 2.5$  and  $\Delta = 0.8$  for  $N = 128$  (light gray) and  $N = 256$  (gray)

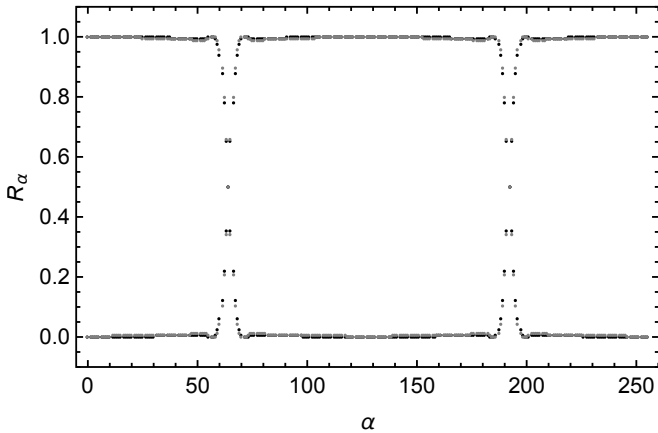


Figure 10: Populations for  $N = 256$ , black denotes coherent state and gray denotes mapping variable

able and coherent state Hamiltonians, by way of Stock-Thoss mapping from discrete electronic states to continuous bases. An alternate form of the coherent state Hamiltonian was also proposed. The bead positions did not converge for a reasonable number of beads in the coherent state case, and appeared to be moving away from those in the mapping variable case. There were other challenges which were not discussed, such as how the MV hessian would consistently yield one negative eigenvalue and  $N - 1$  positive eigenvalues (indicating a first order saddle point), while the CS hessian would consistently give one negative eigenvalue and  $N - 1$  approximately 0 eigenvalues. This and the differences in the nuclear instantons, despite the similar derivations and exact nature, warrant further study.

## Acknowledgements

I would like to thank Dr. Nandini Ananth, for her support this summer, and for inventing MV-RPMD. I would

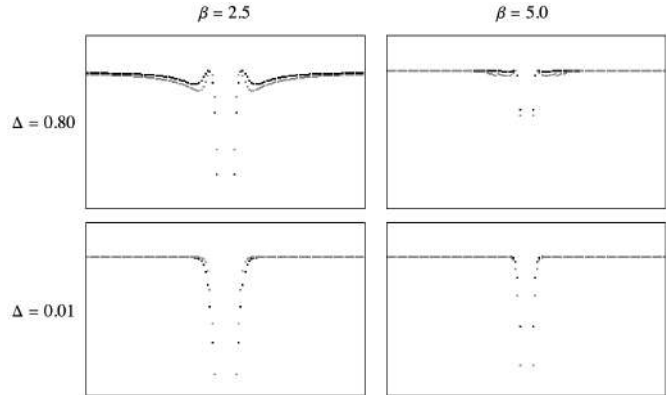


Figure 11: Zoomed in populations for  $N = 256$ , black denotes coherent state and gray denotes mapping variable, each plot is from beads 128 to 256 on the horizontal axis and from population 0.92 to 1.02 on the vertical axis

also like to thank the Cornell Center for Materials Science for providing this REU program. This work was supported by the Cornell Center for Materials Research with funding from the Research Experience for Undergraduates program (DMR-1460428 and DMR-1719875).

## References

- [1] J. Richardson et. al., *Science* **351** (6279), 1310-1313.
- [2] M. Tuckerman, *Statistical Mechanics: Theory and Simulation*, Oxford University Press: New York, 2010.
- [3] N. Ananth, *J. Chem. Phys.* **139**, 124102 (2013).
- [4] S. Chowdhury and P. Huo, *J. Chem. Phys.* **147**, 124109 (2017).
- [5] G. Stock and M. Thoss, *Phys. Rev. Lett.* **78**, 578 (1997).
- [6] R. H. Byrd, P. Lu and J. Nocedal. A Limited Memory Algorithm for Bound Constrained Optimization, (1995), SIAM Journal on Scientific and Statistical Computing, 16, 5, pp. 1190-1208.
- [7] J. Richardson and S. Althorpe, *J. Chem. Phys.* **131**, 214106 (2009).

# Effects of Oxidation Time and Temperature on Supercapacitor Performance of Spinel Ni<sub>1.5</sub>Co<sub>1.5</sub>O<sub>4</sub> Monodisperse Nanoparticles

Whitney Tso<sup>1</sup>, Cindy Chen<sup>2</sup>, Anuj Bhargava<sup>2</sup>, and Richard Robinson<sup>2</sup>

<sup>1</sup>Department of Materials Science and Engineering, University of Illinois Urbana-Champaign, Champaign, IL 61820

<sup>2</sup>Department of Materials Science and Engineering, Cornell University, Ithaca, NY 14853

**Abstract:** Recently, there has been a rising interest in the research of supercapacitors due to their rapid charge and discharge speed and their long discharge cycle life. Nanotechnology has been one of the ways to resolve the increase in demand for better electronics, such as using nanoparticles in a supercapacitor. Ni-Co nanoparticles are synthesized first, then coated on a copper electrode through EPD, then oxidized at various temperatures and durations in the furnace. The supercapacitor performance of the samples are determined by running CV and CD tests on a coin cells with a two-electrode system. The samples are characterized with ICP-MS and TEM to determine the particle shape and stoichiometry. It was observed that samples oxidized at a lower temperature and longer durations are able to retain the size and shape of nanoparticles, and has better supercapacitor performance.

## Introduction

In recent years, there has been a growing interest in the research of supercapacitors. The idea is that a supercapacitor has the ability to store much higher energy density than a normal capacitor and has greater power density than a normal rechargeable battery. Other than the ability to charge and discharge at an amazing rate, it also has a much longer discharge cycle life. There are many applications and potential for supercapacitors in industry. Companies have started to incorporate supercapacitors in their hybrid or electric automobiles for its rapid charging and discharging capabilities.

A supercapacitor has a similar structure compared to a normal capacitor, but works in a very different manner. Normal capacitors are composed of two plates separated by a thick dielectric material that polarizes under an electric field. In a supercapacitor, there are two plates that are separated by a much smaller distance. The two plates are soaked in electrolyte and separated by a thin

separator made from an insulating material. The ions in the electrolyte move towards the plates when charging and away when discharging. Therefore, the capacitance of a supercapacitor is proportional to the effective surface area of the plates.

As the demand for better electronics increases, people started to turn to nanotechnology for answers. Nanoparticles are generally at the scale of 1-100 nm, which means they have a small volume but large surface area relatively. This characteristic of nanoparticles presents a lot of potential in supercapacitors.

Many researches have been done to analyze the supercapacitor performance of metal oxides, especially base transition metal oxides [1]. Study has also shown that binary metal oxides with spinel structure has better performance as it amalgamates the supercapacitor properties of two monometallic oxides, such as Co<sub>3-x</sub>Mn<sub>x</sub>O<sub>4</sub> that combines the properties of Co<sub>3</sub>O<sub>4</sub> and MnO<sub>2</sub> [2]. NiO has shown to have better

electrochemical performance compared to  $\text{MnO}_2$ , therefore the binary metal oxide  $\text{Ni}_x\text{Co}_{3-x}\text{O}_4$  shows great potential in the application of supercapacitors [1]. In this report, we studied the spinel material,  $\text{Ni}_{1.5}\text{Co}_{1.5}\text{O}_4$ , as the performance was found to be the best at near equal ratio of the two metal cations [2].

## Experimental Section

### *Synthesis of monodisperse Ni-Co nanoparticles*

The synthesis method used is modified from a previous experiment [3]. 0.25g of nickel acetate tetrahydrate, 0.25g of cobalt acetate tetrahydrate, 0.64mL of 99.9% oleic acid, and 40mL of diphenylether (DPE) is placed in a 250mL three-neck flask with a glass stir bar. The flask is placed under vacuum first, and then heated to 200°C under nitrogen. 3.5mL of trioctylamine (TOA) and 0.45mL of trioctylphosphine (TOP) is then added into the flask. The temperature of the flask is then increased to 250°C.

In another three-neck flask, 2.12 g of 1,2-dodecanediol and 10mL of DPE is heated to 80°C for 15 minutes under vacuum. The solution is taken out and rapidly injected into the first flask. The solution is allowed 20 minutes to react and nucleate before it is quenched to room temperature in a water bath.

The solution is poured into tubes and centrifuged, causing the nanoparticles to sink to the bottom of the tubes. The liquid is then poured out and hexane is added to suspend the nanoparticles.

### *Electrophoretic deposition (EPD)*

EPD is used to deposit a thin and even layer of Co-Ni nanoparticles on top of the copper plates. Two stainless steel plates are placed at

a small distance apart, parallel to each other. Those are connected to a voltage source at the positive and negative side respectively. A circular copper plate is weighed first, then stuck to the inner side of the positive steel plate.

0.5mL of the nanoparticles in solution is further diluted with 9.5mL of hexane and sonicated in a water bath for at least 2 minutes. The stainless steel plates are placed in the diluted solution. The DC voltage source is set to 600 V. Generally, the process is about 30 seconds to 5 minutes. The target active mass is around 0.1 mg.

The copper plates with metal nanoparticles coated are calcined in the furnace at various durations and temperatures. The heating rate is 10°C/min to ensure all nanoparticles are at the same temperature.

### *Sample Characterization*

The cobalt-to-nickel ratio is analyzed using inductively coupled plasma mass spectrometry (ICP-MS) to ensure that we are synthesizing a material close to equal ratio of the metal cations. The shape and size of metal nanoparticles are analyzed using transmission electron microscopy (TEM). This technique is also used to characterize the metal oxide, such as the state of oxidation and shape of particles, after undergoing various oxidation parameters.

### *Electrochemical measurements*

The electrochemical properties of the samples were studied by cyclic voltammetry (CV) and cyclic charge discharge (CD) on a two-electrode system with the sample as the anode, a carbon cloth as the cathode, and lithium bis(trifluoromethanesulfonyl)imide (LiTFSI) as the electrolyte. The scan rate for CV tests are 50 mV/s, and the scan rate for

CD tests are 0.1 A/g. The energy density (E), power density (P), and specific capacitance (C) were calculated using Eqn. 1, 2, and 3 [2].

$$E = \int \frac{VI}{m} dt \quad [\text{Eqn. 1}]$$

$$P = \frac{E}{\Delta t} \quad [\text{Eqn. 2}]$$

$$C = \frac{I \Delta t}{m \Delta V} \quad [\text{Eqn. 3}]$$

V is the voltage, I is the discharge current density, m is the active mass of the material on the copper electrode, and  $\Delta t$  is the discharge time.

## Results and Discussion

Before oxidizing any samples, the particles are characterized with ICP-MS and TEM. We analyzed the Ni to Co ratio to be 1.48 to 1.52. Fig. 1 shows the Co-Ni particles before oxidation. The average diameter measured is  $20.8 \text{ nm} \pm 1.8 \text{ nm}$ . The relatively low dispersity is another evidence that the synthesized particles are good for testing.

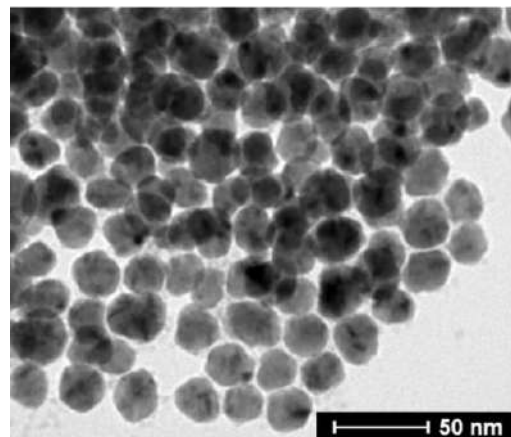
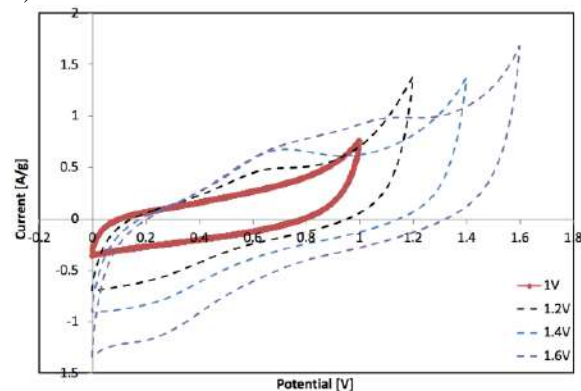


**Fig. 1** TEM images of Co-Ni nanoparticles.

In order to conduct CD tests on the coin cells, the voltage range needs to be optimized. As our goal is to analyze the supercapacitor performance of the samples, we want to

maximize the voltage range, but without having the cell go through irreversible redox reactions. This can be determined by conducting CV tests on the samples. Fig. 2 shows the CV tests conducted on two different coin cells. An irreversible redox reaction can be observed through a peak in the CV curve. As we increase or decrease the voltage limits, a peak at around 0.6 V would appear. This is indicative that we have passed the optimal voltage range. It is determined that the voltage range for further CD tests are from -0.4 V to 1 V. Furthermore, the rectangular CV curve shape that can be seen from Fig. 2 is another sign that the sample exhibits supercapacitor characteristics. The curves are dependent on the change in voltage and capacitance. Since we are keeping the rate constant, the larger area under the curve represents the material having a better capacitance.

a)



b)

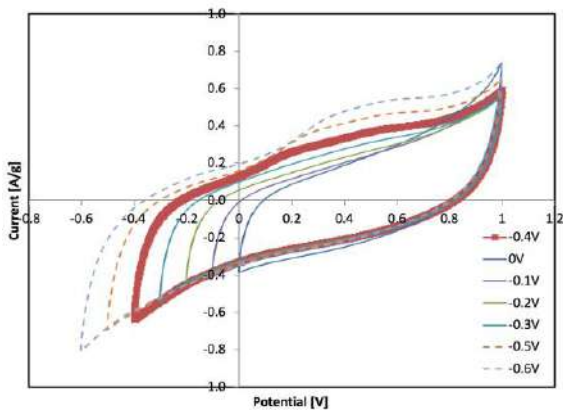


**Fig. 2** CV curves of coin cells to optimize voltage range. The red curve shows the optimal voltage limit. a) testing the upper voltage limit by holding the lower limit at 0 V and changing the upper limit. b) testing the lower voltage limit by holding the upper limit at 1 V.

Fig. 3 shows the different oxidation parameters we have tested. The samples are imaged under TEM to observe the shape of the oxidized particles. Based on other studies, it has been observed that we can oxidize the metal particles into spinel phase at around 200 – 300 °C. We decided to set the temperature at 250 °C as a starting point, and vary the oxidation time.

Sample	Time [hrs]	Temperature [°C]
1	2	250
2	4	250
3	8	250
4	12	225

**Fig. 3** Oxidation parameters of various samples and their respective labelling.

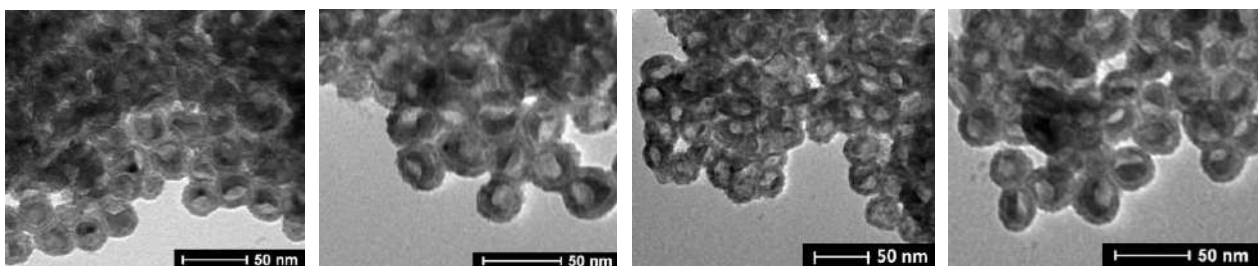


**Fig. 4** TEM images of oxidized Co-Ni nanoparticles. From left to right: Sample 1 (oxidized at 250 °C for 2 hours), Sample 2 (oxidized at 250 °C for 4 hours), Sample 3 (oxidized at 250 °C for 8 hours), and Sample 4 (oxidized at 225 °C for 12 hours).

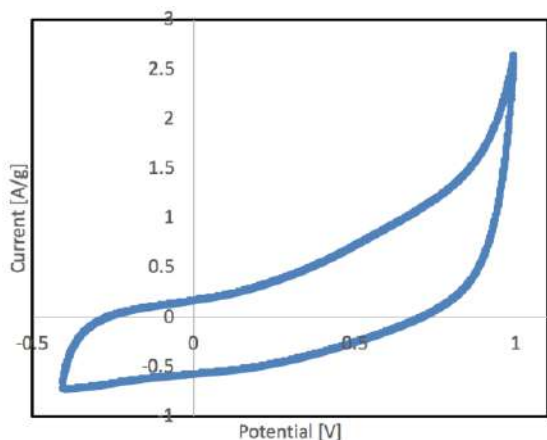
From the TEM image of Sample 1 (Fig. 4a), we observe that the metal oxide particles are nanosized, but has a core-shell structure with a center that is half filled. This is indicative that this sample is partially oxidized. The darker region in the core is the unoxidized Ni-Co, the lighter region in the core is a hole where the metal particles moved outwards to form the metal oxide shell.

The TEM image of Sample 2 (Fig. 4b) also show signs of partial oxidation, but there is an observable increase in the number of particles that are fully oxidized. Then we decided to increase the oxidation time more in order to fully oxidize all the particles.

However, based on the TEM image of Sample 3 (Fig. 4c), we can observe signs of sintering. The nanoparticles have started to fuse together to form one big particle. Even though at this oxidation parameter, we can obtain a more complete spinel material, it has lost the characteristics of a nanoparticle that could potentially make it a better supercapacitor. We then tested another sample at a lower temperature and a longer duration.

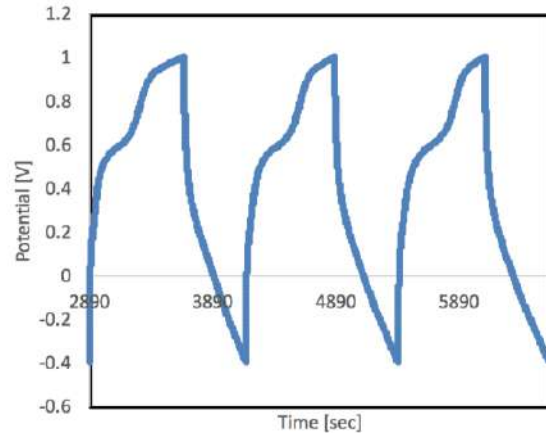
From the TEM image of Sample 4 (Fig. 4d), we can see that, while it is has more partially oxidized particles compared to Sample 3, it has a lower amount of sintering. This sample has better particle structure as it retains more of the nanoparticle characteristics, allowing the sample to have greater surface area.

Fig. S1 in supplementary information shows the CV data collected from the coin cells assembled with the various samples as the cathode material. By increasing the oxidation time, it can be observed that the cells better resemble the rectangular shape, which is an indication that the material performs like a supercapacitor. Sample 4 (Fig. 5) has the largest area under the CV curve, which is a sign that it has the best supercapacitor performance compared to other samples.



**Fig. 5** CV curve of Sample 4.

In order to quantitatively calculate the supercapacitor performance, we conducted the CD test on Sample 4 (Fig. 6). Fig. S2 plots the data of a CD test of Sample 2 that has worse supercapacitor performance in comparison. Using this data, we are able to calculate the energy density, power density, and specific capacitance using Eqn 1, 2, and 3. We only consider the discharge portion of the CD curve for calculation. Fig. 7 tabulates the average energy density, power density, and specific capacitance of all four samples. Based on the calculated values, we can see that Sample 4 has the best supercapacitor performance compared to the other samples.



**Fig. 6** CD curve of Sample 4 with scan rate of 0.1A/g from -0.4 V to 1 V. This is a cropped plot of cycle 2 to 4 only.

Sample	Energy Density [W h/kg]	Power Density [W/kg]	Specific Capacitance [F/g]
1	3.88e-5	0.139	1.05e-3
2	6.99e-6	0.0251	2.15e-6
3	9.25e-6	0.0333	1.58e-6
4	0.142	1.00	37.9

**Fig. 7** Average calculated energy density, power density, and specific capacitance of all the samples.

## Conclusion

In summary, oxidizing monodisperse Co-Ni nanoparticles at lower temperatures and longer durations yield better supercapacitor performances. This could be contributed to the particles being fully oxidized without sintering. However, the supercapacitor performance is still lower than what is expected. Therefore, while this material shows promising results, further studies will be conducted on refining the oxidation parameters and decrease particle size to fabricate better supercapacitor material.

## Acknowledgements

I would like to thank the whole Robinson research group, especially Dr. Richard Robinson and Anuj Bhargava, for their support on this project. I would also like to thank the CCMR REU program funded by NSF for giving me this opportunity to participate in the summer program.

## References

- [1] Wu, Zhibin et al. "Transition Metal Oxides As Supercapacitor Materials." *Nanomaterials in Advanced Batteries and Supercapacitors* (2016): 317-344. Web. 31 July 2018.
  - [2] Perera, Sanjaya D. et al. "Enhanced Supercapacitor Performance For Equal Co-Mn Stoichiometry In Colloidal Co<sub>3</sub>-Xmno<sub>4</sub> Nanoparticles, In Additive-Free Electrodes." *Chemistry of Materials* 27.23 (2015): 7861-7873. Web.
  - [3] Murray, C.B. et al. "Monodisperse 3D Transition-Metal (Co,Ni,Fe) Nanoparticles And Their Assembly Into Nanoparticle Superlattices." *MRS Bulletin* 26.12 (2001): 985-991. Web.
-

## Supplementary Information

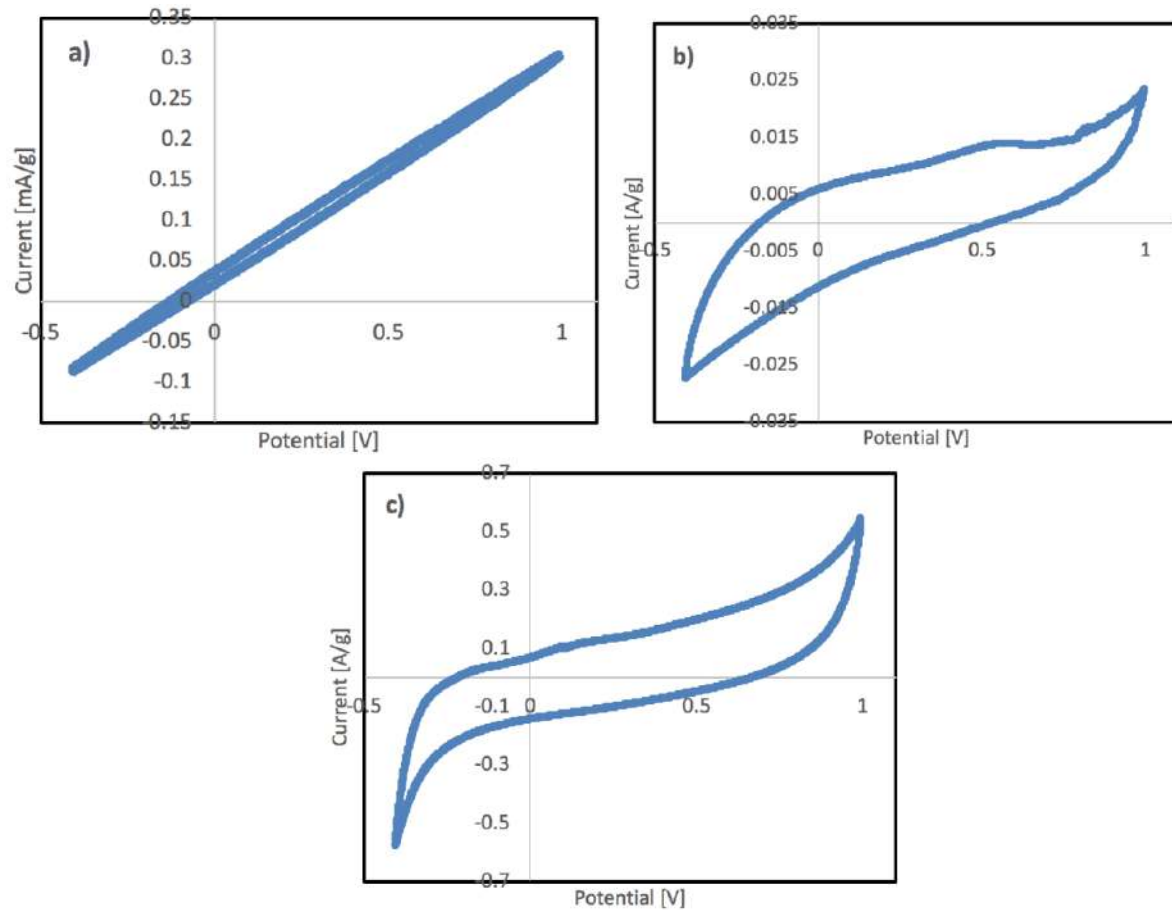


**Fig. S1** CV curves of coin cells with the cathode coated with a) Sample 1, 250 °C for 2 hours, b) Sample 2, 250 °C for 4 hours, and c) Sample 3, 250 °C for 8 hours.

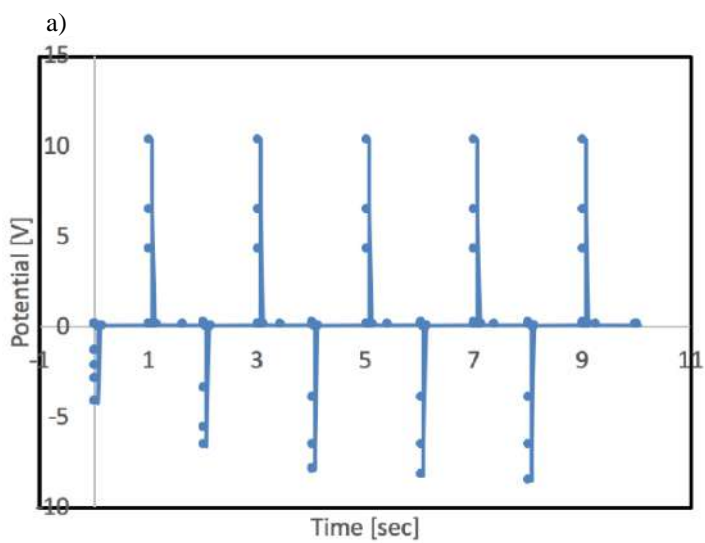


**Fig. S2** a) CD plot of Sample 2 with scan rate of 0.1 A/g from -0.4 V to 1 V.

# Self-folding capillary origami with atomically thin sheets

Maritha A. Wang, Michael F. Reynolds, Kathryn L. McGill, Marc Z. Miskin, Paul L. McEuen

Department of Physics, Cornell University, Ithaca, NY 14853

**Folding flat sheets into three-dimensional (3D) structures with the surface tension of liquid droplets depends on an interplay between capillary and bending forces. Such ‘capillary origami’ can be done by tuning the thickness of polymeric films such that bending energies are significantly smaller than surface energies, leading to millimeter-scale structures. To expand the size regime of this surface tension-driven origami to the sub-50 micron scale, we utilize monolayer Molybdenum Disulfide ( $\text{MoS}_2$ ) sheets, which are atomically thin and have ultralow bending forces. We demonstrate micron-scale capillary origami and further make this origami self-folding via design of appropriate dynamic binary and ternary liquid systems.**

Actuation of flat sheets into 3D structures using liquid droplets enables promising applications such as actuation of micron-scale robots, sensing and capturing of liquid cargo, drug delivery, and separation of emulsions such as oil spills in bodies of water. Furthermore, transformation of flat materials into 3D structures is particularly attractive for microscale fabrication since it is difficult to build complex structures out of plane using conventional photolithography. While several avenues of actuation have been explored including modulating external magnetic fields, applying electric fields, controlling environmental pH, and external thermal actuation<sup>1-8</sup>, the use of surface forces is particularly attractive because there is no need for actuation from outside of the system. Furthermore, design considerations are limited to the bending energy of the sheet and surface interactions with the droplet, simplifying design and fabrication.

Relating bending stiffness  $B$  and interfacial tension  $\gamma$  gives the smallest size of a sheet that can be folded by a liquid droplet, which defines the elastocapillary length:

$$L_{EC} = \sqrt{\frac{B}{\gamma}} \quad (1)$$

Thus, since thinner sheets have smaller bending stiffnesses, they enable smaller structures to be folded. Surface tension-driven folding of sheets has been studied at the millimeter scale by utilizing thin polymer films<sup>9</sup> which have  $L_{EC} \approx 10^{-3}\text{m}$ . However, this regime can be expanded to the micron-scale by using even thinner materials. Some works have indeed achieved capillary origami structures on the order 50-100  $\mu\text{m}$  by utilizing silicon nitride structures<sup>10</sup>. This size regime can be further decreased: Two-dimensional (2D) materials, which are the thinnest class of materials at atom-scale thicknesses, are the ideal candidate for such surface force-driven folding and should enable the folding of flat materials into 3D structures at the smallest possible scale.

Here, we expand the established macroscale regime of droplet-wrapping and capillary origami<sup>9-17</sup> to the sub-50 micron scale by employing the 2D material, monolayer  $\text{MoS}_2$ , which is three atoms thick. Theoretical work on the bending stiffness of monolayer  $\text{MoS}_2$  has shown that the individual Mo and S layers have a similar bending stiffness to that of graphene<sup>18</sup>, which has a measured bending stiffness<sup>19</sup> on the order of  $\sim 1 \text{ keV} \approx 10^{-16} \text{ J}$ . We thus approximate the bending modulus of atomically thin materials, including monolayer  $\text{MoS}_2$ , as  $B \approx 10^{-16} \text{ J}$ . From theoretical studies, we further estimate the stretching modulus<sup>20</sup> as  $Y \approx 10^2 \text{ N/m}$ .  $\text{MoS}_2$  is thus an ideal material for droplet-wrapping: Due to its high out-of-plane flexibility and low in-plane flexibility, it behaves like atomic Saran wrap in the high-bendability regime given by<sup>8</sup>:

$$\frac{B}{w^2} \ll \gamma \ll Y \quad (2)$$

This relationship represents the regime in which the sheet does not stretch but can fold and bend with negligible energetic cost. When these conditions are met, the sheets deform the droplet into geometries that minimize surface energy without stretching the wrapping material. By choosing a system with  $\gamma \approx 10^{-2} \text{ N/m}$ , which is a typical interfacial tension between liquid-liquid interfaces<sup>21</sup>, we remain within this high-bendability regime with  $\text{MoS}_2$  sheets of radius  $W \approx 10^1-10^2 \mu\text{m}$  and can observe how 2D sheets can be transformed into 3D structures via capillary force-driven origami.

## Experimental:

### Sheet Fabrication:

Monolayer  $\text{MoS}_2$  was grown via metal-organic chemical vapor deposition (MOCVD)<sup>22</sup> onto fused silica coverslips (diameter 25 mm, thickness 170 micrometers). Subsequent fabrication was performed by using long-exposure photolithography on poly(methyl methacrylate) (PMMA) spin coated onto the  $\text{MoS}_2$ . This method was chosen to avoid water-based solvents and developers, which caused the  $\text{MoS}_2$  to delaminate.

Circular, square, and triangular mask patterns were designed in L-Edit CAD software and printed on photomasks. The corresponding  $\text{MoS}_2$  geometric shapes were then patterned with standard photolithography techniques and etched with sulfur hexafluoride ( $\text{SF}_6$ ) plasma. For paneled sheets, a mask with typical cube, tetrahedron, cylinder, and flower fold patterns was used. Additionally, a 100 nm layer of copper (Cu) was first patterned and deposited onto the  $\text{MoS}_2$  using e-beam evaporation before etching  $\text{MoS}_2$  shapes around the panels. Following these photolithography steps, the coverslips were soaked in acetone overnight to remove the PMMA layer.

Immediately before conducting capillary origami experiments, the sheets (both un-paneled and paneled) are

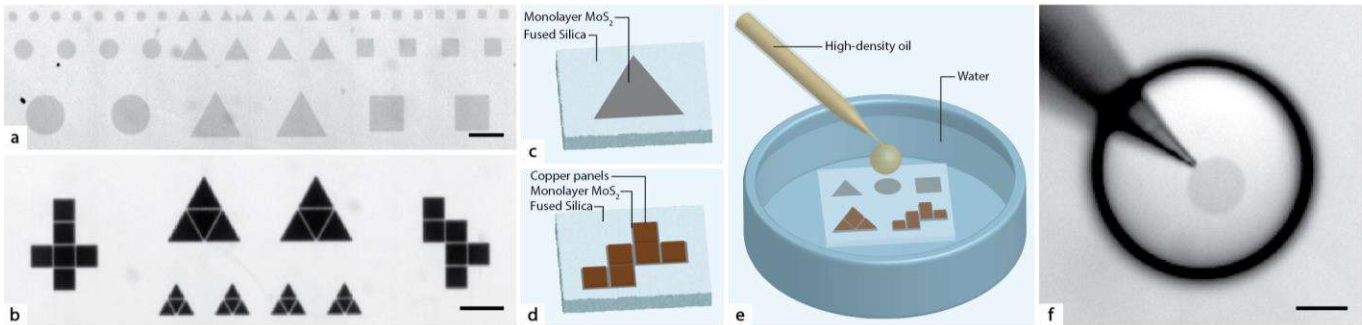


**Fig. 1 | Devices and experimental setup**

**a**, MoS<sub>2</sub> sheets for wrapping microdroplets. **b**, MoS<sub>2</sub> sheets with 100 nm Cu panels. **c, d**, Schematic showing the structure of MoS<sub>2</sub> and paneled MoS<sub>2</sub> sheets. **e**, Schematic of released sheets (after an HF etch) submerged in water with a microdroplet of an organic solvent (attached to a micropipette) above the sheets. **f**, MoS<sub>2</sub> sheet on a Fluorinert microdroplet attached to a micropipette tip submerged in water. All scale bars are 50  $\mu\text{m}$ .

released from the coverslip by a 20-90 sec hydrofluoric acid (HF) etch (1:10 dilution in water). The HF etches the coverslip, undercutting the un-paneled and paneled MoS<sub>2</sub> sheets, thus releasing the sheets from the chip surface. The coverslip is then dipped in a large water bath to dilute the HF to negligible concentrations and is then placed in a home-built cuvette or a plastic petri dish with a glass coverslip bottom for optimal imaging.

#### Experimental Setup:

To observe the capillary origami dynamics, the general scheme involves observing MoS<sub>2</sub> sheets wrapping either Fluorinert FC-70 or 1:1 chloroform/acetone droplets in a water bath (Fig. 1).

After the HF release etch, the petri dish is placed on the stage of an inverted microscope that is lit from above. Bottom view and side view imaging is conducted in transmission mode with a white-light source. (All images shown are transmission white-light images that have undergone linear contrast adjustments.) An electronic micromanipulator is then used to position a glass micropipette (2-10  $\mu\text{m}$  inner diameter) under the water surface and over the MoS<sub>2</sub> shapes. The micropipette, filled with Fluorinert or 1:1 acetone/chloroform, organic solvents with higher density than water, is attached to a PicoPump, allowing pressure spikes to be applied to the fluid within. These pressure spikes generate Fluorinert (for example) droplets, which either remain attached to the pipette tip or detach, depending on the ejection pressures and the amount of time over which the pressure was exerted (typically ~20 psi and 100 ms for attached droplets and ~60 psi and 100 ms for detached droplets). In the case that droplets remain attached, the pipette tip is then lowered to the MoS<sub>2</sub> shapes to pick them up off of the surface. Wrapping dynamics can then be observed by adjusting background holding pressure or using a vacuum pump to controllably shrink the droplets. In the case that droplets detach from the pipette tip, 1:1 acetone/chloroform is used as the droplet liquid. These droplets are dropped on MoS<sub>2</sub> shapes on the surface. Since chloroform is slightly soluble in water (0.8 mg/mL) (and acetone is fully miscible with water), these droplets slowly shrink and the MoS<sub>2</sub> shapes wrap the droplets on the surface.

#### Results and Discussion:

We first observe droplet-wrapping dynamics with MoS<sub>2</sub> sheets (Fig. 1a) adhered to Fluorinert microdroplets on the micropipette tip. For sheets with effective radius  $W$ , Fluorinert

microdroplets of radius  $R \geq W$  were made in the water-filled petri dish (Fig. 1e) using pressure spikes of approximately 20 psi from a PicoPump. The pipette was then lowered and brought in contact with a sheet on the substrate from above. For well-released MoS<sub>2</sub> or MoS<sub>2</sub>/copper sheets, good adhesion between the Fluorinert and the sheet was observed, and sheets could be picked up off of the substrate surface as soon as the droplet appeared to be in contact with the majority of the sheet. With the sheet on the surface of the microdroplet, the microdroplet was then shrunk through the use of ambient back-pressure and/or the use of a vacuum pump (~1 mmHg/in<sup>2</sup>). The MoS<sub>2</sub> sheets not only appeared to remain adhered to the surface of the droplet as it shrank, but wrinkled and folded into geometric shapes, deforming the droplet in the process. The final folded packets remained on the end of the pipette tip.

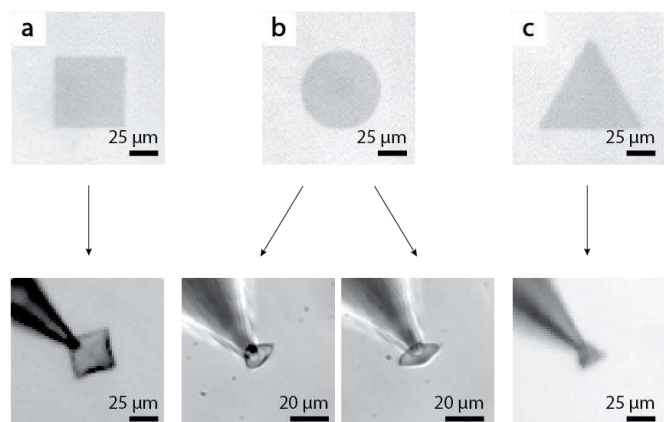


**Fig. 2 | Final wrapping states of MoS<sub>2</sub> sheets**

Representative images of (a) square sheet, (b) circular sheet, and (c) triangular sheet and the most common corresponding wrapped geometries observed.

For these MoS<sub>2</sub> sheets, we observe that each type of starting shape (circle, triangle, square) tends toward certain final geometries at the completion of droplet-wrapping. Triangular sheets tend toward triangular packets, square sheets tend toward square-packets, and circular sheets tend toward either “empanada” geometries or parallelogram-packets (Fig. 2). The existence of two energetically favorable states for circular sheets has been observed at the millimeter scale with polystyrene sheets<sup>9</sup>, and we expected this behavior to scale to 2D sheets, as was observed. Transmission white-light images were taken of the

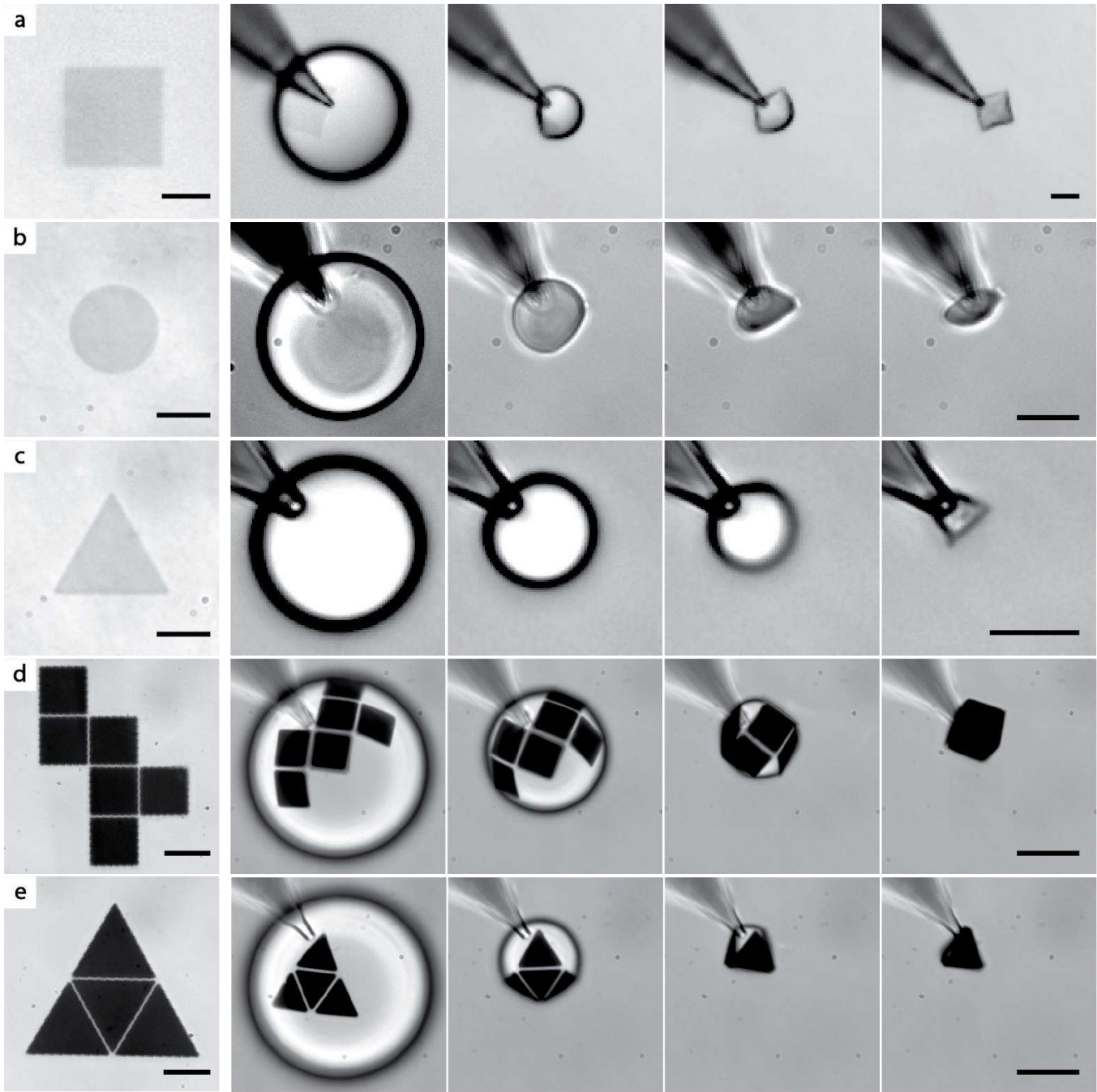


**Fig. 3 | Capillary origami with bare MoS<sub>2</sub> sheets and paneled MoS<sub>2</sub> sheets**

Representative image and image series showing folding dynamics of (a) a square sheet, (b) a circular sheet, (c) a triangular sheet, (d) a paneled cube folding pattern, and (e) a paneled triangular prism folding pattern wrapping a droplet of Fluorinert attached to a micropipette tip in water. Scale bars for (a), (d), and (e) are 30  $\mu\text{m}$ . Scale bars for (b) and (c) are 20  $\mu\text{m}$ .

droplet-wrapping process, and the droplet-wrapping dynamics for these flat sheets are shown in Fig. 3a-c.

Though these MoS<sub>2</sub> sheets do tend towards certain final geometries, the final geometry varies between sheets of the same type simply because such homogeneous sheets can fold and wrinkle in countless ways. However, for many applications including micro-robotics actuation, it is desirable to have precise control to generate reproducible geometries.

We achieve pre-programmed final geometries by introducing rigid copper panels (100 nm thick) to areas of the sheets (Fig. 1b, d), thereby restricting folding to hinges. When microdroplets of Fluorinert are touched to these paneled sheets following the same procedure as with the un-paneled sheets, the paneled sheets similarly adhere to the microdroplet if they are well-released. Upon shrinking the microdroplet, we observe that tetrahedron folding patterns consistently fold into tetrahedrons around

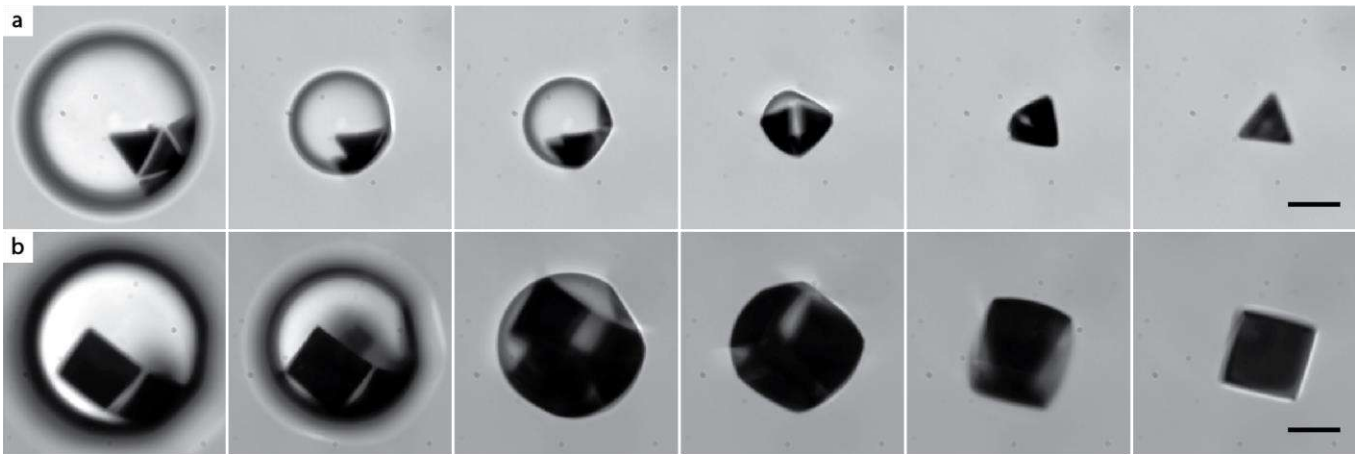


**Fig. 4 | Spontaneous capillary origami**

Image series capturing dynamics of spontaneous folding of (a) a triangular prism folding pattern and (b) a cube folding pattern about a chloroform/acetone microdroplet due to the diffusion of acetone and chloroform into the water phase. Scale bars are 25  $\mu\text{m}$ .

microdroplets while cube folding patterns correspondingly fold into cubes (Fig. 3d, e). These folded packets remain on the pipette tip. Furthermore, due to the large areas of rigid panels, these paneled sheets are more durable than the bare MoS<sub>2</sub> sheets: Upon applying another pressure spike to the micropipette, a microdroplet quickly grows from within these 3D structures, causing them to return to a state similar to when they are first picked up: The panels of the sheets all remain adhered to the droplet surface. By deflating and re-inflating these microdroplets, these tetrahedrons and cubes can be unfolded and folded repeatedly.

In addition to being able to control the final geometries of the wrapped sheet and droplet, it is also desirable to engineer this wrapping process without the need for a pipette tip applying back pressure in order for the wrapping process to occur. Such self-folding processes are useful as they do not require external activation and enable scalability of processes. We design such a process by selecting 1:1 chloroform/acetone as the microdroplet solvent due to chloroform's slight solubility in water. Acetone was added because it was experimentally observed to increase adhesion of the chloroform droplet to the paneled sheets. When chloroform/acetone microdroplets are dropped onto paneled sheets, the sheets wrap the droplets as the droplets shrink due to volume dissolving into the water phase (Fig. 4). While a pipette was still used to drop the chloroform/acetone droplets onto the tetrahedron folding pattern in Fig. 4, we believe that it is possible to achieve large-scale parallelization of self-folding capillary origami by taking advantage of the solubility properties of various liquids.

In our most recent work towards enabling this parallelization of micron-scale self-folding structures, we utilize a ternary system composed of acetone, chloroform, and water and employ the Ouzo effect<sup>23</sup>, which allows us to tune the concentration and size of chloroform microdroplets in a solution of acetone and water by using water/acetone/chloroform miscibility data from Ref. 24. Acetone and chloroform are fully miscible, and acetone and water are fully miscible, while chloroform is only slightly soluble in water. By adding water to a 5.9 wt% solution of chloroform in acetone until the solution appears slightly cloudy, micron-scale chloroform droplets homogeneously nucleate out of the solution.

Since chloroform is much denser than water and acetone, it falls to the bottom of the solution. In our preliminary experiments, we observe that when a substrate with paneled sheets is placed in this acetone/chloroform solution and then water is added, the chloroform droplets tend to gather and grow on the sheets while simply rolling off the rest of the substrate. Figure 5 shows an image of chloroform droplets covering most sheets in the field of view.

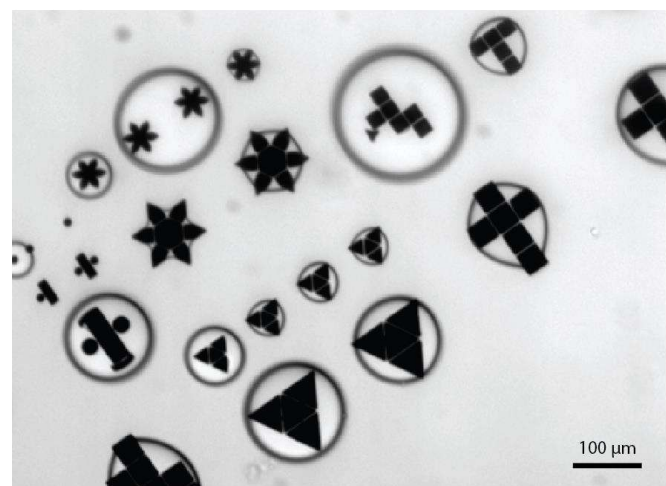


**Fig. 5 | Chloroform droplets on multiple paneled sheets simultaneously**  
By tuning a chloroform/acetone/water ternary system, chloroform homogeneously nucleates out of the solution and gathers on the paneled sheets

While in this particular case, sheets were not fully released from the surface due to an insufficient HF etch time, we believe that this preliminary data shows that this utilization of a ternary system is promising for enabling parallelization of self-folding micron-scale origami.

#### Conclusion:

We have demonstrated capillary force-driven, self-folding origami at the micron scale using MoS<sub>2</sub>, thereby expanding the size regime of capillary origami to the sub-50  $\mu\text{m}$  scale. While unpaneled sheets demonstrate similar folding dynamics as those observed at the millimeter scale, we demonstrate further control

over the final folded geometries through the use of rigid metal panels. By additionally employing tunable binary and ternary liquid systems, we show promising results indicating that parallelization of self-folding structures is feasible. Micron-scale capillary origami enables applications such as the actuation of micron-scale devices in addition to the sensing and capturing of liquid cargo, which may be utilized for applications ranging from drug delivery to liquid separation processes. These surface tension-driven origami techniques can also easily be applied to other 2D materials with other mechanical properties, highlighting the possibility of much more complex micron-scale origami structures. Furthermore, the wide variety of electronic and optoelectronic properties of 2D materials offer the opportunity for micron-scale origami for flexible electronics, sensing, and micro-robotics applications.

#### Acknowledgements:

We would like to acknowledge and thank our collaborators Hui Gao, Kibum Kang, and Jiwoong Park for MoS<sub>2</sub> growth, as well as Itai Cohen.

This work was supported by the Cornell Center for Materials Research with funding from the NSF MRSEC program (DMR-1719875) and the Research Experience for Undergraduates program (DMR-1460428 and DMR-1719875). Both MoS<sub>2</sub> and MoS<sub>2</sub>/copper sheets were fabricated at the Cornell Nanoscale Science and Technology Facility, a member of the National Nanotechnology Coordinated Infrastructure (NNCI), which is supported by the National Science Foundation (Grant ECCS-1542081).

#### References:

- Park, O. K. *et al.* Magnetic field controlled graphene oxide-based origami with enhanced surface area and mechanical properties. *Nanoscale* **9**, 6991–6997 (2017).
- Jamin, T., Py, C., Falcon, E. Instability of the Origami of a Ferrofluid Drop in a Magnetic Field. *Phys. Rev. Lett.* **107**, 204503 (2011).
- Piñeirua, M., Bico, J. & Roman, B. Capillary origami controlled by an electric field. *Soft Matter* **6**, 4491 (2010).
- Ahmed, S., Ounaies, Z., Arrojado, E. A. F. Electric field-induced bending and folding of polymer sheets. *Sensor Actuat. A-Phys.* **260**, 68–80 (2017).
- Mu, J. *et al.* Origami-inspired active graphene-based paper for programmable instant self-folding walking devices. *Sci. Adv.* **1**, e1500533 (2015).
- Geryak, R., Tsukruk, V. V. Reconfigurable and actuating structures from soft materials. *Soft Matter* **10**, 1246–1263 (2014).
- Xu, W. *et al.* Ultrathin thermoresponsive self-folding 3D graphene. *Sci. Adv.* **3**, e1701084 (2017).
- Miskin, M. Z., *et al.* Graphene-based bimorphs for micron-sized, autonomous origami machines. *Proc. Natl. Acad. Sci.* **115**, 466–470 (2018).
- Paulsen, J. D. *et al.* Optimal wrapping of liquid droplets with ultrathin sheets. *Nat. Mater.* **14**, 1206–1209 (2015).
- Van Honschoten, J. W. *et al.* Elastocapillary fabrication of three-dimensional microstructures. *Appl. Phys. Lett.* **97**, 014103 (2010).
- Kumar, D., Paulsen, J. D., Russell, T. P. & Menon, N. Wrapping with a splash: High-speed encapsulation with ultrathin sheets. *Science* **359**, 775 (2018).
- Huang, J. *et al.* Capillary wrinkling of floating thin polymer films. *Science* **317**, 650–653 (2007).
- King, H., Schroll, R. D., Davidovitch, B. & Menon, N. Elastic sheet on a liquid drop reveals wrinkling and crumpling as distinct symmetry-breaking instabilities. *Proc. Natl. Acad. Sci.* **109**, 9716–9720 (2012).
- Bae, J., Ouchi, T. & Hayward, R. C. Measuring the Elastic Modulus of Thin Polymer Sheets by Elastocapillary Bending. *ACS Appl. Mater. Interfaces* **7**, 14734–14742 (2015).
- Py, C. *et al.* Capillary origami: spontaneous wrapping of a droplet with an elastic sheet. *Phys. Rev. Lett.* **98**, (2007).
- Roman, B., Bico, J. Elasto-capillarity: deforming an elastic structure with a liquid droplet. *J. Phys.: Condens. Matter* **22**, 493101 (2010).
- Guo, X. *et al.* Two- and three-dimensional folding of thin film single-crystalline silicon for photovoltaic power applications. *Proc. Natl. Acad. Sci.* **106**, 20149–20154 (2009).
- Jiang, J.-W., Qi, Z., Park, H. S. & Rabczuk, T. Elastic bending modulus of single-layer molybdenum disulfide (MoS<sub>2</sub>): finite thickness effect. *Nanotechnology* **24**, 435705 (2013).
- Blees, M. K. *et al.* Graphene kirigami. *Nature* **524**, 204–207 (2015).
- Andrew, R. C., Mapasha, R. E., Ukpong, A. M. & Chetty, N. Mechanical properties of graphene and boronitrene. *Phys. Rev. B* **85**, (2012).
- Bahramian, A., Danesh, A. Prediction of liquid-liquid interfacial tension in multi-component systems. *Fluid Phase Equilib.* **221**, 197–205 (2004).
- Kang, K. *et al.* High-mobility three-atom-thick semiconducting films with wafer-scale homogeneity. *Nature* **520**, 656–660 (2015).
- Vitale, S. A., Katz, J. L. Liquid Droplet Dispersions Formed by Homogeneous Liquid-Liquid Nucleation: “The Ouzo Effect.” *Langmuir* **19**, 4105–4110 (2003).
- Branner, A. V., Hunter, T. G., Nash, A. W. The Quaternary System Acetic Acid-Chloroform-Acetone-Water at 25 °C. *J. Phys. Chem.* **44**, 683 (1940)

# Lactase CLEAs for the Valorization of Lactose Waste Streams

Deidra Ward<sup>1</sup>, Julie Goddard<sup>2</sup>

<sup>1</sup>Department of Chemical and Biomolecular Engineering, Clemson University, Clemson, SC 29631

<sup>2</sup>Department of Food Science, Cornell University, Ithaca, NY 14853

## Abstract

The formation of cross-linked enzyme aggregates [CLEAs] are a well-studied method of immobilizing enzymes. Immobilizing enzymes have many industrially relevant applications, particularly in the context of dairy processing. One of the byproducts during Greek yogurt production is acid whey. Acid whey is of particular interest since it has been shown by researchers at Corning, Inc. that treating the whey with immobilized lactase can convert this waste product into sweeteners. This treatment would add more value to this waste stream. In this study, we investigated lactase CLEAs for its potential use in the valorization of acid whey waste streams.

## Introduction

The dairy processing industry is a very lucrative and well-established industry. However, it is currently plagued with waste streams that do not have much current value. For example, during the production of Greek yogurt, acid whey is produced. Acid whey currently has no industrial use so it is mainly discarded. This presents both an environmental and economic problem.

However, researchers at Corning, Inc.<sup>1</sup> have discovered a method of treating acid whey with immobilized lactase in order to convert it into a sweetener. This process would add value to this waste stream, allowing the economic and environmental impact to be decreased. The method that these researchers discovered involves immobilizing the lactase onto a porous, inorganic carrier to treat the whey. This process, while successful, presents some issues since it has been shown that immobilization methods that involve

binding to a carrier results in a decrease in catalytic activity due to the introduction of a non-catalytic mass.

In order to overcome this limitation, we want to investigate cross-linked enzyme aggregates [CLEAs] for their potential use in the valorization of waste streams. CLEAs are a carrier-free method of immobilizing enzymes that combines both enzyme purification and immobilization into a single step<sup>2</sup>. This method of immobilizing enzymes is of industrial relevance due to its lower cost, recyclability, quick time-to-market, and its optimizable nature<sup>3</sup>. It has been shown that CLEAs have increased stability to changes in temperature and pH compared to the free enzyme<sup>4</sup>. This is of particular interest since in industrial settings, many streams are at extreme temperature and pH values.

Thus, we are developing a method of producing lactase CLEAs that can be used for the treatment of acid whey streams.

This work can then be expanded to other enzymes, such as glucose isomerase, to valorize waste streams.

## Materials and Methods

### *Lactase Purification*

Before being able to immobilize the enzyme, the lactase must be purified. The lactase was prepared in potassium phosphate buffer (0.1M, pH 6.8) and filtered through a 0.22 $\mu$ m PES syringe filter before centrifugal filtration was performed using the Amicon Ultra – 0.5 Centrifugal Filter Devices (MWCO 10k). Centrifugal filtration was performed for 15 minutes at 14000\*g and then flushed with 135 $\mu$ L of the potassium phosphate buffer twice. The resulting purified free enzyme lactase solution was then tested for its protein content or stored at 4°C.

### *CLEA formation*

**Protein content determination of purified lactase.** The protein content of the purified lactase solution was determined using a microplate BCA protein assay. Absorbance measurement were taken at 562nm and compared against a standard curve created from known concentrations of BSA. We assumed that the concentration of BSA was equal to that of the lactase.

**Production of lactase CLEAs.** After determining the protein content of the purified lactase, the free lactase solution was diluted to a concentration of 7mg lactase/mL potassium phosphate buffer. After diluting, the 320 $\mu$ L of the lactase was separated into 2mL centrifugal tubes and mixed with 1280 $\mu$ L of acetone using a rotator set to 40rpm for 30 minutes. After

mixing, 28.8 $\mu$ L of glutaraldehyde (50%) was added to each lactase-acetone mixture. This mixture was then vortexed for 15 seconds before sitting at room temperature for 22 hours in order to allow cross-linking to occur. After cross-linking, samples were centrifuged for 1 minute at 10 000\*g. The supernatant that resulted from centrifugation was decanted. This resulting CLEA was washed thrice by adding 1 mL of potassium phosphate buffer (0.1M, pH 6.8) and centrifuging for 1 minute at 10 000\*g. CLEAs were then stored in 640 $\mu$ L of the potassium phosphate buffer (0.1M, pH 6.8) at 4°C or characterized using the following methods. CLEAs with varying amounts of glutaraldehyde were made by adding 28.8 $\mu$ L of glutaraldehyde to 640 $\mu$ L of the diluted lactase or adding 14.4 $\mu$ L of glutaraldehyde to 640 $\mu$ L of the diluted lactase.

### *CLEA characterization*

**Scanning Electron Microscopy [SEM].** In order to observe the surface morphology of the CLEAs, SEM was performed. Samples were prepared by placing the CLEA onto aluminum foil and allowing the sample to air dry in a fume hood overnight. The air-dried samples were then sputter coated via gas flow sputtering before analyzing their surface structure.

**Protein content determination of CLEAs.** The protein content of the CLEAs were determined using a microplate BCA protein assay. To prepare the samples, CLEAs were vortexed until they began to break apart in the phosphate buffer. In order to increase this dispersion, CLEAs were physically separated using a syringe tip. Absorbance measurements were taken at 562nm and compared against a standard curve created

from known concentrations of BSA. We assumed that the concentration of the BSA was equal to that of the lactase CLEA.

## Results and Discussion

BCA protein assays for the CLEAs resulted in inconsistent concentration values. We would have expected the concentrations determined based on the BSA standard to all have been consistent. However, we found that concentrations varied greatly within samples, as well as across samples. Figure 1 highlights the inconsistent nature of these samples.

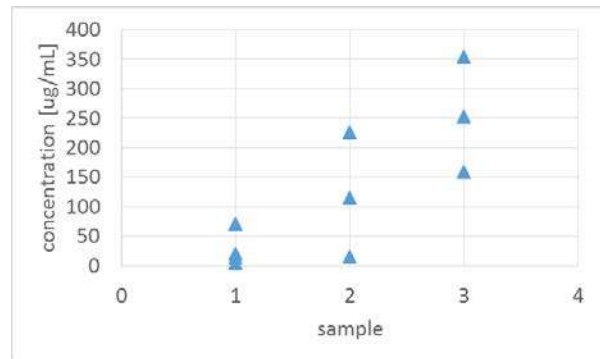


Figure 1. BCA protein analysis results for CLEAs

Because of the inconsistencies in the BCA protein assay, we began to investigate reasons for this discrepancy. Figure 2 showcases the standard curves that were produced from the BCA protein assays. These curves are quite consistent, leading us to determine that protein concentrations calculated via this method should be consistent.

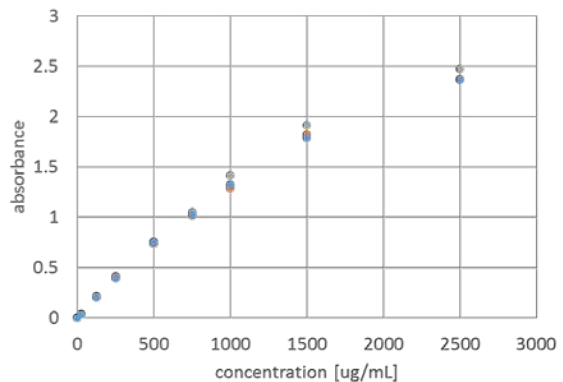


Figure 2. BCA protein assay standard curves used to determine concentrations of unknown samples

One possible reason for this discrepancy could be in the preparation of samples for the BCA protein assay. As described earlier, samples were prepared by vortexing the CLEA in the potassium phosphate buffer and trying to get it to disperse in the buffer by breaking it apart with a syringe tip. Seeing as this is a very crude way of trying to disperse the CLEA, it is highly probable that there was no uniformity across samples. Perhaps another method for dispersion, such as sonication, should be investigated further in the future.

Another possible reason for the inconsistent BCA protein assays could be the CLEA, itself. When cross-linking an enzyme, it is important to prevent excessive cross-linking. When there is excessive cross-linking, the structure of the enzyme changes and the activity is decreased. In order to determine if there was excessive cross-linking, we examined the SEM images of the CLEAs and found that the CLEAs had a smooth surface structure. This led us to hypothesize that the CLEAs were excessively cross-linked and if we decrease the amount of glutaraldehyde added to each sample, we can decrease the cross-linking and have CLEAs that are more easily

dispersed in potassium phosphate buffer. This would then allow us to test for its protein content more consistently.

When we investigated the effect of decreasing glutaraldehyde content on the surface roughness of the CLEAs, we found that as the amount of glutaraldehyde decreased, the roughness increased. We associated this increase in roughness with a decrease in cross-linking. This matched our hypothesis of less glutaraldehyde resulting in less cross-linking. We will investigate whether this results in more consistent characterization in the future.

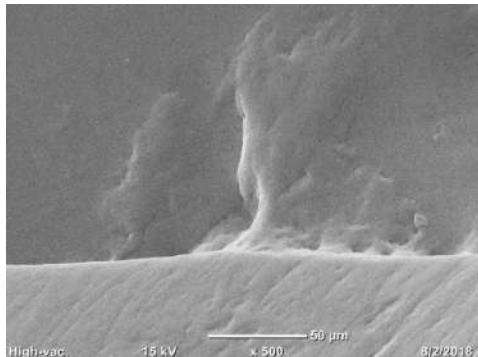


Figure 3. SEM image of CLEA with  $x$  amount of glutaraldehyde

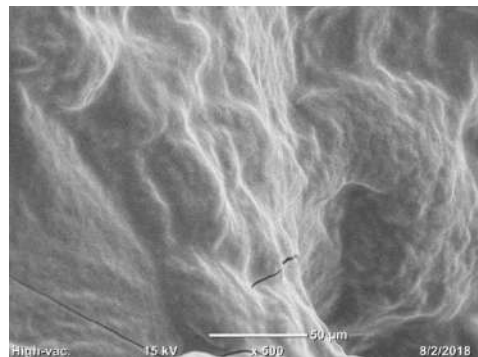


Figure 4. SEM image of CLEA with  $0.5x$  amount of glutaraldehyde

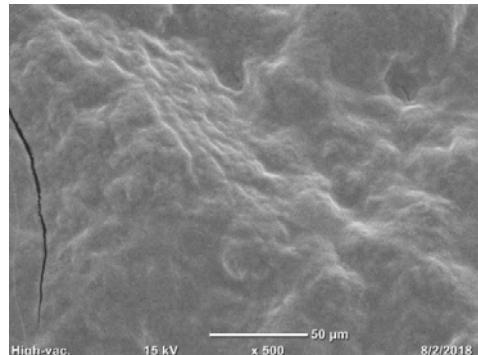


Figure 5. SEM image of CLEA with  $0.25x$  amount of glutaraldehyde

## Conclusions

The initial method that was used to produce lactase CLEAs resulted in CLEAs that were excessively cross-linked. This would have a negative impact on the activity of these enzymes, rendering them useless for our industrial application. However, by decreasing the amount of glutaraldehyde present during the cross-linking process, the degree of cross-linking can be reduced. This can then result in CLEAs that can be tested consistently for their protein content and catalytic activity.

In the future, we hope to develop a means of producing these CLEAs that result in an aggregate that retains enough activity to be used in our industrial application, along with being stable enough to be used at various temperatures and pH values.

## Acknowledgements

Thank you to Dr. Julie Goddard and the Goddard Lab Group for your mentorship and support. Thank you to the CCMR REU program funded by the NSF for this opportunity.

## References

1. Weetall, H., Yaverbaum, S.; (1973);  
*Patent No. 3,852,496*; Corning, NY;  
United States Patent Office
2. Sheldon, R. A.; *Biochemical Society Transactions* **2007**, 35 (06), 1583-1587
3. Sheldon, R. A.; *Organic Process Research & Development* **2011**, 15, 213-223
4. Li, L., Li, G., Coa, L., Ren, G., Kong, W., Wang, S., Guo, G., Liu, Y.; *Journal of Agricultural and Food Chemistry* **2015**, 63, 894-901

# The Statistics of the A-B Transition of $^3\text{He}$ in Thin Slab Confinement

John Wilson<sup>1,2</sup>, Dmytro Lotnyk<sup>2</sup>, Michael Terilli<sup>2</sup>, and Jeevak Parpia<sup>2</sup>

<sup>1</sup>State University of New York at Geneseo, Geneseo, New York <sup>2</sup>Cornell Center for Materials Research, Cornell University, Ithaca, New York

Helium 3 has two superfluid phases. The transition between these phases is first order, displaying hysteresis and supercooling. Here, the effects of confinement to a thin slab geometry on this phase transition are presented. A  $1.1\ \mu\text{m}$  channel connected two chambers filled with liquid helium 3. The first chamber, the heat exchange chamber, was heated and cooled via adiabatic nuclear magnetization. Quartz tuning forks being driven by an AC current were present in both chambers. The frequency and Q factor of these forks were directly measured. Phase transitions correspond to discontinuities within both the Q factor and the frequency of these forks, allowing for the state of the fluid to be inferred. Using this, the location of the A to B transition in the bulk regions were mapped.

## I. INTRODUCTION

Helium is the second most common element in the universe. In nature it has two common isotopes:  $^3\text{He}$  and  $^4\text{He}$ .  $^3\text{He}$  is a fermion with a nuclear spin of  $\frac{1}{2}$ . As a result,  $^3\text{He}$  obeys Fermi-Dirac statistics and, by proxy, the Pauli Exclusion Principle.  $^4\text{He}$  however, is a boson with a spin of 0.  $^4\text{He}$  therefore obeys Bose-Einstein statistics, and notably does not obey the Pauli Exclusion Principle. Both isotopes exhibit interesting properties in low temperature ranges. At atmospheric pressure, helium is the only element to stay liquid until temperatures near absolute zero [4]. Furthermore, both types of isotopes undergo superfluid transitions at low temperatures. A superfluid is a purely quantum mechanical system. As a result, they each provide systems that are extremely interesting to physicists.

## II. MOTIVATION

$^4\text{He}$  undergoes a superfluid transition at  $2.17\ \text{K}$  at vapor pressure.  $^3\text{He}$  meanwhile, undergoes its superfluid transition at a much lower temperature of about  $1\ \text{mK}$  at vapor pressure. Their superfluid transitions differ in temperature by orders of magnitude due to the different statistics governing their composite atoms. This extreme nature of superfluid  $^3\text{He}$  causes it to be harder to study in its superfluid state, but also much more complex and interesting.

### A. Theory

$^3\text{He}$  was theorized to have many different phases of superfluidity. Two sets of scientists each posited the existence of one of the two phases that actually were observed in the bulk. Anderson and Morel proposed a phase with non-s-wave [5] pairing states with two spin substates of  $S_z = \pm 1$ . This became identified with the A Phase. Balian and Werthamer proposed a p-state that could con-

tain the  $S_z = \pm 1$  spin substates as well as the  $S_z = 0$  spin substate [1]. This was identified to be the B phase. The first observation of superfluid  $^3\text{He}$  in 1971 was the subject of the 1996 Nobel Prize, awarded to Lee, Richardson and Osheroff at Cornell.

The existence of two superfluid phases with different possible spin substates creates a system that is much more complex than that of superfluid  $^4\text{He}$ . Furthermore, the transition between these two phases is first order and provides a chance to learn a lot about phase transitions in a system that is purely quantum mechanical [1]. The phases of  $^3\text{He}$  can be seen in Figure 1.

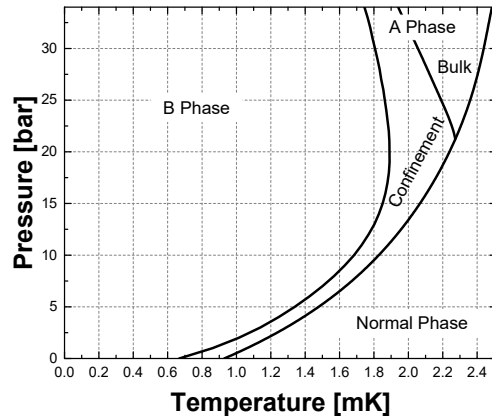


FIG. 1. The Phase Diagram of  $^3\text{He}$ . Note the poly critical point at a Pressure of  $21.22\ \text{bar}$  and Temperature of  $2.23\ \text{mK}$ . The poly critical point is where the A phase and B phase have the same free energy at the superfluid transition. It is also the meeting point of the first order (A to B) transition and second order ( $T_c$  vs  $P$ ) lines. The region close to this poly critical point is of great interest.

$^3\text{He}$ 's net magnetic dipole leads to interesting interactions to study. This net dipole leads to interactions with magnetic fields. This net magnetic dipole also causes superfluid  $^3\text{He}$  to resemble metallic superconductors. When

$^3\text{He}$  undergoes its superfluid transition, the individual atoms act similarly to electrons in Cooper pairs. In the formation of Cooper pairs, an electron travels through a lattice of heavy, positively charged particles. As it travels, a small positive "wake" forms behind it. At low enough temperatures, this positively charged wake is not re-equilibrated. Another electron traveling will be attracted to that positively charged wake, and thus effectively to the first electron [1].

In liquid  $^3\text{He}$  this interaction does not happen at lattice sites, but instead within the viscous liquid. A traveling  $^3\text{He}$  particle will leave a wake of spin polarization opposite to its own. At low enough temperatures, this wake remains long enough for a second  $^3\text{He}$  particle to interact with that wake. The second  $^3\text{He}$  will see the wake as an oppositely polarized magnetic dipole, and be attracted to it. As a result, the  $^3\text{He}$  atoms will essentially be attracted to each other and align their magnetic dipoles to be parallel with each other. The result is two  $^3\text{He}$  particles that now form a  $^3\text{He}$  cooper pair with a spin of 1. This integer spin means the pair can now be described with Bose-Einstein statistics, and form a superfluid [1].

### B. Effects of Confinement

In this paper, we will describe the observation of these transition points in the bulk fluid cooled through a thin slab. Confining the  $^3\text{He}$  to a thin slab geometry changes the interparticle interactions by reducing the dimensions of the chamber to below the mean free path of thermal transport in the bulk. This allows the A phase to form at pressures and temperatures lower than it otherwise would in the bulk phase, as seen in Figure 1, because confinement energetically favors the A phase over the B phase. Within the channel, the A phase is promoted over the B phase because of the manner in which  $^3\text{He}$  particles orbit each other as a cooper pair. Thus, the mechanism causing nucleation of the bulk B phase from the A phase may be studied more closely. Confinement also changes properties of heat flow within the system. This creates an interesting setting for the response and relaxation times of a perturbed system to be studied.

## III. EXPERIMENTAL APPARATUS

In the field of low temperature physics, there are many difficulties to overcome. Reaching low temperatures, measuring the low temperatures without disturbing the system, isolating the experimental apparatus, and transferring cold liquid as well as heat are a few of these [2]. There are also a number of steps prior to cooling that involve purifying the helium gas. Due to how specific each of these steps are, they will not be discussed in detail here. These many challenges cause experimental apparatuses in low temperature physics to require multiple stages and methods for cooling.

### A. Overview

The apparatus used to carry out this experiment is no exception. A brief overview of the setup is presented here and expanded on in later subsections. A precooling stage liquefies the helium before it is transferred to the main dewar. Liquid helium is transferred periodically [6] into the dewar. Inside this dewar, there is an insulated vacuum vessel immersed inside a tank filled with liquid  $^4\text{He}$ .  $^4\text{He}$  is continuously admitted into the chamber, called the 1 K pot. There it is pumped on to achieve a temperature of around 1.2 K. At the same time, pure  $^3\text{He}$  is pumped on in the still of a dilution refrigerator and then returned into the refrigerator. The  $^3\text{He}$  is precooled by the  $^4\text{He}$  liquid, and then sent for further heat exchanging in the refrigerator. There a dilute mixture is used to cool the pure  $^3\text{He}$  further in a series of heat step exchangers. See Figure 2.

Pure  $^3\text{He}$  is independently admitted into the sample chambers. These chambers are linked to the nuclear cooling stage where adiabatic nuclear demagnetization occurs. In the nuclear demagnetization stage, metal nuclei are manipulated with a magnetic field to take advantage of their spin entropy and vary their temperature. This metal cools the heat exchange chamber. The heat exchange chamber is connected to the isolated chamber via a  $1.1 \mu\text{m}$  height channel. The quartz tuning forks are located in these two chambers, and the experiment is carried out within these two. See Figure 3 for a diagram of these chambers.

### B. The Precooling Stage

The precooling stage involves liquefying and pumping on  $^4\text{He}$ . Pumping on a liquid bath decreases the pressure above the liquid. Inherent vapor pressure causes the most energetic of the atoms to leave the liquid at sufficiently low pressures. This process carries away some of the heat from the liquid bath. However, pumping on liquid  $^4\text{He}$  below 1K more than 50% of the  $^4\text{He}$  may be lost due to this process. Pumping much past this point serves only to offset a heat leak, albeit inefficiently.

### C. Dilution Refrigerator

Prior to entering the dilution refrigerator,  $^3\text{He}$  is precooled by contact with  $^4\text{He}$  bath at 4 K. It is then liquefied by contact with the pumped  $^4\text{He}$  bath at 1.2 K. This  $^3\text{He}$  is sent into heat step exchangers. These heat step exchangers are cooled by a  $^3\text{He}/^4\text{He}$  dilution refrigerator. This is depicted in Figure 2. The fridge operates by taking advantage of Fermi-Dirac statistics of the  $^3\text{He}$ . A small amount of  $^3\text{He}$ , 6.4% exactly at 0 K, may be dissolved into solution in superfluid  $^4\text{He}$  at vapor pressure. In this solution it makes sense to approximate the  $^3\text{He}$  particles as having a slightly heavier mass. This is

because of the Kelvin drag [7]. In the mixing chamber of the dilution refrigerator liquid  $^3\text{He}$  sits in its normal state on top of the dilute mixture.

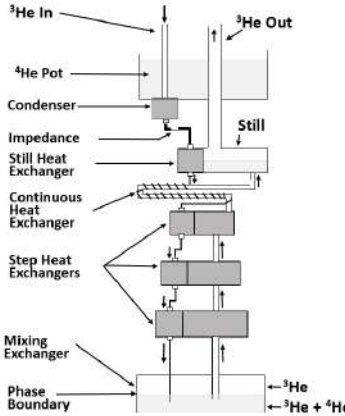


FIG. 2. A labeled diagram of the dilution refrigerator. Note the still where the dilute mix is pumped on is separate from the mixing chamber. Diagram based off a similar diagram from Experimental Principles and Methods Below 1K [2].

This dilute mixture of  $^3\text{He}$  in solution in superfluid  $^4\text{He}$  is pumped on in a still above the mixing chamber.  $^3\text{He}$  atoms are removed first because of their higher vapor pressure. As  $^3\text{He}$  is removed, the remaining solution is cooled via evaporative effects. The  $^3\text{He}$  gas is removed and recirculated back into the fridge. A  $^4\text{He}$  liquid pot cools the incoming  $^3\text{He}$  to about 1.1K. The pressure is kept high on the  $^3\text{He}$  so it condenses back into liquid form. The  $^3\text{He}$  is then cooled by the dilute mixture as it is added back into the mixing chamber through step heat exchangers. When  $^3\text{He}$  is put back into the mixing chamber, the atoms will find it energetically favorable not to enter the dilute mixture again. As a result, as the  $^3\text{He}$  atoms are returned, they return to the pure  $^3\text{He}$  side. When the hotter atoms of  $^3\text{He}$  from the still are drawn off, this results in the extraction of  $^3\text{He}$  from the dilute side of the mixture. To maintain the concentration of  $^3\text{He}$  in  $^4\text{He}$  at 6.4%, enough  $^3\text{He}$  atoms will cross the  $^3\text{He}$  to  $^3\text{He} - ^4\text{He}$  interface to maintain a constant distribution of momenta in the pure and dilute solutions. The act of crossing from the pure to dilute mix is similar to evaporation. As a result, it lowers the energy of the dilute mix, compensates for the heat leak, or provides cooling power.

Up to 1K the quasi-classical nature of  $^3\text{He}$  is apparent, but it still resembles  $^4\text{He}$  in everything besides mass and vapor pressure. However, on the order of 0.1K, the quantum nature governed by Fermi Dirac statistics becomes extremely apparent. The pure  $^3\text{He}$  sample is cooled by heat step exchangers and the refrigerator. After this stage the cooled  $^3\text{He}$  is sent into the sample chambers.

#### D. Nuclear Demagnetization

The final step in the cooling process is the adiabatic demagnetization of Copper and Praesodymium nuclei. These nuclei have been spin polarized by contact with the dilution refrigerator and being placed in a strong magnetic field on the order of 7.5 T. They are cooled using a dilution refrigerator to about 7 mK. This causes the spin entropy to be reduced significantly as the spins increasingly populate the lowest energy states. When the demagnetization stage is isolated thermally, the entropy stays constant save for the effects of a heat leak. Thus, the temperature of the stage can be varied by raising or lowering the magnetic field.

A metal sinter is connected to one of the two sample chambers. The result is a thermocoupling between the nuclear cooling stage and one chamber of the experimental apparatus. This experimental apparatus can be seen in Figure 3. The two sample chambers are filled with pure  $^3\text{He}$ , so cooling the metallic nuclei and the connected sinter also cools the  $^3\text{He}$ . In this way the temperature of our  $^3\text{He}$  could be varied to observe transitions within the  $^3\text{He}$  with extremely small heat currents. This technique is usable for roughly a month: due to stray heat leaks it must be regenerated and can't be run as a truly continuous process.

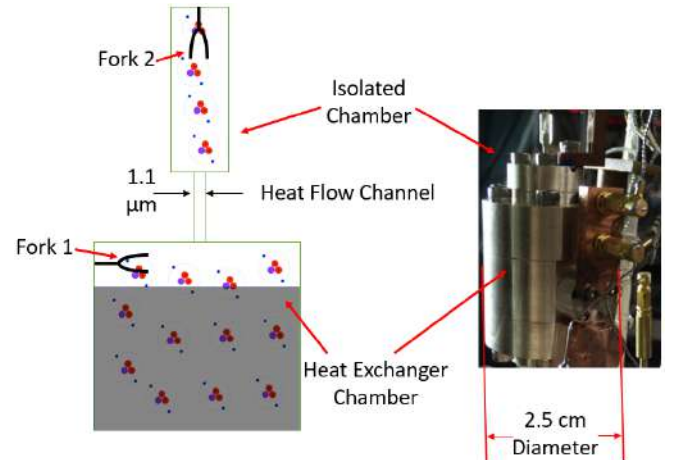


FIG. 3. The heat exchange and isolated chambers. In each of these chambers there are quartz tuning forks. The chambers are connected via a small channel where confinement occurs. The isolated chamber has a volume of 0.14 cc, the heat exchange chamber has a volume of 1.5 cc.

## IV. EXPERIMENTAL METHODS

In the experimental space there was a heat exchange chamber, and an isolated chamber. In each of the chambers there was a quartz tuning fork. The quartz tuning forks were driven via an AC current. From these forks the frequency and Q factor were recorded. The Q factor

is defined as:

$$Q \stackrel{\text{def}}{=} \frac{f_r}{\Delta f} \quad (1)$$

Where  $f_r$  is the resonant frequency and  $\Delta f$  is calculated from the full width half max of a measured distribution, and then related to frequency. The resonant frequency is measured from the input signal or alternating current.  $\Delta f$  is calculated from the resulting power loss of the forks as they oscillate in the liquid. This power loss relates to the frequency distribution of the forks oscillation.

A transition in  $^3\text{He}$  corresponds to sharp changes in both frequency and Q. By measuring Q, we were able to identify both superfluid to normal state transitions. The second order normal to superfluid transition is accompanied by a discontinuity in the slope of Q factor versus temperature. The first order transition between A and B phase corresponds to a discontinuity of Q factor versus temperature. Measuring Q factor and frequency also allowed us to calculate the temperature of the superfluid in the isolated chamber, even though it was weakly thermally coupled from the melting curve thermometer.

### A. Challenges of Low Temperature Thermometry

Here we will justify the use of a quartz tuning fork to indirectly measure temperature rather than a more traditional thermometer. One of the biggest challenges to low temperature thermometry is the necessity of calibration points within the system. At temperatures below 4.2 K only helium remains in the liquid phase. At 2.17 K  $^4\text{He}$  undergoes its lowest known transition to a superfluid. As a result, only  $^3\text{He}$  provides phase transition points for calibration before this point.

A common measurement technique for temperature is a resistor with a known function of resistance to temperature. For example thermocouples with differing metal conductors could have been used. These leads could be connected to the point of interest. The problem with this method is that at the thermometer power decreases rapidly at low temperature.

A capacitor may be used for temperatures below the superconducting transition point. A capacitor could measure the pressure of a gas or liquid by correlating it to the bowing of a thin plate. Then, the pressure may be measured and correlated to a temperature. This works because vapor pressure is closely related to the temperature of a substance. Alternatively, the capacitance of a liquid filled space may be measured. The density of the liquid may then be transduced because the atoms will have a dielectric constant. More atoms between the capacitors causes a greater dielectric contribution, or a higher capacitance. Unfortunately, this is a weak thermometer and is not usable in temperature regimes of interest here. A resistor could be used until its superconducting transition, then one could switch to a parallel plate capacitor and measure vapor pressure. The

problem with this is that the resistor and capacitor duo would still need to be supplemented by an instrument that could directly provide the state of the substance being measured. Another problem is the thermal coupling of the thermometer to the liquid  $^3\text{He}$ . The thermometer would have to remain in constant equilibrium with the system in order to give accurate temperature.

### B. Justification for a Quartz Tuning Fork

Many of these problems are avoided entirely if we instead use a quartz tuning fork to measure the viscosity of the substance. In both liquid and superfluid  $^3\text{He}$  viscosity is directly correlated by temperature in well characterized ways. Therefore, using the Q factor to infer the viscosity, we may calculate the temperature of the  $^3\text{He}$ . This removes the challenge of thermal coupling because a quartz tuning fork relies only on inertial and viscosity mediated interactions. The exact process for calculating temperature is expanded on in the data analysis section.

Yet another benefit of the quartz tuning fork is discontinuities and jumps in the Q factor and frequency correspond with the first and second order phase transitions of  $^3\text{He}$  at low temperatures. This creates the calibration points necessary to correlate the Q factor to temperature.

## V. DATA COLLECTION

Two modes of data collection were employed to gather statistics. Both essentially changed the temperature at constant pressure. These two methods were: slow temperature change ramps through transition points, and overdriving the quartz tuning forks to create pulses of heat.

### A. Nuclear Magnetization Controlled Temperature Ramps

The first method, slow cooling or warming ramps, was done with adiabatic demagnetization. The theory behind this was discussed earlier in the experimental set up section. A magnetic field can be decreased slowly to offset a heat leak, or quicker to cool the fluid. Conversely, a magnetic field may also be increased to heat the fluid. Heating and cooling ramps were often at rate of about 0.01 mK/hr. This method provides precise control over temperature and was used to identify the superfluid transition as well as the A-B transition. The benefits of this method include minimizing the heat current between chambers. This allowed for a closer observation of the mechanisms causing the phase transition. Having a high heat current runs the risk of initiating the process that causes B phase nucleation. Moreover, the slow temperature ramps allow for more accurate temperature measurements of points exactly where the transitions were

occurring. A slower temperature ramp directly translates to a higher resolution of points for each transition. From this form of data collection, statistics on the phase transitions of  $^3\text{He}$  were recorded.

### B. Overdriving the Quartz Tuning Forks

The second method, overdriving the tuning forks, was done by greatly increasing the AC amplitude driving their oscillation. This was usually done for about 100 seconds, although the time varied up to 300 seconds for very low temperatures. Overdriving caused them to vibrate at much larger amplitude, adding mechanical heat to the system. This provided two interesting pieces of data. The increase in temperature allowed us to observe phase transitions in the presence of a high heat current during the thermal re-equilibration, while perturbing the fluid allowed us to observe the relaxation time of the fluid.

In experiments discussed here, the fork in the isolated chamber was overdriven, bringing the fluid above the normal to superfluid transition point. The fluid was then allowed to cool back into equilibrium. This allowed us the chance to observe both the superfluid transition, as well as the AB transition. From this, the relaxation time of the fluid as well as the temperature at which the AB transition occurred were recorded.

## VI. DATA ANALYSIS

Python and Matlab were used for data treatment. Python was used for fitting and treating data obtained from slow temperature ramps. Matlab was used for fitting the data gathered while pulsing and for determining the relaxation time.

### A. Temperature Ramp Analysis

Data collected at a particular pressure was imported and treated using a class structure. The class structure allowed us to create a program that could uniformly treat all the data with the same operations and assign important statistics of the run as attributes to the class. The data was cut to only work with one monotonically changing temperature ramp at a time. The temperature recorded from the melting curve thermometer was then fit with a low order polynomial. Pressure was input and converted into a known superfluid transition temperature using data from Greywall [3]. This temperature is consistent for a known pressure. As a result, when the superfluid transition point was identified in the heat exchange chamber, we may account for the offset of the melting curve temperature to read this. This can be seen in Figure 4.

Because fork 1 is in the heat exchange chamber, the melting curve thermometer gives temperature readings

that are close to the true temperature of the fork, aside from a small thermal lag. Using the superfluid transition point, we can find the temperature of the melting curve at that time, and shift it up or down to match the temperature given by Greywalls formula. This shift comes in the form of a small correction to the constant term in our temperature fit. It is usually on the order of 0.01 mK. Even though the heat exchange chamber is thermally coupled to the point the melting curve thermometer reads temperature, this offset may have been caused by a small thermal lag. Due to this adjustment, the temperature fit may be used for the temperature near fork 1.

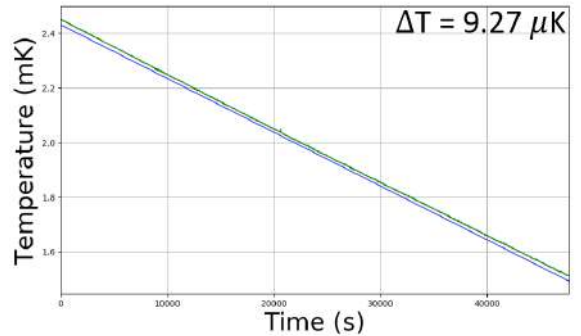


FIG. 4. Temperature of the Melting Curve Thermometer (Green) and Temperature of our fit (Blue) after shifting temperatures to the correct normal phase to superfluid transition point.

In  $^3\text{He}$  the viscosity changes with temperature [1]. In damped harmonic oscillators in a fluid, the Q factor also changes with viscosity. Therefore, given that we know the temperature of fork 1 and its Q factor, we may correlate the two. Thus, we can fit fork 1's Q as a function of time. We can then correlate Fork 1's Q factors to the corrected and fitted temperature for the same time.

We fit Q to time with a high order polynomial and a step function of the following form:

$$Q(t) = \sum_{n=0}^N a_n * t^n + b * u(t - t_{AB}) \quad (2)$$

Where b is the magnitude of the discontinuous jump in Q factor at the A to B transition, and  $t_{AB}$  is the time of the jump. Using a step function along with a polynomial fit allows us to account for the first order phase transition without wasting time on an extremely high polynomial fit. This is shown in Figure 5.

Furthermore, we can use the Q factor in fork 2 to identify the superfluid transition point within this fork. Like in fork 1, the measured Q factor is related to the temperature at that time. As a result, we were able to correlate the temperature at this point to the superfluid transition point in fork 1. Using that point as a start, we applied a nearest neighbor closest point search via a binary sort.

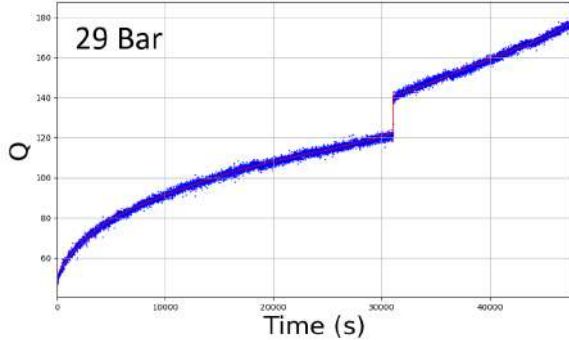


FIG. 5. The Q factor of Fork 1 being fit with a high order polynomial and a step function. In this specific example, the polynomial is a 7<sup>th</sup> order polynomial.

Using this, we mapped each point in fork 2 to a point in fork 1 in Q space. The correlation between Q and temperature meant that we could then correlate the points in fork 2 to temperatures at points with similar Q factors in fork 1. As a result, we could find the temperature of A to B transitions in both bulk and in isolation.

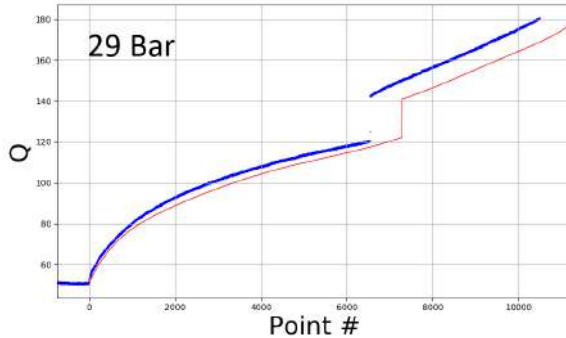


FIG. 6. The fit of Fork 1 overlaid on the Q factor from Fork 2. The points of the normal to superfluid transition were shifted to match so that the k-NN Search could be applied. Notice point number was used for the search instead of time, this was to help use a consistent indexing of the data when searching..

This allowed us to identify transition points in pressure-temperature space and relate them to the phase diagram of <sup>3</sup>He.

### B. Pulsing Data

The pulsing data was treated in Matlab. The data was cut so that the temperature was monotonically increasing or decreasing. This allowed for the pulses to be indexed, and the temperature to be fit with a low order polynomial. When looking at Q over time, pulses in superfluid were inverted compared to pulses in the normal state. This can be seen in Figure 7.

The background would be removed using a polynomial fit of points just before the pulse was launched. These

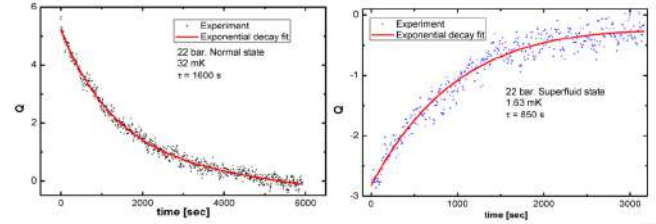


FIG. 7. Fits of pulses in both the superfluid and normal state of <sup>3</sup>He. The pulses are inverted because Q increases with rising temperature in the normal state due to lower viscosity, while it decreases with rising temperature in the superfluid.

pulses would have a median filter applied to them to reduce the noise. After this filter, an exponential fit would be applied. The fit would be in the form:

$$Q(t) = B + A_0 * \exp\left(\frac{-t + t_0}{\tau}\right) \quad (3)$$

This was used to estimate the parameters B,  $A_0$ ,  $t_0$ , and  $\tau$ . Then, a small linear time dependent term was used to further reduce error as it appears from removing the background. In this second fit, the parameters from the first fit were used as guesses for the second fit. The second fit came in the form:

$$Q(t) = B + K * t + A_0 * \exp\left(\frac{-t + t_0}{\tau}\right) \quad (4)$$

Where K is a correction to the background removal in the form of a linear slope. From this we recorded the relaxation time,  $\tau$ .

## VII. RESULTS

Statistics were gathered on the transition points within the bulk heat exchange chamber, as well as within the isolated chamber. The timing and temperature at which these transitions occurred were recorded. Collecting the timing gave us insight into which chamber was nucleating the A-B transition first. While the temperature at which the phase transition occurred helped us understand when supercooling occurred, and what conditions made the A or B phase more favorable in confinement. The points can be seen overlaid on the <sup>3</sup>He Phase Diagram in Figure 8.

The A to B Transition in cooling occurred first in time in the Heat Exchange Chamber for intermediate pressures, at both 25 bar and 22 bar. However, at the highest pressure of 29 bar, the transition in both chambers was observed to occur at the same time. For lower pressures below the poly critical point, A to B transitions were only observed in the isolated chamber, and no B to A transitions were observed in heating.

During pulsing, the relaxation time of the superfluid and normal state were measured. The measured  $\tau$  in

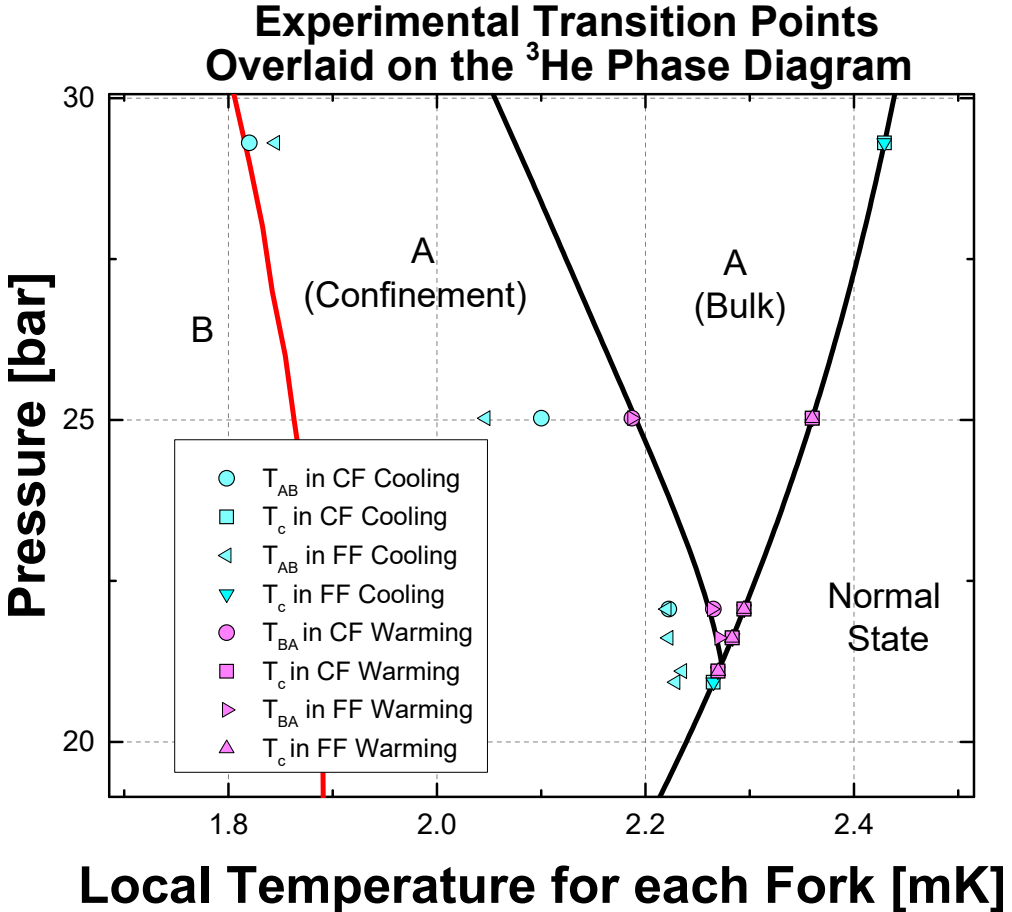


FIG. 8. Experimental transition points overlaid on the  $^3\text{He}$  phase diagram within the region of interest surrounding the poly critical point. HE stands for the heat exchanger chamber. IC stands for the isolated chamber.

normal state is shown in Figure 9, on the left. The relaxation time was measured across a large temperature range. The  $\tau$  was compared to the expected relaxation time calculated using Greywalls thermal conductivity and heat capacity data [3]. The thermal resistance was also calculated using  $\tau$  and the heat capacity. The thermal resistance is equal to relaxation time divided by the heat capacity. This resistance is shown in Figure 9, on the right. Low temperature behavior of relaxation time is expected to scale with  $T^2$ , but instead shows scaling with  $T$ . This is not explained here, but we hypothesize that it is possibly due to the confined geometry. The thermal transport mean free path exceeds the separation of the parallel plates at both zero bar and 22 bar.

### VIII. DISCUSSION

At the highest pressure, the two chambers underwent the A to B phase transition at the same time. This suggests one of two results. The first is that the nucleation

was occurring in the  $1.1 \mu\text{m}$  channel and nucleating both the heat exchange chamber and the isolated chamber at the same time. The second is that the transition occurred in the heat exchange chamber below the A-B transition point within confinement. This may have then nucleated the channel, which would in turn cause the A to B transition in the isolated chamber. This entire process would happen quickly enough that it would appear instantaneous to our measurement equipment. This can be seen in Figure 10a.

However, at intermediate pressures the heat exchange chamber underwent the A to B transition earlier in time, seen in Figure 10b. This might be expected, because in cooling the heat exchange chamber will reach lower temperatures first. However, the A to B transition occurred at different local temperatures for both channels. This suggests that the heat exchange chamber underwent the A to B transition, then sometime later the isolated chamber underwent a separate A to B transition. This suggests that a different mechanism was causing the nucleation of the B phase here compared to high pressures.

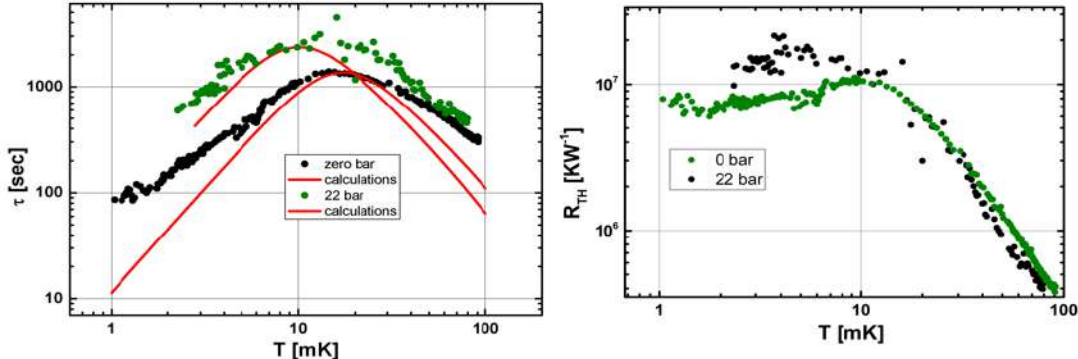


FIG. 9. Relaxation time (left, directly measured) and thermal resistance (right, calculated using data from the Greywall text [3]) .

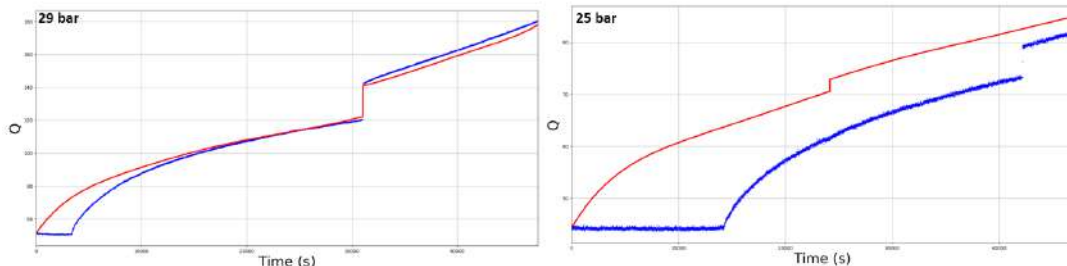


FIG. 10. Q factor over time for both forks at two different pressures. Note that 29 bar shows the transition happening simultaneously while the 25 bar shows the transitioning happening first in the heat exchange chamber.

We see the B phase nucleation occur first in time in the heat exchange chamber, but still at lower temperatures than predicted by the phase diagram of  ${}^3\text{He}$ . The fact that the heat exchange chamber is undergoing its A to B transition first suggests that supercooling is less energetically favorable than in the isolated chamber. This is likely due to the presence of the sinter, this presents a diversity of sites where the B phase may be nucleated first. A short time later, we see fork 2 show signs that the isolated chamber has undergone its own A to B transition. The fact that the supercooling of the A phase continues longer in the isolated chamber suggests that it has less sites on its surface to promote the B phase and disrupt the supercooling.

At pressures below the poly critical point, we no longer see the A phase in the heat exchange chamber. Since there is no magnetic field, the A phase should not be nucleated in the bulk below the poly critical point. Because there is no observed A phase in the heat exchange chamber, we can conclude that there is no stray magnetic field on the experiment cell. We continue to observe the A to B transition in the isolated chamber, further demonstrating the supercooling of phases within the isolated chamber. The appearance of the supercooled A phase below the poly critical point can only be due to the present of the A phase in the channel. Rather than creating the energetically preferred B phase, the fluid follows a path where

the interfacial energy between the confined  ${}^3\text{He}$  and the bulk  ${}^3\text{He}$  in the isolated chamber is minimized by seeding the A phase into the isolated chamber. Thus, the A phase observed below the poly critical point is solely present due to interfacial physics. On warming only the B phase is observed until the critical temperature in the isolated chamber.

On warming, we see slight time differences between the heat exchange chamber's and the isolated chamber's B to A transition. However, upon accounting for offsets, the B to A transition occurs at the thermodynamically appropriate temperature. Thus, it is apparent there is no superheating of the B to A transition. This is likely because the A phase at a minimum is present in the channel and can seed the B to A transition when it is the preferred phase.

## IX. CONCLUSION

While results presented here indicate new mechanisms may be responsible for the A to B phase transition, these mechanisms are not yet well characterized. In the future, experiments will aim to characterize these mechanisms and learn more about the effects of confinement on  ${}^3\text{He}$ .

Experiments will also be done to further explore the high pressure regime and learn more about the effects

occurring there. The energetically favored phase in the channel and exploration of supercooling in the channel is particularly interesting. Regions of pressure below the poly critical point will also need to be explored. In these

regions super cooling is observed in the isolated chamber but not in the heat exchange chamber. Studying this region will provide further insight into the mechanism causing nucleation of the B phase in the A phase.

- [1] Dobbs. *Helium Three*. Oxford University Press, 2000.
- [2] Lounasma. *Experimental Principles and Methods Below 1K*. London and New York: Academic Press, 1974.
- [3] D. Greywall, Page 33, **Volume 33, Number 11**, Physical Review B, 1986.
- [4] Phase is a bulk property of a substance, at temperatures very near to absolute zero single atoms or particles are usually being manipulated or measured. As a result, describing the phase of an element at pico-Kelvin temperatures is a rather abstract thing to do. However, at temperatures in the mili-Kelvin or even micro-Kelvin scale helium is the only fluid element.
- [5] S-wave pairing refers to the common naming convention of

the angular momentum of electrons in orbital shells. The s-wave pairing refers to the first state that has no angular momentum, and therefore only one possible projection onto the z-axis. Non-s-wave pairing implies that the state of zero angular momentum does not exist as an outcome of this interaction.

- [6] Transfer occurred every 3 to 4 days throughout the duration of this experiment.
- [7] Kelvin drag refers to the interactions of  $^3\text{He}$  particles and the  $^4\text{He}$  superfluid caused by the inertia of the  $^4\text{He}$  particles. It is not the same as a viscosity of the liquid, which is effectively nonexistent because  $^4\text{He}$  is in its superfluid state here.

# Optimizing Pulse-Echo Ultrasound Instrumentation Using Two-Dimensional Computational Modeling

Jiatian Wu<sup>1</sup>, Sayak Ghosh<sup>2</sup>, and Brad Ramshaw<sup>2</sup>

<sup>1</sup>Department of Physics, Emory University, Atlanta, GA 30322

<sup>2</sup>Department of Applied and Engineering Physics, Cornell University, Ithaca, NY 14853

**Abstract**—An unique pulse-echo ultrasound technique is developed to measure the speed of sound in condensed matters and helps identify the second-order phase transitions of the matters. On the one hand, ultrasound measurement is advantageous for its simplicity and efficiency compared to other thermodynamics measurements. The current apparatus setup is sensitive to detect subtle changes of vibrations due to its use of high-frequency sound waves. On the other hand, its sensitivity occasionally leads to wave interference in the results for some unknown reason. Thus, a computational model is built to simulate the wave propagations of a sample in the apparatus in order to find out the potential factors affecting the wave propagations and be able to optimize the design for future sound velocity measurements in numerous materials.

## I. INTRODUCTION

The thermodynamic properties of condensed matters, such as superconductors and heavy fermion compounds, have some peculiar behaviors regarding to their phase transitions, including heat capacity  $C_p = -T\partial^2F/\partial^2T$ , magnetic susceptibility  $\chi = T\partial^2F/\partial H^2$ , and elastic modulus  $c_{ij} = \partial^2F/\partial\epsilon_i\partial\epsilon_j$  [3]. In the macroscopic view, these properties are the second order derivatives of the free energy  $F$  with respect to temperature and become discontinuous at the point of a critical temperature  $T_c$ . In the microscopic view, the electronic structure of a material changes during its phase transition and result in breaking the original symmetry of the system[5].

While the phase transitions of conventional materials are usually simple for being the first order derivative of the Gibbs free energy, examples like the transformation of ice from water, the second-order phase transitions have much more interesting physical properties and complex structures in condensed matters. Some well-known second-order phases are like superconductivity and magnetism. For example, when iron reaches a curie temperature 1034K, its magnetization changes drastically and it becomes paramagnetic. Thus, thermodynamics plays an important role in todays condensed matter research as it is an efficient way to find phase transitions. Studying thermodynamics of a range of different materials helps us categorize their phases and possibly identify the "hidden order" phase of materials.

Elastic modulus is one of the thermodynamic properties that our lab adopts to find the phase transitions of materials. It is a coefficient that describes how a material is being deformed elastically by the force. In a mathematics sense, the elastic modulus  $c_{ij}$  is the curvature of the free energy

with respect to strain  $\epsilon$ . However, the elastic modulus is not easy to be measured directly. Instead, we measure the speed of sound  $v$  traveling in the material, because elastic modulus  $c_{ij}$  is correlated to the speed of sound as  $v = \sqrt{c_{ij}/\rho}$ , where  $\rho$  is the material density.

Our lab uses a pulse-echo ultrasound technique which applies the high-frequency sound waves through a piezoelectric transducer to a testing sample to probe the speed of sound of the material. The technique was first developed by Suslov et al. to measure the speed of sound of a material and its attenuation as a function of a external variable, like temperature or magnetic field [7]. Our group modifies the technique so that it can both eliminate large fraction of electrons and allow digital post-processing [4]. Since phase transitions often happen abruptly, ultrasound measurement has its advantages in tracking even the subtle change of phase compared to other thermodynamics measurements. The technique is also efficient in collecting data because the whole measurement usually takes place in tens of microsecond or hundreds of nanosecond.

However, when we tested the samples using the ultrasound technique in the previous work, some wave interference happened occasionally and prevented us from measuring the accurate attenuation of the material. To better understand the cause of the interference and be able to reduce it, a computational simulation of the instrumentation is needed to probe the wave propagation in the sample.

## II. METHODS

### A. Pulse-Echo Ultrasound Instrumentation

The instrumentation was set up as shown in Fig. 1 below. By applying a short burst of electronic signals on a piezoelectric transducer, the signals were converted from electrical signals to sound waves and transmitted through a crystal sample. The waves traveled back were received by the same transducer and created an "echo train" in the plot (see Fig.3). As the waves propagated in the sample, we could measure the absolute phase  $\phi$ , the distance between the "echo trains" and hence calculate the absolute speed of sound  $v$ ,  $v = 2\pi fl/\phi$ , where  $f$  is the frequency we apply to the transducer, and  $l$  is twice the sample length. The phase transition happens instantaneously and hence is easy to miss if the measurement is not precise enough. To further improve the precision, we measured the phase velocity of the pulse waves instead of

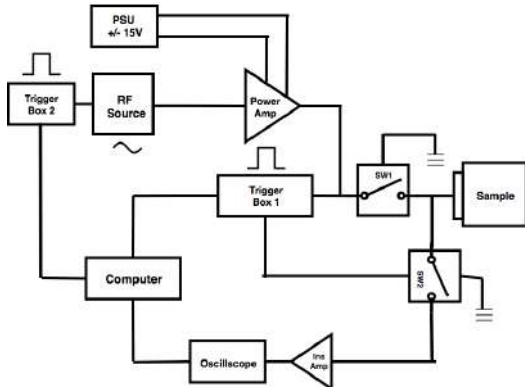


Fig. 1: Schematic representation of the ultrasound instrumentation. The instrumentation has a complete power supply and filter system. The program LabVIEW first sends out a short burst of electronic signals to trigger box 1 [Tektronix AFG1062] to generate square-pulse signals. A trigger box controls a switch(SW) [ZFSWHA-1-20+]. At the same time, a radio-frequency(rf) source [Agilent 83650B] generates continuous microwaves and the waves are amplified by a power amplifier [Mini-Circuits® 15542] with the 15V power supply(PSU) [BK Precision 1672]. The two signals combine together to create a mix of standing waves. The waves travel back and forth through a sample and send back as electrical signals. The signals are amplified by a instrumentation amplifier [MITEQ]. The signals are received by a oscilloscope [Tektronix MDO3104] and processed by the computer.

its group velocity. We calculated the change of the speed of sound,  $\Delta v$ ,

$$\Delta v = -2\pi f l \frac{\Delta\phi}{\phi^2},$$

where  $\Delta\phi$  is the phase shift of the sound waves in an echo. The sample was placed in a low-temperature environment and its change in speed of sound was recorded by lowering the temperature. We would also need to know the fundamental frequency of the transducer since the transducer is excited when the harmonic resonances are applied.

The technique was different from Suslovs setup as it could record the positions of each microwave inside an "echo train" instead of estimating the positions of all waves by averaging. Having more data points improved the accuracy of attenuation of the sample as it could now calculate the exponential decay function by data fitting and get the loss factor  $\Gamma$ .

### B. Computational Model

A finite-element analysis program COMSOL Multiphysics was used to simulate the wave propagations in a crystal sample on the top of a piezoelectric transducer to find out the cause of the wave inference. The built-in package Piezoelectric Device module included both Structural Mechanics and Electric Potential modules and therefore was used for the simulation. The simulation was solved deliberately as a

two-dimensional problem for its significantly smaller computational cost. A pulse-echo electric potential was applied on a side of the transducer to simulate the processed signals sent from the instrumentation. The governing differential equation for the linear elastic material is given to solve for the material's displacement field  $\vec{u}$ ,

$$\rho \frac{\partial^2 \vec{u}}{\partial t^2} = \nabla \cdot s + \vec{F}v,$$

where  $\rho$  is the density, and  $s$  is stress.

The material we chose was Tungsten for the crystal sample for its high density and lithium niobate( $LiNbO_3$ ) for the transducer for its common use in the lab (see Table 1 for parameter values). The boundary conditions of the sample were suppose to be free on all four sides but instead set to be low-reflective on the left and right sides to reduce the wave reflection distractions (see Fig.2a). The damping coefficients of both the sample and transducer were taken from the literatures [1] if possible and, otherwise, estimated to match with the experiment results (see Table 2). In consideration of damping effects, eq.2 is modified to be as

$$\rho \frac{\partial^2 \vec{u}}{\partial t^2} + \alpha_{dM} \rho \frac{\partial \vec{u}}{\partial t} = \nabla \cdot (s + \beta_{dK} \frac{\partial S}{\partial t}) + \vec{F}v,$$

where  $\alpha_{dM}$  is the mass damping parameter for the sample and  $\beta_{dK}$  is the stiffness damping parameter for the transducer. Mesh was also taken care due to the short time duration of the high-frequency pulse.

TABLE I: Mechanical and electrostatic properties of the materials used in the COMSOL model

Material Name	Tungsten	Lithium Niobate	"Half" Tungsten *
Density ( $kg/m^3$ )	17800	4700	8900
Young's modulus (Pa)	3.6e11	N/A	1.8e11
Poisson's ratio	0.28	N/A	0.14

\* "Half" Tungsten is used later for adding an extra layer in between the sample and the transducer.

A time-domain study was taken in each simulation, and the time step was determined by obtaining at least five or more degree of freedom within the wavelength of ultrasound  $\lambda$ [2]. We then took a frequency-domain study to test the resonances of the transducer. Parametric Sweep was implemented in the time domain study to verify the results.

Several aspects of the sample were tested to see how the change would affect the wave propagation in it and thereby optimize the design, including increasing the roughness of the sample surfaces, finding the better sample width, and adding an extra layer between the sample and the transducer.

The roughness of a surface can be described by the composition of many elementary waves and the spatial frequency of the surface oscillations (see Fig. 2b). According to Sjodin, surface roughness can be quantified as follows,

$$f(x) = \sum_{m=-M}^{M} a(m) \cos(2\pi(mx) + \phi(m)),$$

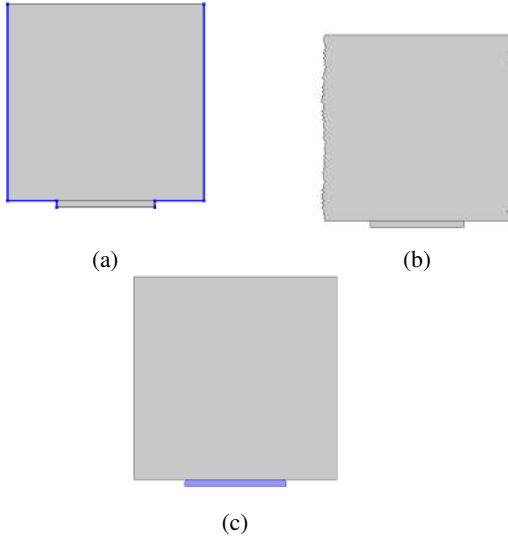


Fig. 2: (a) Low-reflective boundary conditions. (b) Adding fillets on the edges. (c) Increasing the surface roughness of the sample.

where  $x$  are spatial coordinate, and  $m$  are spatial frequency [6]. By increasing both the amplitude and spatial frequency, we studied the effect of surface roughness on wave propagations. Sample size and wave interference were studied as well.

TABLE II: Parameters used by default.

Variable	Value (unit)	Description
$f$	5 (MHz)	Frequency
$N$	50	Spatial frequency resolution
$b$	0.5	Spectral exponent
$W_t$	3 (mm)	Transducer width
$H_t$	0.2 (mm)	Transducer height
$W_s$	6 (mm)	Sample width
$H_s$	6 (mm)	Sample height
$\beta_{dk1}$	2e-10 (s)	Sample stiffness damping
$\beta_{dk2}$	2e-7 (s)	Transducer stiffness damping parameter

\* Some parameters values change in the simulation for testing purpose.

### III. RESULTS

The default simulation has a  $6\text{mm} \times 6\text{mm}$  sample and a  $3\text{mm} \times 0.2\text{mm}$  piezoelectric transducer. The wave function is  $\sin(2\pi ft)$ , where  $f$  is  $5\text{MHz}$  and  $t$  is  $2.5e - 5$  seconds in  $3e - 9$  time step. The results shows the ideal situation if no wave interference occurs (see Fig.3).

The same setting is applied to a frequency domain study, and we get the following harmonic resonances of the transducer (see Fig.4). The resonance happens at around the expected frequency value where the transducer length is a multiple of half of its corresponding wavelength,  $L = n(\lambda/2)$ . Wavelength  $\lambda$  can be calculated as  $\lambda = v/f$ , where  $v$  is the speed of sound in the material.

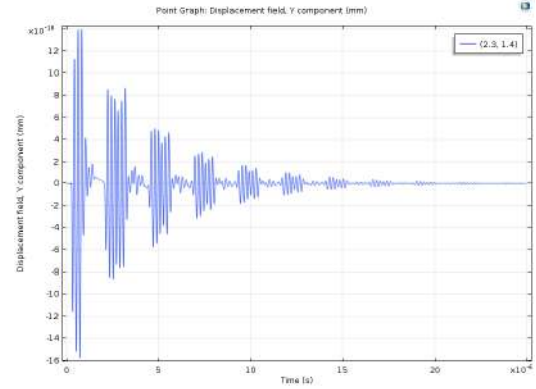


Fig. 3: The wave propagation in the sample. The electric signals turn into sound waves and traverse in the sample with no wave interference. The displacement of a point (2.3,1.4) is plotted as a function of time.

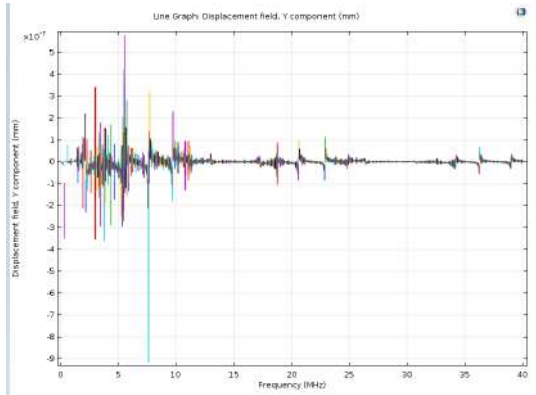


Fig. 4: The resonance of the transducer in a frequency domain when the transducer is 1mm. The simulated resonances happened around 6.68, 20.6, 34.4 MHz, as calculated.

#### A. Size

We defined relative width  $W_r$  as the ratio of the transducer and the crystal sample,  $W_r = W_{transducer}/W_{sample}$  and tested different transducer widths in a  $4\text{mm} \times 4\text{mm}$  sample. The relative width is critical to the wave propagation, as neither being too wide or too narrow helps reduce the wave interference. When the relative width was larger than  $3/4$ , the wave fronts were too wide and quickly hit the sample boundaries before reaching to the other side; when the relative width was smaller than  $1/8$ , the edges of the transducer were too close to each other and generated relatively large wave interference. The relative width around  $1/4$  had the minimized wave interference (see Fig.5). Adding fillets on the corners of the transducer also helped reduce the interference greatly, as expected (see Fig. 2c).

#### B. Surface Roughness

The surface roughness helped noise reduction in some degree when the waves echo back for three times or more, depending on the wave frequency. In order for the roughness to take effect, the spatial wavelength of the surface roughness

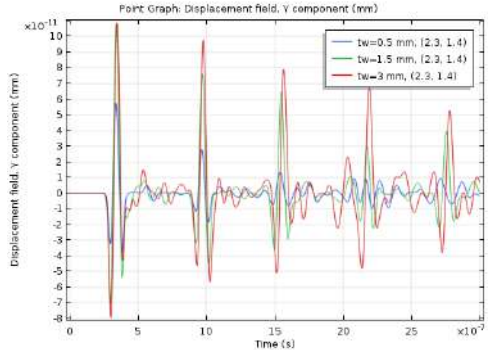


Fig. 5: The wave propagations in the sample when the width of the transducer varies.

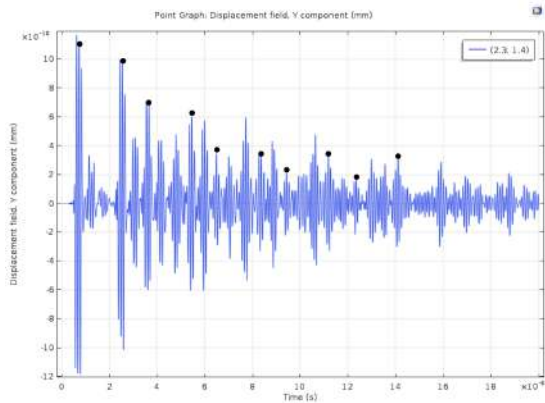


Fig. 6: The wave propagation in the sample when an extra layer of 1.25mm thickness is added in between. Knowing the relative speed of sound, we can distinguish when the sound wave reaches to the point (2.3, 1.4), and they are marked in black dots in the figure. The sixth and eighth wave echoes have a smaller amplitude than the seventh and ninth echoes, which is caused by the wave interference. When the wave travels through the added layer, it allows the layer to vibrate and generate additional waves. The two waves have a phase difference, and they combine in the sample, creating constructive and destructive interferences shown in the plot.

should be approximately equal to or smaller than the order of magnitude of the sound wave, which was tens of micrometers if a 50MHz sound wave was applied.

### C. Wave Interference

A layer was added in between the sample and the transducer to simulate the potential interference of the glue that is used to attach the two parts together in the experiment. An observation was found as the thickness of the layer increased. When the thickness of the layer was an odd multiple of the quarter sound wavelength  $\frac{n}{4}\lambda$  ( $n = 1, 3, 5, \dots$ ), the wave propagation showed similar wave patterns where the superpositions of the waves occurred at the same positions. Such wave interference would intervene the wave amplitude measurement and hence lead to a wrong value of the loss factor  $\Gamma$  (see Fig. 6).

## IV. CONCLUSION

The work was done to show that the wave interference in the previous experiments may cause by the excessive amount of glue between the sample and transducer. Since the experiment runs in micrometer-scaled system, it is not an easy task to reduce the glue thickness to be insignificant compared to the rest of the setup. Further optimization is needed to find a thickness that can generate in-phase waves to avoid the wave interference. Further work can be done to find the quantitative correlation between the wave frequency and surface roughness of sample materials to minimize the noise.

## ACKNOWLEDGEMENT

I would like to thank Ramshaw group for welcoming me to their group in this summer, especially Dr. Brad Ramshaw and Sayak Ghosh for their kind help and support. This project was supported by the Cornell Center for Materials Research and the Research Experience for Undergraduates program.

## REFERENCES

- [1] I Chowdhury and S Dasgupta. Computation of rayleigh damping coefficients for large systems. 2003.
- [2] W Frei. Simulation tools for solving wave electromagnetics problems. 06 2015.
- [3] K Modic, Maja D. Bachmann, Brad Ramshaw, Frank Arnold, Kent Shirer, Amelia Estry, Jon Betts, Nirmal Ghimire, E D. Bauer, Marcus Schmidt, M Baenitz, Eteri Svanidze, Ross McDonald, Arkady Shekhter, and Philip J. W. Moll. Resonant torsion magnetometry in anisotropic quantum materials. 02 2018.
- [4] Brad Ramshaw, K Modic, Arkady Shekhter, Philip J. W. Moll, M K. Chan, Jon Betts, Fedor Balakirev, A Migliori, Nirmal Ghimire, E D. Bauer, F Ronning, and Ross McDonald. Annihilation of weyl nodes in the extreme quantum limit of taas. 04 2017.
- [5] J. P. Sethna. Order Parameters, Broken Symmetry, and Topology. *eprint arXiv:cond-mat/9204009*, April 1992.
- [6] B. Sjodin. How to generate random surfaces in comsol multiphysics®. 2017.
- [7] A. Suslov, Bimal K. Sarma, J. Feller, and J. Ketterson. Ultrasonic instrumentation for measurements in high magnetic fields. i. continuous magnetic fields. *Review of Scientific Instruments*, 77(3):035104, 2006.